

Institute of Low Temperature and Structure Research
Polish Academy of Sciences



Doctoral dissertation

Synthesis, modeling and
spectroscopic evaluation of selected
 Tm^{3+} , Pr^{3+} , Ho^{3+} doped
and Yb^{3+} co-doped colloidal photon
avalanching nanoparticles

mgr inż. Magdalena Dudek

Supervisor: prof. dr hab. inż. Artur Bednarkiewicz,
Auxiliary Supervisor: dr Katarzyna Prorok

2023
Wrocław (Poland)

Acknowledgements

I would like to sincerely acknowledge:

My **Supervisor prof. Artur Bednarkiewicz** for the inspiration for scientific work, substantive discussions and guidance, help in the analysis of research results and in the preparation of scientific articles and the doctoral dissertation, as well as for the support and motivation shown in good and bad moments,

My **auxiliary Supervisor Dr Katarzyna Prorok** for the help given to me from the beginning of my scientific research, especially for the introduction to the research matters, accurate suggestions for the research, help during preparation of doctoral dissertation as well as for the support,

Colleagues, especially former and current members of the **LuNASI group** for their help and friendly working atmosphere,

Zuzanna Korczak and **Wojciech Piotrowski** for their support during the doctoral studies,

My **Friends** for faith in my abilities, interest in my research topics, inspiring discussions, motivation and spent time,

My **Parents, Sister** and **Grandparents** for their love, constant support, understanding, patience, faith in my abilities and help in moments of doubt.

This work was supported by the projects 2018/31/B/ST5/01827 and 2021/43/B/ST5/01244 funded by National Science Center Poland (NCN).

Calculations have been carried out using resources provided by Wroclaw Centre for Networking and Supercomputing (<http://wcss.pl>), grant No. 529

I. Table of contents

I. Table of contents	5
List of abbreviations	9
List of symbols	13
1. The purpose of the dissertation	15
2. Abstract	17
3. Streszczenie w języku polskim	21
4. Scientific resume of the author	25
5. Statement on contribution to the scientific articles preparation	30
6. Composition of the doctoral dissertation	33
II. Introduction	35
7. Luminescence	36
8. Lanthanide ions	39
8.1. Spectroscopic properties	40
8.1.1. Energy level structure	40
8.1.2. Energy transfer mechanisms	46
8.1.3. Mechanisms of upconversion emission	48
8.2. Choice of host lattices for upconversion	51
9. The phenomenon of photon avalanche	52
9.1. Mechanism and key conditions	52
9.2. History and literature review	54
9.2.1. PA in thulium ions	56
9.2.2. PA in praseodymium ions	58
9.2.3. PA in holmium ions	60
9.3. Applications of photon avalanching materials	63
9.3.1. Medium IR photon counters	63
9.3.2. Photon avalanche lasers	64
9.3.3. Thermometry	65
9.3.4. Superresolution imaging	66
9.3.5. Biosensing	69
9.3.6. Optical computing	70

III. Experimental	71
10. Materials – syntheses and characteristics methods	71
10.1. Synthesis methods	72
10.1.1. Preparation of precursor in a form of lanthanide acetates	72
10.1.2. Core β - NaYF_4 nanocrystals	73
10.1.3. Core LiYF_4 nanocrystals	74
10.1.4. Ellipsoidal β - NaYF_4 core@shell nanoparticles.....	75
10.1.5. Spherical shell deposition.....	75
10.1.6. LiYF_4 core@shell nanoparticles	76
10.1.7. LiYF_4 microcrystals.....	77
10.2. Structure and morphology characteristics.....	77
10.3. Spectroscopic measurements	77
10.3.1. Absorption spectra	78
10.3.2. Excitation spectra, emission spectra and lifetimes	78
10.3.3. Optical avalanche characteristics.....	78
11. Theoretical ESA absorption spectra calculations	80
12. Calculations of S and PA_{TH} values.....	83
13. Simulations of PA	84
IV. Results and discussion	86
14. PA in Tm^{3+} doped LiYF_4 crystals	86
14.1. Materials	86
14.2. Results	88
14.3. Conclusions	96
15. PA in Pr^{3+} and Yb^{3+} co-doped β - NaYF_4 nanocrystals	97
15.1. Materials	97
15.1.1. Singly Pr^{3+} doped β - NaYF_4 colloidal nanocrystals	97
15.1.2. x% Pr^{3+} and 15% Yb^{3+} co-doped β - NaYF_4 colloidal nanocrystals.....	100
15.1.3. NaYbF_4 and β - NaYF_4 crystals	102
15.2. Spectroscopic results.....	104
15.2.1. Basic spectroscopy measurements	104
15.2.2. Anti-Stokes emission	107
15.2.3. PA in a function of temperature	113
15.3. PA Simulations.....	115
15.4. Conclusions	125

Table of contents

16. Other PA investigations.....	127
16.1. PA in Tm ³⁺ doped as well as Tm ³⁺ and Yb ³⁺ co-doped NaYF ₄ nanocrystals	127
16.2. Ho ³⁺ doped as well as Ho ³⁺ and Yb ³⁺ co-doped NaYF ₄ nanocrystals	131
16.3. Er ³⁺ and Yb ³⁺ co-doped NaYF ₄ nanocrystals.....	136
17. Conclusions	139
18. References.....	143
V. Annexes.....	159
List of samples synthesized by author of the dissertation.....	159
Index of Figures	161
Index of Tables	167

List of abbreviations

A – acceptor

ABS – absorption

ANP – avalanche nanoparticles

ATPE – energy transfer upconversion, fr. *addition de photon par transferts d'énergie*

bAC – bulk avalanching crystal

BS – beam splitter

cANP – avalanching core nanoparticle

CD – energy downconversion

C-Dots – carbon dots

CET – cooperative energy transfer

CL – cooperative luminescence

CR – cross-relaxation

csANP – avalanching core-shell nanoparticle

CT – charge transfer

D – donor

DM – dichroic mirror

DNA – deoxyribonucleic acid

DRE – differential rate equations

ED – electric dipole

EDS – Energy Dispersive X-Ray Spectroscopy

EMU – energy migrated-mediated upconversion

ESA – excited state absorption

ET – energy transfer

EtOH – ethanol

ETU – energy transfer upconversion

FM – flipped mirror

FMS – Stark double frequency modulation

FMUS – Stark ultrasound double frequency modulation

FPs – fluorescent proteins

FRET – Förster Resonance Energy Transfer

FWHM – Full width at half maximum

GSA – ground state absorption

HRTEM – high-resolution transmission electron microscopy

ICSD – Inorganic Crystal Structure Database

IR – infrared

IRQC – infrared quantum counter

Ln – Lanthanides

Ln^{3+} – lanthanide ion

LS – Russel-Saunders coupling

MD – magnetic dipole

MeOH – methanol

MIR – medium infrared

MPA – migrating photon avalanche

MPR – multi-phonon relaxation

NDF – neutral density filter

NIR – near infrared

NSOM – near-field scanning optical microscopy

OA – oleic acid

ODE – 1-octadecene

PA – photon avalanche

PAET – phonon assisted energy transfer

PASSI – photon avalanche super resolution imaging

PA_{TH} – photon avalanche pump power threshold

PFS – point spread function

PM – power meter sensor

PMT – photomultipliers

QDs – quantum dots

RE – rare earths

RNA – ribonucleic acid

RT – room temperature

S – slope of the s-shaped dependence of luminescence intensity in a function of pump power density

SEM – Scanning Electron Microscopy

SPA – sensitized photon avalanche

STED – Super resolution stimulated emission depletion

TEM -Transmission Electron Microscopy

TFA – trifluoroacetic acid

UC – energy upconversion

UCNPs – upconverting nanoparticles

UV – ultra violet

XRD – X-Ray Powder Diffraction

μAC – avalanching microcrystal

List of symbols

List of symbols

A_{aCS}, A_{CS} – absorption cross section [cm^2] (ESA spectra calculations)

D_{AV} – parameter describing an increase of luminescence intensity
when doubling pump power density

H_E – Hamiltonian of the electron system

H_O – Hamiltonian of the interaction of each valence electron with the atomic nucleus

$H_{S.O.}$ – Hamiltonian of the spin – orbit coupling

I_L – luminescence intensity

I_P – pump power density $\left[\frac{W}{cm^2}\right]$

P_c – critical pump power density $\left[\frac{W}{cm^2}\right]$

W_{CR} – rate of cross – relaxation [s^{-1}]

$W_{JJ'}$ – probability of nonradiative transition between J and J' energy levels

W_{NR} – rate of non – radiative transition [s^{-1}]

$[Xe]$ – electron configuration of Xenon

k_B – Boltzman constant, $0.695 [cm^{-1} \cdot K^{-1}]$

m_s – Spin Quantum Number

r_i – distance of the "i" electron

$t_{50\%}$ – time necessary to achieve the half of luminescence intensity counting
from switch the laser on [s]

t_{avr} – average lifetime [s]

σ_{ESA} – absorption cross section from excited energy level [cm^2]

σ_{GSA} – absorption cross section from ground energy level [cm^2]

τ_R – rise time [s]

$\hbar\omega$ – matrix phonon energy [cm^{-1}]

E – photon energy [J], [eV]

c – speed of the light; $c = 3 \cdot 10^{10} \left[\frac{cm}{s}\right]$

F – Lorentz force; $F = 1.8$ (ESA spectra calculations)

λ_a – wavelengths between Stark components (ESA spectra calculations)

F – photoexcitation flux

J – total angular momentum

L – orbital moment

$N(x)$ – population of respective energy level (DRE calculations)

P – number of phonons required for overcome energy gap

S – spin moment

T – temperature [K]

U – parameter strictly connected with an electronic transition

V – Columb interaction

b – branching ratio

l – Orbital Quantum Number

m – Magnetic Quantum Number

n – Principal Quantum Number

n – refractive index of the matrix

e – elementary charge; $e = 1.60218 \cdot 10^{-19}$ [C]

h – Planck constant; $h = 6.626 \cdot 10^{-34}$ [J · s]

ΔE – energy gap [cm^{-1}]

Ω – Judd – Ofelt parameter depending on the matrix [cm^2]

β – parameter descrbing probabilitly of photon avalanche

λ – wavelength [nm]

ξ – constant of spin orbit – coupling

τ – lifetime [s]

1. The purpose of the dissertation

The main objective of the present dissertation was to synthesize and comprehensively evaluate spectroscopic properties of colloidal fluoride nanoparticles doped with lanthanide ions (Ln^{3+}) exhibiting the photon avalanche (PA) phenomenon. To achieve this goal, numerous technical, synthetic, spectroscopic and modelling tasks have been undertaken.

The first technical goal was to design and build a setup to synthesize and optimize the procedure of thermal decomposition of lanthanide salts synthesis of colloidal NaYF_4 and LiYF_4 nanocrystals in a core and core-shell architectures. The second task was to synthesize a series of nanocrystals doped individually with lanthanide ions, mainly Tm^{3+} , Pr^{3+} , Ho^{3+} in a variable concentrations. Some particles, especially noteworthy samples with Pr^{3+} ions were co-doped with Yb^{3+} ions.

The next specific task was to evaluate, based on X-ray Powder Diffraction (XRD) measurements, if synthesized materials are crystallographically pure. Secondly, the detailed goal was to prepare size distributions of synthesized crystals using Transmission Electron Microscopy (TEM) pictures of the materials. The next task was to perform basic spectroscopic characteristic of synthesized materials by measurements of absorption, excitation and luminescence spectra as well as luminescence kinetics for selected doped and co-doped nanocrystals. The specific goal were PA investigations of particular synthesized materials. Because of complex nature of photon avalanche phenomenon and numerous sophisticated and not commonly available measurement techniques, the studies presented in this dissertation would be not possible without strong cooperation between chemist and physics in the research group. The objectives were to determine, what optical ions concentration is optimal for PA, how PA properties change with the avalanching material sizes as well as learning about the impact of passivation of the crystallites with an undoped shell on PA features. The next detailed objective was to compare the experimental results with theoretical, obtained by differential rate equations (DRE) simulations of PA and their interpretation. Moreover, theoretical modeling of PA behavior helps to understand mechanism of the phenomenon and predict of influence of different energy transitions on the PA features. Because PA requires negligible absorption from ground energy state comparing with effective excited state absorption and the measurements of absorption spectra from the excited energy level of the ion are complicated, to gain additional knowledge, theoretical ESA spectra were calculated. All these theoretical calculations and simulations were aiming at understanding PA mechanism and further facilitating the design of PA materials.

2. Abstract

Among different kinds of energy excitation upconversion (UC) processes, where the emitted photons have higher energy than the one absorbed, photon avalanche – PA is unique due to a highly nonlinear photoluminescence intensity increase in a response to a minute rise of photoexcitation source pump power density. As a result, the dependence of luminescence intensity in a function of pump power density exhibit a characteristic “S”-shape. A characteristic feature of PA process is a distinct PA pump power threshold (PA_{TH}), above which the luminescence intensity increases in highly nonlinear way following power law with power factor, slope (S) of the s-shaped curve, larger than 5. The PA itself, was first observed in the 1979 year in Pr^{3+} doped $LaCl_3$, which were investigated aiming to design of medium IR (MIR) photons quantum counter. From those times, the phenomenon became an interesting topic for many researchers, who have reported it in materials doped with different lanthanide ions. Initially, PA was investigated in bulk crystals, glasses and waveguides, mostly in cryogenic temperatures. However, it became clear that the observation of avalanche emission at the micro or nanoscale would enable a range of new applications of avalanche materials, such as use in bioimaging or in the design of active elements in biosensors. Until recently, obtaining the PA at nanoscale was a challenge, however PA emission was finally demonstrated in Tm^{3+} doped $NaYF_4$ nanocrystals at room temperature (RT) for the first time. The optimal concentration was found as 8% of Tm^{3+} . Typically, cross-relaxation (CR) processes, which are more efficient at high dopant concentrations, lead to luminescence concentration quenching and are competitive to emission or energy UC processes. However, in the case of avalanche emission, CR processes are highly desirable, because they increase an effectiveness of a positive feedback (energy loop) leading to the multiplication of the population of the level responsible for effective absorption from the excited state. Beside Tm^{3+} doped, PA was observed also in Pr^{3+} , Yb^{3+} co-doped nanocrystals. Nevertheless, the impact of materials size on PA properties have not been studied before and the present dissertation reports it. Two sets of $LiYF_4$ crystals were prepared and studied – the behavior of crystals doped with 3% and 8% Tm^{3+} was compared, with size as a variable parameter. In the first case, nano and microcrystals were compared with the corresponding 3% Tm^{3+} doped single crystal. In the second

case, nano and microcrystals with higher, 8% Tm^{3+} doping, were compared. In addition, the nanocrystals came in two versions – a doped core and identical nanocrystals whose surface as passivated with an undoped LiYF_4 . The materials were excited by a single mode solid-state laser generating 1064 nm wavelength beam and the PA emission at 800 nm and 475 nm was observed. The characteristic properties of avalanche emission – nonlinearity and threshold were investigated. It has been observed that the PA threshold values decrease as the size of the test material increases, simultaneously, an increase in the slope of the “S” curve with decrease of the material size was observed. The presented results related to PA in Tm^{3+} doped crystals were enriched with modeling of the avalanche emission behavior aiming to understand a mechanism of PA observed in Tm^{3+} ions. A practical demonstration of avalanche nanoparticles (ANP) for sub-diffraction imaging was prepared in collaboration. Sub-diffraction imaging of core-shell nanocrystals doped with 3% of Tm^{3+} ions confirmed the possibility to achieve down to 125 nm spatial resolution.

The present dissertation include also the description of PA phenomenon observed in a Pr^{3+} (0.1%, 0.3%, 0.5% or 0.7%) and Yb^{3+} (15%) co-doped core and core-undoped shell NaYF_4 nanocrystals. The materials were excited with a single mode diode generating 852 nm wavelength beam and consequently the PA emissions at 482 nm and 607 nm were observed. While multicolor avalanche emission in materials co-doped with Yb^{3+} and Pr^{3+} ions has been previously demonstrated, the results presented in this dissertation contain important, new elements as well as enrich and clarify knowledge. Firstly, an influence of crystals architecture, namely core and core-shell on a PA properties was investigated. Moreover, the influence of broad Pr^{3+} ions concentration (0.1%, 0.3%, 0.5%, 0.7%) on the PA characteristics was reported. Furthermore, some articles wrongly assign the emission of Pr^{3+} ions around 610 nm as coming from the $^1\text{D}_2$ level. In a present work, the correct origin of the 607 emission in fluorides was experimentally verified and attributed to the $^3\text{P}_0 \rightarrow ^3\text{H}_6$ energy transition. Moreover, a relatively simple theoretical model of PA in a Pr^{3+} , Yb^{3+} co-doped system was prepared aiming to understand, how particular energy transitions influence the PA emission properties. The phenomenological model evidenced, that under excitation conditions studied here, PA is present only in a Pr^{3+} and Yb^{3+} co-doped materials, in contrast

to singly Pr^{3+} doped materials. This feature was also confirmed experimentally. Namely, core and core-shell NaYF_4 nanocrystals singly doped with Pr^{3+} ions in a wide range concentration: 0.1%, 0.5%, 1%, 3%, 5%, and 8% were excited with 852 nm, however no emission was observed.

The present dissertation includes also investigations aiming to verify the possibility of obtaining PA in nanocrystals doped with other lanthanide ions. Characteristic features of PA phenomenon were observed in Tm^{3+} (3%, 8%) doped as well as 20% Yb^{3+} and Tm^{3+} (4% or 8%) co-doped cores-shell NaYF_4 nanocrystals under 1059 nm photoexcitation. Moreover, NaYF_4 nanocrystals doped with Ho^{3+} ions (0.5%, 2%) as well as co-doped with 20% Yb^{3+} and 0.5%, 1%, 2%, 4% or 8% of Ho^{3+} ions were investigated under 1059 nm and 980 nm photoexcitation, however these excitation condition were not suitable to generate PA emission. Furthermore, core and core-shell nanocrystals co-doped with 20% Yb^{3+} and Er^{3+} ions (2% and 20%) were synthesized and will be future investigated under appropriate photoexcitation scheme. In the aforementioned cases, where avalanche emission could not be observed, the most serious challenge is to choose the light excitation wavelength to meet the initial requirements (i.e. effective ESA and unlikely GSA). Learning about the behavior of PA at the micro- and nanoscale is essential to think about future applications of this phenomenon in many disciplines of (bio)technology and biomedical engineering. The presented results contributes to understanding of crystal size dependent PA characteristic properties, and although foreseeable to some extent, this has not been studied so far. The resulting knowledge enable a better understanding the PA mechanism, prediction of the PA features of synthesized materials, and thus the possibility of intentional design of the luminescent properties of these highly nonlinear (nano)phosphors.

3. Streszczenie w języku polskim

Wśród różnych rodzajów procesów konwersji energii wzbudzenia w górę (UC), w których emitowany foton ma energię wyższą niż zaabsorbowany, lawinowa emisja fotonów – PA jest wyjątkowa ze względu na wysoce nieliniowy wzrost intensywności fotoluminescencji w odpowiedzi na niewielki wzrost gęstości mocy fotowzbudzenia. W rezultacie, zależność intensywności luminescencji w funkcji gęstości mocy wykazuje charakterystyczny kształt litery S. Cechą charakterystyczną procesu PA jest wyraźny próg gęstości mocy PA (PA_{TH}), powyżej którego intensywność luminescencji wzrasta w wysoce nieliniowy sposób zgodnie z prawem potęgowym o wykładniku potęgi większym niż 5. PA po raz pierwszy zaobserwowano w 1979 roku w $LaCl_3$ domieszkowanym jonami Pr^{3+} podczas badania tego materiału z myślą o zastosowaniu go w konstrukcji licznika kwantowego fotonów średniej podczerwieni. Od tego czasu zjawisko to stało się interesującym tematem dla wielu badaczy, którzy opisywali je w materiałach domieszkowanych różnymi jonami lantanowców. Oryginalnie badane materiały miały postać monokryształów, szkielek i światłowodów, a PA obserwowano w większości przypadków jedynie w temperaturach kriogenicznych. Jednakże stało się jasne, że obserwacja lawinowej emisji w mikro- lub nanoskali umożliwiłaby szereg nowych zastosowań materiałów lawinowych, na przykład wykorzystanie w bioobrazowaniu lub w konstrukcji elementów aktywnych w bioczuJNIkach. Do niedawna uzyskanie PA w nanoskali było wyzwaniem, jednak emisja PA została po raz pierwszy zademonstrowana w nanokryształach $NaYF_4$ domieszkowanych jonami Tm^{3+} w temperaturze pokojowej (RT). Stwierdzono, że optymalne stężenie jonów Tm^{3+} wynosi 8%. Zazwyczaj procesy relaksacji krzyżowej (CR), bardziej wydajne przy wysokich stężeniach domieszek, prowadzą do wygaszania koncentracyjnego luminescencji i postrzegane są jako konkurencyjne w stosunku do procesów emisji lub konwersji energii w górę. Jednak w przypadku emisji lawinowej procesy CR są wysoce pożądane, ponieważ zwiększają efektywność pozytywnego sprzężenia zwrotnego (ang. Energy loop) prowadzącego do zwielokrotniania populacji poziomu odpowiedzialnego za efektywną absorpcję ze stanu wzbudzanego. Oprócz materiałów domieszkowanych jonami Tm^{3+} , PA zaobserwowano także w nanokryształach współdomieszkowanych Pr^{3+} i Yb^{3+} . Niemniej jednak, wpływ wielkości materiału na właściwości PA nie był wcześniej badany, a niniejsza rozprawa doktorska przedstawia takie badania. Przygotowano i zbadano dwa zestawy kryształów $LiYF_4$ - porównano zachowanie kryształów domieszkowanych 3% oraz 8% jonów Tm^{3+} , przy czym zmiennym

parametrem był ich rozmiar. W pierwszym przypadku porównano nano oraz mikrokryształy z odpowiednim monokryształem domieszkowanym 3% jonów Tm^{3+} . W drugim przypadku porównano nano i mikrokryształy domieszkowane 8% jonów Tm^{3+} . Dodatkowo nanokryształy występowały w dwóch wersjach – domieszkowanego rdzenia, oraz tożsame nanokryształy których powierzchnię pasywowano niedomieszkownym płaszczem LiYF_4 . Materiały były wzbudzone przez jednomodowy laser półprzewodnikowy generujący wiązkę o długości fali 1064 nm i zaobserwowano emisję PA przy długości fali 800 nm oraz 475 nm. Zbadano charakterystyczne właściwości emisji lawinowej – nieliniowość zachowania oraz próg. Zaobserwowano, że wartości progowe PA zmniejszają się wraz ze wzrostem wielkości badanego materiału, równocześnie zauważono wzrost nachylenia krzywej „S” wraz ze zmniejszeniem wielkości materiału. Przedstawione wyniki związane z PA w kryształach domieszkowanych Tm^{3+} zostały wzbogacone o modelowanie zachowania emisji lawinowej w celu zrozumienia mechanizmu PA obserwowanego w jonach Tm^{3+} . W ramach współpracy przygotowano praktyczną demonstrację zastosowania nanocząstek lawinowych (ANP) do obrazowania dyfrakcyjnego. Przeprowadzono nadrozdzielcze obrazowanie nanokryształów typu rdzeń-otoczka domieszkowanych 3% jonów Tm^{3+} , osiągając rozdzielczość przestrzenną do 125 nm.

Niniejsza rozprawa zawiera również opis zjawiska PA obserwowanego w nanokryształach NaYF_4 typu rdzeń i rdzeń-otoczka, w których rdzeń był współdomieszkowanych jonami Pr^{3+} (0.1%, 0.3%, 0.5% lub 0.7%) i Yb^{3+} (15%). Materiały zostały wzbudzone za pomocą diody jednomodowej generującej wiązkę o długości fali 852 nm, w wyniku czego zaobserwowano emisję PA o długości fali 482 nm i 607 nm. O ile emisja lawinowa w materiałach współdomieszkowanych jonami Yb^{3+} i Pr^{3+} została wcześniej zademonstrowana, wyniki prezentowane w niniejszej rozprawie zawierają istotne, nowe elementy oraz wzbogacają i precyzują wiedzę. Po pierwsze, zbadano wpływ architektury kryształów, a mianowicie rdzeń i rdzeń-otoczka na właściwości PA. Ponadto opisano wpływ stężenia jonów Pr^{3+} w szerokim zakresie (0,1%, 0,3%, 0,5%, 0,7%) na właściwości PA. Co więcej, niektóre artykuły błędnie przypisują emisję jonów Pr^{3+} w okolicy 610 nm jako pochodzącą z poziomu $^1\text{D}_2$. W niniejszej pracy eksperymentalnie zweryfikowano prawidłowe pochodzenie emisji 607 nm we fluorkach i przypisano ją przejściu energetycznemu $^3\text{P}_0 \rightarrow ^3\text{H}_6$. Ponadto, przygotowano stosunkowo prosty teoretyczny model procesu PA w układzie domieszkowanym jonami Pr^{3+} i Yb^{3+} w celu zrozumienia, w jaki sposób

poszczególne przejścia energetyczne wpływają na właściwości emisyjne PA. Model fenomenologiczny wykazał, że w zastosowanych warunkach wzbudzenia, PA występuje tylko w materiałach współdomieszkowanych Pr^{3+} i Yb^{3+} , w przeciwieństwie do materiałów domieszkowanych pojedynczo jonami Pr^{3+} . Zostało to również potwierdzone eksperymentalnie. Mianowicie, nanokryształy NaYF_4 w architekturze rdzeń i rdzeń-otoczka pojedynczo domieszkowane jonami Pr^{3+} w szerokim zakresie stężeń: 0.1%, 0.5%, 1%, 3%, 5%, and 8% były wzbudzane wiązką o długości fali 852 nm, jednak nie zaobserwowano żadnej emisji.

Niniejsza rozprawa zawiera również badania mające na celu zweryfikowanie możliwości uzyskania PA w nanokryształach domieszkowanych innymi jonami lantanowców. Cechy charakterystyczne zjawiska PA zaobserwowano w nanokryształach NaYF_4 domieszkowanych jonami Tm^{3+} (3%, 8%), jak również w nanokryształach współdomieszkowanych 20% jonów Yb^{3+} i Tm^{3+} (4% lub 8%) po wzbudzeniu wiązką o długości fali 1059 nm. Ponadto przy wzbudzeniu 1059 nm i 980 nm badano nanokryształy NaYF_4 domieszkowane jonami Ho^{3+} (0.5%, 2%), jak również współdomieszkowane 20% Yb^{3+} i 0.5%, 1%, 2%, 4% lub 8% jonów Ho^{3+} , jednakże wzbudzenie tymi długościami fali nie pozwoliły na generowanie lawinowej emisji fotonów. Co więcej, zsyntezowano nanokryształy w architekturze rdzeń i rdzeń-otoczka domieszkowane 20% jonów Yb^{3+} i Er^{3+} (2% lub 20%), które będą w przyszłości badane pod kątem istnienia PA w odpowiednich warunkach fotowzbudzenia. W wymienionych przypadkach, w których nie udało się zaobserwować lawinowej emisji, najpoważniejszym wyzwaniem jest dobranie odpowiedniej długości fali wzbudzenia w celu spełnienia wstępnego wymagania (tzn. efektywna ESA i mało prawdopodobna GSA). Poznanie zachowania PA w mikro- i nanoskali jest niezbędne, aby myśleć o przyszłych zastosowaniach tego zjawiska w wielu dyscyplinach (bio)technologii i inżynierii biomedycznej. Prezentowane wyniki przyczyniają się do zrozumienia charakterystycznych właściwości PA zależnych od wielkości kryształitów i choć w pewnym stopniu możliwe do przewidzenia, nie były wcześniej badane. Uzyskana w ten sposób wiedza umożliwia lepsze zrozumienie mechanizmu PA, przewidywanie cech PA syntetyzowanych materiałów, a tym samym możliwość intencjonalnego projektowania właściwości luminescencyjnych tych wysoce nieliniowych (nano)luminoforów.

4. Scientific resume of the author

CURRICULUM VITAE

MSc. Eng. Magdalena Dudek

PhD student

DATA: E-mail: M.Dudek@intibs.pl
Date of birthday: 09.02.1995
 : 0000-0002-1663-6279
 : Magdalena Dudek (researchgate.net)



EDUCATION and PROFESSIONAL ACTIVITIES

- XII 2019 – XII 2023** Doctoral Studies
Wrocław Doctoral School of Institutes of Polish Academy
of Science Division of Biomedical Physicochemistry
- II 2018 – VII 2019** Wrocław University of Science and Technology: second-cycle,
full-time studies
Faculty of Chemistry
Field of Study: Chemical and Process Engineering
Specialization: Chemical Process Engineering
Master's thesis title: Influence of dispersing method on the
stability of dispersed system – work carried out in cooperation with
the Selena Labs Sp. z o. o. company
- X 2014 – I 2018** Wrocław University of Science and Technology: first-cycle,
full-time studies
Faculty of Chemistry
Field of Study: Chemical and Process Engineering
Title of Engineering thesis: Design of the installation
for concentration of sodium nitrate – water solution
- IX 2011 – VI 2014** IX High school named Juliusz Słowacki in Wrocław

SCIENTIFIC EXPERIENCE

- 2023** Involved in realization of the research tasks of in a NCN OPUS 22 project, entitled "Sensitizing photon avalanche emission in colloidal core-shell nanocrystals doped with lanthanide ions: new materials for super-resolution imaging" 2021/43/B/ST5/01244
- VIII – IX 2022** Supervisor of trainees Julia Wnętrzak (WUST) and Jastin Popławski (WUST)
- 2019 – 2022** Contractor in a NCN OPUS 16 project entitled "Photon Avalanche in colloidal nano and sub-micron sized inorganic crystals doped with lanthanide ions." 2018/31/B/ST5/01827

PUBLICATIONS

2023

1. **Dudek M.**, Korczak Z., Prorok K., Bezkravnyy O., Sun L., Szalkowski M., Bednarkiewicz A., (2023), Understanding Yb³⁺- sensitized photon avalanche in Pr³⁺ co-doped nanocrystals: modelling and optimization, **Nanoscale** 15, 18613–18623 (2023), doi:10.1039/d3nr04409b, IF=8.307, ministerial points: 140
2. Korczak Z., **Dudek M.**, Majak M., Misiak M., Marciniak Ł., Szalkowski M., et al., Sensitized photon avalanche nanothermometry in Pr³⁺ and Yb³⁺ co-doped NaYF₄ colloidal nanoparticles, **Low Temperature Physics** 49, 351–359 (2023), doi:10.1063/10.0017243, IF=1.618, ministerial points: 40 (special issue supporting Ukrainian scientist)

2022

3. **Dudek M.**, Szalkowski M., Misiak M., Cwierzona M., Skripka A., Korczak Z., Piatkowski D., Wozniak P., Lisiecki R., Goldner P., Mackowski S., Chan E. M., Schuck P. J., & Bednarkiewicz A., Size-Dependent Photon Avalanching in Tm³⁺ Doped LiYF₄ Nano, Micro, and Bulk Crystals. **Advanced Optical Materials** 10, (2022), doi: 10.1002/adom.202201052, IF=10.05, ministerial points: 140

2021

4. Szalkowski M., **Dudek M.**, Korczak Z., Lee C., Marciniak Ł., Chan E. M., Schuck P. J., & Bednarkiewicz A., Predicting the impact of temperature dependent multi-phonon relaxation processes on the photon avalanche behavior in Tm³⁺: NaYF₄ nanoparticles. **Optical Materials: X** 12, (2021), doi: 10.1016/j.omx.2021.100102, IF=2.48, ministerial points: 70

SCIENTIFIC CONFERENCES

2023

1. VII Conference of Doctoral Students of the PAS, **oral presentation** entitled: *Photon avalanche in Pr³⁺, Yb³⁺ co-doped crystals – experimental and simulated results*, 10-15 October 2023, Wrocław, Poland
2. International Conference on Excited State Absorption of Transition Elements (ESTE 2023), **oral presentation** entitled: *Understanding Photon Avalanche in Pr³⁺, Yb³⁺ co-doped crystals*, 3-8 September 2023, Świeradów Zdrój, Poland
3. XVI COPERNICAN DOCTORAL SEMINAR, **poster presentation** entitled: *Photon Avalanche in NaYF₄ nanocrystals co-doped with Pr³⁺ and Yb³⁺ ions*, 29–30 June 2023, Toruń
4. PhoBIA Annual Nanophotonics Interational Conference PANIC Summer School 2023, **poster presentation** entitled: *Photon Avalanching in Pr³⁺ and Yb³⁺ co-doped NaYF₄ nanocrystals*, 15-19 May 2023, Wrocław

2022

5. 21st International Dynamical Processes in Excited States of Solids DPC 2022 in Wrocław, **poster presentation** entitled: *Photon Avalanche in Pr³⁺ and Yb³⁺ co-doped β-NaYF₄ nanocrystals*, Wrocław, 5-9 September 2022
6. 7th International Workshop on Advanced Spectroscopy and Optical Materials IWASOM 2022 in Gdańsk, **poster presentation** entitled: *Size-dependent photon avalanching in Tm³⁺ doped LiYF₄ nano, micro and bulk crystals*, Gdańsk, 10-15 July 2022
7. 1st International Conference on Advanced Materials for Bio-Related Applications AMBRA 2022, **poster presentation** entitled: *Photon avalanche in Pr³⁺ and Yb³⁺ co-doped β-NaYF₄ nanocrystals*, Wrocław, 16-19 April 2022

2021

8. 3rd Conference on Properties, Design, and Applications of Upconversion Nanomaterials UPCONline 2021, **poster presentation** entitled: *Photon avalanching in Tm³⁺ doped LiYF₄ nano, micro and bulk crystals*, on-line conference France, 6-9 April 2021

PROFESSIONAL PRIZES

2022

1. Best poster award „*Photon Avalanche in Pr^{3+} and Yb^{3+} co-doped β - $NaYF_4$ nanocrystals*” during international DPC 2022 conference, Wrocław
2. Best poster award „*Size-dependent photon avalanching in Tm^{3+} doped $LiYF_4$ nano, micro and bulk crystals*” during international IWASOM 2022 conference, Gdańsk

SCIENCE POPULARIZATION

2023

1. Co-conducting chemical and physical experiments during the XXVI Dolnośląski Festiwal Nauki (DFN) organized in the Institute of Low Temperature and Structure Research, Polish Academy of Science in Wrocław
2. Co-conducting a lecture on luminescence in a Public Salesian Basic School in Wrocław
3. Co-conducting a lecture on luminescence in a CODA Maciejówka in Wrocław

2018

4. Conducting experiments during a summer camp in Darłówko for children from primary school in Siechnice

2017 – 2019

5. Conducting chemical experiments for children in community centers in the municipality the Czernica

FOREIGN LANGUAGES

- English: Good oral and written knowledge to perform professional duties
- Spanish: Elementary level
- German: Elementary level

SCIENTIFIC INTERESTS

- Synthesis of colloidal β - $NaYF_4$ and $LiYF_4$ nanocrystals in core and core-shell architecture by thermal decomposition of lanthanide salts method
- Spectroscopic investigations of crystals
- Photon avalanche phenomenon in materials doped and co-doped with lanthanide ions
- Modeling of the photon avalanche in a lanthanide doped and co-doped systems
- Science popularization

NON-SCIENTIFIC INTERESTS

- Music – saxophone playing, education in a first and a second degree music school (2006 – 2016);
saxophone player in a folk ensemble Gieni Dudki (2018 – currently)
- Education – work as a chemistry teacher in a Public Salesian Basic School in Wrocław (2019-2020)
- Swimming, baking of cakes, firefighting, painting

5. Statement on contribution to the scientific articles preparation

2023

Dudek M., Korczak Z., Prorok K., Bezkrivnyi O., Sun L., Szalkowski M., Bednarkiewicz A., (2023), Understanding Yb³⁺- sensitized photon avalanche in Pr³⁺ co-doped nanocrystals: modelling and optimization, **Nanoscale** 15, 18613–18623 (2023), doi:10.1039/d3nr04409b, IF=6.98, ministerial points: 140

My tasks during preparation of this article were:

- Conceptualization,
- Synthesis of all investigated β -NaYF₄ singly Pr³⁺ doped as well as Pr³⁺ and Yb³⁺ co-doped nanocrystals in a core and core-shell architecture (24 chemical compounds),
- Versatile measurements in a Stokes mode of excitation and emission spectra as well as luminescence lifetimes,
- Interpretation of results from measurements of absorption spectra,
- Interpretation of the X-ray Powder diffraction measurements for all synthesized materials,
- Developing or DRE equations and modeling of the PA process in singly Pr³⁺ doped as well as Pr³⁺ and Yb³⁺ ions co-doped system,
- Preparation of size distributions of all synthesized materials based on TEM images,
- Preparation of figures: Figure 1, Figure 4 as well as all Figures from SI,
- Co-preparation of figures: Figure 2, Figure 3,
- Preparation of the article draft and follow-up discussion with all co-authors.

2023

Korczak Z., **Dudek M.**, Majak M., Misiak M., Marciniak Ł., Szalkowski M., et al., Sensitized photon avalanche nanothermometry in Pr³⁺ and Yb³⁺ co-doped NaYF₄ colloidal nanoparticles, **Low Temperature Physics** 49, 351–359 (2023), doi:10.1063/10.0017243, IF=0.923, ministerial points: 40 (special issue supporting Ukrainian scientist)

My tasks during preparation of this article were:

- Synthesis of the investigated NaYF₄:0.5%Pr³⁺,15%Yb³⁺@NaYF₄ nanocrystals (2 chemical compounds),
- Preparation of the size distribution of synthesized core and core-shell nanocrystals based on TEM images,
- Interpretation of the X-ray Powder diffraction measurements for synthesized nanocrystals,
- Preparation of the Figure 1 depicting structure and morphology characteristics of investigated samples
- Measurements of luminescence lifetimes of excited energy levels for synthesized nanocrystals in order to determine the origin of the emission at 607 nm,
- Participation in article draft preparation and submission.

2022

Dudek M., Szalkowski M., Misiak M., Cwierzona M., Skripka A., Korczak Z., Piatkowski D., Wozniak P., Lisiecki R., Goldner P., Mackowski S., Chan E. M., Schuck P. J., & Bednarkiewicz A., Size-Dependent Photon Avalanching in Tm³⁺ Doped LiYF₄ Nano, Micro, and Bulk Crystals. **Advanced Optical Materials** 10, (2022), doi: 10.1002/adom.202201052, IF=9.926, ministerial points: 140

My tasks during preparation of this article were:

- Synthesis of LiYF₄:3%Tm³⁺@LiYF₄ nanocrystals (1 chemical compound),
- Calculations of theoretical excited state absorption spectra for Tm³⁺ ions,
- Participation in simulations of PA phenomenon in Tm³⁺ doped nanocrystals,
- Preparation of figures: Figure 1, Figure 4, Figure S1, Figure S2, Figure S8,
- Participation in the article draft preparation.

2021

Szalkowski M., **Dudek M.**, Korczak Z., Lee C., Marciniak Ł., Chan E. M., Schuck P. J., & Bednarkiewicz A., Predicting the impact of temperature dependent multi-phonon relaxation processes on the photon avalanche behavior in Tm^{3+} : $NaYF_4$ nanoparticles. **Optical Materials: X** 12, (2021), doi: 10.1016/j.omx.2021.100102, IF=4.22, ministerial points: 70

My tasks during preparation of this article were:

- Co-preparation of the Figure 1,
- Participation in article draft preparation.

In preparation

Szalkowski M., Kotulska A., **Dudek M.**, Korczak Z., Marciniak Ł., Misiak M., Prorok K., Schuck J., Bednarkiewicz A.* Photon avalanche luminescence in inorganic lanthanide doped nanomaterials - a review

My tasks during preparation of this article thus far were:

- Literature review on materials where PA was observed,
- Calculations of probabilities of energy transitions going inside the lanthanide ions,
- Descriptions of materials doped with Nd^{3+} , Tm^{3+} , Tb^{3+} , Dy^{3+} , where the PA was observed with preparation of tables containing the energy transition, which had led to observe the process as well as transition which can probably lead to observe the PA,
- Preparation or co-preparation of the diagrams of lanthanide ions: Pr^{3+} , Nd^{3+} , Sm^{3+} , Eu^{3+} , Tb^{3+} , Dy^{3+} , Ho^{3+} , Er^{3+} , Tm^{3+} presenting transitions, which have led or can lead to observe the PA process,
- Preparation of the *Overview graphs of PA processes*, which include schemes of PA observed in lanthanide doped and co-doped materials,
- Co-preparation of the table entitled: *Comparison of most representative examples of photon-avalanche and photon-avalanche-like luminescence in Ln^{3+} doped nanomaterials*
- Co-preparation of the figure entitled *Energy levels of Tm^{3+} and scheme of PA in Tm^{3+} doped materials, as well as comparison of the probabilities of phonon absorption (n^p) and emission ($(n + 1)^p$)*

6. Composition of the doctoral dissertation

The present dissertation is composed of three main parts, which follow chapters on the table of contents, the purpose of the dissertation, abstract, abstract in polish, scientific resume of the author as well as statement on contribution to the scientific articles preparation. Firstly, theoretical information are presented, including the Chapters from 7 to 9. These information are introducing successively the issues leading to the explanation of the phenomenon of avalanche photon emission, which is the heart of this dissertation. Therefore, at the beginning was described the luminescence phenomenon, pointing the energy UC process. Afterwards, the lanthanide ions with theme unique luminescence features were described. The Chapter 8 includes also a descriptions of energy transitions in lanthanide ions as well as kinds of energy UC processes. Subsequently, are describe the matrices, indicating their features, which can provide the optimal conditions for UC processes. Finally, citing the aforementioned information made it possible to discuss the photon avalanche phenomenon with its characteristic features, key conditions for its occurrence and also its history, especially for materials doped with Tm^{3+} , Pr^{3+} and Ho^{3+} ions. Next, applications of materials exhibiting avalanche photon emission were described concluding the theoretical part of the paper. Subsequently, the methodology of performed investigations was presented in Experimental section. The information of synthesis methods, characteristics of materials structure and morphology, spectroscopic measurements, a way of theoretical excited state absorption spectra calculations and slope and PA threshold calculations as well as simulations method are included in the Chapters 10-13. Afterwards, the results are described in the Results and discussion section. Initially, the investigations of PA in LiYF_4 crystals, successively PA observed in Pr^{3+} and Yb^{3+} co-doped NaYF_4 nanocrystals. Subsequently, the investigations, which have not been published yet. Namely, the results of PA observation in Yb^{3+} and Tm^{3+} nanocrystals were presented. Moreover, an investigations which so far have not led to PA observations in materials doped with Ho^{3+} as well as co-doped with Yb^{3+} and Ho^{3+} ions were included. There were described also nanocrystals co-doped with Er^{3+} and Yb^{3+} ions, which have been characterized, however the PA existence have not been investigated yet. Considerations of the all results are summarized with collective conclusions followed by references. At the end of the dissertation are placed indexes of figures and tables.

II. Introduction

Photon avalanche phenomenon, heart of the present dissertation, is one of the mechanisms, the energy upconversion process is achieved leading to emission of higher energy photons than phonons of excitation light. Comparing to the other upconversion processes PA is unique due to highly non-linear photoluminescence increase in a response to minute rise of excitation source pump power density. The dependence of photoluminescence intensity in a function of pump power density possess characteristic “S-shape” and PA is characterized by S of the curve as well as the PA_{TH} indicating the pump power above which PA exists. PA first was observed in the $LaCl_3$ and $LaBr_3$ quantum counters doped with Pr^{3+} ions in 1979. The materials were excited with green light matching the absorption from 3H_5 excited energy level of Pr^{3+} ions and simultaneously staying off resonant with absorption from ground state of these ions. This is one of the key conditions necessary to observe PA. Moreover, the intermediate 3H_5 energy level has to be populated during CR processes to ensure efficient absorption. The mechanism of looping the population of the intermediate energy level is a reason of highly non-linear PA emission. Initially, PA was observed in bulk materials, waveguides and fibers doped with different lanthanide ions, mostly at low temperatures. Reducing the size of the photon avalanching materials, what until recently was a challenge, would enable a number of new applications, for instance to design biosensors or use as labels in a super-resolution imaging. Nevertheless, the PA was not successfully observed until 2021, when all characteristic features of PA phenomenon were demonstrated in $NaYF_4$ nanocrystals doped with Tm^{3+} ions. Further investigation lead to observation of the PA phenomenon in Pr^{3+} , Yb^{3+} co-doped $NaYF_4$ nanocrystals. Because of scientific curiosity as well as having in mind potential applications of these highly non-linear materials, further studies are needed to understand the properties of the PA phenomenon in response to numerous physical and chemical factors. The present dissertation for the first time presents the impact of material size on the properties of the PA process. In addition, in order to intentionally design PA materials with a range of desirable characteristics, it is important to know the PA mechanism responsible for this phenomenon. Therefore, computer simulations were carried out to show how individual energy transfer processes within the avalanche ion (Tm^{3+}) or between the avalanche ion and the sensitizer ion (Pr^{3+} , Yb^{3+}) affect the characteristics of the PA process.

7. Luminescence

The term “luminescence” first was used in 1888 by a German physicist Eilhard Wiedemann to differ the phenomenon, initially called as “cold light” from the emission light owing to incandescence such as firelight, candles, gas light or oil lamps, known as “hot light” [1]. While incandescence (hot light) is usually an effect of direct heating of matter to high temperatures, luminescence occurs at lower temperatures and owes the emission of radiation to excitation with energy source as ultraviolet (UV) light, X-rays, electric field or energetic particles from radioactive decay, etc. [1]. Depending on the excitation source, there are several kinds of luminescence, namely electroluminescence (excitation owing to an electric field), radioluminescence (excitation with ionizing radiation), cathodoluminescence (excitation by cathode rays), chemiluminescence (emission caused by a chemical reaction), triboluminescence (emission caused by the fracture of crystals or mechanical stress to crystal), while the heart of present dissertation is the photoluminescence, where the emission owes to an excitation by irradiation with electromagnetic radiation. Materials showing luminescence are called phosphors, or luminescent materials. Emitted waves can be higher or lower energetic than exciting radiation. If energy of emitted light is smaller (longer wave) than exciting energy, the process is called as down conversion (DC) of energy (**Figure 1a**). In the opposite situation, when emitted wavelength is shorter, i.e. has higher energy than absorbed one, the phenomenon is term as UC of energy (**Figure 1c**). These processes are called Stokes and anti-Stokes shifts, respectively. The Stokes shift, illustrated in the **Figure 1b**, represents the difference between maxima of emission and absorption spectra bands, where, excitation wave is shorter than emitted one. Anti-Stokes shift, which is crucial from the view of present dissertation, is presented in the **Figure 1d** and corresponds situation, where emitted wave is shorter than the excitation one.

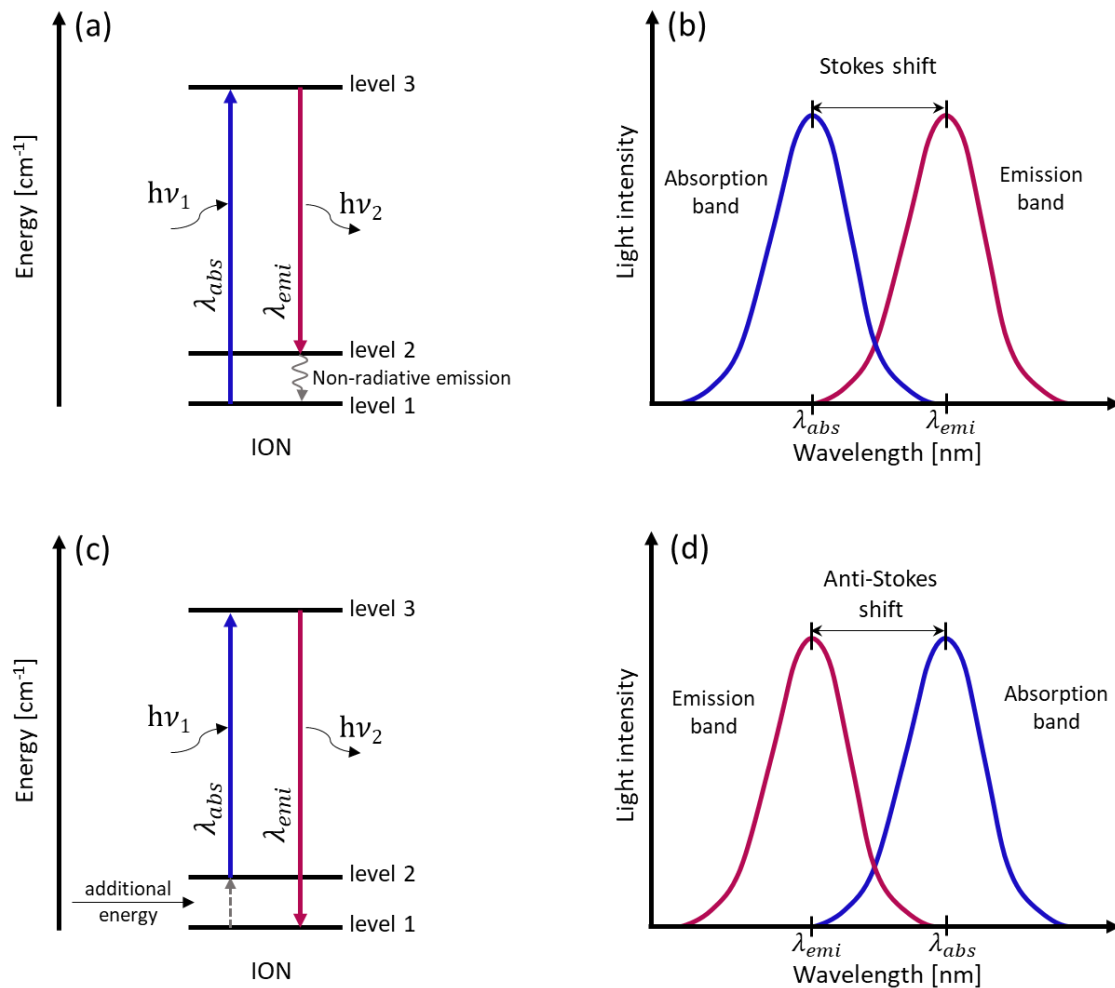


Figure 1. Illustrations of (a, b) Stokes and (c, d) anti-Stokes luminescence features: (a, c) Schematic illustration of changes of energy going between ion's levels (b, d) Charts presenting of absorption and emission bands.

Among the luminescent materials upconverting nanoparticles (UCNPs), semiconductor quantum dots (QDs), carbon dots (C-Dots) or fluorescent proteins (FPs) are known [2]. The UCNPs, consisting from the host lattice (typically NaYF_4) and lanthanide ions, possess unique features, which make them the most promising for application in bioimaging of biosensing. In contrast to the other mentioned materials, UCNPs exhibit anti-Stokes emission. The excitation in the near infra-red (NIR) enables deep tissue penetration and results in less autofluorescence and less phototoxicity compared to UV and visible light. Emission bands of UCNPs are clearly narrower compared to other luminescent materials. QDs emission is size dependent, e.g. the emission maximum shifted from 550 nm to 660 nm with increase of the CdS QDs diameter from 2.9 nm to 3.8 nm [3]. An analogous dependence of emissions on size is also observed for C-Dots.

The emission wavelength of UCNPs is independent on the particles size and doping concentration. Lifetimes of luminescence of UCNPs are longer, in the range of μs to ms , comparing with remaining luminescent materials. FPs and C-Dots luminescence lifetimes are in ns regime. QDs possess longer, however still shorter than UCNPs lifetimes in the range 10 ns - 300 ns. Thanks to modification of UCNPs architecture, i.e. coating with inert shell, the lifetimes are longer, thanks to limitation of surface quenching effects. Methods for biofunctionalization of UCNPs are much more difficult than for FPs. In order to guarantee stability of colloidal dispersion, nanoparticles must have a coating to prevent aggregation. Nanoparticles obtained by thermal decomposition of lanthanide salts in high-boiling solvents are coated with a hydrophobic layer. In order to use them for biological applications, it is necessary to provide hydrophilic groups such as $-\text{COOH}$, $-\text{NH}_2$ or $-\text{OH}$ on the surface of the nanocrystals. A number of methods have been successfully developed to achieve this goal, among them ligand oxidation, ligand exchange, ligand removal, amphiphilic polymer coating and encapsulation in an inorganic coating or noble metal layer [2]. The ways to modify the surface of QDs are similar to those used for UCNPs, however, in addition to ensuring colloidal stability, preventing leakage of toxic heavy metal ions is key [2]. In the case of C-Dots, as the surface is modified to disperse in water, the optical properties of these materials change [2]. Chemical stability is a very important aspect of materials from the perspective of biological applications. FPs are among the most stable phosphors. QDs are quite chemically unstable, under acidic conditions, CdSe/CdS QDs decompose with the release of Cd^{2+} ions [4]. UCNPs, especially NaYF_4 , appeared to be chemically inert, however, dilute dispersions of the particles were shown to dissolve in an aqueous environment at RT [5]–[9]. C-Dots, which were discovered relatively recently in 2004, show remarkable chemical stability [10], [11]. The UCNPs can be synthesized in wide size distributions in different shapes, contrary to QDs or C-Dots. Moreover, the C-Dots suffer from weak repetitive and uniformity after the synthesis. Despite many important features, the UCNPs suffer from low quantum yield and small absorption cross sections. Nevertheless, the UCNPs still are materials with high potential of application and will be feature studied.

8. Lanthanide ions

The fifteen chemical elements from Lanthanum (La) to Lutetium (Lu) with atomic numbers from 57 to 71 are commonly recognized as the *lanthanides* (Ln). However, according some sources, La is excluded from this group, due to empty 4f orbital [12]. Therefore, the term *lanthanoids* were adopted to include all mentioned fifteen chemical elements [13]. Nevertheless, considering the commonness of couple of the elements from La to Lu into one lanthanide group, also for the purpose of the present dissertation this concept is adopted. Lanthanides together with Scandium (Sc) and Yttrium (Y) are determined as *rare earths* (RE). There are no deposits of RE elements in pure form in nature. They occur in a chemical compounds, as oxides, carbonate minerals, silicates or phosphate minerals in rock materials containing rare earth minerals, such as bastnaesite, monazite or xenotime. The electron configuration of Ln^{3+} could be written with the general formula: $[\text{Xe}]4f^n 5d^{0-1} 6s^2$. Characteristic feature of Ln^{3+} is a gradual filling of the orbital 4f with the electrons, while La has no 4f electrons, thus, as mentioned above, sometimes is omitted from the lanthanide group. The electronic configuration of particular lanthanides is presented in the **Table 1**. In the lanthanide series, as the atomic number increases, the charge of the nucleus increases, the consequence of which is a decrease of lanthanide atomic radii. This is the so-called contraction of lanthanides. Lanthanides usually exists at +3 oxidation state, however some of them also at +2, namely Sm^{2+} , Eu^{2+} , Tm^{2+} , Yb^{2+} , or +4, as Ce^{4+} , Pr^{4+} , Tb^{4+} ions. It is usually due to more stable electron configuration of f^0 , f^7 or f^{14} [14]. The Ln^{3+} electron configuration is presented in the **Table 1**.

Table 1. Lanthanides with atomic number and electron configuration

Chemical element	Abbreviation name	Atomic number	Abbreviated electron configuration	Ln ³⁺ electron configuration
Lanthanum	La	57	[Xe] 5d ¹ 6s ²	[Xe]
Cerium	Ce	58	[Xe] 4f ¹ 5d ¹ 6s ²	[Xe] 4f ¹
Praseodymium	Pr	59	[Xe] 4f ³ 6s ²	[Xe] 4f ²
Neodymium	Nd	60	[Xe] 4f ⁴ 6s ²	[Xe] 4f ³
Promethium	Pm	61	[Xe] 4f ⁵ 6s ²	[Xe] 4f ⁴
Samarium	Sm	62	[Xe] 4f ⁶ 6s ²	[Xe] 4f ⁵
Europium	Eu	63	[Xe] 4f ⁷ 6s ²	[Xe] 4f ⁶
Gadolinium	Gd	64	[Xe] 4f ⁷ 5d ¹ 6s ²	[Xe] 4f ⁷
Terbium	Tb	65	[Xe] 4f ⁹ 6s ²	[Xe] 4f ⁸
Dysprosium	Dy	66	[Xe] 4f ¹⁰ 6s ²	[Xe] 4f ⁹
Holmium	Ho	67	[Xe] 4f ¹¹ 6s ²	[Xe] 4f ¹⁰
Erbium	Er	68	[Xe] 4f ¹² 6s ²	[Xe] 4f ¹¹
Thulium	Tm	69	[Xe] 4f ¹³ 6s ²	[Xe] 4f ¹²
Ytterbium	Yb	70	[Xe] 4f ¹⁴ 6s ²	[Xe] 4f ¹³
Lutetium	Lu	71	[Xe] 4f ¹⁴ 5d ¹ 6s ²	[Xe] 4f ¹⁴

8.1. Spectroscopic properties

Ln³⁺ poses very unique spectroscopy features, namely narrow and well-separated absorption and emission bands, as well as long lifetimes of the excited states. The features are connected with the richness of discrete energy levels as well as the transitions occurring inside Ln³⁺ ions and will be explained in the present subsection.

8.1.1. Energy level structure

The determination of the energy level structure and electron transition between energy levels of RE ions is based on the system's Hamiltonian. In the case of a trivalent RE ion, the corresponding Hamiltonian is expressed as follows:

$$H_{isolation\ center} = H_E + H_{S.O.} = H_O + V + H_{S.O.} \quad \text{Equation 1}$$

where H_E indicates Hamiltonian of the electron system, $H_{S.O.}$ is connected with the spin-orbit interaction of the f electrons (the most important magnetic interaction). H_O makes a main part of H_E and is connected with the interaction of each valence electron with

the atomic nucleus, which ensures the electronic orbits of the 4f valence electrons leading to form the configuration of $4f^n$. V describes the Coulomb interactions between electrons of orbital 4f and leads to split of the $4f^n$ configuration for many different energy states. Each of the states can be indicated by L and S letters (the LS term). However, the LS configuration is not obvious, therefore can be ignored. The $H_{S.O.}$ Hamiltonian can describe the interaction between the angular momentum and the spin of electrons:

$$H_{S.O.} = \sum_i \xi(r_i) l_i \cdot S_i \quad \text{Equation 2}$$

where ξ is the constant of spin orbit coupling and makes a function of distance of the i electron, r_i .

According to the Russell-Saunders Coupling (LS coupling) the Hamiltonian $H_{S.O.}$ can be expressed by L (orbital moment) and S (spin moment) as $\zeta L \cdot S$ separating L and S as states composed of series of quantum numbers L, S and J (total angular momentum).

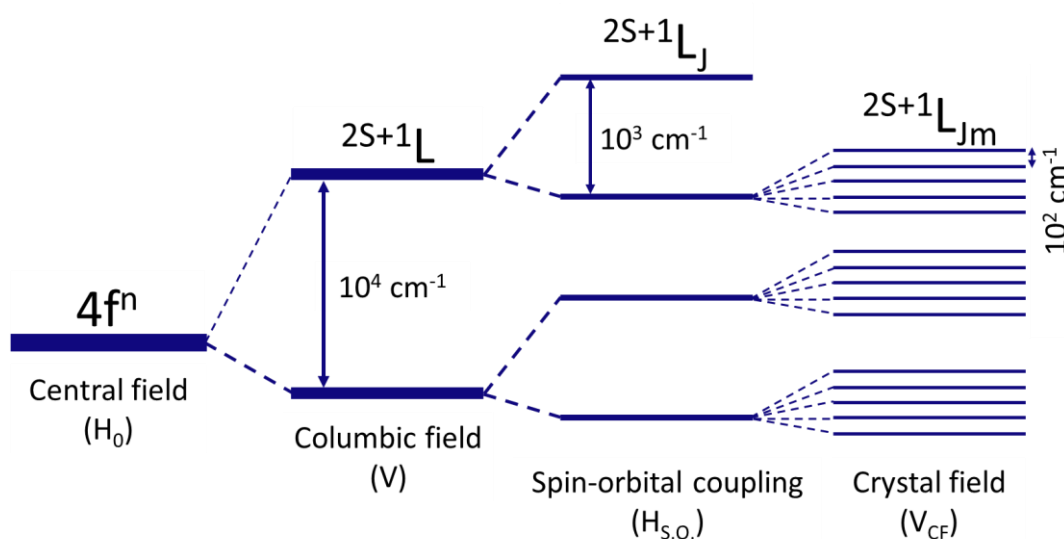


Figure 2. Simplified illustration of the effect of Coulombic field, spin-orbital coupling, and crystal field interaction on the splitting of the $[Xe]4f^n$ configuration [15].

It means, that the approximation in which each electron is described by four quantum numbers (Principal Quantum Number: n , Orbital Quantum Number: l , Magnetic Quantum Number: m and Spin Quantum Number: m_s) is not sufficient to describe the spectra of multi-electron atoms. Several or more different energy levels (electron terms) of an atom may belong to a single electron configuration, due to the electrostatic

interaction between the electrons (**Figure 2**), the consequence of which is that none of the electrons is in a strictly spherically symmetric field. The various quantum states of an atom's electron shell corresponding to such terms differ in the values of the quantum numbers and characterize no longer the individual electrons, but their entire ensemble. The Russell-Saunders term symbol is given by:

$$^{(2S+1)}L_J \quad \text{Equation 3}$$

where: $L = \sum l_i$; $S = \sum m_{s_i}$; and $J = L + S, \dots |L - S|$.

The L value corresponds to respective term letter, namely $L=0, 1, 2, 3, 4 \dots$ corresponds $S, P, D, F, G \dots$, respectively. Calculating L , only unpaired electrons are considered.

L	0	1	2	3	4	5	6	7	8	9
Symbol	S	P	D	F	G	H	I	K	L	M

The m_{s_i} value is 0 for paired electrons and $\frac{1}{2}$ in the case of unpaired electron. Wishing to determine the name of the basic term, the maximum possible J is taken as the value of J when electrons fill more than half of the orbital and, conversely, the smallest J value for an orbital filled less than half. Let's consider the basic terms for three ions which are in focus of the dissertation.

a) Thulium Tm³⁺:

Thulium cation Tm³⁺ is formed by donating three electrons including two from the 6s² orbital and one from the 4f orbital. Thus, the electron configuration of Tm³⁺ is: [Xe] 4f¹². In this case, the cage configuration notation of orbital 4f of Tm³⁺ ions, considering the Hund's rule, can be shown on the following scheme (the arrows represent particular electrons):

	↑ ↓	↑ ↓	↑ ↓	↑ ↓	↑ ↓	↑	↑
l_i	-3	-2	-1	0	1	2	3
m_{s_i}	0	0	0	0	0	$\frac{1}{2}$	$\frac{1}{2}$

$$L = 2 + 3 = 5 \Rightarrow H$$

$$S = 1$$

$$2S + 1 = 3 \Rightarrow {}^3H$$

$$J = L + S = 6$$

$$J = L - S = 4$$

The 4f orbital is filled in more than half therefore a larger value of J should be taken to describe the fundamental term. Thus the symbol of basic term of Tm^{3+} ions is: 3H_6 .

b) Praseodymium Pr^{3+}

The electron configuration of Pr^{3+} is following: $[Xe]4f^2$, therefore,

	↑	↑						
l_i	-3	-2						
m_{s_i}	$\frac{1}{2}$	$\frac{1}{2}$						

$$|L| = 5 \Rightarrow H$$

$$S = 1$$

$$2S + 1 = 3 \Rightarrow {}^3H$$

$$J = L + S = 6$$

$$J = L - S = 4$$

Considering, that the electrons occupy less than half of 4f orbital, lower value of J is chosen for basic term, therefore it is described as 3H_4 .

c) Holmium Ho^{3+}

The configuration of Ho^{3+} ions is following $[Xe]4f^{10}$. The cage recording of the electron configuration according to Hund's rule looks as follows.

	 	 	 				
l_i	-3	-2	-1	0	1	2	3
m_{s_i}	0	0	0	$\frac{1}{2}$	$\frac{1}{2}$	$\frac{1}{2}$	$\frac{1}{2}$

$$L = 1 + 2 + 3 = 6 \Rightarrow I$$

$$S = 2$$

$$2S + 1 = 5 \Rightarrow {}^5H$$

$$J = L + S = 8$$

$$J = L - S = 4$$

The basic term of Ho^{3+} ion is 5H_8 .

The energy levels of 4f lanthanide ions are presented in the Dieke diagram (**Figure 3**).

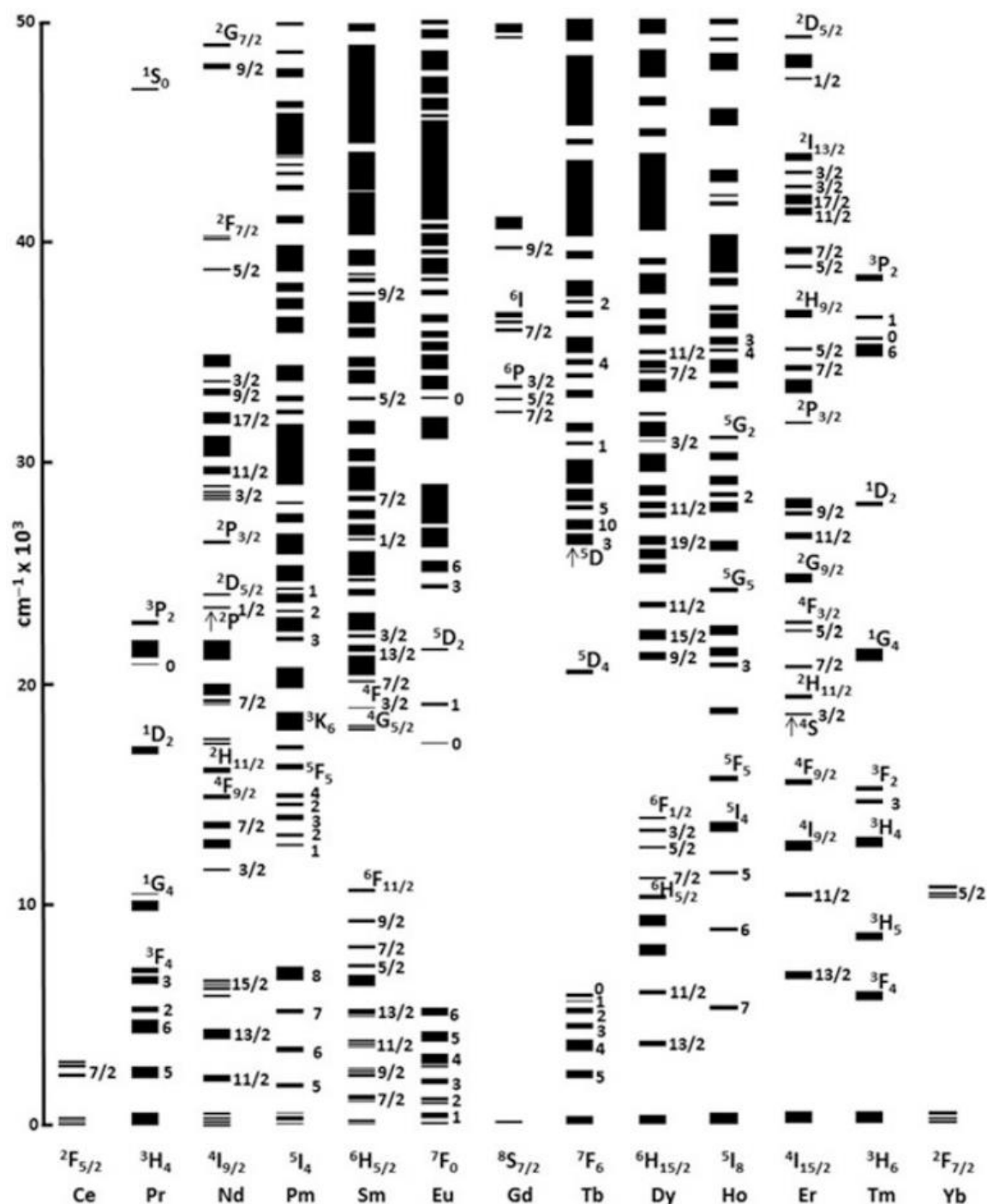


Figure 3. Energy level structure of lanthanide ions based on computed crystal-field energies in the range of 0-50 000 cm^{-1} with labels of ^{2S+1}L and/or J [1].

There are three kinds of electronic transitions existing inside the Ln^{3+} ions, among which there are intra-configurational $f-f$ transitions, inter-configurational $d-f$ transitions as well as inter-configurational charge transfer (CT) transitions. Most of the optical transitions observed in the visible region of the Ln^{3+} electromagnetic spectrum exist between 4f orbital states. Considering the Laporte rule electric dipole (ED) transitions

are forbidden in centrosymmetric molecules and atoms. However, these transitions become allowed with a change of parity. Therefore, $4f-f$ ED transitions are prohibited, however exist due to impact of crystal field. Lowering the symmetry of the matrix relaxes the selections rules and favors $f-f$ transitions. In Ln^{3+} ions exists also magnetic dipole (MD) transitions, which are allowed for the same parity. Considering the influence of electric field, ED transitions can be coupled with vibrations and MD transitions. The characteristic unique features of Ln^{3+} ions emission are the consequence of the induced electric dipole $4f-f$ transitions [16]. Moreover, the $4f$ is a deep-lying orbital, which is protected from the chemical environment influence by shielding $5s^2$ and $5p^6$ orbitals [17]. The s and p orbitals are responsible for bonding with the host material [17], therefore the matrix has a weak influence on $4f$ electrons, i.e. the electron-phonon coupling is low. Considering the mentioned $4f$ orbital features it is clear to understand the unique Ln^{3+} ions spectral properties including narrow, stable, well-separated bands of emissions and absorption spectra and relatively long lifetimes in the range from hundreds of microseconds to milliseconds [17]. However, the intensities of the $f-f$ transitions are lower comparing with the $5d-4f$ allowed transitions. The $5d-4f$ transitions are very sensitive for environment, because the $5d$ electrons are engaged in forming a bond with the matrix. Therefore, these emission bands are broader than for $f-f$ transitions and excited state lifetimes are significantly shorter [17]. The inter-configurational (CT) is also allowed and occurs for lanthanide ions having the tendency to reduction. CT leads on electron transfer from ligand to the lanthanide ion, thus depends on chemical environment and electron configuration.

8.1.2. Energy transfer mechanisms

The energy transfer (ET) process goes between two molecules: donor (D) and acceptor (A) of energy. The first, D, after absorption of energy, $h\nu_{\text{exc}}$, is excited to excited state and consequently has the ability to transfer a part of the energy to a neighboring A luminescence center. It is important to mention, that the emission band of D has to overlap with absorption region of A. As a consequence, the fluorescence of A can be enhanced, however the D luminescence decreases. The two kinds of ET processes are distinguished, namely radiative and non-radiative.

a) Radiative ET

In the case of radiative ET, D molecule, being in the excited state, emits the energy in a radiative way. The emitted radiation is absorbed by neighboring A molecule. The lifetime of D is not changed. Emission region of D ion overlaps with the absorption of A, what leads to reabsorption of radiation by A and, as a consequence, enhance the A photoluminescence. However, when the ET goes between similar or the same molecules, can sometimes lead to self-quenching effect. The D and A molecules are sometimes called as sensitizer and activator, respectively. The radiative energy transfer occurs for molecules being in large distance. Radiative luminescence lifetimes – the inherent lifetimes of the excited level in perfect conditions, i.e. without any energy losses caused by non-radiative transitions, are possible to measure in very diluted sample, in bulk crystals without near-surface effects and at ultra-low temperatures, what hinder all multi-phonon relaxation.

b) Non-radiative ET

In non-radiative ET process, D molecule also absorbs an excitation energy, however the transfer of energy to acceptor undergoes in non-radiative manner. It means, that D does not emit radiation. D in excited state non-radiatively gives the energy to A, which has similar energy of excited level. As in the case of radiative ET, the energy of D decreases, while the A energy increases, however, no photons are emitted. As a consequence of the process, the lifetime of D excited state is reduced. In Ln^{3+} , the 4f-f luminescence is caused by non-radiative ET from ligands (in the case of RE^{3+} complexes) or sensitizer (for inorganic RE^{3+} materials) which efficiently absorb the UV energy. Thanks to this, Ln^{3+} , as acceptors, emit the energy in visible region. The non-radiative ET can be resonant or non-resonant. The resonant non-radiative ET occurs because of weak electromagnetic coupling between electrons on the energy D and those on the A [1]. Depending on the distance between D and A the process occurs either according to Dexter electron transfer or Förster Resonance Energy Transfer (FRET) mechanism. However, dexter electron transfer requires wave function overlap between D and A and occurs at short distances, typically within 1 nm. For bigger distances, within 10 nm, the dominant resonant ET process is FRET, which is connected with

Columb interactions. In the case of weak electron-phonon coupling and when the emission of D does not overlap with the absorption of acceptor, the resonant ET may be not possible [1]. In this case the non-resonant, ET can occur with the phonon-assisted ET.

8.1.3. Mechanisms of upconversion emission

Because of metastable character of many excited levels of the lanthanides, a lot of unconventional processes may occur. During UC process, absorption of two or more photons of low energy leads to emission higher energy radiation. For example, photons from NIR region are converted into visible or even UV region [1]. Firstly, the phenomenon was proposed by N. Bloembergen in 1959 [1]. Thanks to very rich energy level structure, the Ln³⁺ are well known as appropriate for upconversion processes. Usually, the five following mechanisms of UC are considered:

- Excited state absorption (ESA),
- Energy transfer upconversion (ETU known also as APTE, from French: *addition de photon par transferts d'énergie*),
- Photon avalanche (PA),
- Cooperative energy transfer (CET) and Cooperative luminescence (CL),
- Energy migrated-mediated upconversion (EMU).

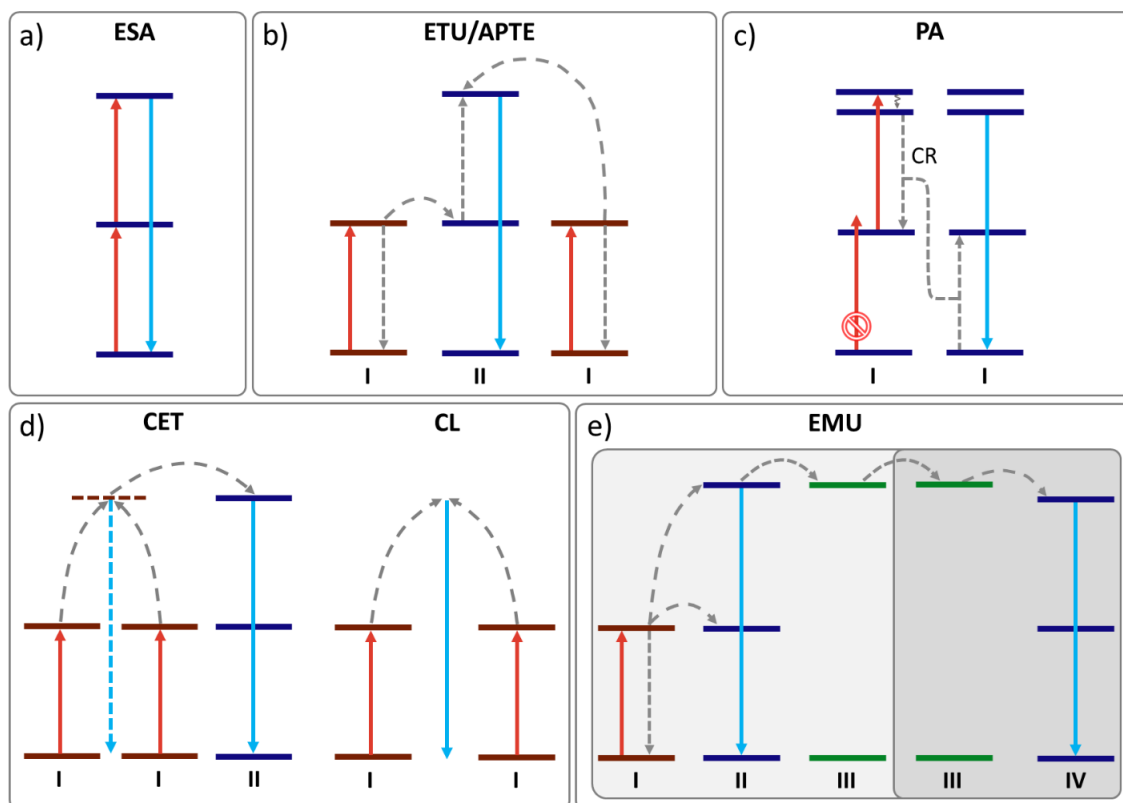


Figure 4. Schematic presentation of upconversion emission mechanisms occurring in lanthanide ions: (a) excited state absorption (ESA), (b) energy transfer upconversion (ETU), (c) photon avalanche (PA), (d) cooperative energy transfer (CET) and cooperative luminescence (CL), (e) Energy migrated-mediated upconversion (EMU) in nanocrystals of core-shell architecture.

The ESA process (**Figure 4a**) goes into one ion and rely on sequential absorption of two low energy photons, which are in resonance with absorption from ground, as well as excited state. The intermediate level should be stable with appropriate electron population and ready for absorption of a second photon. The ESA process can be facilitated by a strong absorption cross section as well as high pump power density. What is important, ESA is more probable for low ions concentrations, because it reduces the probability of non-radiative CR processes, which will decrease the luminescence intensity.

The ETU process (**Figure 4b**) usually exists between different ions: two sensitizer ions and activator ion, while sensitizer exhibits larger absorption cross section [1]. The sensitizers absorb and then transfers the energy to the activator ion in non-radiative way by dipole-dipole resonant interaction. Activator ion go into higher excited state, from which photons are emitted. Comparing with ESA, the ETU process is more efficient and is less vulnerable to external environment. The Yb^{3+} ion is commonly known

and efficient sensitizer and makes pairs with Er^{3+} , Tm^{3+} or Ho^{3+} for which the upconversion is the most efficient.

The PA phenomenon (**Figure 4c**) typically exists within single type of dopants. Excitation wavelength has to be resonant with absorption from excited energy state and simultaneously far from the resonance with absorption from ground energy level (GSA) of excited ion. The intermediate level, from which ESA occurs, is populated during the CR process (**Figure 4c**). CR relies on non-radiative ET between two ions, from which one is in a higher excited energy state and the second is in the ground (or lower excited) energy level. Consequently, population of intermediate energy level increases exponentially, thus the ESA occurs more efficiently, resulting in highly nonlinear increase of photoluminescence intensity. The PA process, as the main topic of this dissertation, will be described in more details in the separate chapter (**Chapter 9**).

In the cooperative processes, namely CET and CL (**Figure 4d**), participate both kinds of ions, i.e. two sensitizers and an activator. These two sensitizer ions are cooperatively activated to fulfill a virtual excited state. Simultaneously sensitizer ions transfer their energy to the activator ion [1]. In the case of CET the sensitizers energy is combined aiming to excite the activator to emitting state without intermediate energy level. For CL the emitting level of activator is also a virtual level. As a consequence, the emission from activator ions is observed, however sometimes also low-efficiency emission of the sensitizer ions is present.

The EMU process (**Figure 4e**) goes between active centers placed in core-shell designed nanostructures [1]. Initially, sensitizer absorbs the excitation photon. Because excited levels are metastable (long living), the sensitizer may additionally be responsible for energy migration (III) (Yb^{3+} , Gd^{3+}) or accumulation (II) of energy in the system [1]. Subsequently, the energy is transferred to the activator ions (e.g. Pr^{3+}). The ions responsible for energy migration have to be placed in a core-shell structure of nanocrystals. If both types of ions were placed in the same part of the nanocrystal, such as in the core, the process of energy exchange could lead to the quenching of luminescence, therefore core-shell architecture plays key role in EMU process. Thereafter, the energy is trapped by neighboring activator ions and finally photon emission occurs.

8.2. Choice of host lattices for upconversion

Lanthanide based phosphors consists of these elements ions, called as activators, sometimes sensitizers ions are also present, as well as with a host lattice. Choose both, the activators and the lattice has a significant influence on UC process properties. As was mentioned and explained earlier, Ln^{3+} are appropriate for UC processes. Due to the weak electron-phonon coupling the energy of Ln^{3+} levels in different lattices are similar as in a free ions [18]. In order to ensure the high efficiency of energy UC process, it is important to provide asymmetrical crystal field by low site symmetry of Ln^{3+} . The probability of mixing of opposite parities increases with increase of crystal field asymmetry and simultaneously the amount of absorption and emission transitions increases. The MD transitions are much less dependent on crystal field. Considering the example of Er^{3+} ions in a cubic $\alpha\text{-NaYF}_4$ lattice with the most symmetric O_h symmetry with hexagonal $\beta\text{-NaYF}_4$ with lower C_{3h} symmetry, more intense luminescence comes from $\beta\text{-NaYF}_4$ doped lattice [19]–[21]. Beside crystal field, the lattice phonon energies are important in the point of view of UC efficiency. The phonon energies appropriate for UC process should be low, to reduce the influence of the nonradiative multiphonon relaxations transitions on photoluminescence emission intensity. High phonon energies increase the probability of non-radiative transitions, therefore easier extinguished the luminescence. Low phonon energies, below 300 cm^{-1} are available in heavy halides such as chlorides, bromides and iodides, however these chemical compounds have reduced applicability because they are hygroscopic [22]. Chemically stable oxides have high phonon energies, around 500 cm^{-1} . Materials that combine desirable low phonon energy with good chemical stability are fluorides. Their phonon energies are typically around 350 cm^{-1} and therefore are excellent for UC processes. Comparing the impact of the two effects, i.e. lattice symmetry and phonon energy on upconversion efficiency, the phonon energy is a more significant. The example can be $\beta\text{-NaYF}_4$ matrix, in which Ln^{3+} occupy a crystalline site with a relatively high C_{3h} symmetry, however, low phonon energies make this lattice one of the best for upconversion of energy [22], [23]. Therefore, for the purposes of this work, $\beta\text{-NaYF}_4$ as well as LiYF_4 fluorides were synthesized, which also have low phonon energies.

9. The phenomenon of photon avalanche

9.1. Mechanism and key conditions

Among different kinds of UC processes PA is unique due to highly non-linear increase of photoluminescence intensity in response to minute rise of an excitation source pump power density. As a consequence, the figure of luminescence intensity (I_L) in a function of pump power density (I_P) is a characteristic for PA s-shape curve (**Figure 5a**). The dependence is described by following power law:

$$I_L = I_P^S \quad \text{Equation 4}$$

The S indicates slope of the curve and is a first parameter describing the PA process. Secondly, the process is characterized by P_{TH} , which indicates the value above which PA exists (**Figure 5a**).

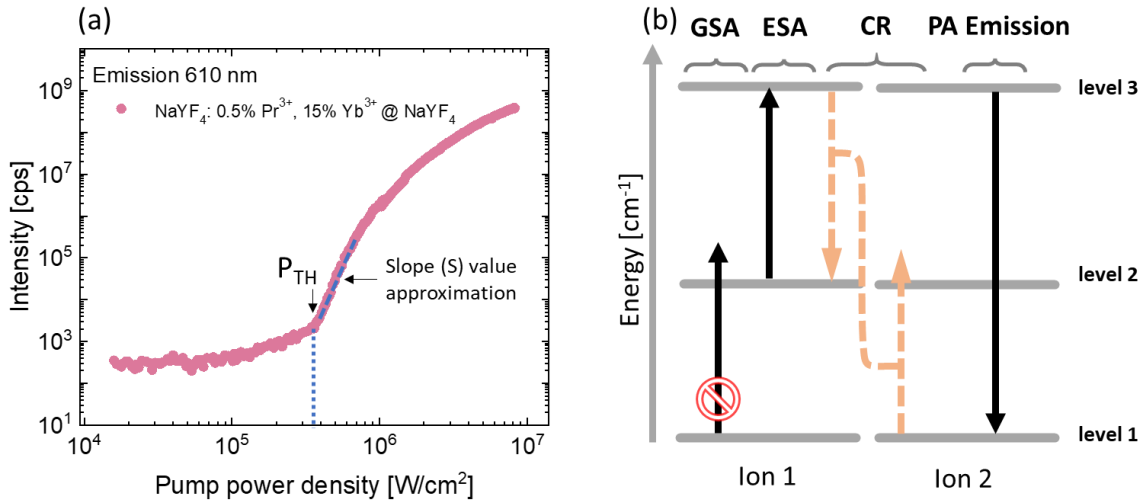


Figure 5. Characteristic features and mechanism of PA emission: (a) example of PA s-shape curve of luminescence intensity in a function of pump power density measured for NaYF₄: 0.5%Pr³⁺,15%Yb³⁺@NaYF₄ nanocrystals with indication of PA parameters: S and P_{TH} , (b) schematic energy diagram for two neighboring ions illustrating PA key conditions.

There are several key conditions necessary to observe PA. First of all, excitation wavelength has to be resonant with ESA and simultaneously far from the resonance with GSA. Moreover, the absorption cross section from excited state (σ_{ESA}) has to be much higher than from ground state (σ_{GSA}). The relationship between σ_{ESA} and σ_{GSA} is described by β parameter, as following ratio:

$$\beta = \frac{\sigma_{ESA}}{\sigma_{GSA}} \quad \text{Equation 5}$$

And for PA β should be higher than 10^4 [24]. Finally, the intermediate level, from which ESA occurs has to be populated during CR processes. CR is a non-radiative process and relies on exchange of energy between two neighboring ions, donor and acceptor. Donor, which initially is in a higher energy state, loses his energy, ΔE , and decays to a lower (intermediate) energy state, while acceptor, which initially is in a ground state or lower excited state is promoted to a higher – intermediate energy level – by absorbing of energy ΔE . The occurrence of CR requires matched, near the same, ΔE energy gap of donor and acceptor ions. First initiation of CR doubles the population of intermediate state, and then, the population of this level increases in a loop. CR could be a parasitic process leading to concentration quenching in conventional GSA based phosphors, however in the case of PA is very desired, because it contributes to more efficient ESA. Another characteristic feature of PA are slow luminescence rise times, τ_R , near the PA_{TH} , which are a consequence of multistep looping of energy (during CR) within dopants before emission. The τ_R is power density dependent, reaches even hundreds of millisecond near PA_{TH} and further gets shorter with pump power increase. In the present dissertation, $t_{50\%}$ value indicates the time necessary to achieve the half of luminescence intensity counting from switching-on the laser. Considering the long rise times which are characteristic feature of PA, the parameter $t_{50\%}$ is important to evidence the existence of pure PA emission and was calculated from the experimentally measured luminescence rise times. One another feature of PA is PA gain, which describe an increase of luminescence intensity when doubling pump power density, the D_{AV} parameter was adopted:

$$D_{AV} = \frac{I_L(2 \cdot I_P)}{I_L(I_P)} \quad \text{Equation 6}$$

In conventional materials D_{AV} equals 2, for UC equals 4-6, for PA often exceeds 100. Sometimes, additional sensitizers ions are required to observe PA. Usually Yb^{3+} ions play sensitizer role and transfer the energy to the activator ions. The CR process goes typically between sensitizer and activator ions. That kind of PA was named as sensitized PA (SPA) [25].

9.2. History and literature review

Before the PA process was discovered, other energy UC processes were successively observed and studied. The ESA mechanism was proposed in the year 1959 by Bloembergen based concept of infrared quantum counter (IRQC), which was the inspiration for PA [26]. Before, all photoluminescence emitters were based on Stokes emission, where the excitation wavelength was shorter than the emission one. The ESA mechanisms mostly requires two laser beams, from which one is resonant with GSA, and the second matches ESA. The exception are ions, in which the energy gap between the ground level and the first excited level is close to the gap between levels, where ESA occurs. In this case the energy differences can be overcome by phonons. In this case, the use of a single excitation wavelength is sufficient. Bloembergen proposed detecting and counting infrared photons by sequential absorption in the excited state, however, it was difficult to achieve efficient sequence of absorption from the ground state. In the future, in order to obtain more efficient quantum counters, ETU (APTE) mechanisms between the sensitizer and activator ions have been presented. Initially, until the mid-1960s, energy transfer from the sensitizer ions, being in the excited state, to the acceptor ions, being initially in the ground state, was known. The ETU process leading to the excitation of acceptor ions from an excited state to a higher excited state was demonstrated in 1966 between Yb³⁺, Tm³⁺ and Yb³⁺, Er³⁺ ions [27]. The process was independently interpreted also as a cooperative mechanism [27]. The PA history dates back to the 1979 year, when the LaCl₃ and LaBr₃ crystals were investigated by Jay S. Chivian et al [28]. They observed the remarkable nonlinear luminescence emission coming from these crystals acting as quantum counters. The materials were excited with green continuous-wave dye laser matched the $^3H_5 \rightarrow ^3P_{J(J=0,1,2)}$ transition in Pr³⁺ ions. It was expected to observe the red emission from Pr³⁺ under excitation of 4.5 μm, which has populated the excited 3H_5 Pr³⁺ level. It was achieved, however unexpectedly, the intensity of luminescence increased rapidly, about two orders of magnitude, upon the increase of pump power density around the critical pump, P_c , value (1.2-12.2 W/cm²). The PA was caused by the CR process during which the intermediate 3H_5 level was populated what led to the efficient ESA leading to observe the non-linear increase of photoluminescence

emission. Considering technical advantages of PA, it is worth to mention, that to obtain the process, the excitation wavelength has to be resonant only with the ESA, therefore one excitation beam is sufficient. To ensure efficient CR process, the ions concentration should be high in order to obtain efficient interaction between these ions. Initially, PA was shown in bulk single crystals, fibers and glasses doped with different Ln³⁺ from low to RTs [27]. Beside Pr³⁺ doped, also different quantum counters, for example LaBr₃:Sm³⁺ [29], CeCl₃:Nd³⁺ [30] shown PA phenomenon. The PA mechanism became an interesting way to achieve upconverting lasers [27], [31], [32]. Multicolor upconverting emission from different lanthanides was reported, namely Pr³⁺ and Sm³⁺ ions emitted red light around 644 nm [28], [29], [32], [33], optically active centers of Tm³⁺ ions emit blue (480 nm) [34], [35] and red (800 nm) [36] light. Green PA emission was observed from Er³⁺ ions [37], [38] and Nd³⁺ ions emitted violet light at 413 nm [31]. Beside classical PA, also SPA mechanism is known. Example of SPA can be process observed between Pr³⁺ and Yb³⁺ ions, where, under infrared excitation, emission was observed at 635 nm [39].

Developments in the synthesis of nanoparticles doped with Ln³⁺, the design of advanced synthesis of the nanostructures in core-shell architecture, have led to greater interest in these materials [24], [40]–[49] as well as greater control that enabled to design their spectral properties. For a long time obtaining the PA at nanoscale was a challenge, but it was achieved and firstly presented for Tm³⁺ doped NaYF₄ nanoparticles [24] in 2021. Subsequently, PA was presented in Tm³⁺ doped LiYF₄ micro and nanocrystals, where the influence of lattice size on PA features was investigated [50]. There are also known the articles reporting SPA in Pr³⁺, Yb³⁺ co-doped NaYF₄ core-shell nanocrystals [25]. In that examples, the Yb³⁺ ions played the role of sensitizer and formed the energy migration network hosting the migrating PA mechanism. Therefore the mentioned SPA process has been also called as migrating PA (MPA). There were attempts of showing PA in materials doped with Ho³⁺ ions, however, the resulted slopes were relatively low, what indicates the observed processes are rather energy looping than PA, which most probably are due to non-radiative losses, insufficient energy looping or insufficient ratio between ground and excited state absorption [51], [52]. Also, nanomaterials doped with Nd³⁺ ions were investigated,

however the obtained emission demonstrate PA-like features rather than PA, which is evidenced by lack of slowing down of the risetimes or relatively low slopes [53]–[56]. Interestingly the signs of PA emission in Nd^{3+} have been found in ultra-low phonon materials at RT [57]. The detailed literature review of PA mechanisms will be describe in details for Tm^{3+} , Pr^{3+} and Ho^{3+} ions, which are the subject of present work.

9.2.1. PA in thulium ions

Thulium ions, Tm^{3+} have demonstrated emission spanning from UV, through visible (blue, red) up to NIR spectral region. The emitting levels of this ions are $^1\text{D}_2$, $^1\text{G}_4$, $^3\text{H}_4$ and $^3\text{F}_4$ [58], [59]. Also emission from $^3\text{P}_0$ is known, however is rarely investigated [58]. Out of the four considered energy levels, the $^1\text{D}_2$ emits the highest energy UV ~ 365 nm and blue ~ 450 nm luminescence, which correspond $^1\text{D}_2 \rightarrow ^3\text{H}_6$ and $^1\text{D}_2 \rightarrow ^3\text{F}_4$, transitions, respectively. The transitions from $^1\text{G}_4$ level, namely $^1\text{G}_4 \rightarrow ^3\text{H}_6$ and $^1\text{G}_4 \rightarrow ^3\text{F}_4$ are assigned to visible emissions at 480 nm (blue) and 650 nm (red), respectively. NIR emission at 800 nm was attributed to $^3\text{H}_4 \rightarrow ^3\text{H}_6$ transition. The longest wavelength radiation, around 1800 nm, corresponds the $^3\text{F}_4 \rightarrow ^3\text{H}_6$ transition. Upconversion processes, including PA were successfully observed in Tm^{3+} doped materials [60]. Initially, PA was observed in bulk materials, glasses, waveguides and fibers from low to RT [27]. Among these materials are LiYF_4 crystal [34], YAP (YAlO_3) [35], YAG ($\text{Y}_3\text{Al}_5\text{O}_{12}$) [61], LaF_3 , YSO (Y_2SiO_5) single crystals [62], BiGaZrZr fluoride glasses [63], Y_2O_3 crystals [64], ZBLAN fibre [65], fluoroindate glasses [66] [34] [35] [61] [62] [63] [64] [65] [66]. In the most of mentioned cases the blue PA emissions at around 450 nm ($^1\text{D}_2 \rightarrow ^3\text{F}_4$) (**Figure 6** EMI₁) and around 480 nm ($^1\text{G}_4 \rightarrow ^3\text{H}_6$) (**Figure 6** EMI₂) were observed as a consequence of red or infrared excitation (**Figure 6** ESA₁₋₄). It is worth to note, that the emission at 480 nm was observed more frequently [35], [61], however, in some materials both 450 nm and 480 nm emissions were present, for example in the case of Y_2O_3 crystal fibre [64], [67], BiGaZrZr fluoride glasses [66], YSO (Y_2SiO_5) single crystal [62], fluoroindate glasses [66] and ZBLAN fiber [65]. For many years, obtaining PA in nanomaterials and at RT was a challenge. For the first time the PA in nanoscale was observed in 2021 year in NaYF_4 core-shell nanocrystals doped with Tm^{3+} ions [24]. The concentration of Tm^{3+} ions in core covered by undoped shell was various as 1%, 4%, 8%, 20% and even 100%. The PA emission at 800 nm attributed to the

${}^3\text{H}_4 \rightarrow {}^3\text{H}_6$ (**Figure 6 EMI₃**) transition was obtained under excitation with 1064 nm (**Figure 6 ESA₁**), which is resonant with absorption from excited state: ${}^3\text{F}_4 \rightarrow {}^3\text{F}_{2,3}$ and simultaneously far from the resonance with absorption from the ground state. What is interesting, under excitation with 1450 nm (**Figure 6 ESA₂**) corresponding ${}^3\text{F}_4 \rightarrow {}^3\text{H}_4$ transition, non-linear emission was also observed. However the slopes were lower, around 5, than in the case of excitation with 1064 nm, where slopes reached a value around 30. The $\text{NaYF}_4:8\% \text{ Tm}^{3+}$ nanocrystals, with slopes of 26 and thresholds around 6 kW/cm^2 were found optimal for PA. With the use of these nanoparticles a PA Super-Resolution Imaging (PASSI) was demonstrated [24], however the idea of PASSI was suggested and demonstrated earlier [68]. It was shown experimentally and by modelling, that for this nanocrystals, it is possible to obtain image with resolution exceeding the diffraction limit (70 nm) using diffraction limited gaussian excitation beam with pump power corresponding PA (7.6 kW/cm^2). Other way to sub-diffraction imaging is super resolution Stimulated Emission Depletion (STED) Microscopy. This approach was realized with use of Tm^{3+} and Yb^{3+} co-doped NaYF_4 nanocrystals [69]. The nanoparticles were excited with 980 nm, and then simultaneously with 980 nm and 808 nm. The emission from ${}^3\text{H}_4$ level dominated. Under 980 nm and 808 nm excitation there was observed clear decrease of emissions intensities from ${}^1\text{D}_2$ and ${}^1\text{G}_4$ levels for nanoparticles including high concentration of Tm^{3+} ions comparing with single 980 nm excitation. For lower – 1% Tm^{3+} doped nanocrystals, the effect of inhibiting blue emission was less visible. The reason of the high depletion effect were CR processes which are more efficient for higher concentration of Tm^{3+} ions. In this case PA-like features was observed, however the excitation wavelength, comparing with pure PA, was not non-resonant with GSA [69]. Recently, pure PA was observed in LiYF_4 crystals in different sizes, from bulk, to micro, to nanocrystals [50]. All materials were investigated under NIR excitation around 1060 nm, which is resonant with ESA ${}^3\text{F}_4 \rightarrow {}^3\text{F}_{2,3}$ and simultaneously far from the GSA. PA emissions were observed at 475 nm and 800 nm. It was noted that as the size of the crystal decreased, the PA_{TH} moved to higher values. These results are a part of present dissertation and will be described in details in the *Results and discussion* section. With the use of Tm^{3+} ions, migrating PA process was also shown [70] – Tm^{3+} were co-doped into four-layer core-shell nanostructure:

$\text{NaYF}_4:\text{Yb}/\text{Pr}$ (15/0.5%) @ $\text{NaYF}_4:\text{Yb}/\text{Tm}$ (3/4%) @ $\text{NaYF}_4:\text{Yb}/\text{Pr}$ (15/0.5%) @ NaLuF_4 . The nanocrystal were excited with 852 nm, which initiated PA looping in the core, afterwards the energy was transferred to Tm^{3+} ions and PA blue emission at 452 nm (transition $^1\text{D}_2 \rightarrow ^3\text{F}_4$) was observed. Similar experiment, under excitation with 852 nm, was performed for singly Tm^{3+} doped as well as Tm^{3+} and Yb^{3+} co-doped crystals, however in this cases no emission was observed, what means, that the presence of Pr^{3+} and Yb^{3+} looping ions and Yb^{3+} migrating ions plays key role.

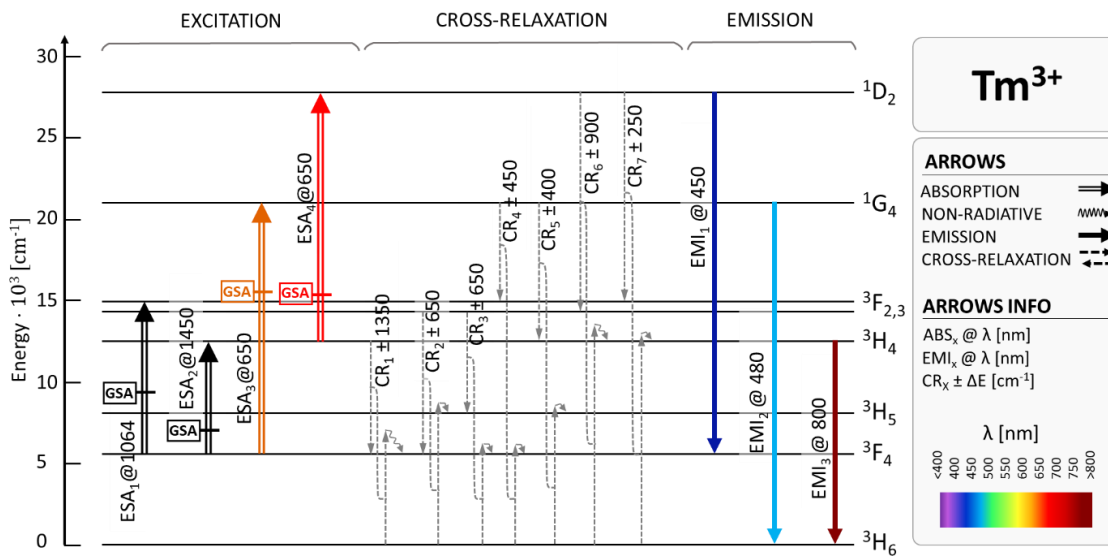


Figure 6. Transitions and energy transfers responsible for PA in Tm^{3+} doped materials. Presented excitation wavelengths were proposed in the literature as leading to observe PA. GSA indicates how particular wavelength matches ground state absorption. The example CR processes are presents with the energy mismatch. In the diagram are included typically emissions reported as PA emissions.

9.2.2. PA in praseodymium ions

Trivalent praseodymium ion, Pr^{3+} , is commonly used in laser techniques [71]–[74], spectroscopy [75]–[78] and optoelectronics [79], [80]. The ability to emit light in the NIR region, which coincides with the transmission window of biological tissues [81], enables the Pr^{3+} ions to be useful for biodetection and bioimaging [82], [83]. Moreover, materials doped with Pr^{3+} ions have been tested as promising candidates for therapy, particularly as sensitizers in radiotherapy [84], [85]. Depending on host material, the Pr^{3+} ions show different emission bands. Emission from $^3\text{P}_1$ and $^3\text{P}_0$ levels terminated at $^3\text{H}_4$, $^3\text{H}_5$, $^3\text{H}_6$, $^3\text{F}_2$, $^3\text{F}_3$ and $^3\text{F}_4$ levels are typically observed, however the presence of $^1\text{D}_2$ level emission is dependent of the matrix. The energy gap between $^3\text{P}_0$ and $^1\text{D}_2$ level is about 3850 cm^{-1} , which in the case of a matrix of low-energy phonons, such as fluorides,

is difficult to relax using non-radiative transitions, as it would require quite a number of phonons (for NaYF₄ as many as eleven). Therefore, in these matrices, energy is emitted in a radiative way from the ³P₀ level before it has time to overcome the energy gap going to the ¹D₂ level [86], [87]. Nonetheless in oxides, where the phonon energies are higher, the ¹D₂ emission is observed [88]. Pr³⁺ ions absorb the energy the most efficiently in the range 440 nm – 480 nm, which corresponds to transitions from ³H₄ to ³P₀, ³P₁, ¹I₆, and ³P₂ levels [74], [78], [87]. The absorption around 594 nm corresponding to ³H₄→¹D₂ transition was also reported [78]. In the LaCl₃ and LaBr₃ quantum counters doped with Pr³⁺ ions (concentration of 4.88%) PA was observed first time in the year 1979 [28]. The material was excited with 4.5 μm (**Figure 7** ABS₂) and 529 nm (**Figure 7** ESA₂). NIR radiation provided population of excited ³H₅ level, from which ESA occurred leading to ³H₅→³P₁ transition in response to 529 nm excitation. The 529 nm wavelength being resonant with the mentioned transition is simultaneously far from the resonance with from the GSA of Pr³⁺ ions, which is prerequisite for PA. Fluorescence output intensity increases above two orders of magnitude near well-defined value of P_c in the range 1.2 – 12 W/cm² depending on emission transitions, which were detected as ³P₀→³H₆ (**Figure 7** EMI₄), ³P₁→³F₂ (**Figure 7** EMI₅) and ³P₀→³F₂ (**Figure 7** EMI₆). There are reports demonstrating the PA in Pr³⁺ ions under excitation with 677 nm corresponding the ³F₃→³P₁ transition (**Figure 7** ESA₃) [32], [89].

PA was also reported in Pr³⁺, Yb³⁺ co-doped materials, where Yb³⁺ ions played the sensitizer role. Recently, SPA emission was observed in Pr³⁺ and Yb³⁺ co-doped nanocrystal. However, earlier such process was reported in ZBLAN fibers as well as LiYF₄ crystals, which were investigated under infrared excitation (**Figure 7** ABS₁, ESA₁) and the emission of ³P_{0,1} energy levels was observed [90], [91]. Reducing the size of materials gives a possibility to interesting applications of PA nanoparticles – for example in super-resolution imaging or in bioimaging. Therefore the important achievement is PA presented in NaYF₄ nanocrystals co-doped with Pr³⁺ and Yb³⁺ ions. The Yb³⁺ ions act as sensitizers and form an energy migration network, supporting the mechanism of migrating PA from the looping ions (Yb-Pr) acting as a ‘work horse’. The important feature, which enables such complex and effective sequence of processes originate from the ability to split looping ions from activator ions within core-multiple-shell

nanoparticles designs. The nanocrystals were excited with around 852 nm (**Figure 7** ABS_1 , ESA_1), which is resonant with excited state absorption of Pr^{3+} ions and simultaneously far from resonance with GSA of these ions. PA emission was observed at around 480 nm (**Figure 7** EMI_1) and 610 nm (**Figure 7** EMI_4). With the aforementioned studies, the feasibility of using avalanche materials for subdiffraction imaging [92] and luminescence nanothermometry [25] has been confirmed, as previously predicted [68], [93]. However, further investigations of sensitization of avalanche emission of Pr^{3+} ions by Yb^{3+} ions are needed in order to learn and clarify the exact mechanism of this process.

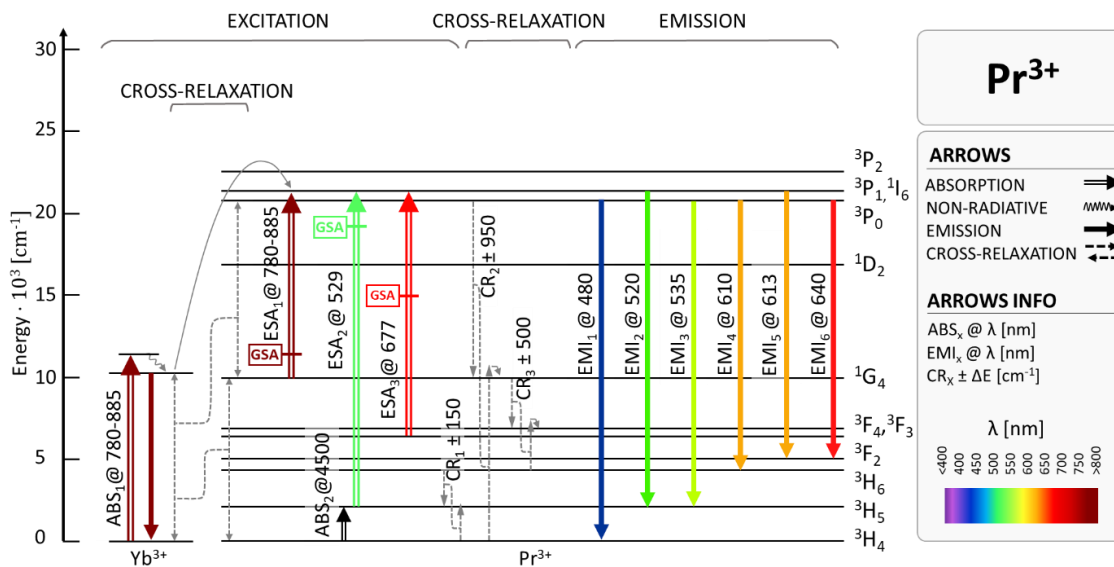


Figure 7. Transitions and energy transfers responsible for PA in Pr^{3+} singly doped as well as Yb^{3+} and Pr^{3+} co-doped materials. Presented excitation wavelengths were proposed in the literature as leading to observe PA. GSA indicates how particular wavelength matches ground state absorption. The example CR processes are presents with the energy mismatch. In the diagram are included typically emissions reported as PA emissions.

9.2.3. PA in holmium ions

Holmium ions, Ho^{3+} , like Tm^{3+} and Pr^{3+} ions have the ability to upconversion of energy. The ions under red and IR radiation emit visible green, blue or red light [94]–[98]. First Ho^{3+} based lasers worked at low temperatures and possessed garnet hosts, namely YAG, YSGG or YSAG [99]–[101]. Nowadays, lasers composed of Ho^{3+} work at RT, are one of the most widespread and have a lot applications for example in medical treatments [102]. PA like mechanism in Ho^{3+} doped ZBLAN matrix was reported in 1996 year [103]. In this case the material was excited in the range from 570 nm to 600 nm. At 585 nm

excitation (**Figure 8** ESA₄), which is resonant with ESA $^5I_7 \rightarrow ^5G_6$ transition, green light at 522 nm and 543 nm (**Figure 8** EMI₄) with accompanying red light ranging 630 nm - 670 nm (**Figure 8** EMI₅) was observed. Similarly, PA like mechanism was demonstrated in YAP, YAG, YLF, ZBLAN and ZrF₄ doped with Ho³⁺ ions [96], [104], [105]. Other possible PA mechanism in Ho³⁺ ions based materials, among others in fluoroindonate glasses, fluoride nanophase glass ceramics or YAP, was reported under excitation with around 750 nm wave [94], [97], [98], [106], [107]. The 750 nm wavelength is resonant with both GSA (**Figure 8** GSA₁) and ESA (**Figure 8** ESA_{3,4}) of Ho³⁺ ions, however the absorption cross section for GSA $^5I_8 \rightarrow ^5I_4$ transition was reported as much weaker comparing with absorption cross section for ESA $^5I_7 \rightarrow ^5S_2, ^5F_4$ transition. Moreover, the intermediate 5I_7 level has long lifetime, around 17 ms [105], what facilitates the ESA after weak GSA absorption. However, the mechanism is rather similar to traditional ESA than PA. Under 750 nm excitations blue, green and red emissions were observed and correspond to $^5F_3 \rightarrow ^5I_8$ (~490 nm) (**Figure 8** EMI₃), $^5F_4, ^5S_2 \rightarrow ^5I_8$ (~545 nm) (**Figure 8** EMI₄) and $^5F_5 \rightarrow ^5I_8$ (~650 nm) (**Figure 8** EMI₅) transitions, respectively. The blue emission was weak. In one of the mentioned articles also UV emission corresponding $^5G_4 \rightarrow ^5I_8$ transition was reported (**Figure 8** EMI₁) [97]. The efficient ESA is provided by CR processes populating the intermediate state. Widely reported CR process between Ho³⁺ ions is $(^5S_2, ^5I_8) \rightarrow (^5I_4, ^5I_7)$ [94], [104], [106]. Moreover, following CR processes leading to populate 5I_7 energy level were proposed: $(^5S_2, ^5I_8) \rightarrow (^5I_4, ^5I_7)$ (**Figure 8** CR₁), $(^5F_3, ^5I_8) \rightarrow (^5F_5, ^5I_7)$ (**Figure 8** CR₂), $(^5F_3, ^5I_8) \rightarrow (^5I_7, ^5F_5)$ (**Figure 8** CR₃), $(^5I_5, ^5I_8) \rightarrow (^5I_7, ^5I_7)$ (**Figure 8** CR₄), $(^5I_4, ^5I_8) \rightarrow (^5I_7, ^5I_6)$ (**Figure 8** CR₅) or $(^5S_2, ^5I_8) \rightarrow (^5I_7, ^5I_4)$ (**Figure 8** CR₆) [94], [103], [104]. In the described examples, the luminescence intensities of reported PA emissions were presented as a function of pump power [mW] and the dependence possessed relatively low S values, mostly around 2, therefore it is difficult to claim pure PA behavior. However characteristic for PA slow τ_R were reported [94], [96], [104]. Next to Ho³⁺ doped materials, also Ho³⁺ and Yb³⁺ co-doped matrices were investigated in order to check the presence of PA. The materials were excited with 759 nm, 840 nm or 976 nm [106]–[108]. Under 750 nm and 840 nm the green emission ($^5S_2 \rightarrow ^5I_8$) (**Figure 8** EMI₄) was observed with slopes around 3.3 [106],

[107]. The presence of Yb^{3+} ions moved the PA_{TH} to lower values, because of energy transfer between Ho^{3+} and Yb^{3+} ions, which populated the intermediate, starting for ESA , $^5\text{I}_7$ level [106]. Spherical Gd_2O_3 nanoparticles co-doped with Ho^{3+} and Yb^{3+} ions excited with 976 nm (**Figure 8** ABS_1 , ESA_1 , ESA_2) shown UV, green, red and blue emission, while blue was weak [108]. Beside CR processes going inside the Ho^{3+} ions, an energy transfer between Ho^{3+} and Yb^{3+} ions led to populate the metastable $^5\text{I}_6$ level: $(\text{Ho}:^5\text{S}_2, \text{Yb}:^2\text{F}_{7/2}) \rightarrow (\text{Ho}:^5\text{I}_6, \text{Yb}:^2\text{F}_{5/2})$ and $(\text{Ho}:^5\text{I}_8, \text{Yb}:^2\text{F}_{5/2}) \rightarrow (\text{Ho}:^5\text{I}_6, \text{Yb}:^2\text{F}_{5/2})$, from which also ESA occurred [106]–[108]. PA-like photoluminescence of Ho^{3+} ions was investigated in the presence of Tm^{3+} ions, which enhanced its intensity [103]. MPA process was reported for Ho^{3+} ions in a presence of Yb^{3+} and Pr^{3+} ions under excitation with 852 nm [70]. There were synthesized following four-layers NaYF_4 nanocrystals $\text{NaYF}_4: \text{Yb/Pr}(15/0.5\%) @ \text{NaYF}_4:\text{Yb/Ho}(3/4\%) @ \text{NaYF}_4:\text{Yb/Pr}(15/0.5\%) @ \text{NaLuF}_4$. Effective PA was obtained in a Pr^{3+} , Yb^{3+} co-doped core and then an energy was transferred to Ho^{3+} ions. Consequently, PA emission of Ho^{3+} ions was observed at 541 nm ($^5\text{S}_2/^5\text{F}_4 \rightarrow ^5\text{I}_8$) (**Figure 8** EMI_4) and 646 nm ($^5\text{F}_5 \rightarrow ^5\text{I}_8$) (**Figure 8** EMI_5). However, at the same experimental conditions, i.e. under 852 nm excitation, for nanocrystals doped singly with Ho^{3+} ions as well as co-doped with Ho^{3+} and Yb^{3+} ions no PA emission was monitored.

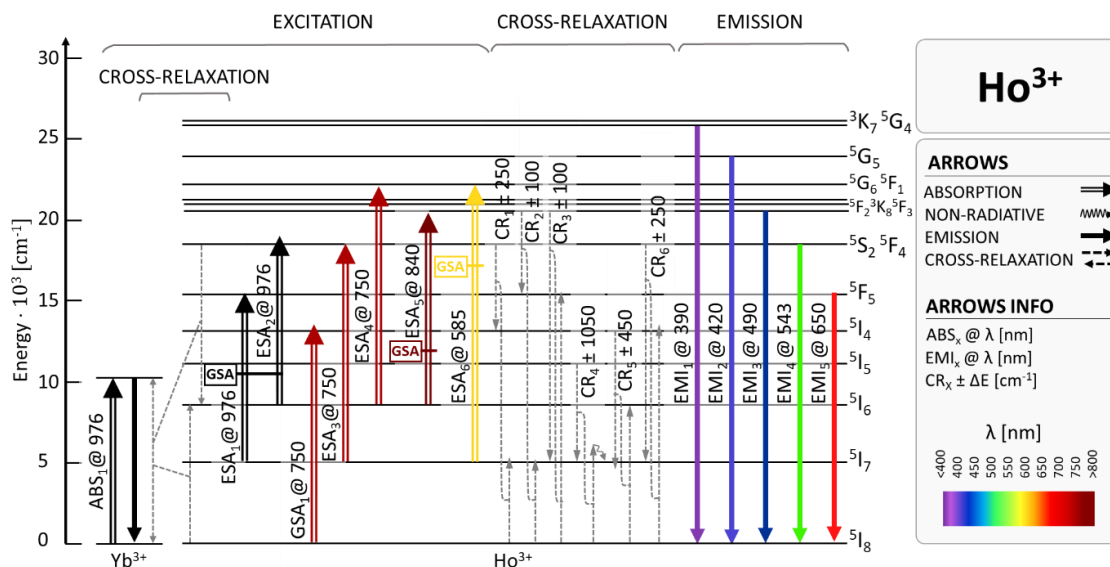


Figure 8. Transitions and energy transfers responsible for PA-like mechanism in Ho^{3+} singly doped as well as Yb^{3+} and Ho^{3+} co-doped materials. Presented excitation wavelengths were proposed in the literature as leading to observe PA. GSA indicates how particular wavelength matches ground state absorption. The example CR processes are presents with the energy mismatch. In the diagram are included typically emissions reported as PA emissions.

9.3. Applications of photon avalanching materials

Initially investigated PA materials were applied as a quantum counters of MIR photons [28], [109], [110] or as an upconversion laser sources [27], [32], [111], [112]. Reducing the size of photon avalanching materials as well as obtaining the effect at RT opened absolutely novel possibilities of their applications, e.g. nanothermometers, super resolution imaging or biosensing. The mentioned applications will be shortly described below.

9.3.1. Medium IR photon counters

There is a great demand for the detection of MIR photons falling in the wavelength range from 3 μm to 20 μm . This radiation has many applications including spectroscopy, (bio) imaging, metrology, astronomy or molecular analysis of gases. The available detectors had insufficient sensitivity in the required wavelength range [113], and, in addition, detection was hampered by the high level of noise resulting from natural emission above absolute zero in the infrared range. Therefore, there was a need to develop new MIR photon counters. One of the solutions proposed was to convert the MIR signal to visible radiation, i.e., through the UC of energy [117]. The sensitivity of generally available detectors in the visible range is much higher. The idea of an IR quantum counter (IRQC) based on a two-step energy UC process was proposed by Bloembergen in 1959 [26]. The first step in the mentioned process was excitation of crystal containing rare earths or transition group ions by IR radiation to an intermediate level, from which intense absorption to the emitting level followed. Based on this idea of Bloembergen, Esterowitz et al. in 1968 suggested 165 patterns suitable for detection of IR radiation in Ln^{3+} [109]. This number could have been significantly increased by the addition of another dopant, such as Yb^{3+} ions. However, the schemes were developed for the detection of IR radiation shorter than 3 μm . The discovery of the PA phenomenon by Chivian et al. in 1979 marked the first description of MIR quantum counters (MIRQC) [28]. Near the avalanche threshold, the intensity of 4.5 μm photons causing Pr^{3+} ions to transition from the ground state to the $^3\text{H}_5$ intermediate level was sufficient to trigger avalanche emission. A quantum counter operating at wavelengths greater than 5 μm is also known, based on a $\text{LaBr}_3:\text{Sm}^{3+}$ crystal [29]. It was sensitive in the spectral range from

2 μm to 10 μm . In this case, the avalanche photon emission observed above 3 kW/cm^2 became a limitation, causing difficulties in conducting experiments and ensuring stability of the pump intensity. The high demand for MIR detectors due to their wide range of applications is motivating many researchers to develop sensitive and cost-effective detection systems. New opportunities for detecting MIR photons at the nanoscale may be opened up by the development of new nanomaterials that exhibit avalanche photon emission.

9.3.2. Photon avalanche lasers

The first upconversion laser known since 1971 was a BaY_2F_8 crystal co-doped with Ho^{3+} and Yb^{3+} ions, which [114]. Subsequently, bulk and fiber lasers were developed using other RE ions as well [114]. The most common mechanism leading to laser emission were ESA and ETU processes [27], [115]. In the case of the ESA mechanism, a low dopant concentration is optimal to initiate the laser action because the process occurs within a single ion. In the case of the ETU mechanism, interaction between nearby ions is necessary, and for this reason higher dopant concentrations of active ions and Yb^{3+} ions as a sensitizer are optimal. However, too high concentrations of ions lead to concentrative quenching of photoluminescence. PA has become an alternative to the a mentioned processes [111]. The first laser based on the PA scheme was described in 1990 in LaCl_3 fluorides doped with Pr^{3+} ions [32]. The Pr^{3+} ions were excited with a wavelength of 677 nm, which they converted to an output energy of 644 nm with an efficiency of 25%. Laser action was also observed in LiYF_4 materials doped with Nd^{3+} ions converting 604 nm excitation to emission at 413 nm [31] and doped with Tm^{3+} , which showed 483 nm blue emission under 629 nm or 647 nm excitation. Lasers based on the PA phenomenon have also been described for the $\text{Pr}^{3+}, \text{Yb}^{3+}$ ions system by first doping the LiYF_4 (1% Pr^{3+} , 10% Yb^{3+}) matrix, where 720 nm or 639.5 nm emission followed 830 nm excitation [116], or BaY_2F_8 (1.25% Pr^{3+} and 6% Yb^{3+}), where emissions were observed at 607.5 nm and 638.7 nm [112], [117], [118]. PA emission was also monitored in materials doped with 1.5% Er^{3+} ions, which emitted 549.8 nm ($^4\text{S}_{3/2} \rightarrow ^4\text{I}_{15/2}$) after 791.3 nm excitation matched with ESA $^4\text{I}_{13/2} \rightarrow ^2\text{H}_{11/2}$. The development of PA lasers is also related to optical fiber materials. After excitation in the 780 nm- 880 nm range, ZBLAN optical fiber doped with Pr^{3+} and Yb^{3+} ions showed multicolor emission

of $^3P_{0,1}$ energy levels at 482 nm, 530 nm, 610 nm and the most efficient beam at 636 nm (power 300 mW, efficiency 52%) [73]. The laser emission produced by PA materials includes a wide range of visible radiation. The most common is red emission, but also green and blue. The most efficient lasers have been constructed based on Pr^{3+} doped and Pr^{3+} , Yb^{3+} co-doped materials. Particular development of lasers took place during the 1990s and early 2000s. Therefore, the current development of nanotechnology has not affected this field. Today known $NaYF_4$ core-shell nanomaterials doped with Tm^{3+} ions show very promising properties [69], [119]. Continuous laser light at 800 nm and 450 nm has been reported at RT for these nanoparticles mounted on 5 μm diameter polystyrene microspheres under excitation with 1064 nm [120], [121]. Avalanche-like laser emission has been demonstrated in $NaYF_4$ nanocrystals co-doped with Er^{3+} and Yb^{3+} ions [122]. Avalanche lasers based on RE ions offer new possibilities. The choice of pumping wavelength is much greater as well as a selection of possible laser lines is wider. Large ion doping is allowed and even desirable, which, in the case of PA, leads to efficient CR processes favorable to the process due to increasing the population of ions in the intermediate state, the initial state for ESA. This leads to an increase in the absorption cross section, as well as an increase in brightness. However, PA lasers require high power densities exceeding the value of optimal operation [111].

9.3.3. Thermometry

Thermometric luminophores are used to monitor temperature under the skin surface for controlled hyperthermia, stroke or cancer research and also for in vitro observation of living cells and subcellular structures by optical microscopy. Luminescence nanothermometry uses the temperature dependence of the luminescence properties of the materials under study. These parameters are typically emission intensity, band-shape, polarization, bandwidth, lifetime and spectra position [123]. For thermal imaging of an object, the light generated by the object is analyzed. Most current technologies use the luminescence intensity ratio of emission bands at two different wavelengths or luminescence lifetimes [123]–[129]. These solutions are relatively fast but costly. In addition, the shape of the luminescence spectrum can be modified due to the medium in which the luminophore is located or the medium

between the luminophore and the detector, which contributes to falsification of the measurement [123]–[130]. For this reason, alternative luminescent thermometers are being sought, and the PA phenomenon may offer new and advantageous opportunities. Also known is the single-band-ratiometric approach based on the opposite dependence of the luminescence of two bands as a function of temperature [56] [131]. In the case of PA, the luminescence intensity of a single band can be monitored in two excitation lines, i.e., by absorption in the ground state and also in the excited state. It is technically easier and cheaper to switch between two excitation sources and record a band at one wavelength in a single spectral channel than vice versa, that is, to monitor two spectral signals in response to a single photo-excitation line. Due to the use of the same spectral range of emission, the risk of interference with the temperature reading caused by the medium will be eliminated. The richness of the energy levels of Ln³⁺ ions opens up a number of possibilities that allow their use in thermometry based on the ESA process. Such an approach has recently been proposed and applied to nanomaterials doped with Nd³⁺, Tb³⁺, Eu³⁺ and Pr³⁺ ions [131]–[137]. Using numerical simulations, the relative sensitivity of PA-based luminescent thermometers was predicted to reach tens of %/K over a wide temperature range [93]. The effect of temperature (-175°C to 175°C) on the characteristics of PA has been studied for NaYF₄ nanocrystals co-doped with 0.5% Pr³⁺ and 15% Yb³⁺ ions [25]. Changes in the nonlinearity of the PA process (slope 4.5-9) and PA_{TH} (of <100 to 700 kW/cm²) were observed. The maximum temperature sensitivity was 7.5%/°C at 0°C.

9.3.4. Superresolution imaging

Fluorescence microscopy has many advantages, such as high sensitivity, in situ processing capability and non-invasiveness [138]. An example is confocal laser scanning microscopy (CLSM), which reduces background noise improving imaging performance [139]–[141]. Multiphoton microscopy with long excitation wavelengths is useful for imaging at deeper penetration depths [142]. However, despite the technical developments of fluorescence microscopes, until recently, according to Abbe's diffraction limit, it was impossible to distinguish two luminescent species staying apart at distance equal roughly less than half the emission wavelength (λ). Recently, there has been a great development of techniques that allow imaging of single fluorescent species

with resolution below the diffraction limit. The breakthrough in this field came with the work of Stefan W. Hell, William E. Moerner and Eric Betzig. Their work led to the development of single-molecule imaging techniques and to the construction of a high-resolution fluorescence microscope. The aforementioned microscope was constructed in 2000 by Stefan W. Hell and operated using STED microscopy. However, the scientist had already theoretically demonstrated the STED fluorescence microscopy methodology in 1994, demonstrating that a resolution of 35 nm could be achieved through it [143], [144]. A practical application of STED theory was carried out by S. Hell in 2000 imaging *E. coli* bacteria and *S. cerevisiae* yeast [145]. STED microscopy requires two laser beams. The first is a low intensity excitation beam, which causes excitation and results in a fuzzy spot. The second beam is the STED beam, which is ring-shaped and high intensity. It causes extinction of luminescence except in the center of the spot with a diameter of a few nanometers. The spot size becomes effectively smaller when the intensity of the depletion beam decreases. The second Nobel Prize-winning method is Single-Molecule Microscopy, to the development of which William E. Moerner and Eric Betzig. In 1989, E. Moerner was the first to measure the light absorption by measuring emitted fluorescence of a single molecule [146]. To do this, he used a combination of Frequency Modulation Spectroscopy techniques: Frequency Modulation Stark double modulation (FMS) and Frequency Modulation ultrasound double modulation (FMUS), which made it possible to remove background signals [143]. Inspired by this discovery, E. Betzig in 1993 examined the luminescence of single carbocyanine molecules using Near-field Scanning Optical Microscopy – NSOM [147]. This is one of the methods to break the diffraction limit methods, however, due to the small range of the beam, it is difficult to image intracellular structures. The next step in the development of super-resolution microscopy was the proposal by E. Betzig of a new way to determine the position of a large number of light spots with known spectral properties [148]. The first step was to image separately each set of particles with the same spectral properties. Then the means (point spread function-PSF) were determined for each imaged point. The next step in the development of super-resolution microscopy was the Photoactivated Localization Microscopy (PALM) technique introduced by E. Betzig

in 2006 [149]. The method was demonstrated based on differences in the luminescence fading time of proteins, which were randomly activated under 404 nm excitation and then fluoresced under 480 nm excitation, which contributed to determining the localization of each protein. After the first set of proteins was quenched, subsequent ones could be activated until all groups were imaged. Despite strong absorption coefficient and typically high fluorescence quantum efficiency, the organic dyes are problematic because they exhibit broad and overlapping absorption and emission bands, undergo photobleaching and typically require short wavelength (UV up to green) photoexcitation, which not only scatters in heterogenous biological samples, but also may be photochemically harmful for biological species.

The unique properties of Ln^{3+} - narrow excitation and visible and NIR emission bands, excellent photostability, long luminescence lifetimes have led to the use of nanoparticles doped with these elements in super-resolution microscopy techniques.

Returning to the STED technique, it also found application in YAG nanoparticles doped with Pr^{3+} ions [150]. An excitation beam of 609 nm and a STED beam of 532 nm were used to image them, resulting in a spatial resolution of 50 nm. Another scheme using STED was proposed for NaYF_4 nanocrystals doped with Yb^{3+} and Tm^{3+} ions, which were excited with a 980 nm laser beam [69]. Emission from the $^1\text{D}_2$ level was observed. The doughnut-shaped STED beam was 808 nm long and allowed a spatial resolution of 28 nm. A similar scheme was applied to matrices doped with Tm^{3+} ions obtaining a resolution of 50 nm [69], [144], [149]–[154]. Avalanche materials were used to improve optical resolution. The PA contributed to this. It was theoretically predicted that the use of avalanche nanoparticles would make it possible to obtain a resolution comparable to the results obtained with STED [68]. Thus, by means of scanning avalanche nanocrystals with a Gaussian beam of power above the PA threshold, it is possible to circumvent the diffraction limit obtaining a sharp PSF. This is because a small increase in excitation power causes gigantic changes in luminescence brightness. This approach is PASSI and was demonstrated for, among others, NaYF_4 nanocrystals doped with 8% Tm^{3+} [24] and LiYF_4 : 3% Tm^{3+} [50] which were excited with a wavelength around 1060 nm matched with ESA. The spatial resolutions obtained were below 70 nm and 125 nm, respectively.

9.3.5. Biosensing

Measurements of biological responses such as enzyme reaction, antibody and DNA binding, or organelle and whole cell activity are possible with devices called biosensors. Biosensors are widely used in medical diagnostics, checking food quality or monitoring the environment. Recent advances in nanomanufacturing techniques have enabled the miniaturization of biosensors [155]. Luminescent nanomaterials are used as biosensors of proteins, antigens, DNA/RNA fragments, cell components or eukaryotic cells [156], [157]. Materials for such applications must be characterized by biorecognition and bio specificity. These features can be intrinsic or acquired through biofunctionalization. The biosensors should be small in size and non-toxic. Signals from biosensors must be easily distinguishable from background or tissue autofluorescence. One of the most important advantages of Ln^{3+} is their excellent photostability, as it allows long-term imaging over continuous illumination.

However, Ln^{3+} ions have low active cross sections for absorption and emission, due to the forbidden nature of f-f transitions [158]. Therefore, organic antennas or plasmonic enhancements have been proposed and evaluated as enhancements [159]–[162]. Crucial for biological applications is the small size of lanthanide-doped nanoparticles, below 10 nm, which is technically achievable using current synthesis methods [49], [163]. However, in small particles, the large surface area-to-volume ratio results in most of the optically active ions being exposed to surface ligands and solvents causing luminescence quenching. Despite these issues, the energy UC process in Ln^{3+} -doped nanoparticles relative to other luminescent materials, is the most efficient in 2-photon scenario [164]. However, the quantum efficiency of these materials decreases significantly with decreasing size. Although Ln^{3+} are not susceptible to local chemical environments, they do undergo quenching under the vibration of -OH groups (3300 cm^{-1}). An important feature of Ln^{3+} is the location of their absorption and emission bands, which falls in the NIR region coinciding with the transmission region of biologically relevant fluids and components. Examples include Yb^{3+} and Nd^{3+} ions, which absorb at 980 nm and 800 nm, respectively, while emissions are observed at 860 nm, 1060 nm and 1020 nm. Yb^{3+} ions are commonly used as sensitizer ions, however, excitation at 980 nm corresponds to the excitation spectrum of water,

through which unwanted heating of biological material can be caused. The development of a method to excite with Nd^{3+} ions at 800 nm does not cause as much overheating allowing to obtain efficiency and luminescence brightness similar to that of Yb^{3+} ions [165]. Promising for biological applications are Tm^{3+} ions, in which the avalanche effect was achieved after NIR excitation at 1064 nm [24], [50].

9.3.6. Optical computing

The electronic computing devices in use today are sophisticated and their further development with existing technologies is limited. Because of this, other solutions are being sought to enable efficient data processing. As an alternative, optical computing devices are considered, which operate by encoding input or output data as modulation of light parameters (i.e., phase or intensity). Such devices enable high energy efficiency in operation, as well as reduce heat emission. Avalanche materials have the characteristics necessary for such applications, as they enable all-optical data processing and memory effects [166]. Calculations based on avalanche materials can be compared to the function of synapses in the nervous system. Features of synapses, such as the threshold intensity of the stimulus, below which it is bypassed, and the facilitation effect of paired impulses are analogous to the action of avalanche materials. Among other things, optical synapses allow signals to be transmitted by light. Nanocrystalline Photonic Synapse with photon avalanching was recently reported [167], where $\text{NaYF}_4:8\%\text{Tm}^{3+}@ \text{NaYF}_4$ nanocrystals, whose luminescence dynamics depended on the population of the $^3\text{H}_4$ metastable level were used. In this experiment, the sample was pulse-excited at near-threshold power. The time intervals between pulses were close to the luminescence lifetime of the mentioned metastable level of Tm^{3+} ions. Consequently, the population of this level before each subsequent excitation pulse was slightly higher than that of the previous one. Thus, the luminescence response to each successive excitation pulse was enhanced.

III. Experimental

In the present chapter are described methods of synthesis, spectroscopy investigations as well as calculations to perform presented investigations.

10. Materials – syntheses and characteristics methods

Thanks to low-phonon energies, which is a desirable feature for UC, fluoride matrices were chosen for all investigations in this dissertation [168]. In contrast to high-phonon energy materials, luminescence intensity in matrices of low-phonon energies is stronger, because non-radiative relaxations are restricted [169]. Here, under investigations were β -NaYF₄ and tetragonal LiYF₄ colloidal nanocrystals. Synthesis methods of these materials as colloidal nanocrystals in a core and core-shell architecture are well known. The synthesized nanocrystals have an oleic acid (OA) on a surface, which prevented the particles from aggregating and rendered them hydrophobic. Core-shell architecture provide highly desirable features of upconverting materials. Firstly, undoped shell provides higher photoluminescence intensity of active Ln³⁺ placed in the core of nanocrystal by surface passivation. Secondly, subsequent shells can be intentionally doped with some ions providing energy transfer between these ions, what is specially desirable in EMU process.

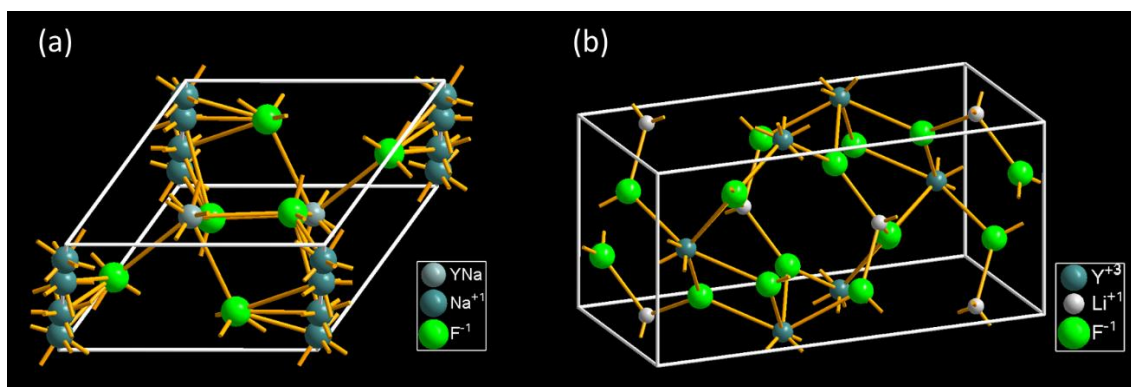


Figure 9. Crystallographic cell of a) β -NaYF₄ and b) LiYF₄ crystal.

The crystallographic cells of the synthesized materials are presents in the **Figure 9 a** and **b**. The Ln³⁺ dopants substitute the Y³⁺ ions into the NaYF₄ as well as LiYF₄ crystal structure. The hexagonal NaYF₄ crystallizes in the $P6_3/m$ space group. The Y³⁺ ions is bonded in a 9-coordinated geometry to nine F⁻ atoms in two inequivalent sites [170].

The LiYF_4 crystallizes in a tetragonal $I4_1/a$ space group. The Y^{3+} ion is bonded in a 8-coordinate geometry to eight equivalent F^- atoms [171].

10.1. Synthesis methods

The synthesized $\beta\text{-NaYF}_4$ nanoparticles were doped with thulium (Tm^{3+}), praseodymium (Pr^{3+}), holmium (Ho^{3+}), erbium (Er^{3+}) or co-doped with ytterbium (Yb^{3+}) ions. The LiYF_4 nanocrystals were synthesized as doped with Tm^{3+} ions. All nanocrystals were prepared based on a thermal decomposition of lanthanide salts in high-boiling organic solvents [172]. $\beta\text{-NaYF}_4@ \text{NaYF}_4$ core-shell materials were synthesized in a two shapes: as an ellipsoidal and as a spherical nanocrystals. All core nanocrystals, ellipsoidal $\beta\text{-NaYF}_4$ nanoparticles obtained after shell deposition as well as shell on LiYF_4 nanocrystals were synthesized by a thermal decomposition of lanthanide oleates. Spherical shell deposition on $\beta\text{-NaYF}_4$ cores was obtained by a thermal decomposition of lanthanide trifluoroacetates.

10.1.1. Preparation of precursor in a form of lanthanide acetates

Preparation of the precursor in a form of lanthanide acetates is a first step to obtain the $\beta\text{-NaYF}_4$ and LiYF_4 core nanocrystals as well as deposition of shell on LiYF_4 and ellipsoidal shell on $\beta\text{-NaYF}_4$ nanocrystals. Stoichiometric amount of lanthanide oxides (total 2.5 mmol) was placed in a Teflon-lined vessel with 50% water solution of acetic acid (**Figure 10 a**). As prepared mixture was maintained in 200°C for two hours to obtain lanthanide acetates. Afterwards, a residual water and an acetic acid were evaporated by using a rotary evaporator in pre-vacuum ($<8\text{hPa}$). The final precursor was dried at 140°C for 12 hour (**Figure 10 c**). The oxides amount for synthesis of $\beta\text{-NaYF}_4$ and LiYF_4 core nanocrystals as well as to deposit the ellipsoidal shell on $\beta\text{-NaYF}_4$ cores was total 2.5 mmol. In the case of shell deposition on LiYF_4 cores, the oxide amount was 1.25 mmol, because the shell was deposited for a half of core particles sample. Preparation of precursor in a form of lanthanide trifluoroacetates

The precursor in a form of trifluoroacetates was prepared aiming spherical undoped shell deposition on $\beta\text{-NaYF}_4$ nanocrystals. Stoichiometric amount of Y_2O_3 yttrium oxide (2.5 mmol) was placed in a round-bottom flask with 50% water solution of trifluoroacetic acid (TFA) (20 cm^3) (**Figure 10 b**). The prepared mixture was kept in 90°C for one hour

to form an yttrium trifluoroacetates. The final precursor was obtained by evaporation of a remaining water and an acetic acid on a rotary evaporator in pre-vacuum (<8hPa) and drying in 140°C for 12 hour (**Figure 10 c**).

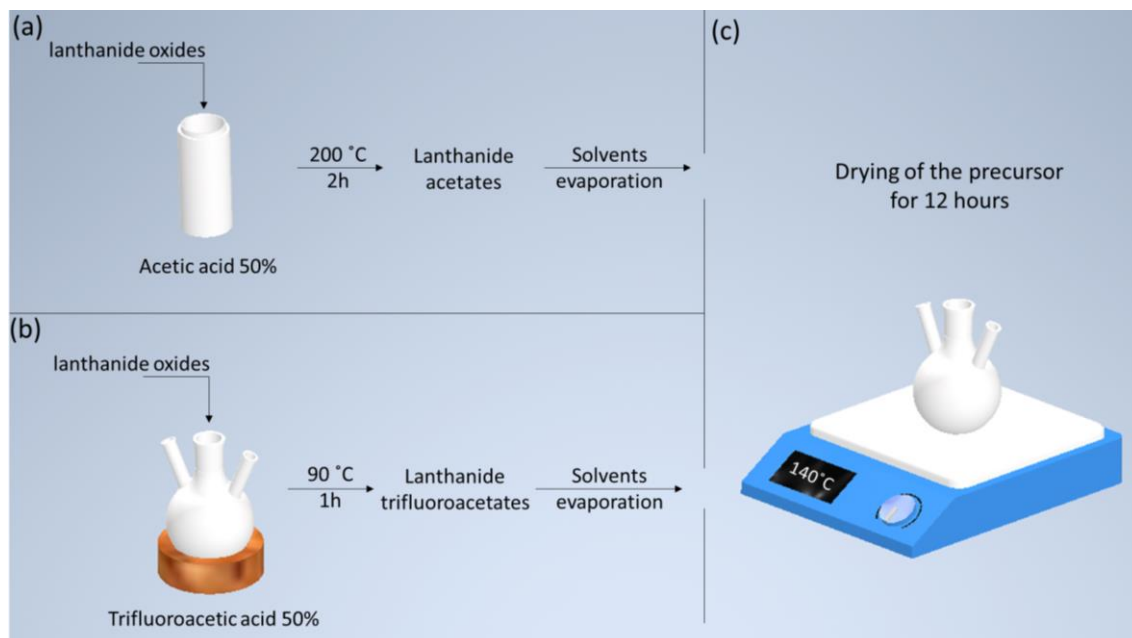


Figure 10. Scheme of the precursors preparation: (a) steps required to obtain lanthanide acetates, (b) steps leading to obtain lanthanide trifluoroacetates, (c) drying of precursor prepared according (a) or (b).

10.1.2. Core β -NaYF₄ nanocrystals

Core nanocrystals were synthesized by the thermal decomposition of lanthanide oleates. Initially, an oleic acid (OA) (30 cm³) and an 1-octadecene (ODE) (75 cm³) were added to a round-bottom flask with the as prepared precursor in a form of lanthanide acetates (**Figure 11**). The solution was stirred and heated to 140°C under nitrogen atmosphere. In this temperature, under vacuum, the mixture was kept for half an hour to form oleates and to remove a residual water and an oxide (**Figure 11**). Afterwards, the solution was cooled to 60°C and a mixture of NaOH (12 mmol) and NH₄F (20 mmol) in methanol (MeOH) (13 mL) was added (**Figure 11**). The mixture was stirred for 10 minutes, and then, the temperature was increased to 85°C and the flask was opened for half an hour to evaporate methanol. Thereafter, temperature was increased to 110°C and the solution was kept under vacuum for 15 minutes to remove the residual methanol (**Figure 11**). Subsequently, the mixture was heated to 300°C and a proper synthesis took 1 hour under an nitrogen atmosphere (**Figure 11**). After this, the solution was cooled down to RT and ethanol (EtOH) was added to precipitate the nanocrystals,

which were centrifugated with 10 000 rpm for 10 minutes. Then, small amount of n-hexane (4 mL) and EtOH (20 mL) was added and nanoparticles were centrifugated at 14 000 rpm for 10 minutes. Finally, obtained nanocrystals were dispersed in chloroform (10 mL).

10.1.3. Core LiYF_4 nanocrystals

The LiYF_4 nanocrystals were synthesized in a similar way as core $\beta\text{-NaYF}_4$ nanocrystals. The first difference is that instead of NH_4F and NaOH the solution of $\text{LiOH}\cdot\text{H}_2\text{O}$ (12.5 mmol) and NH_4F (20 mmol) in MeOH (15 mL) was added to the mixture after it was cooled down to 60°C . Moreover, the time of the synthesis is longer, namely one and a half hour. The obtained nanocrystals after washing and centrifugation were dispersed in a 8 mL of chloroform. Over time, the white precipitate containing unreacted LiF sedimented and was separated from the colloidal core LiYF_4 nanoparticles by decantation. Clear solution was used for further experiments.

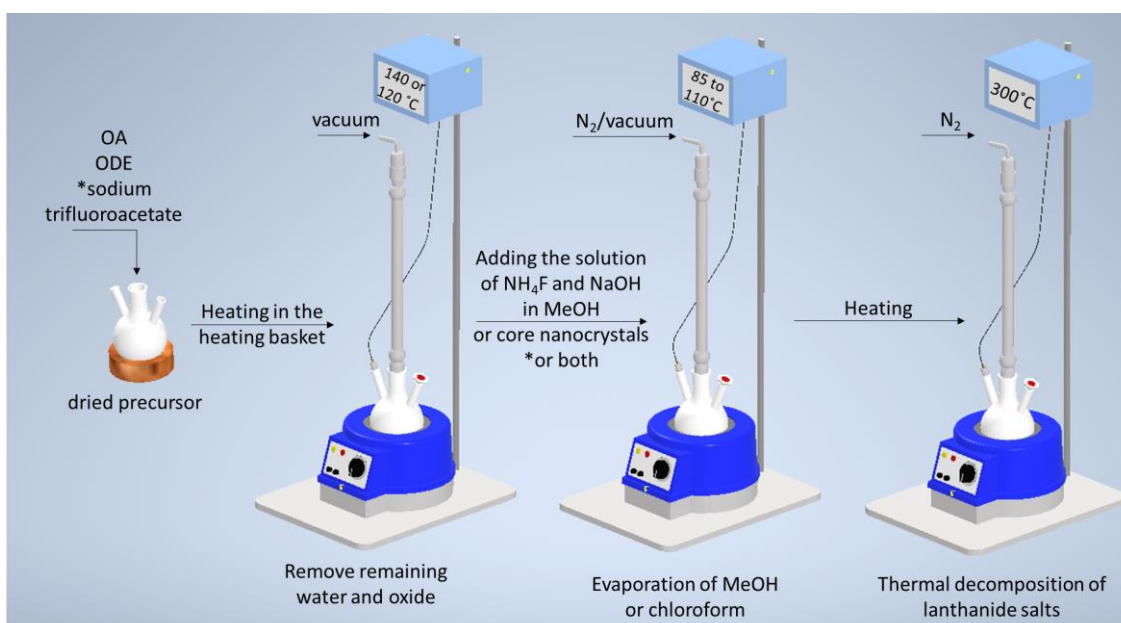


Figure 11. Colloidal fluoride nanocrystals synthesis scheme: adding of high-boiling solvents to precursor *and sodium trifluoroacetate in the case of spherical shell deposition; removing of residual water and oxides; adding solution of NH_4F and NaOH in methanol (MeOH) in the case of core synthesis or core nanoparticles while spherical shell deposition *or both during ellipsoidal shell deposition; solvents evaporation; appropriate synthesis.

10.1.4. Ellipsoidal β -NaYF₄ core@shell nanoparticles

All procedure is similar to the synthesis of the core nanocrystals, with one additional step, containing addition of core nanocrystals to the reaction mixture. At the beginning, a precursor in a form of lanthanide acetates was prepared, as was described earlier. OA (30 cm³) and ODE (75 cm³) were added to a round-bottom flask with the precursor and the mixture was kept for 30 minutes under vacuum in 140°C to form an oleates and to remove a residual water and an oxide (**Figure 11**). Subsequently, the solution was cooled to 60°C and the core nanoparticles dispersed in a chloroform (10 mL) were added (**Figure 11**). The mixture was stirred for 10 minutes in a closed flask. Then, the temperature was increased to 80°C and the flask was opened for 15 minutes. Subsequently, solution was kept under vacuum for 15 minutes to remove residual chloroform (**Figure 11**). Afterwards, the temperature of the solution was decreased to 60°C and a mixture of NaOH (12 mmol) and NH₄F (20 mmol) in MeOH (13 mL) was added (**Figure 11**). The solution was stirred for 10 minutes in a closed flask and then the temperature was increased to 85°C. The flask was opened for 30 minutes. Subsequently, the temperature was increased to 110°C and the solution was kept under vacuum for 15 minutes to remove remaining methanol (**Figure 11**). A proper synthesis was conducted under nitrogen atmosphere at 300°C for one hour (**Figure 11**). After this time, the solution was cooled down to the RT. Afterwards, nanocrystals were precipitated with EtOH by centrifugation at 10 000 rpm for 10 minutes. Then, a minimal amount of n-hexane (4 mL) and an EtOH (20 mL) were added and nanocrystals were centrifugated at 14 000 rpm for 10 minutes. Finally, the nanoparticles were dispersed in 10 mL of chloroform.

10.1.5. Spherical shell deposition

Initially, a precursor in a form of lanthanide trifluoroacetates was prepared, as described above. Thereafter, sodium trifluoroacetate (5 mmol), OA(40 mL) and ODE (40 mL) were added to a round-bottom flask with the precursor (**Figure 11**). A solution was stirred, heated to 120°C and kept for half an hour under vacuum to remove residual water and oxide (**Figure 11**). Afterwards, the solution was cooled to 60°C and, under nitrogen atmosphere, 5 mL of core nanoparticles dispersed in a chloroform was added to the reaction mixture (**Figure 11**). The solution was stirred for 10 minutes in a closed flask.

Then, the temperature was increased to 80°C and the flask was opened for 20 minutes to evaporate chloroform. Subsequently, the temperature was increased to 110°C and the solution was kept under vacuum for 15 minutes to remove residual chloroform (**Figure 11**). A proper synthesis was conducted in 300°C under nitrogen atmosphere for 1 hour (**Figure 11**). Afterwards, the reaction mixture was cooled to RT. Obtained nanocrystals were isolated by addition of EtOH and centrifugation at 10 000 rpm for 10 minutes. Then n-hexane (2 mL) and EtOH (10 mL) were added and the nanocrystals were centrifugated at 14 000 rpm for 10 minutes. Finally, nanoparticles were dispersed in 5 mL of chloroform.

10.1.6. LiYF₄ core@shell nanoparticles

The shell on LiYF₄ core nanoparticles was deposited on core nanocrystals in a similar way as ellipsoidal shell on β-NaYF₄ nanocrystals. However, in this case the inert shell layer was deposited on a half amount of LiYF₄ core nanocrystals. The solvents as OA (15 mL) and ODE (38 mL) were added to the round-bottom flask with the as prepared 2.5 mmol of yttrium acetate salts. The prepared mixture was heated to 140°C, stirred and kept for half an hour to remove residual water and oxygen. During this step, the oleates were formed from the acetates. Afterwards, the solution was cooled down to 60°C 4 mL of previously synthesized core nanocrystals were added to the flask. The chloroform was evaporated during increase of the temperature. Subsequently, the mixture was cooled down to the 50°C and solution of LiOH·H₂O (6.25 mmol) and NaYF₄ (10 mmol) in MeOH (10 mL) was added. The solution was stirred in this temperature for 15 min under a nitrogen atmosphere. Then the flask was opened and MeOH was evaporated in a higher temperatures (85°C-120°C). Further the mixture was kept under vacuum for 15 min. After MeOH evaporation the temperature was increased to 300°C and the reaction mixture was stirred under nitrogen atmosphere. The proper synthesis continued for one and a half hour. After this time, the solution was cooled down to the RT. The nanocrystals were centrifugated at 14 000 rpm for 10 minutes. Then the nanoparticles were washed with n-hexane (4mL) and EtOH (20 mL), centrifugated and dispersed in a chloroform (4 mL). The white sedimented precipitate containing unreacted LiF was separated by decantation from the colloidal LiYF₄ core-shell nanocrystals before further experiments.

10.1.7. LiYF₄ microcrystals

The LiYF₄ microcrystals doped with Tm³⁺ were synthesized by hydrothermal synthesis method with some modifications [173]. 20 mmol of Y(NO₃)₃ and Tm(NO₃)₃ lanthanide nitrates were dissolved in 15 mL of distilled water. Then, the solution was dropwise added to 1.06 g of EDTA solution and the mixture was energetically stirred for one hour at RT (solution A). Subsequently, 60 mmol of NH₄F and 20 mmol of LiF were mixed in a 30 mL of distilled water (solution B). Afterwards, the solution A was dropwise added to the still stirred solution B and the whole was stirred for 30 minutes. Then, the solution was transferred to a 100 mL Teflon-lined autoclave and placed in the drying apparatus in 200°C for 12 hours. After the synthesis, the product was cooled down to the RT. White precipitate was separated by centrifugation from the supernatant. Afterwards, the isolated precipitate was washed with distilled water and EtOH several times. As obtained microcrystal were dried at 100°C for 2 hours on a hot plate.

10.2. Structure and morphology characteristics

In order to verify a phase structure purity of synthesized materials, XRD measurements at RT were performed. The diffractograms were measured in the range of 10-90°2θ of Bragg-Brentano geometry. Obtained reflexes were compared with reference patterns from Inorganic Crystal Structures Database (ICSD). Average dimensions of obtained materials were manually specified based on TEM images. Additionally, deposition of passive shell was evidenced in an indirect way by comparing dimensions of core and core-shell estimated based on TEM images. For representative sample, Energy Dispersive X-Ray Spectroscopy (EDS) map and profile of appropriate ions were measured, which served as a direct proof of undoped shell deposition.

10.3. Spectroscopic measurements

Synthesized materials were investigated in order to check PA existence with use of custom built system enabling a change of pump power density of excitation source. Beside PA measurements, basic investigations were performed, namely absorption, emission and excitation spectra as well as lifetimes were measured.

10.3.1. Absorption spectra

Absorption spectra were measured using Cary 5000 UV-Vis-NIR Spectrophotometer (Agilent Technologies). The colloidal nanocrystals were placed in a spectrophotometer cuvette.

10.3.2. Excitation spectra, emission spectra and lifetimes

Excitation and emission spectra as well as lifetimes were collected with a FLS1000 (Edinburgh Instruments). Colloidal nanocrystals were placed in a spectrophotometer cell. The amount of investigated samples was near the same. Measurement were performed in a Stokes mode.

10.3.3. Optical avalanche characteristics

To experimentally check, if the synthesized materials exhibit PA photoluminescence, a special, custom-built optical microscope system (**Figure 12**) was constructed in the our group by Dr Eng. Marcin Szalkowski and M.Eng. Zuzanna Korczak, under supervision of prof. A. Bednarkiewicz. Dr Eng. Marcin Szalkowski and M.Eng. Zuzanna Korczak have performed most of the pump-power PA measurements presented here. The setup allows measurements of the luminescence intensity in a function of pump power density of excitation source as well as evaluation luminescence rise and decay times. Samples doped with Pr^{3+} and co-doped with Pr^{3+} , Yb^{3+} ions were excited with a single mode diode (FPL852S – 852 nm, 350 mW, Butterfly Laser Diode, SM Fiber, FC/APC) generating 852 nm wavelength beam. The samples doped with Tm^{3+} as well as co-doped with Tm^{3+} and Yb^{3+} ions were excited mainly by a single mode laser module (1064CHP, 3SP Technologies) generating 1064 nm wavelength beam. Additionally, a part of these samples was excited with 976 nm wavelength, which was provided by single mode fiber coupled laser diode (BL976-SAG300). Nanocrystals singly Ho^{3+} doped as well as Yb^{3+} , Ho^{3+} co-doped were investigated under 808 nm (single mode laser module LU0808M250), 852 nm, 976 nm and 1059 nm excitation, however this conditions were not enough to observe PA emission. The power density of excitation laser could be automatically and precisely regulated in the range from 10^2 to 10^7 W/cm^2 by neutral density filters (NDF1, NDF2). The power density value is controlled by an optical power meter sensor (PM), to which a part of beam is directed by beam splitter (BS). However, most of the light (90%) goes through the BS and with the help

of specially selected dichroic mirror (DM1) is directed to the side port of the microscope, where enters the objective lens and is focused on a sample. Afterwards, the emission is collected back by the same objective lens. Then, the emission beam is transmitted by the DM and goes through the set of two filter wheels utilized to limit the intensity of signal. There are two detecting modules in the setup, where emitting beam is directed by the flipped mirror (FM). One of these modules enables measurements of emission spectra and the second constructed with two photomultipliers (PMT1, PMT2) is adapted for collect emission beam luminescence intensity in a function of excitation beam power density.

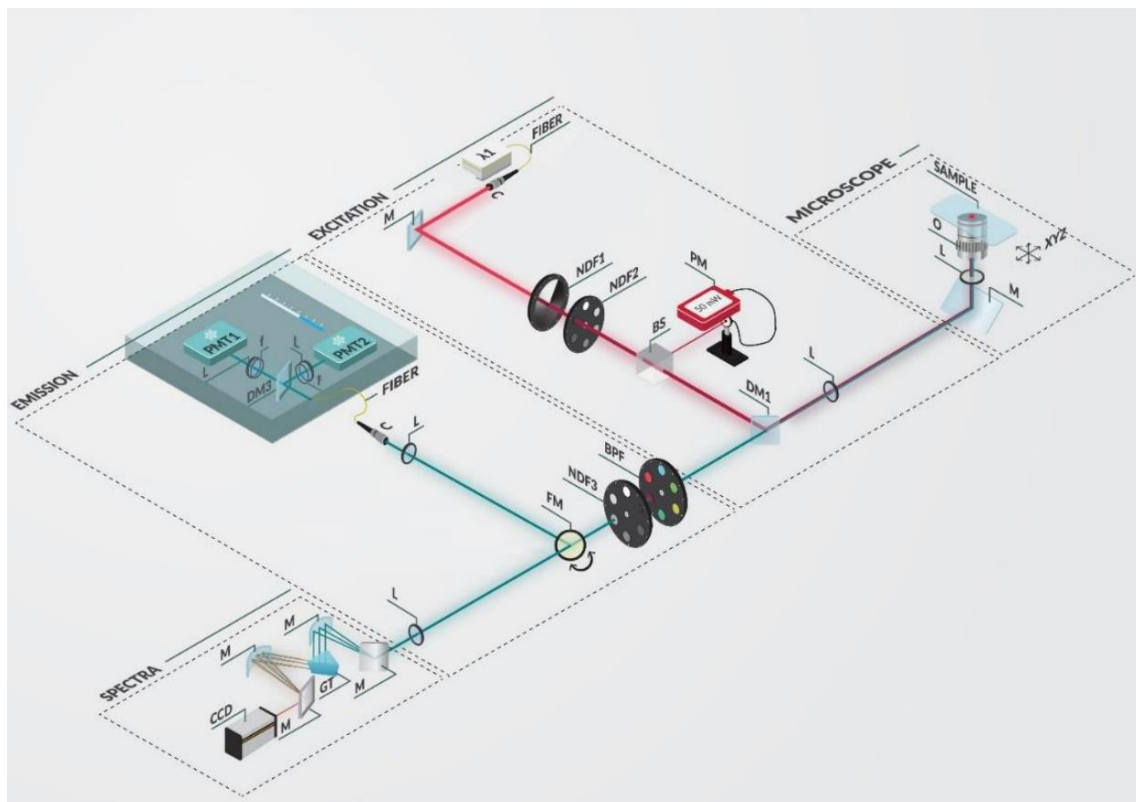


Figure 12. Home-built microscopic setup used for measurements of luminescence intensity in a function of excitation source pump power density as well as luminescence rise- / decay- times.

11. Theoretical ESA absorption spectra calculations

Because we do not have the tools to measure ESA spectra, the only way to identify the excitation wavelength appropriate for PA is by simulating the ESA spectrum. To calculate theoretical absorption spectra for selected transitions from starting (X) to ending (Y) energy level it is important to know Stark components of these levels. The number of Stark components of X and Y levels is necessary to count number of possible transitions between these levels (symbol a in the **Equation 8**). Afterwards, based on energies of X and Y levels Stark components, energies of particular transitions are calculated and finally average energy of the transition ($\bar{\lambda}$) is achieved. In a present work, the theoretical absorption spectra were calculated for ${}^3F_4 \rightarrow {}^3F_2$ and ${}^3F_4 \rightarrow {}^3F_3$ ESA transitions. The oscillator strength of corresponding radiative transition is calculated according to the equation:

$$A_{ij} = \sum_{t=2,4,6} \Omega_t \cdot \left| \langle 4f^{11} \alpha[SL] J \| U^{(t)} \| 4f^{11} \alpha[S'L'] J' \rangle \right|^2 \quad \text{Equation 7}$$

where Ω is a Judd-Ofelt parameter depending on the matrix and includes the influence of crystal field on electronic transitions in a given material. The Ω values used for present calculations are presented in the **Table 2**.

Table 2. The values of Ω parameter for particular matrices.

Matrix	Ω_2 ($\cdot 10^{-20} \text{cm}^2$)	Ω_4 ($\cdot 10^{-20} \text{cm}^2$)	Ω_6 ($\cdot 10^{-20} \text{cm}^2$)	Reference
LiYF ₄	2.43	1.08	0.67	[174]
LiLuF ₄	2.12	1.17	1.11	[175]
KY ₃ F ₁₀	1.907	1.531	1.465	[176]
YAlO ₃	0.67	2.3	0.74	[174]
Y ₃ Al ₅ O ₁₂	0.7	1.2	0.5	[174]
YVO ₄	13	6	0.082	[174]
GdVO ₄	8.13	1.45	1.35	[177]
LuVO ₄	8.44	1.82	1.78	[177]
KGd(WO ₄) ₂	2.64	5.84	14	[178]
KYb(WO ₄) ₂	0.14	0.21	0.1	[178]
KLu(WO ₄) ₂	9.01	1.36	1.43	[179]

Parameter U is strictly connected with a specific ion and is constant for particular transition. The U parameters adopted for these calculations are presented in the **Table 3**.

Table 3. Squared Reduced-Matrix Elements $|\langle 4f^{11}\alpha[SL] J || U^{(t)} || 4f^{11}\alpha[S'L'] J' \rangle|^2$ parameters for Tm^{3+} ion for transition from level start J to level end J' .

Transition $J \rightarrow J'$	$t = 2$	$t = 4$	$t = 6$	Reference
${}^3F_4 \rightarrow {}^3F_2$	0.287	0.163	0.074	[174]
${}^3F_4 \rightarrow {}^3F_3$	0.081	0.344	0.264	[174]

Spectral range to calculate absorption spectra was chosen based on the wavelength of corresponding transitions. For all wavelengths from the chosen range, absorption cross section (A_{CS}) for each corresponding Stark transitions was calculated according to the **Equation 8**:

$$Aa_{CS} = \frac{\frac{(n^2+2)^2}{9n} \frac{2\pi e^2}{3hc} \lambda \cdot A_{ij} \cdot F}{a \cdot \pi (\lambda - \lambda_a)^2 + F^2} \quad \text{Equation 8}$$

where:

n – refractive index of the matrix ,

e – elementary charge; $e = 1.60218 \cdot 10^{-19} \text{ C}$,

h – Planck constant; $h = 6.63 \cdot 10^{-27} \frac{\text{g}}{\text{cm}^2 \cdot \text{s}}$,

c – speed of the light; $c = 3 \cdot 10^{10} \frac{\text{cm}}{\text{s}}$,

F – Lorentz force; $F = 1.8$,

λ – specific wavelength of spectral range,

λ_a – particular wavelengths between Stark components.

Absorption cross section for particular wavelengths from spectral range is a sum of Aa_{CS} calculated for all λ_a :

$$A_{CS} = \sum_{a=1}^{a=x} Aa_{CS} \quad \text{Equation 9}$$

where a corresponds number of particular transition between the Stark levels of J and J' .

Table 4. Refractive indexes used in calculations of theoretical absorption spectra.

Matrix	Refractive index	Source
LiYF_4	1.4445	[180]
LiLuF_4	1.464	[181]
KY_3F_{10}	1.49	[182]
YAlO_3	1.96	[183]
$\text{Y}_3\text{Al}_5\text{O}_{12}$	1.8328	[180]
YVO_4	1.99822	[184]
GdVO_4	2.01234	[184]
LuVO_4	2.03486	[184]
$\text{KGd}(\text{WO}_4)_2$	2.01348	[185]
$\text{KYb}(\text{WO}_4)_2$	3.28412	[186]
$\text{KLu}(\text{WO}_4)_2$	2.113	[187]

12. Calculations of S and PA_{TH} values

Because of highly non-linear dependencies observed in PA materials, manual determination basic properties of the this phenomena is highly susceptible to errors originating from the operator and chosen data range, which motivated us to develop user independent algorithm to derive S and D_{AV}. The code was written by my Supervisor prof. Artur Bednarkiewicz and is available in our web repository (<https://github.com/LuNASlanalysis/Photon-Avalanche-PA->). The algorithm fits the linear function, point by point, to the logarithm from the raw data (what is the analogous to fitting the exponential function to raw data). Fit, for each of the points, covers the maximal range of the surrounding data which fulfils the given certainty. Due to the influence of noise on the determined S values was limited. As the presented S parameters were chosen the highest slope values of analyzed dataset. The values of PA_{TH} were determined as the power corresponding to cross-section point of the lines tangent to logarithm of the raw data for pre-avalanche region and tangent to logarithm of the raw data in the range of max S value. The measurements of s-shape curves were performed a few (2-4) times and based on it, the average values of S, PA_{TH} and D_{AV} were determined together with the standard deviation.

13. Simulations of PA

Beside experimental measurements of PA in synthesized crystals, theoretical calculations were performed in order to understand the contribution and mechanism standing behind this phenomenon. At the beginning were defined energy diagrams for the investigated ions. The diagrams include possible energy transitions under fixed excitation conditions. For as prepared diagrams, were developed differential rate equations (DRE), where particular equations corresponded to variation in populations of individual level over time, including average income and outcome rates of electrons number from these levels. In the present dissertation the proper DRE are presented in a chapter *Results and discussion*. However, the following exemplary energy diagram (**Figure 13**) with DRE **Equations 10-13** are mentioned here to explain the DRE preparation procedure.

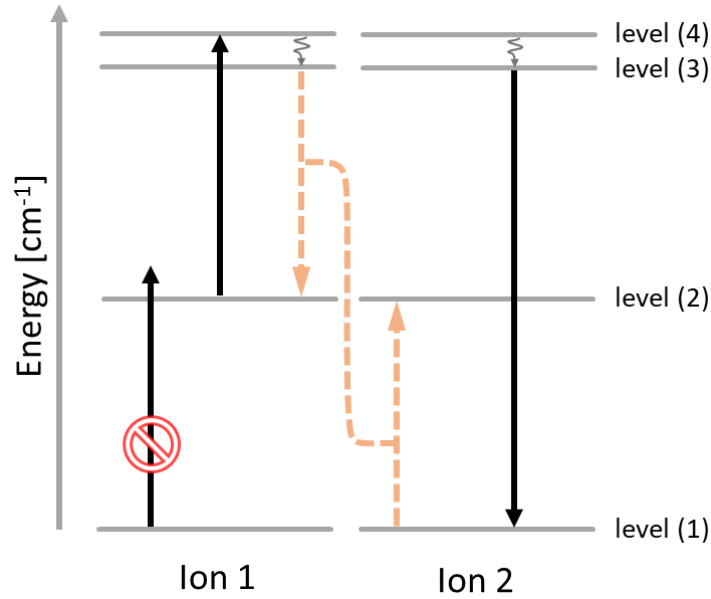


Figure 13. Exemplary energy diagram illustrations energy transfers between two ions under wavelength excitation matched ESA and off-resonant with GSA. This diagram was used to write DRE (Equations 10-13) aiming to explain description of particular processes.

$$\frac{dN_1}{dt} = -F \cdot \sigma_{GSA} \cdot N(1) - WCR \cdot N(1) \cdot N(3) + \frac{N(3)}{\tau_3} \quad \text{Equation 10}$$

$$\frac{dN_2}{dt} = F \cdot \sigma_{GSA} \cdot N(1) - F \cdot \sigma_{ESA} \cdot N(2) + 2 \cdot WCR \cdot N(1) \cdot N(3) \quad \text{Equation 11}$$

$$\frac{dN_3}{dt} = WNR \cdot N(4) - WCR \cdot N(1) \cdot N(3) - \frac{N(3)}{\tau_3} \quad \text{Equation 12}$$

$$\frac{dN_4}{dt} = F \cdot \sigma_{ESA} \cdot N(2) - WNR \cdot N(4) \quad \text{Equation 13}$$

The values $N(x)$ indicate respective levels populations. F corresponds a photoexcitation flux and was calculated using following formula:

$$F = \frac{I_P}{E} = \frac{I_P * \lambda}{h * c} \quad \text{Equation 14}$$

where I_P is a pump power density $\left[\frac{W}{cm^2}\right]$, λ indicates an excitation wavelength, h is a Plank constant ($6.626 \cdot 10^{-34} J \cdot s$), and c signify a speed of light in vacuum ($299792458 \frac{m}{s}$). To describe particular processes, appropriate values of rates were used. Depending on whether a process leads to population or depopulation of a given level, it is recorded with a plus or minus, respectively. The absorptions from ground and excited state are described by absorption cross sections values: σ_{GSA} and σ_{ESA} , respectively, times flux and population of appropriate level (**Equations 10, 11, 12**). Emission is described as population of emitting level split into lifetime, τ , of this level (**Equations 10, 12**). The rate of CR was quantified here as W_{CR} term and has to be multiplied by populations of the two levels between which occurs (**Equations 10, 11, 12**). Last energy transfer considered here is a nonradiative transition occurring for small energy gaps. W_{NR} indicated rate of this process and is multiplied by population of appropriate level (**Equation 12, 13**).

IV. Results and discussion

14. PA in Tm^{3+} doped LiYF_4 crystals

PA at nanoscale first was observed in nanocrystals doped with Tm^{3+} ions [24]. However the influence of host matrix size on PA features have not been investigated earlier. Therefore, investigations aiming to check, how materials size influence the PA features were performed as a part of present dissertation. The results are described in the present chapter and have been published in the article “Size Dependent Photon Avalanching in Tm^{3+} doped LiYF_4 Nano, Micro, and Bulk Crystals” [50].

14.1. Materials

Because we own a bulk LiYF_4 doped with 3% of Tm^{3+} ions avalanching crystal (bAC), which was earlier reported as showing PA emission [188], a materials at smaller scales of the same structure and doping composition, namely avalanching LiYF_4 microparticles (μAC) as well as avalanching LiYF_4 core nanoparticles (cANP) and LiYF_4 core-shell avalanching nanoparticles (csANP) were synthesized. The optimal concentration of Tm^{3+} ions for PA was established as 8% [24]. Therefore, even though we did not have our own bulk crystal the LiYF_4 :8% Tm^{3+} μAC , cANP and csANP were synthesized. The majority of LiYF_4 crystals were synthesized by Dr Małgorzata Misiak. A morphology characteristic of all synthesized materials was prepared. The samples shown pure tetragonal LiYF_4 crystallographic phase (**Figure 14 a,b**).

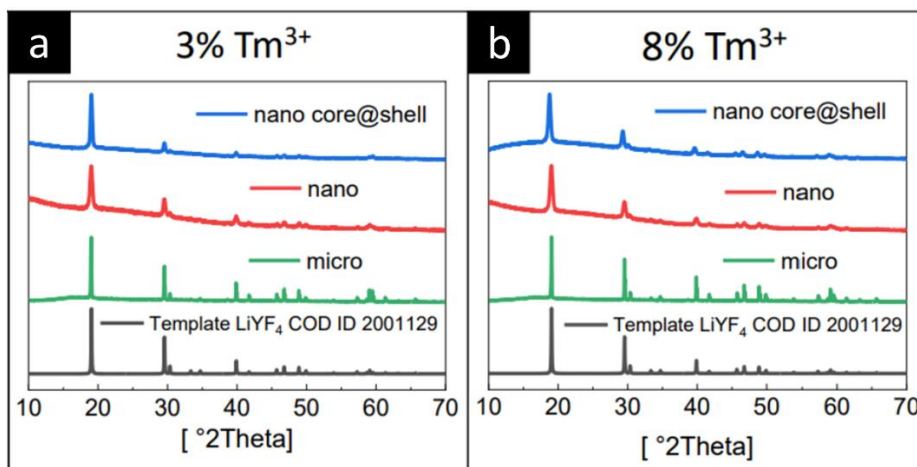


Figure 14. XRD pattern of LiYF_4 crystals with XRD patterns of synthesized materials doped with (a) 3% and (b) 8% of Tm^{3+} ions. Based on [50].

The TEM images of synthesized cANP and csANP were prepared and are presented in the **Figure 15 a, b** and **e, f** for 3% and 8% doping of Tm^{3+} ions, respectively. Scanning Electron Microscopy (SEM) images of μAP are presented in the **Figure 15 c, g**. LiYF_4 single crystal is presented in the **Figure 15 d** and is around 3 mm large. The cANP, csANP and μAP show narrow size distributions. Dimensions of all the materials are presented in the **Table 5**. The cANP doped with 3% of Tm^{3+} ions have around 24.6 nm in width and 41.9 nm in length. Their core-shell counterparts have around 30.8 nm and 49.5 nm in width and length, respectively. The cANP doped with 8% of Tm^{3+} ions have average 23.4 nm in width and 37.9 nm in length. After shell deposition the csANP have 30.8 nm and 42.7 nm in width and length, respectively. Shell thicknesses were calculated in an indirectly way based on average cANP and csANP dimensions and for 3% Tm^{3+} doped csANP total 3.1 nm and 3.8 nm in width and length, respectively. For 8% Tm^{3+} doped csANP shell was 2 nm in long and 2.4 nm in a short dimension.

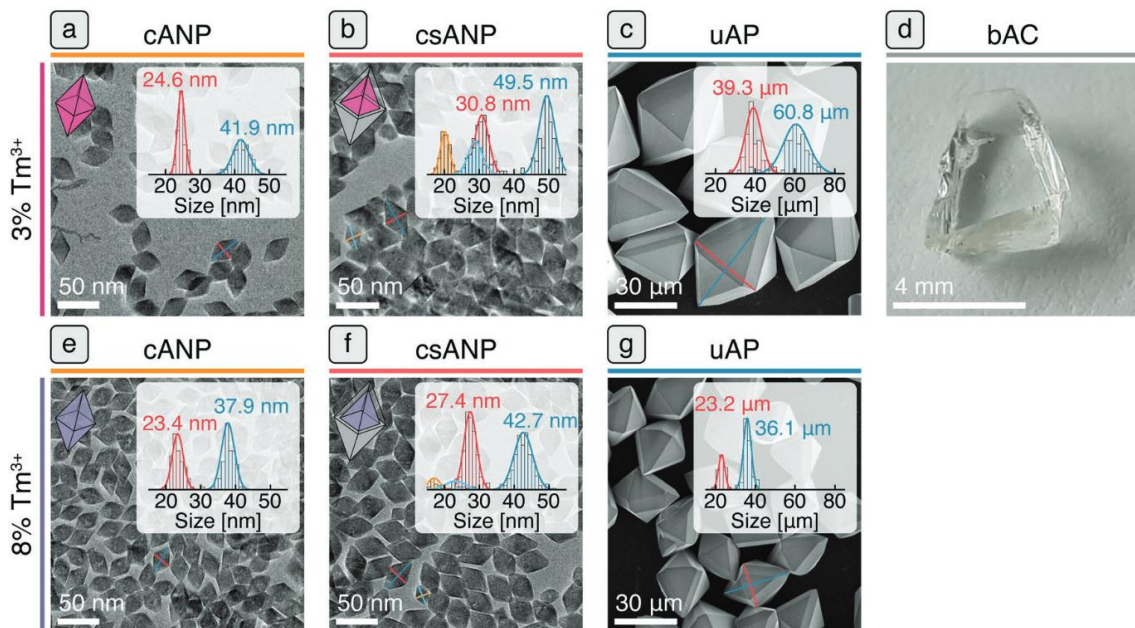


Figure 15. Size comparison of investigated LiYF_4 crystals: TEM pictures of cANP (a),(e) and csANP (b),(f) doped with 3% and 8% of Tm^{3+} ions, respectively; SEM of 3% (c) and 8% (g) Tm^{3+} doped μAP ; bAC (d). Based on [50].

Table 5. Average dimensions for Tm³⁺ doped cANP, csANP, μ AP and bAC.

Sample	Dimension	3% Tm ³⁺		8% Tm ³⁺		Units
		Size	Shell thickness	Size	Shell thickness	
cANP	Short	24.6 ± 1.1		23.4 ± 1.6		[nm]
	Long	41.9 ± 2.3		37.9 ± 1.8		[nm]
csANP	Short	30.8 ± 2.0	3.1	27.4 ± 1.8	2.0	[nm]
	Long	49.5 ± 2.2	3.8	42.7 ± 2.7	2.4	[nm]
μ AP	Short	39.3 ± 4.0		23.2 ± 1.6		[nm]
	Long	60.8 ± 6.3		36.1 ± 1.9		[nm]
bAC		≈3				[mm]

14.2. Results

All the mentioned materials were investigated under 1064 nm wavelength excitation beam generated by single mode laser module, which is resonant with $^3F_4 \rightarrow ^3F_{2,3}$ ESA and simultaneously far from the resonance with GSA of Tm³⁺ ions. While measurement of ground state absorption spectra is possible with commercial instruments, measurement of absorption from excited state presents a serious challenge. To estimate the absorption cross-section for ESA of Tm³⁺, I have calculated the theoretical absorption spectra for Tm³⁺ ion. Depending on a matrix, absorption cross section at particular wavelength can differ. For the purpose of our investigations published in the mentioned article, I have calculated the absorption spectra for LiYF₄ crystal. Moreover, I have been prepared calculations of absorption spectra for other matrices doped with Tm³⁺ ions. The calculations can be future necessary do predict appropriate conditions to obtain PA in other materials.

The resulted theoretical absorption spectra for LiYF₄ matrix matrices, for both $^3F_4 \rightarrow ^3F_2$ and $^3F_4 \rightarrow ^3F_3$ ESA transitions, are presented in the **Figure 16 a** and **b**, respectively. Based on as prepared theoretical absorption spectra as well as cross section of GSA ($8.09 \cdot 10^{-24} \text{ cm}^2$) calculated in a similar way, the β parameters (**Equation 5**) for 1064 nm excitation wavelength were estimated and total 265.65 and 3.35 for $^3F_4 \rightarrow ^3F_2$ and $^3F_4 \rightarrow ^3F_3$ transitions, respectively.

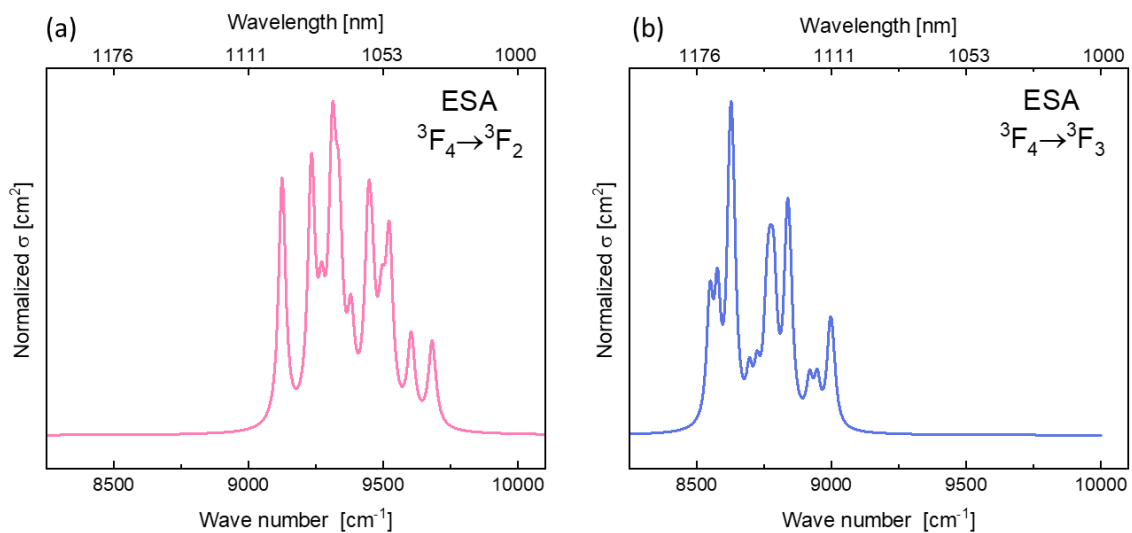


Figure 16. Theoretical excited state absorption spectra calculated for Tm^{3+} ions in LiYF_4 matrix for (a) ${}^3\text{F}_4 \rightarrow {}^3\text{F}_2$ and (b) ${}^3\text{F}_4 \rightarrow {}^3\text{F}_3$ transition.

The remaining theoretical absorption spectra calculated for the other matrices for both ${}^3\text{F}_4 \rightarrow {}^3\text{F}_2$ and ${}^3\text{F}_4 \rightarrow {}^3\text{F}_3$ ESA transitions are presented in the **Figure 17a** and **b**, respectively.

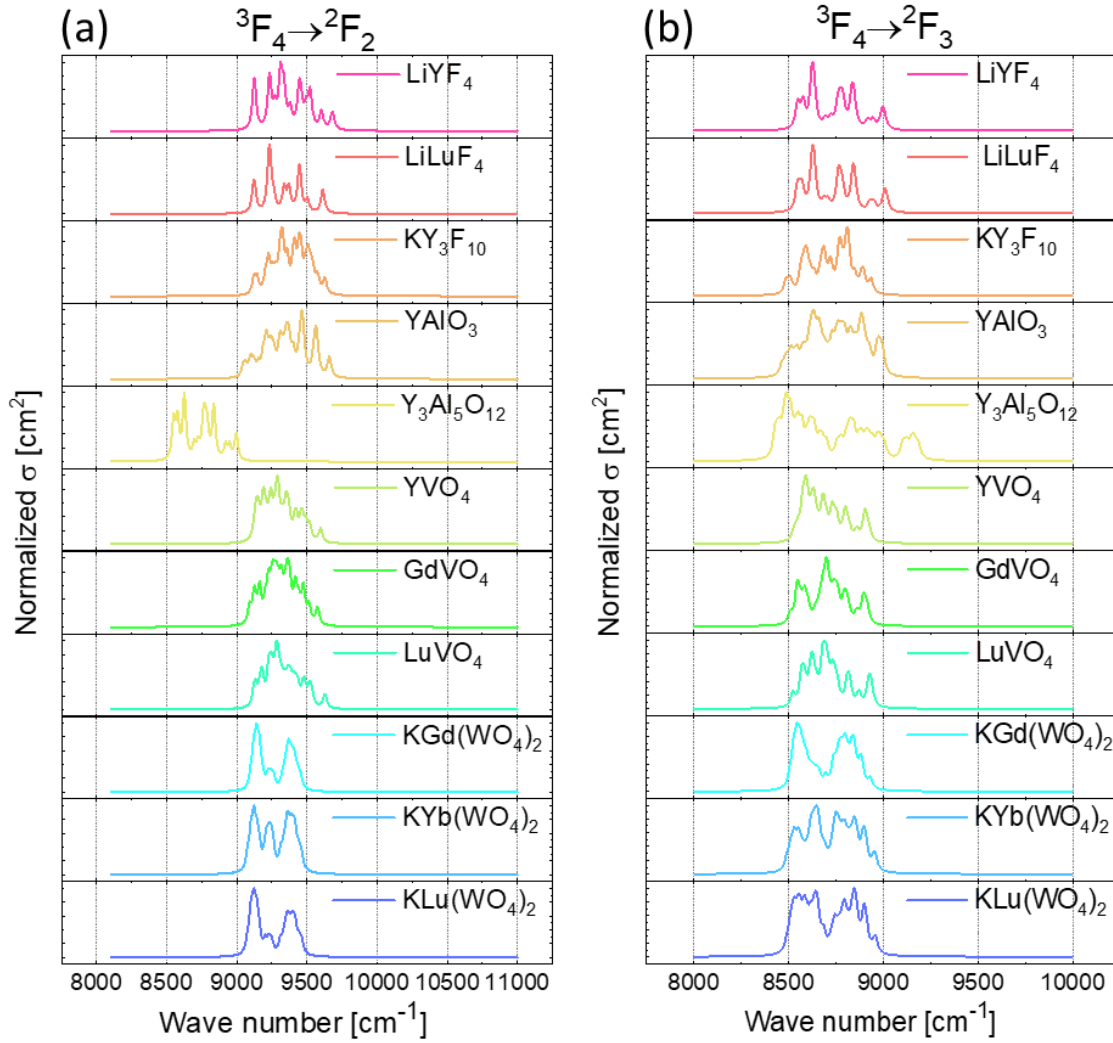


Figure 17. Theoretical excited state absorption spectra calculated for Tm^{3+} ions in different matrices for (a) $^3\text{F}_4 \rightarrow ^2\text{F}_2$ and (b) $^3\text{F}_4 \rightarrow ^2\text{F}_3$ transition.

The optical properties of all the materials were investigated by Dr Eng. Marcin Szalkowski and M. Eng. Zuzanna Korczak, often with my assistance, using the same custom-developed optical setup and methodology. Colloidal nanoparticles were drop-casted on a glass slide and measured after evaporation of the medium. The samples were measured in 10 different places and the signal was averaged. Micro sized avalanching particles were measured as individual microparticles. The position of the sample relative to the beam was optimized each time individually by the highest signal intensity at fixed photoexcitation intensity. Successfully, the PA emissions features were observed for all the investigated materials at 800 nm ($^3\text{H}_4 \rightarrow ^3\text{H}_6$) and 475 nm ($^1\text{G}_4 \rightarrow ^3\text{H}_6$), while the emission at 475 nm was significantly weaker than 800 nm emission. The 1064 nm wavelength matches the $^3\text{F}_4 \rightarrow ^3\text{F}_2$ ESA transition. After population of $^3\text{F}_2$ energy

level, follows the non-radiative relaxation to lower ³H₄ energy state. Then, the energy can be emitted to the ground state (800 nm) or populated ³H₄ will become a starting level for ESA of 1064 nm, what leads to populate the ¹G₄ energy level, from which the 475 nm emission occurs. Higher intensity of 800 nm emission indicates, that the emission of energy by ³H₄ level is more probable than ESA absorption from this level, however both exists. The presented PA emissions were characterized by S, PA_{TH}, D_{AV} as well as the t_{50%} parameter (**Figure 18** and **Figure 19**). Considering the s-shape lines (first rows in the **Figure 18** and **Figure 19**), one can see, that lower PA_{TH} values for 8% of Tm³⁺ were observed for μAP than for nanoparticles and for the lower 3% Tm³⁺ doped materials, the lowest threshold values were observed also for the biggest host crystal - bAC. For set of LiYF₄ crystals doped with 3% of Tm³⁺ ions, μAP shown threshold higher than bAC, however the values were still lower than for cANP and csANP. It can be partially caused by the geometric relation between the focused spot of the laser beam and the material of a given size. For both 3% and 8% of Tm³⁺ ions doped crystals, csANP shown lower PA_{TH} than their corresponding cANP, what indicated the protective role of the inert shell, which insulated the optically active ions from the chemical environment influence. However, the differences in PA_{TH} values are not so big, especially for 3%Tm³⁺ doped crystals. Let's consider the ET process to the surface in two regimes of power densities, namely before PA_{TH} and at the PA_{TH}. Below the PA threshold, the probability of ET is higher than for the increased power densities, because in the latter case most of the ions are in the same energy state, making ET impossible. Thus, energy migration to surface quenchers is impeded. For this reason, the passive coating does not have a significant effect on the observed PA_{TH}, but quenching of ions near the surface should be expected. Increasing the concentration of optically active ions should contribute to the probability of ET, and thus the probability of energy migration to the surface is still high. So, in this case, the role of the passive shell is more significant, thus the difference between PA_{TH} of cANP and csANP doped with 8%Tm³⁺ ions is bigger than for doped with 3% of Tm³⁺ ions (first row **Figure 18** and **Figure 19**). In an analogous way, considering the value of the slope, the role of the inert shell is greater for nanocrystals doped with 8% Tm³⁺ ions for which the slope of the s-shape curve derived from csANP is 12.0 and for cANP is 8.4, while the slope of cANP and csANP samples for doping with

3% Tm^{3+} does not change significantly. Although the passive coating does not significantly change PA_{TH} , S or D_{AV} for nanocrystals doped with 3% Tm^{3+} ions, it does improve the luminescence brightness about tenfold over that of csANP. In addition, about eight times longer rise times are observed for csANP than for cANP. The increase in nonlinearity and decrease in PA_{TH} in the 8% Tm^{3+} doped sample are more significant than for 3% Tm^{3+} , suggesting that these effects are rather due to concentration of optically active ions than of inert shell presence.

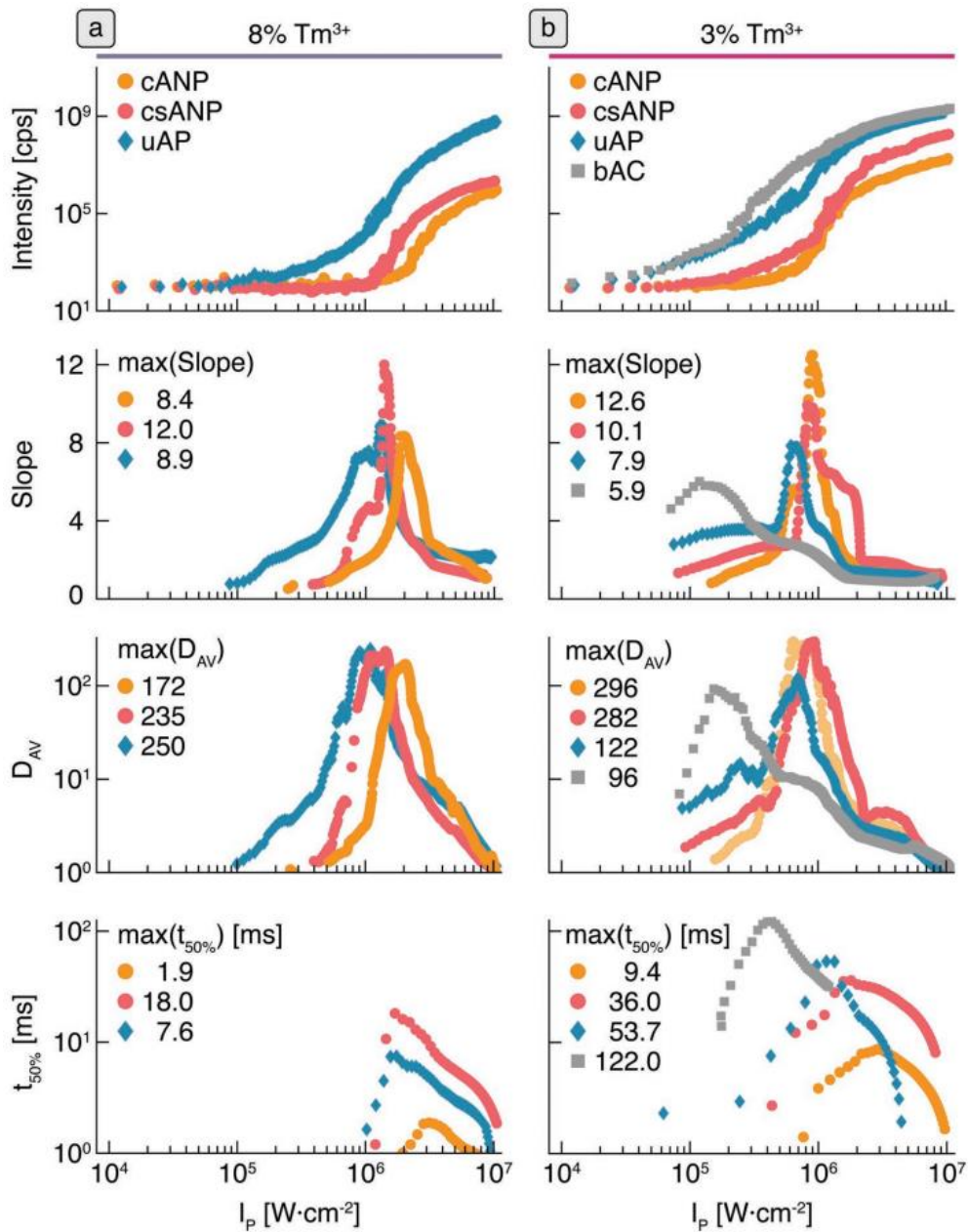


Figure 18. Pump power dependent photon avalanche luminescence of Tm^{3+} at 800 nm – characteristics for nano, micro and bulk PA crystals doped with a) 8% and b) 3% Tm^{3+} ions. Pump power dependent comparison of: row 1 – PA emission intensity, row 2 – PA slopes, row 3 – PA gains and row 4 – 50% risetimes. Based on [50].

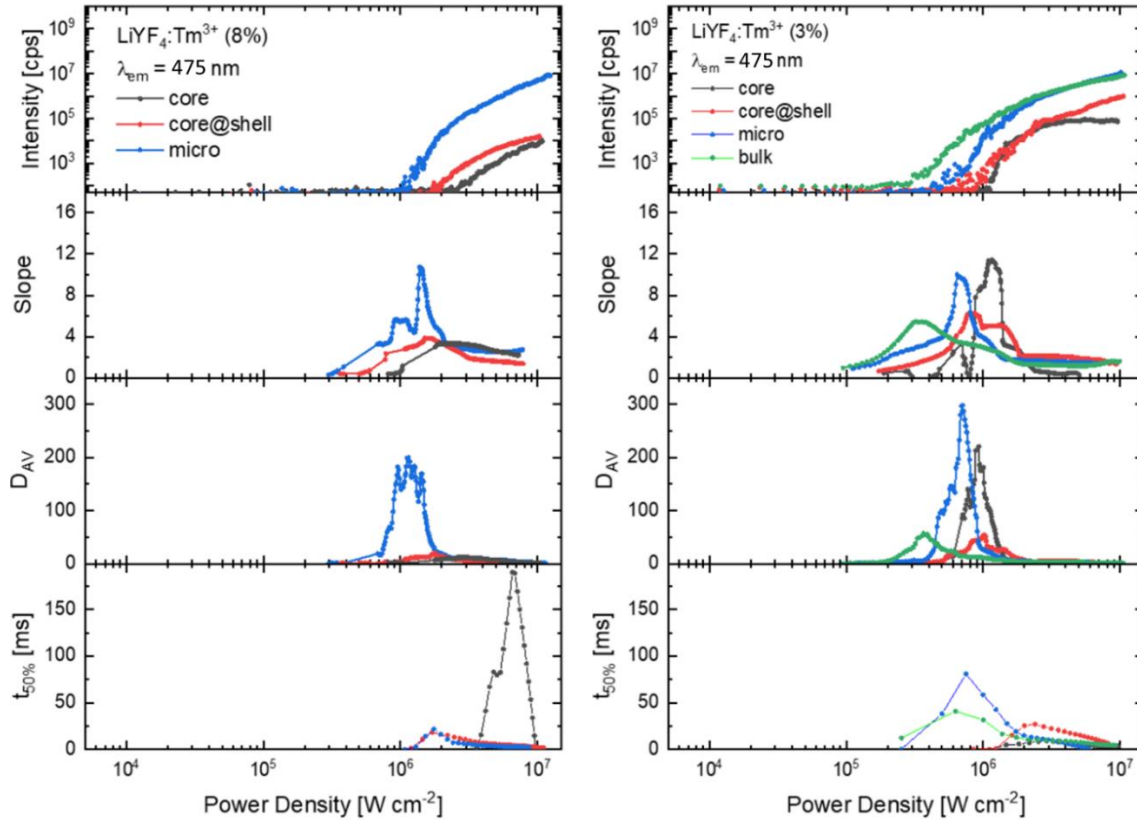


Figure 19. Characteristics of PA emission at 475 nm (1064 nm excitation) of: bulk crystals (green), microcrystals (blue), core nanocrystals (gray), and core-shell nanocrystals (red) for the LiYF_4 materials doped with 3% (right column) and 8% (left column) of Tm^{3+} ions. The slopes (S), gains (D_{AV}) as well as risetimes ($t_{50\%}$) were calculated automatically with use of a home developed software. Based on [50].

In order to understand the role of particular energy transfer processes leading to the observation of the PA emission in Tm^{3+} ions, theoretical DRE simulations were performed. I have participated in part of these simulations learning the way of calculations, however the presented here results were prepared by my supervisor prof. Artur Bednarkiewicz. At the beginning there was prepared the energy diagram of Tm^{3+} ions with energy transitions leading to observe the 800 nm PA emission. The A_3 and A_2 processes indicate the radiative rates of emissions from $^3\text{H}_4$ and $^3\text{H}_6$ energy levels, respectively. The k_3 and k_2 are connected with the non-radiative emission rates of these levels. The factors f_{ESA} and f_{CR} are connected with rated of ESA and CR and enable modulations of these energy transfers depending on experimental conditions. Then, particular energy levels (black levels in the **Figure 20**) of the diagram were described by DRE and resolved in Matlab. As prepared phenomenological model enables to verify, how individual parameters influence the PA features. Hence, it is possible to change particular parameters, while the other remain constant, and monitoring the

changes of s-shape curve S and PA_{TH} . The results of these calculation are presented in the **Figure 20**. Particular panels represent individual parameters, for example panels **b** and **c** represent the changes of parameter A_2 . The panel **b** shows different s-shapes corresponding modified values of parameter A_2 , which was increased and decreased around their original value ($A_2=162 \text{ cm}^{-1}$). The S parameters were calculated for all these s-shape curves and are presented below in the panel **c**. Each parameter is represented by different colors, with saturated shades representing higher values of a parameter, while lighter shades are associated with lower values. The black s-shape curves represent results obtained for pristine values. What is important, the energy transfer values A_2 , A_3 , k_2 , k_3 , f_{ESA} and f_{CR} can be directly related to the features of materials. The A_2 and A_3 parameters are calculated as an inverse of radiative lifetime of corresponding levels, which are influenced by crystal field of matrix. The crystal field can also influence the incompatibility of energy, because the strong crystal field increase the splitting of Stark levels. The k_2 and k_3 parameters are connected with non-radiative multiphonon relaxation, which are more probable in higher temperatures. Matrices with high phonon energies will promote the non-radiative processes. The k_2 and k_3 parameters are also connected with the surface to volume ratio. The value f_{ESA} is related with the matching of excitation wavelength to the energy break. In other words, f_{ESA} mirrors, how the excitation laser matches the ESA absorption spectra. The cross-relaxation factors are connected with distances between luminescence centers, so with the concentration of doping ions and suggest, that the relatively high optically active ions concentration is required to observe the PA phenomenon.

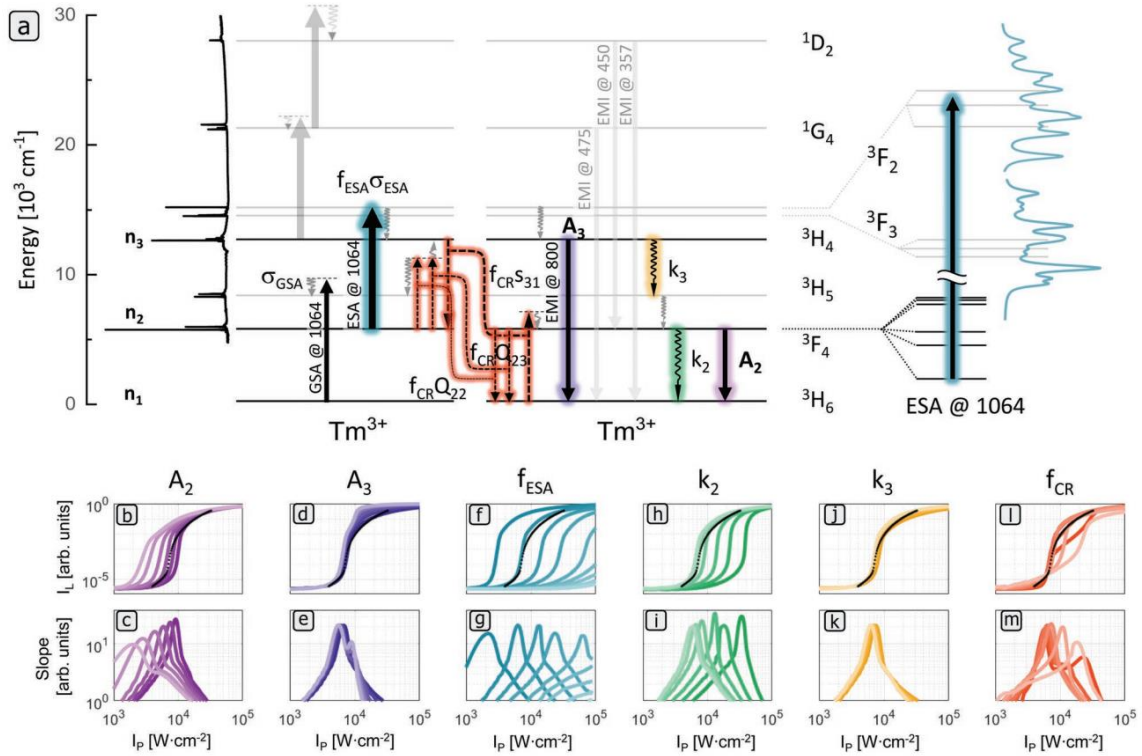


Figure 20. a) Energy diagram of Tm³⁺ ions with transitions leading to obtain PA emission, absorption spectra of Tm³⁺ in LiYF₄: left – measured ground state absorption spectra, right – calculated excited state absorption spectra. Bottom: Power dependent simulated behavior of PA emission – [middle row: (b), (d), (f), (h), (j), (l)] PA emission intensity and [bottom row: (c), (e), (g), (i), (k), (m)] PA slopes in response to changes of phenomenological parameters: $A_2 = 250, 200, 150, 100, 50, 20 \text{ s}^{-1}$, $A_3 = 1000, 500, 250, 100, 50, 25 \text{ s}^{-1}$, $f_{\text{ESA}} = 5, 2, 1, 0.5, 0.2, 0.1, 0.05, 0.02, 0.01$; $k_2 = 1000, 500, 250, 100, 50, 25 \text{ s}^{-1}$, $k_3 = 2000, 1000, 500, 250, 50, 25 \text{ s}^{-1}$ and $f_{\text{CR}} = 0.5, 0.2, 0.1, 0.05, 0.02, 0.01$. Individual parameters were varied one at a time, while the other were fixed. More saturated color indicates higher values. Black dotted lines correspond experimental data obtained for 8%Tm³⁺-doped NaYF₄@NaYF₄ colloidal nanocrystals at RT. Based on [50].

Although I did not perform sub-diffraction imaging by myself, the sample used to verify the feasibility of obtaining PASSI imaging below the diffraction limit (i.e. LiYF₄: 3% Tm³⁺ @ NaYF₄) was synthesized and analyzed by me. Practical demonstration of ANP applications, such as sub-diffraction imaging was prepared in collaboration with M. Kopernik UMK University (Dr D. Piątkowski, prof. S. Maćkowski). One can note a pump power dependent (**Figure 21 a-c**) PASSI images of an individual ANP, which follow the prediction from [68]. The cross sections of the images along the dashed lines (**Figure 21 a-c**) are presented in panel **d**. From these cross-sections, full width at half maximum (FWHM) values were derived to demonstrate below the diffraction limit capabilities.

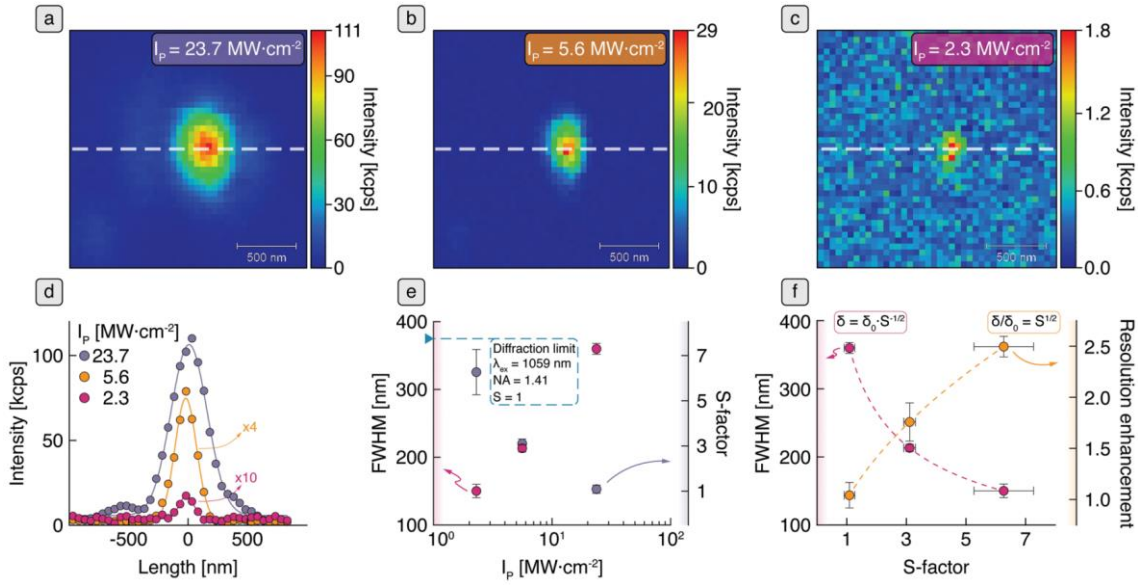


Figure 21. PASSI imaging demonstrations on single LiYF_4 : 3% Tm^{3+} @ NaYF_4 nanocrystal at various pumping powers. a–c) presents PASSI maps for different pumping intensities, d) PA emission cross sections for particular power densities, e) values of FWHM (left axis) and S (right axis) corresponding to the cross-sections and f) demonstration of the imaged spot FWHM changes with varying S (left axis) and the resolution enhancement (right axis). Based on [50].

14.3. Conclusions

In summary, the presented investigations allow to understand the relationship between the material size and PA emission features. The two set of materials were prepared and characterized. Firstly, the series of LiYF_4 crystals doped with 3% of Tm^{3+} ions, namely bulk crystal, microcrystals as well as core and core-shell nanocrystals were prepared. Secondly, the set of LiYF_4 crystals doped with 8% of Tm^{3+} was synthesized and was composed of microcrystals as well as core and core-shell nanocrystals. Unfortunately, we did not have a bulk crystal of the same composition, however it was interesting to investigate crystals with this doping, because the 8% Tm^{3+} concentration was found as an optimal for PA [24]. All investigated material successfully shown the PA emissions at 475 nm and 800 nm under an excitation with matches ESA 1064 nm wavelength. The photoluminescence show high nonlinearity with slopes from 6 to 12. The risetimes slowdown dependent on pump power density was observed. The PA features of investigated materials, as S parameters, PA_{TH} , D_{AV} and $t_{50\%}$ values were compared. Moreover, the theoretical simulations of PA in Tm^{3+} doped system were performed aiming to verify the influence of particular energy transfers of PA properties.

15. PA in Pr³⁺ and Yb³⁺ co-doped β-NaYF₄ nanocrystals

Results presented in the chapter describe experimental and theoretical investigations on PA in Pr³⁺, Yb³⁺ co-doped crystals and were published in the article: “Understanding Yb³⁺-sensitized photon avalanche in Pr³⁺ co-doped nanocrystals: modelling and optimization” [189].

15.1. Materials

Two series of β-NaYF₄ nanocrystals, first doped with Pr³⁺ ions, second co-doped with Pr³⁺ and Yb³⁺ ions, were synthesized aiming to verify the possibility to achieve PA emission. All the nanoparticles were prepared in core and core-shell architecture by thermal decomposition of lanthanide salts method. Spherical cores synthesis as well as ellipsoidal shell deposition were performed by thermal decomposition of lanthanide oleates. Spherical shells were overlaid by thermal decomposition of lanthanide trifluoroacetates. The synthesis methods are described in details in the Experimental section (**Chapter 10.1**). Future investigations leading to observe PA emission in nanocrystals co-doped with Pr³⁺ and Yb³⁺ ions were an inspiration to check, if the phenomenon exists, when these ions are placed in different crystals or in different crystal layers. Samples synthesized for these investigations are described also in present paragraph.

15.1.1. Singly Pr³⁺ doped β-NaYF₄ colloidal nanocrystals

The first series of nanoparticles consisted of β-NaYF₄ nanocrystals singly doped with Pr³⁺ ions in a wide range concentrations, namely 0.1%, 0.5%, 1%, 3%, 5%, 8% of Pr³⁺ ions. Initially, the samples structure and morphology were characterized. To confirm the crystallographic purity of synthesized materials, X-ray powder diffractions investigations were performed and obtained diffractograms were compatible with the template of β-NaYF₄ phase (**Figure 22**). Sizes of the prepared nanocrystals were estimated based on TEM pictures. Exemplary particular nanoparticles TEM images together with an appropriate histograms including average dimensions of nanocrystals are presented in the **Figure 23**. The core dimensions are in the range from 15.8 nm to 19.2 nm. Shell deposition was indirectly evidenced relating on the average dimensions of core and corresponding core-shell nanocrystals. Most of core-shell prepared nanoparticles

have ellipsoidal shape with length in the range from 23.6 nm to 31.3 nm and width within 18.7 nm – 23.5 nm. Based on these dimensions, average shell thickness of the presented nanocrystals is around 5 nm in length and below 2 nm in width. Specific shell thickness values for appropriate samples have been provided in the **Table 6**. One of prepared core-shell sample was synthesized with spherical shape. This was done deliberately to subsequently compare this sample with an analogous one, which has an additional 15% Yb³⁺ in the core composition. In this case, smaller, presumably undoped β -NaYF₄ nanoparticles crystallized alongside the larger core-shell nanoparticles. Successfully applied shell has a thickness around 2.5 nm (**Table 6**). Considering, that the thickness of presented later spherical core-shell nanocrystals (**Table 6**) is around 4.2 nm, it can be evidenced, that part of shell material crystallized as smaller, undoped β -NaYF₄ nanocrystals.

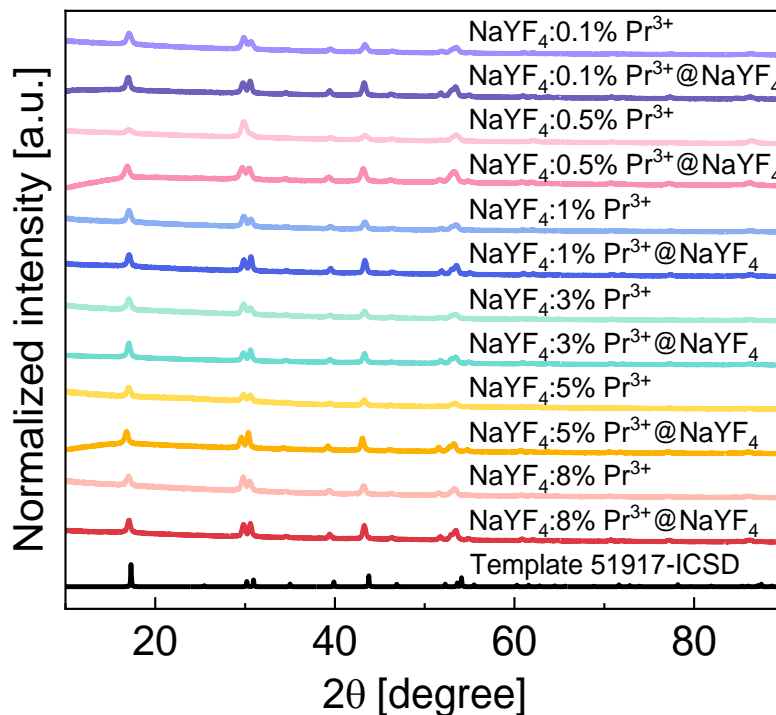


Figure 22. XRD for singly doped with 0.1%, 0.5%, 1%, 3%, 5% and 8% of Pr³⁺ ions core and core-shell β -NaYF₄ nanocrystals as well as the template of the β -NaYF₄ structure.

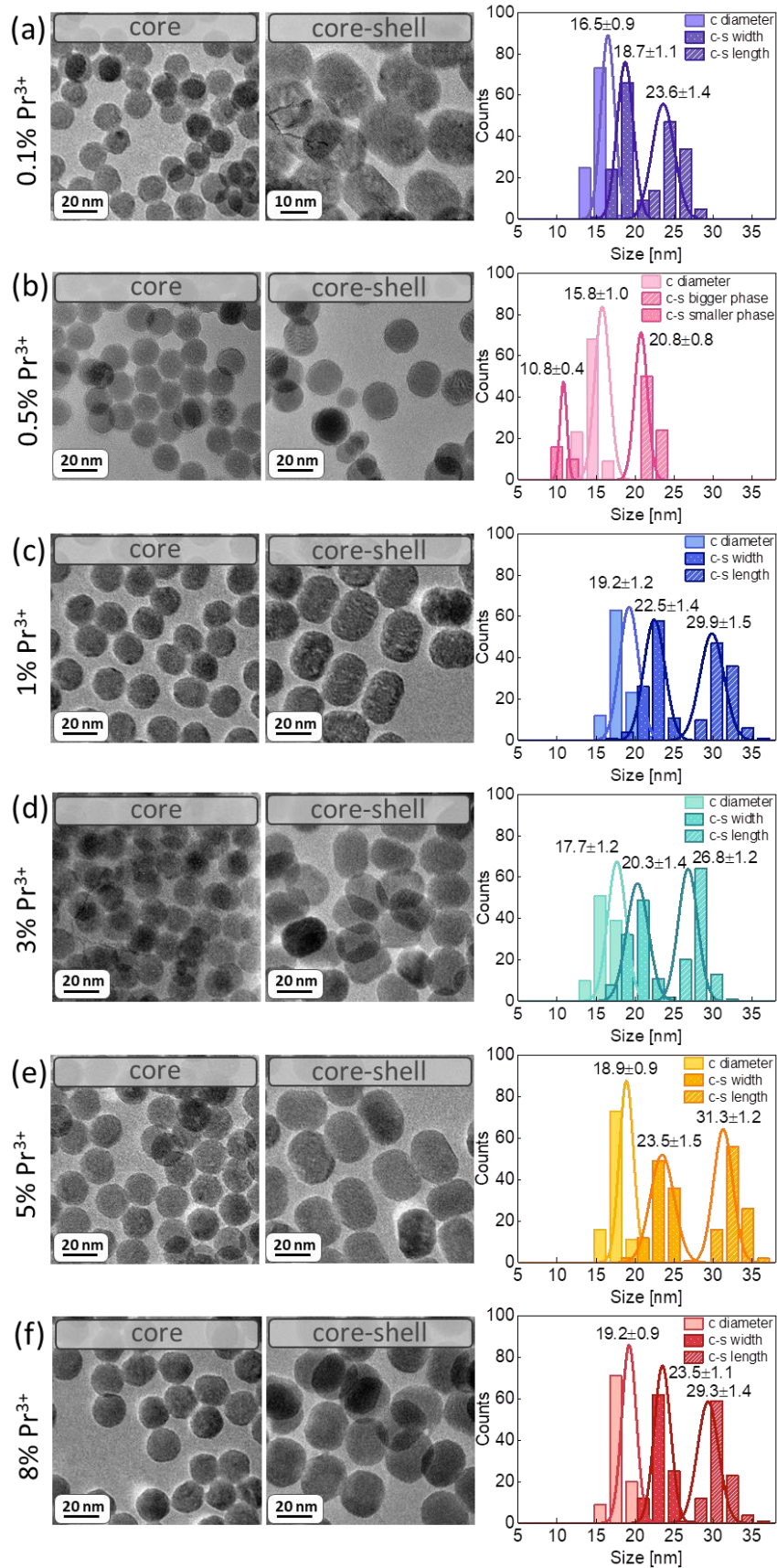


Figure 23. Morphology characteristics of β-NaYF₄ nanocrystals singly doped with Pr³⁺ ions: TEM images as well as histograms presenting average sizes of the core and core-shell nanocrystals doped singly with (a) 0.1%, (b) 0.5%, (c) 1% and (d) 3%, (e) 5% and (f) 8% of Pr³⁺ ions.

Table 6. Average dimensions and shell thicknesses of β -NaYF₄ nanocrystals singly doped with Pr³⁺ ions.

Dopant:	Average core diameter [nm]	Average core-shell width [nm]	Average core-shell length [nm]	Average shell thickness in width [nm]	Average shell thickness in length [nm]
0.1% Pr ³⁺	16.5±0.9	18.7±1.1	23.6±1.4	1.1±1.0	3.6±1.2
0.5% Pr ³⁺	15.8±1.0	20.8±0.8		2.5±0.9	
1% Pr ³⁺	19.2±1.2	22.5±1.4	29.9±1.5	1.7±1.3	5.4±1.4
3% Pr ³⁺	17.7±1.2	20.3±1.4	26.8±1.2	1.3±1.3	4.6±1.2
5% Pr ³⁺	18.9±0.9	23.5±1.5	31.3±1.2	2.3±1.2	6.2±1.1
8% Pr ³⁺	19.2±0.9	23.5±1.1	29.3±1.4	2.2±1.0	5.1±1.2

15.1.2. x% Pr³⁺ and 15% Yb³⁺ co-doped β -NaYF₄ colloidal nanocrystals

Beside singly Pr³⁺ ions doped, x% Pr³⁺ (x=0.1%, 0.3%, 0.5% and 0.7%) and 15% Yb³⁺ ions co-doped β -NaYF₄ nanocrystals were synthesized. The idea was inspired by earlier publication on MPA phenomenon observed in Pr³⁺ and Yb³⁺ co-doped nanocrystals [70]. Here, all the samples were synthesized in the core and core-shell architecture by thermal decomposition of lanthanide salts. The amount of Yb³⁺ ions was constant at 15% with a variable, wider range of Pr³⁺ ions concentration, namely 0.1%, 0.3%, 0.5% or 0.7%. Morphology and structural characteristics of synthesized materials was performed. All Pr³⁺ and Yb³⁺ co-doped nanocrystals have been crystallized in a pure hexagonal β -NaYF₄ phase (**Figure 24**). Exemplary TEM images are presented in the **Figure 25** panels **a, d, g, j** and **b, e, h, k** for the core and core-shells, respectively. Histograms with average dimensions of nanocrystals were prepared based on appropriate TEM images and are presented in the **Figure 25** panels **c, f, i** and **l**. Cores diameter is average around 20 nm and core-shells dimension is around 28 nm. Relying on average nanocrystals dimension, thickness of shell was estimated to be above 4 nm. Specific dimensions are placed in the **Table 7**. The shell deposition was additionally directly evidenced by exemplary EDS map and profile of Yb³⁺ and Y³⁺ ions for NaYF₄: 0.5% Pr³⁺, 15%Yb³⁺@NaYF₄ nanocrystal (**Figure 26 a, b**). As expected, Yb³⁺ ions are placed only in core, while Y³⁺ are present both in core and core-shell parts.

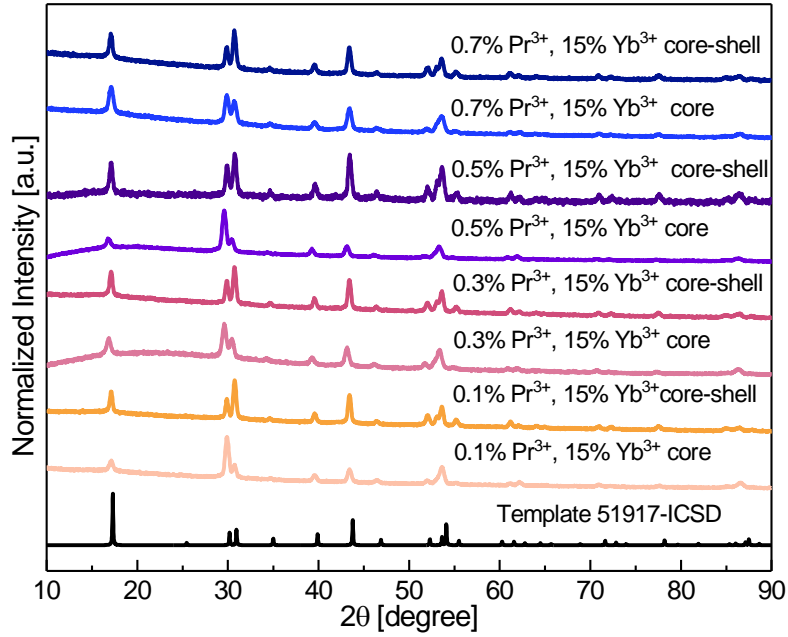


Figure 24. XRD for core and core-shell β-NaYF₄ nanocrystals co-doped with x% Pr³⁺ and 15% Yb³⁺ ions as well as the template of the β-NaYF₄ structure.

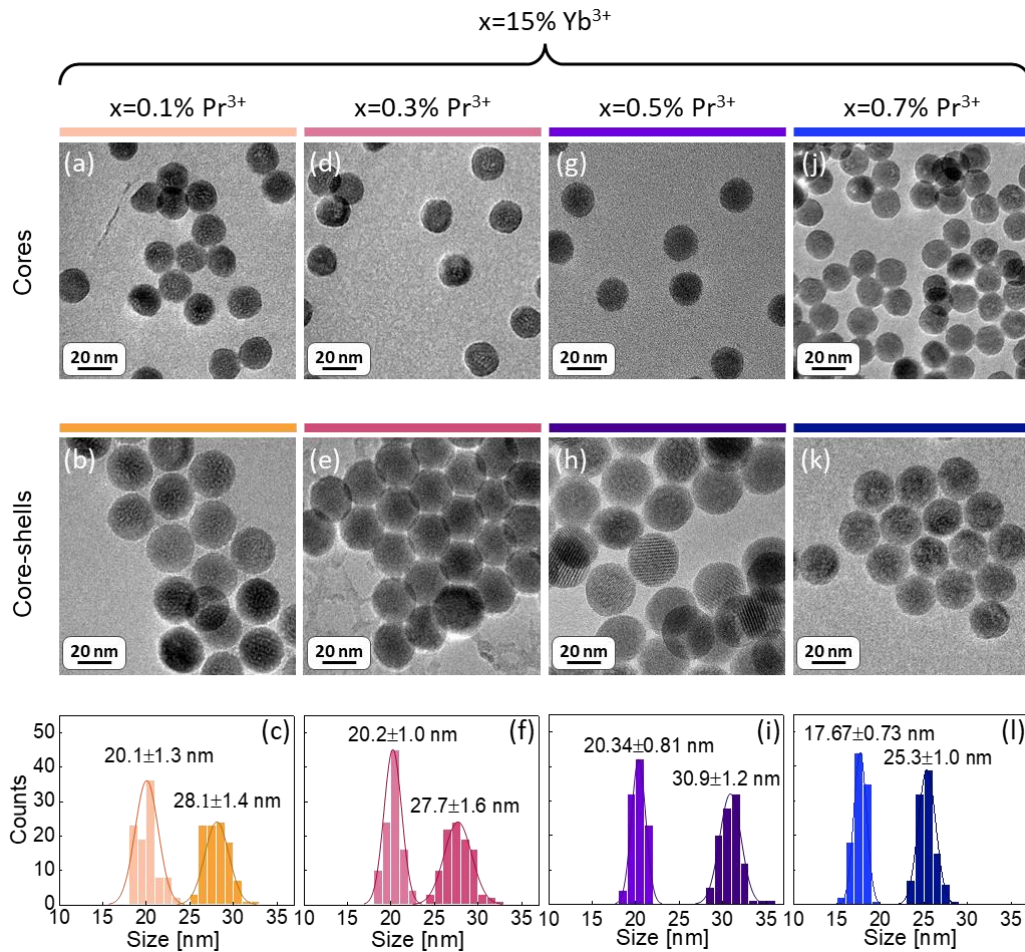


Figure 25. Characteristic of β-NaYF₄ nanocrystals co-doped with Pr³⁺ and Yb³⁺ ions: TEM pictures of core nanoparticles (a, d, g, j); TEM of core-shell nanocrystals (b, e, h, k); Histograms presenting average sizes of core and core-shell nanocrystals (c, f, i, l).

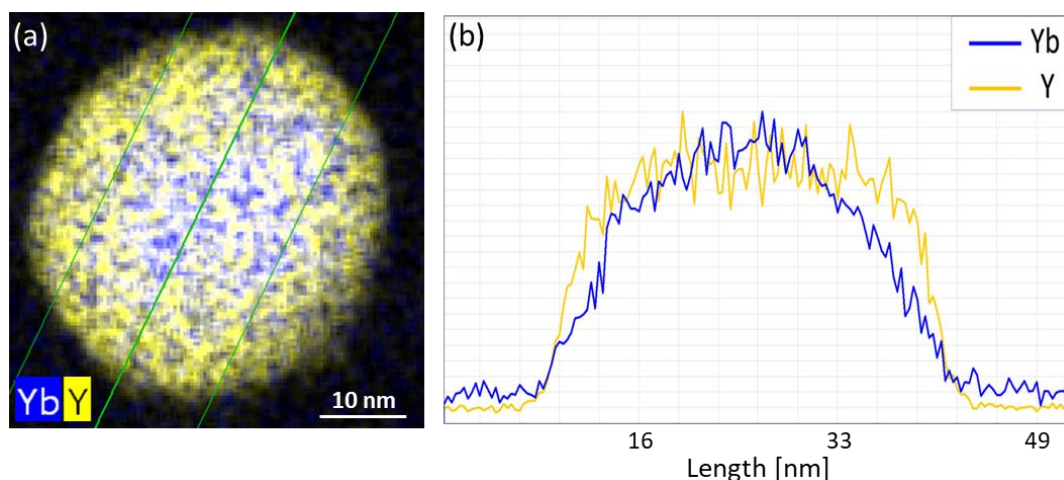


Figure 26. (a) EDS map and (b) EDS profile of Yb^{3+} and Y^{3+} ions in $\text{NaYF}_4: 0.5\% \text{Pr}^{3+}, 15\% \text{Yb}^{3+} @ \text{NaYF}_4$ nanocrystal.

Table 7. Average dimensions and shell thicknesses of $\beta\text{-NaYF}_4$ nanocrystals co-doped with Pr^{3+} and Yb^{3+} ions. Based on [189].

Dopant:		Average core diameter [nm]	Average core-shell diameter [nm]	Average shell thickness [nm]
15% Yb^{3+}	0.1% Pr^{3+}	20.1±1.3	28.1±1.4	4.0±1.4
	0.3% Pr^{3+}	20.2±1.0	27.7±1.6	3.8±1.3
	0.5% Pr^{3+}	20.34±0.81	30.9±1.2	5.3±1.0
	0.7% Pr^{3+}	17.67±0.73	25.3±1.0	3.8±0.9

The impact of Pr^{3+} ions concentration as well as architecture of prepared nanocrystals on PA was investigated.

15.1.3. NaYbF_4 and $\beta\text{-NaYF}_4$ crystals

After successful observation of PA in nanocrystals co-doped with Yb^{3+} ions and a small amount of Pr^{3+} ions, the idea was born, whether it would be possible to observe PA when Pr^{3+} and Yb^{3+} ions are placed in separate crystals or separate layers of crystals. Such results would evidence of energy transfer between separate crystals or layers of nanoparticles. One idea was to mix the NaYbF_4 crystals with $\text{NaYF}_4:0.5\% \text{Pr}^{3+}$ particles. Therefore these samples were synthesized. The core $\text{NaYF}_4:0.5\% \text{Pr}^{3+}$ nanocrystals were prepared by standard thermal decomposition method described in the **Chapter 10.1**. To obtain the NaYbF_4 crystals (**Figure 27**), the thermal decomposition of lanthanide salts synthesis method was optimized and finally, crystallographic pure phase was obtained

when the solvents ODE and OA were in the volume ratio 2:1 and the synthesis temperature was 320°C. The obtained crystals were relatively large, around 340 nm.

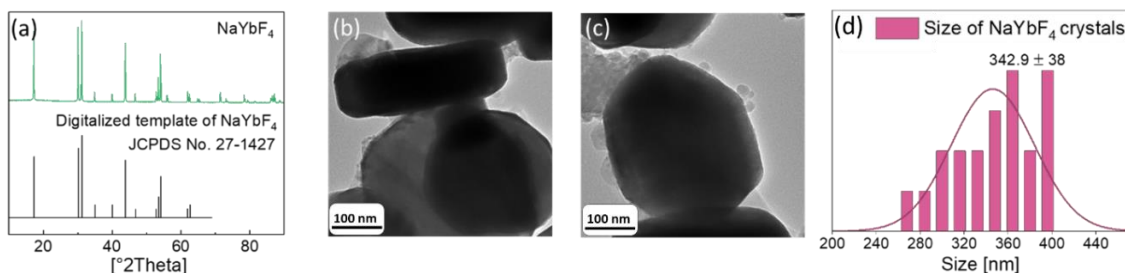


Figure 27. Characteristics of NaYbF₄ crystals: (a) XRD of NaYbF₄ crystal phase (template) and for synthesized sample; (b),(c) TEM images; (d) Histogram with average particles sizes.

The second idea was to investigate, if PA is possible to observe, when the Pr³⁺ and Yb³⁺ ions are placed in separate crystal layers, therefore the following sample NaYF₄:40%Yb³⁺@ NaYF₄:0.5%Pr³⁺@NaYF₄ was synthesized. This sample was synthesized in three steps, namely first was synthesized the core as NaYF₄:40%Yb³⁺, then core@shell sample as NaYF₄:40%Yb³⁺@ NaYF₄:0.5%Pr³⁺ and finally the inert shell layer was applied to obtain the NaYF₄:40%Yb³⁺@ NaYF₄:0.5%Pr³⁺@NaYF₄ nanocrystals. After particular steps, the crystallographic structure was investigated by XRD (**Figure 28**) and TEM images were prepared (**Figure 29**). Increase of particle size is an evidence of deposit the shell on previous core (**Figure 29**).

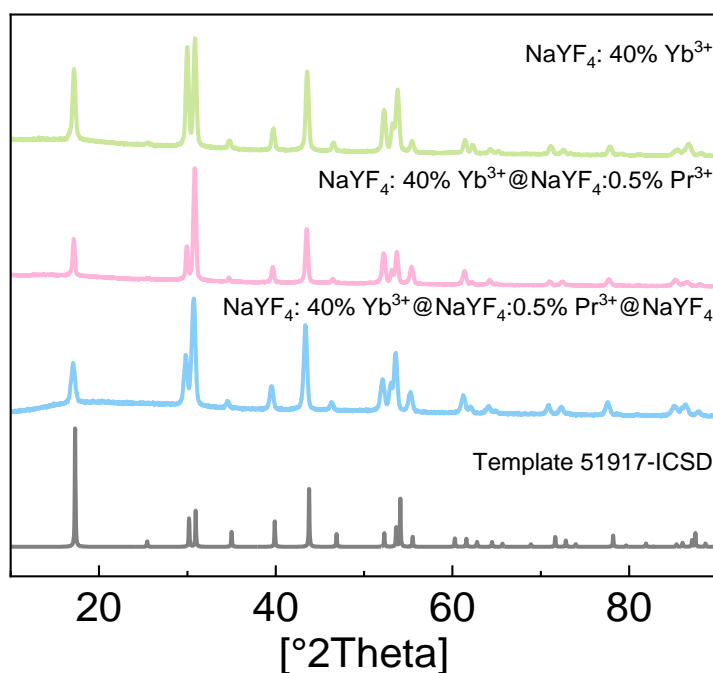


Figure 28. XRD of β-NaYF₄ structure (template) and of NaYF₄:40%Yb³⁺, NaYF₄:40%Yb³⁺@ NaYF₄:0.5%Pr³⁺ and NaYF₄:40%Yb³⁺@ NaYF₄:0.5%Pr³⁺@NaYF₄ crystals.

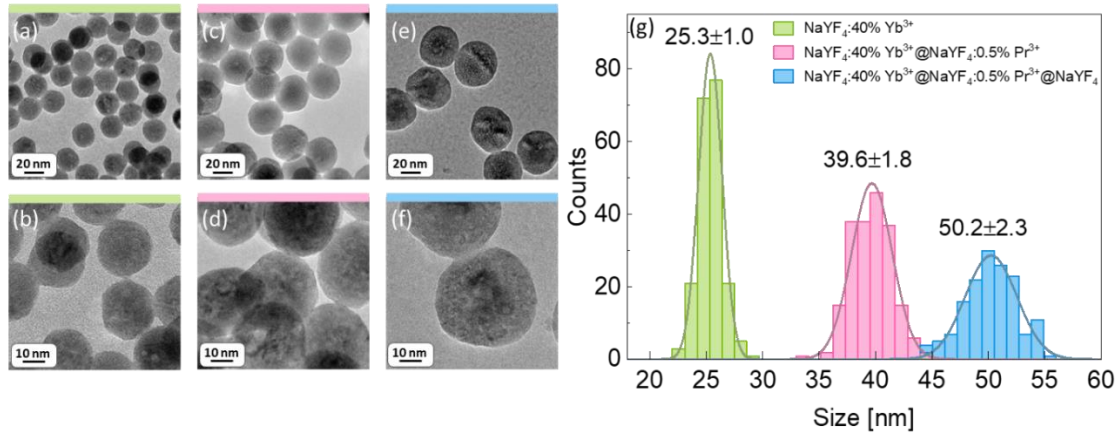


Figure 29. TEM images of: (a,b) $\text{NaYF}_4:40\%\text{Yb}^{3+}$, (c,d) $\text{NaYF}_4:40\%\text{Yb}^{3+}@ \text{NaYF}_4:0.5\%\text{Pr}^{3+}$ and (e,f) $\text{NaYF}_4:40\%\text{Yb}^{3+}@ \text{NaYF}_4:0.5\%\text{Pr}^{3+}@ \text{NaYF}_4$ crystals as well as (g) corresponding histograms with average particles sizes.

15.2. Spectroscopic results

For synthesized nanocrystals mentioned in the paragraphs 11.1.1. and 11.1.2. was prepared spectroscopy characteristics, including measurements of absorption, excitation and emission spectra as well as lifetimes. Afterwards, all materials were investigated in order to check PA existence under 852 nm excitation wavelength using special, custom built setup.

15.2.1. Basic spectroscopy measurements

Absorption spectra of all the synthesized samples were measured (Figure 30 a, b). In Pr^{3+} and Yb^{3+} co-doped nanocrystals concentration of Yb^{3+} ions was constant, namely 15%. It is confirmed by similar absorbance at 980 nm, the peak corresponding Yb^{3+} ions $^2F_{5/2} \rightarrow ^2F_{7/2}$ absorption, for all samples (Figure 30 a). Absorbance at wavelengths corresponding Pr^{3+} ions is different for all samples and obviously increases with Pr^{3+} ions amount (Inserts in the Figure 30 a, b). To choose the most appropriate wavelength to excite the samples in a Stokes mode, excitation spectra were measured (Figure 30 c, d). Monitoring emission at 980 nm and 607 nm, for co-doped with Pr^{3+} , Yb^{3+} ions and singly Pr^{3+} doped samples, respectively, the most appropriate for excitation turned to be 444 nm wavelength for which luminescence was the most intensive. A surface area under the peak 444 nm was calculated (inserts in the Figure 30 c, d). For core-shell co-doped samples, intensity decreases with Pr^{3+} ions concentration, but in the case of cores firstly increases (from 0.1% to 0.3% of Pr^{3+}) and then decreases (Figure 30 c). It probably means, that higher amount of Pr^{3+} causes more efficient energy

transfer to Yb³⁺ ions instead of emission. For singly Pr³⁺ doped nanocrystals firstly, intensity increases with Pr³⁺ ions concentration, from 0.1% to 3%, and successively decreases, from 3% to 8% of Pr³⁺ ions (**Figure 30 d**). The decrease is probably connected with concentration quenching effect, which take a place for high concentration of dopant. Emissions spectra were measured under excitation with 444 nm and are presented in the **Figure 30 e** and **f**. The most intense emissions were observed at 482 nm (³P₀→³H₄) and 607 nm (³P₀→³H₆). For Pr³⁺ and Yb³⁺ co-doped samples luminescence intensity increases with Pr³⁺ ions concentration, what is intuitive (insert in the **Figure 30 f**). Core-shell nanocrystals show higher intensity of luminescence as compared to the core only samples (insert in the **Figure 30 e**), what indicates protective role of inert shell. In the case of singly Pr³⁺ ions doped samples the luminescence intensity initially increases and subsequently, for higher Pr³⁺ ions concentrations, decreases, what confirms the concentration quenching effect.

Synthesis, modeling and spectroscopic evaluation of selected Tm^{3+} , Pr^{3+} , Ho^{3+} doped and Yb^{3+} co-doped colloidal photon avalanching nanoparticles

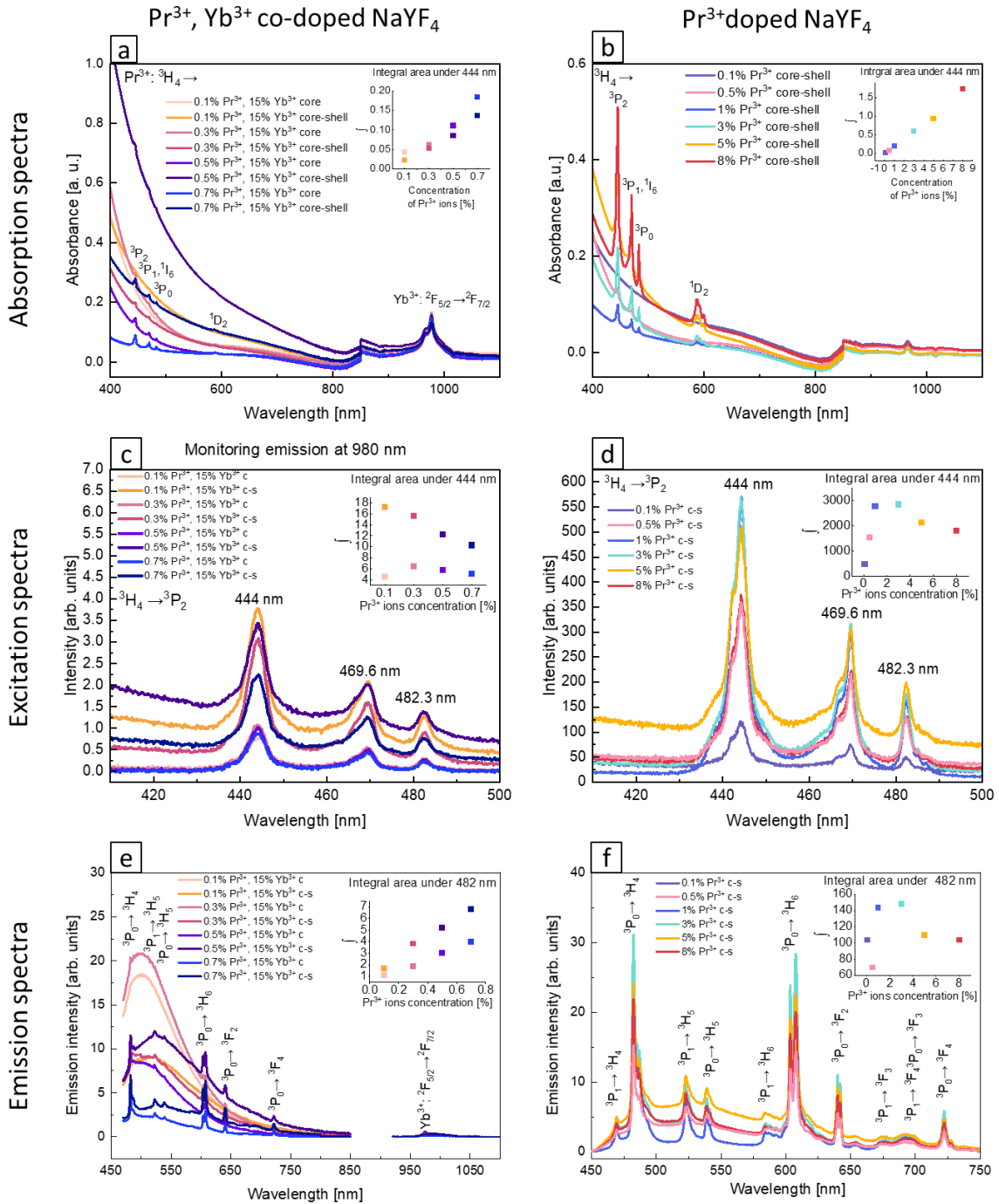


Figure 30. Spectroscopic measurements for β -NaYF₄ nanocrystals: Absorption and scattering spectra of β -NaYF₄ nanocrystals: (a) cores and core-shells co-doped with Pr³⁺ and Yb³⁺ ions (b) core-shells doped with Pr³⁺ ions; Excitation spectra for (c) cores and core-shells co-doped with Pr³⁺ and Yb³⁺ ions monitoring emission at 980 nm (d) core-shells doped with Pr³⁺ ions monitoring emission at 607 nm; Emission spectra under excitation with 444 nm for (e) cores and core-shells co-doped with Pr³⁺ and Yb³⁺ ions (f) core-shells doped with Pr³⁺ ions. Inserted plots: in absorption and scattering spectra (a) and (b) present integral area under the peak at 444 nm; in excitation spectra show changes of the integral area under the peak at 444 nm with concentration of Pr³⁺ ions for (c) core and core-shell samples co-doped with Pr³⁺, Yb³⁺ ions (d) core-shell singly Pr³⁺ doped nanocrystals; in emission spectra show changes of the integral area under the peak at 482 nm with concentration of Pr³⁺ ions for (e) core and core-shell samples co-doped with Pr³⁺, Yb³⁺ ions (f) core-shell singly Pr³⁺ doped nanocrystals.

15.2.2. Anti-Stokes emission

For investigations in terms of PA existence, the 852 nm wavelength was chosen as an excitation one. This wavelength is resonant with ESA in Pr³⁺ ions and simultaneously far from resonance with GSA in these ions, which is a one of the key conditions for PA existence. Firstly, core-shell β-NaYF₄ singly Pr³⁺ doped nanocrystals were investigated, however any emission was observed **Figure 31 a**. In contrast, samples co-doped with x% Pr³⁺ (x=0.1, 0.3, 0.5, 0.7) and 15% Yb³⁺ ions, both in core and core-shell architecture, successfully shown multicolor emission in a visible range (**Figure 31 b, c**). Comparing luminescence intensity of core (**Figure 31 b**) and core-shell (**Figure 31 c**) nanocrystals one can see, that core-shells show higher luminescence intensity. Quantitative comparison of the intensity of emission spectra may be subject to error, because the concentration of measured nanocrystals were not exactly the same in all case, but explicit difference in all core and appropriate core-shell samples indicates key role of inert shell, which protects optically active ions from environment influence. The appropriate transitions were assigned to emissions bands: ³P₁→³H₄ (468 nm), ³P₀→³H₄ (482 nm), ³P₁→³H₅ (522 nm), ³P₀→³H₅ (538 nm), ³P₁→³H₆ (583 nm), ³P₀→³H₆ (607 nm), ³P₀→³F₂ (641 nm), ³P₁→³F₃ (672 nm), ³P₁→³F₄ (693 nm) and ³P₀→³F₄ (720 nm) **Figure 31 c**.

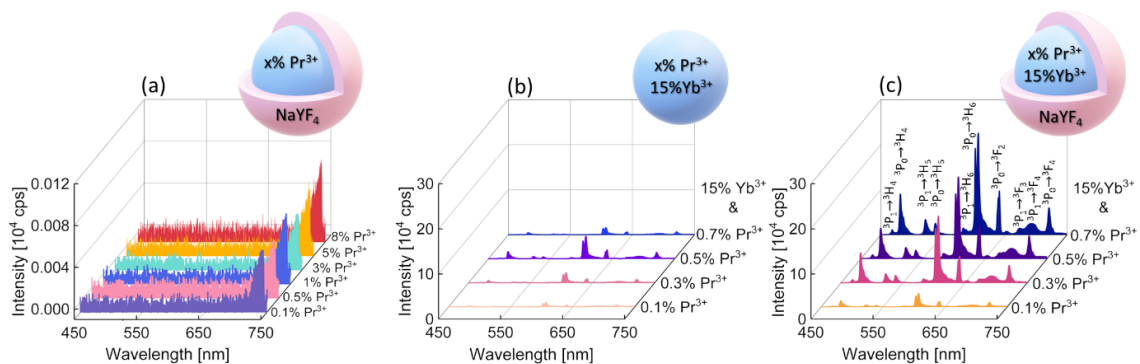


Figure 31. Anti-Stokes emission spectra of β-NaYF₄ nanocrystals (a) core-shells singly doped with Pr³⁺ ions, (b) cores co-doped with x% Pr³⁺, 15% Yb³⁺, (c) x% Pr³⁺, 15% Yb³⁺ co-doped cores with passive shell, with assigned transitions. Presented emission spectra were measured under 852 nm excitation (1.5 MW/cm²) at RT. Based on [189].

In the literature the assignment of emission bands in the range 580-620 nm is presented differently. Some sources assigned the emissions in the range 580-620 nm as coming from ³P_{0,1,2} and the other from ¹D₂ [27], [70], [91], [190]–[192]. The present

investigations have led to correctly attribute the emission at 607 nm to the ³P₀→³H₆ transition. The energy gap between levels ³P₀ and ¹D₂ is 3850 cm⁻¹. Pr³⁺ ions effectively absorb the energy around 444 nm, what leads to ³H₄→³P_{0,1,2} transition, therefore overcoming of mentioned energy gap by multi-phonon relaxation will be necessary to observe emission from ¹D₂ level. However, in low phonon energy matrices, as β-NaYF₄ fluorides with 350 cm⁻¹ phonon energy, a significant (here 11) amount of phonons would be necessary to non-radiatively relax from ³P₀ to ¹D₂ level. Therefore, the emission from level ¹D₂, in contrast to fluorides, is highly probable in other matrices, as oxides with higher phonon energies [193], [194]. Moreover, the energy of 607 nm photon equals 16 475 cm⁻¹ and is closer to the ³P₀→ H₆ transition (16 400 cm⁻¹) than to the ¹D₂→³H₄ (16 800 cm⁻¹) transition. The emission at 482 nm origins from the ³P₀ level, therefore, to prove attribution of the 607 nm emission, the fluorescence lifetime decay curves at these both emission wavelengths were measured for NaYF₄: 15%Yb³⁺, 0.5%Pr³⁺@ NaYF₄ nanocrystals. The research were conducted in a function of temperature from around -200°C to 300°C. The fluorescence lifetime decay curves of excited levels measured for both 482 nm and 607 nm were near the same and measurement at RT is presented in the **Figure 32**. The excitation level lifetimes measured at RT total 13.60 μs and 17.65 μs for 607 nm and 482 nm, respectively. Parameters of short and long components of fluorescence lifetime decay curves in a function of temperature have similar trends for 482 nm and 607 nm (**Figure 33**). Average fluorescence lifetimes were calculated according to the formula

$$t_{avr} = \frac{A_1 t_1 + A_2 t_2}{A_1 + A_2} \quad \text{Equation 15}$$

and at RT amount to 17.65 μs and 13.60 μs for 482 nm and 607 nm, respectively. Fluorescence lifetime decay curves measurements confirmed the validity of the attribution of the emission at 607 nm.

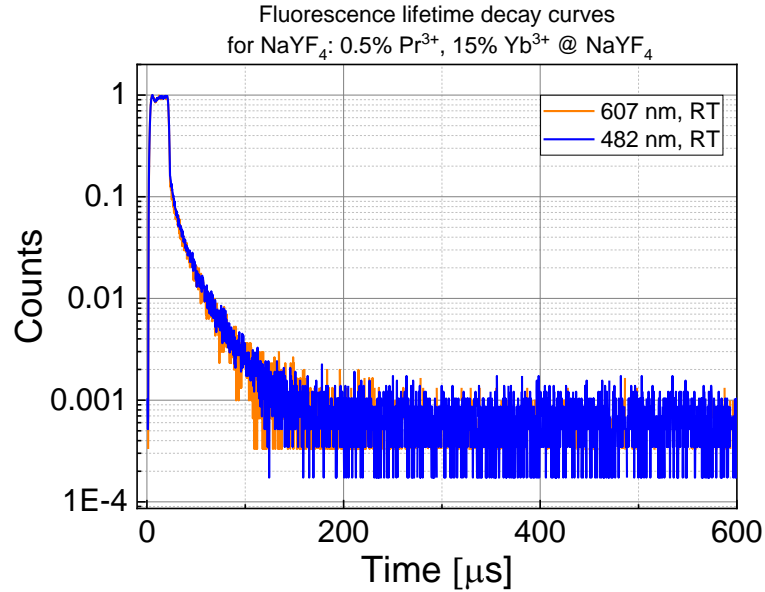


Figure 32. Fluorescence lifetime decay curves of NaYF₄:0.5 % Pr³⁺, 15% Yb³⁺ @ NaYF₄ nanocrystals measured at 482 nm (blue curve) and 607 nm (orange curve) under 444 nm excitation wavelength at RT. Based on [189].

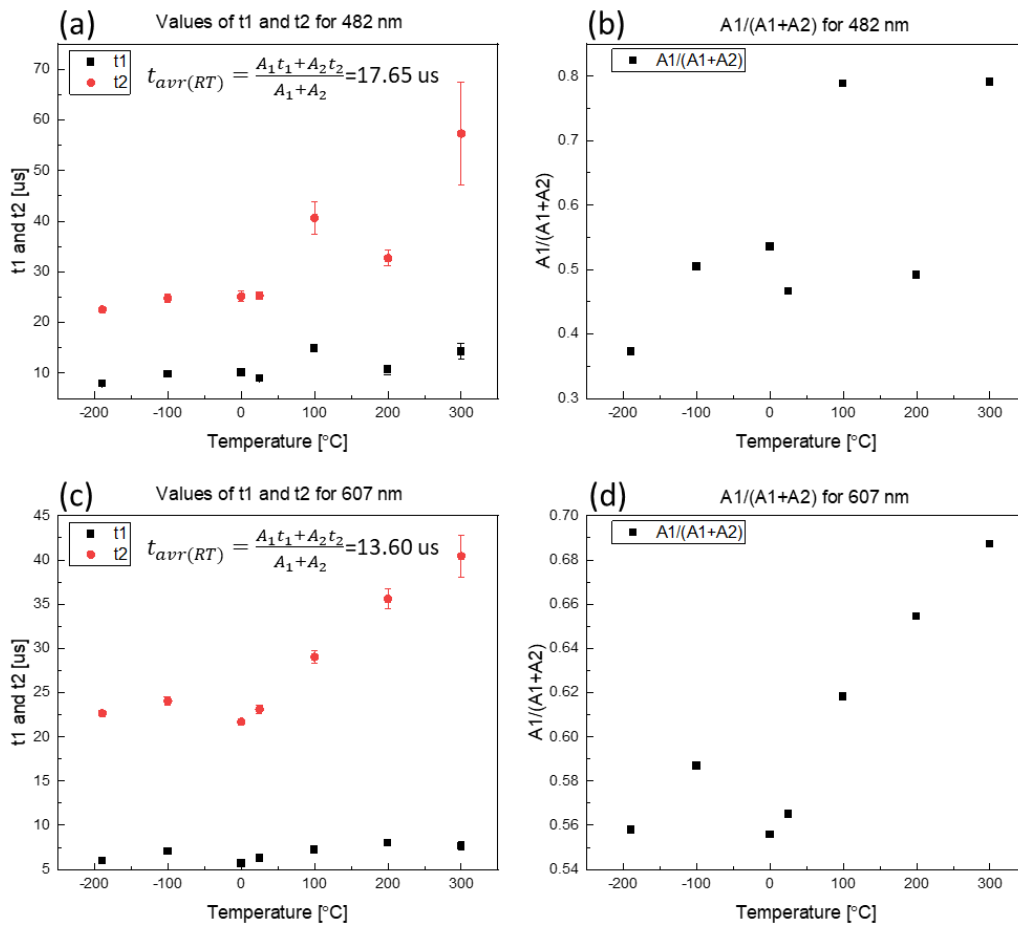


Figure 33. Parameters of short and long components of fluorescence lifetime decay curves of NaYF₄:0.5 % Pr³⁺, 15% Yb³⁺ @ NaYF₄ nanocrystals measured at wide range of temperatures at (a-b) 482 nm and (c-d) 607 nm. Based on [189].

Considering the obtained emission spectra of nanocrystals co-doped with Pr^{3+} and Yb^{3+} ions, the most intensive peaks, namely at 482 nm and 607 nm corresponding the ${}^3\text{P}_0 \rightarrow {}^3\text{H}_4$ and ${}^3\text{P}_0 \rightarrow {}^3\text{H}_6$ transitions, respectively, were chosen in order to check PA existence. All Pr^{3+} and Yb^{3+} co-doped $\beta\text{-NaYF}_4$ core and core-shell nanocrystals were excited with 852 nm wavelength, which pump power density was increasing from 10^4 W/cm^2 to around 10^7 W/cm^2 with small step of pump power value (between 1000 and 2000 W/cm^2 per step). PA features were successfully observed for both emissions in all these samples. The dependences of photoluminescence intensity of pump power density have a characteristic for PA s-shapes (**Figure 34 a, b**). The curves were measured at least two times and average maximum slopes and maximum thresholds were calculated (**Figure 34 c-f Table 8**). Higher S values, namely 6-9 were obtained for core-shell samples comparing with only cores, where the slopes were in the range 5-8. In the case of PA_{TH} , smaller values, indicating that PA is easier to obtain, were noted for core-shells compare with cores. These results confirm, that the inert shell, which protects optically active ions from the environment influence, enhance PA process. S values increase with the Pr^{3+} ions concentration up to 0.5% and then decrease a bit. For core-shells nanoparticles PA_{TH} decrease with Pr^{3+} ions concentration up to 0.5% and then increase. In the case of cores, thresholds still increase. The biggest slopes, namely 8.6 and 9 as well as the lowest PA_{TH} values, i.e. 286 kW/cm^2 and 281 kW/cm^2 for emissions at 607 nm and 482 nm, respectively, were obtained for $\beta\text{-NaYF}_4$ nanocrystals co-doped with 15% Yb^{3+} and 0.5% Pr^{3+} ions, thus the optimal composition for PA was confirmed [70]. Considering, that Yb^{3+} ions are essential to obtain PA emission from Pr^{3+} ions under 852 nm excitation, the process was called as SPA.

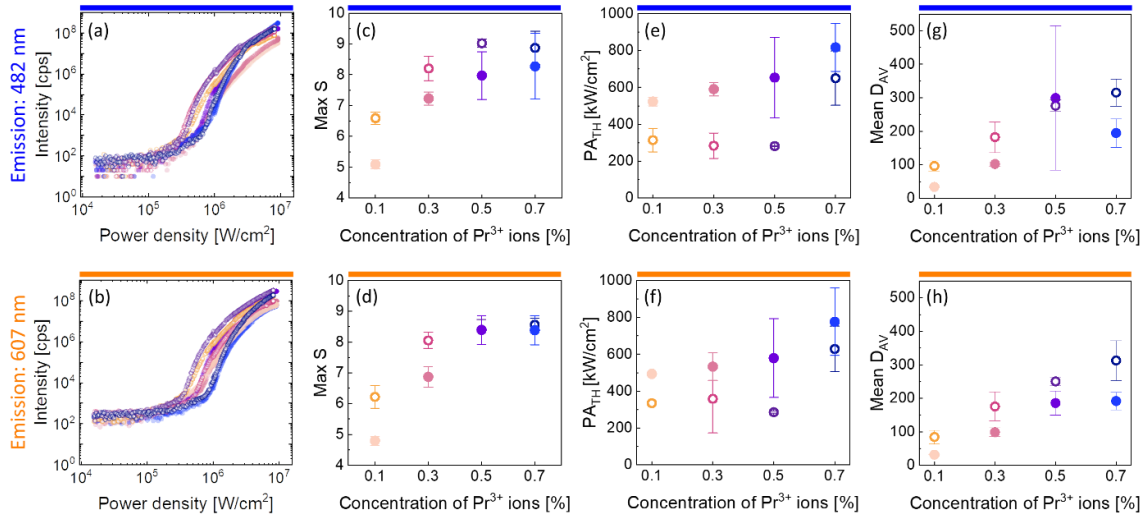


Figure 34. Spectroscopic PA characteristics of core and core-shell β -NaYF₄ nanocrystals co-doped with 15% Yb³⁺ and x% Pr³⁺ ions (x=0.1, 0.3, 0.5 or 0.7). PA features recorded for core (●) and core-shell (○) nanoparticles top row: at 482 nm and bottom row: at 607 nm: **(a),(b)** pump-power dependence of PA luminescence; **(c),(d)** Maximum values of S, which are a measure of nonlinearity of the PA process (Equation 2); **(e),(f)** PA_{TH} pump powers in a function of concentration of Pr³⁺ ions. **(g),(h)** Mean values of D_{AV} parameters indicating efficiency of PA process. Average values and standard deviations for **(c, d, e, f)** were calculated based on a few (2-4) measurements of curve of intensity in a function of pump power density. Based on [189].

Table 8. Values of average maximum slopes and average thresholds with standard deviations of PA emission at 482 nm and 607 nm of core-shell nanocrystals co-doped with 15% Yb³⁺ and 0.1%, 0.3%, 0.5% or 0.7% of Pr³⁺ ions. Based on [189].

Emission at 482 nm		
Sample	Average maximum S	Average PA _{TH} [kW/cm ²]
NaYF ₄ :0.1%Pr	5.09 ± 0.14	523 ± 23
NaYF ₄ :0.3%Pr	7.23 ± 0.21	591 ± 37
NaYF ₄ :0.5%Pr	7.97 ± 0.78	654 ± 218
NaYF ₄ :0.7%Pr	8.3 ± 1.1	817 ± 130
NaYF ₄ :0.1%Pr@NaYF ₄	6.59 ± 0.20	315 ± 64
NaYF ₄ :0.3%Pr@NaYF ₄	8.20 ± 0.40	284 ± 69
NaYF ₄ :0.5%Pr@NaYF ₄	9.02 ± 0.13	281.3 ± 2.9
NaYF ₄ :0.7%Pr@NaYF ₄	8.87 ± 0.54	650 ± 147
Emission at 607 nm		
Sample	Average maximum S	Average PA _{TH} [kW/cm ²]
NaYF ₄ :0.1%Pr	4.79 ± 0.15	493.4 ± 7.5
NaYF ₄ :0.3%Pr	6.87 ± 0.33	533 ± 75
NaYF ₄ :0.5%Pr	8.40 ± 0.47	579 ± 214
NaYF ₄ :0.7%Pr	8.39 ± 0.47	776 ± 183
NaYF ₄ :0.1%Pr@NaYF ₄	6.22 ± 0.37	335 ± 42
NaYF ₄ :0.3%Pr@NaYF ₄	8.06 ± 0.26	358 ± 185
NaYF ₄ :0.5%Pr@NaYF ₄	8.60 ± 0.14	285.6 ± 6.1
NaYF ₄ :0.7%Pr@NaYF ₄	8.56 ± 0.21	629 ± 123

The observation of avalanche emission in nanocrystals co-doped with Pr³⁺ and Yb³⁺ ions became the inspiration to see if avalanche emission would be observed when Pr³⁺ and Yb³⁺ ions were placed in separate crystals or in separate layers of the nanocrystal. Such results would confirm energy transfer between separate crystals or between adjacent layers of the nanocrystal. The materials described in section 15.1.3 of this dissertation were used to carry out this research. Under 852 nm excitation, NaYF₄:40%Yb³⁺@NaYF₄:0.5%Pr³⁺@NaYF₄ core-shell-shell nanocrystals and also NaYbF₄ crystals mixed with NaYF₄:0.5%Pr³⁺ nanocrystals were studied. Short-lived white emission visible to the naked eye was observed. However, until now,

we had no control over which part of the sample we hit during the measurement, because the manual microscope table, the only one available for these experiments, did not allow for sufficient precision. Therefore, a thorough study, allowing precision scanning of the sample, is planned.

15.2.3. PA in a function of temperature

The sample NaYF₄: 0.5% Pr³⁺, 15% Yb³⁺@NaYF₄ synthesized by me, which was found as optimal for PA under 852 nm photoexcitation was studied in a function of temperature and reported [25]. The morphology characterization was prepared by me and is presented in the **Figure 35**.

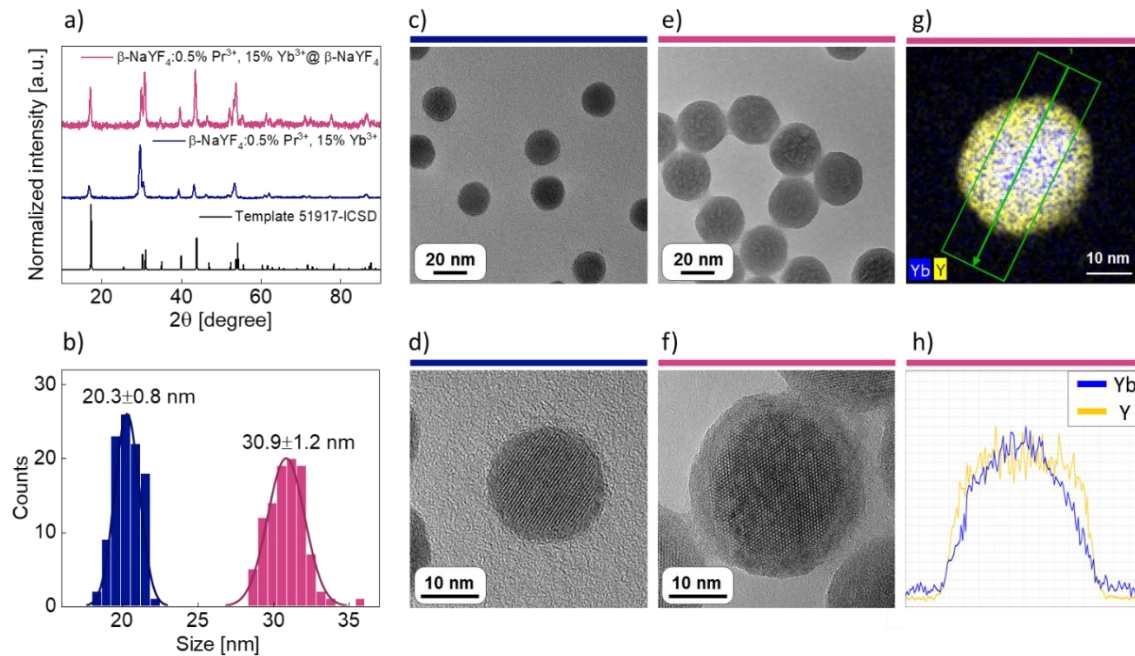


Figure 35. Core NaYF₄:0.5%Pr³⁺, 15%Yb³⁺ and core-shell NaYF₄:0.5%Pr³⁺, 15%Yb³⁺@NaYF₄ nanocrystals characteristics. a) XRD patterns, b) histograms presenting materials sizes, c) core and e) core-shell nanocrystals TEM image; d) core and f) core-shell nanocrystals high-resolution transmission electron microscopy (HRTEM) images; g) EDS map and h) EDS profiles of Yb³⁺ and Y³⁺ ions in the representative core-shell nanocrystal [25].

Two emission bands of Pr³⁺, at 482 nm and 607 nm were measured versus pump power. Aiming to verify the origin of emission at 607 nm I have performed luminescence lifetimes measurements presented in the previous paragraph (**Figure 32** and **Figure 33**). The PA measurements in a function of temperature were conducted by M. Eng. Zuzanna Korczak (**Figure 36**) and results obtained for emission at 607 nm are presented here.

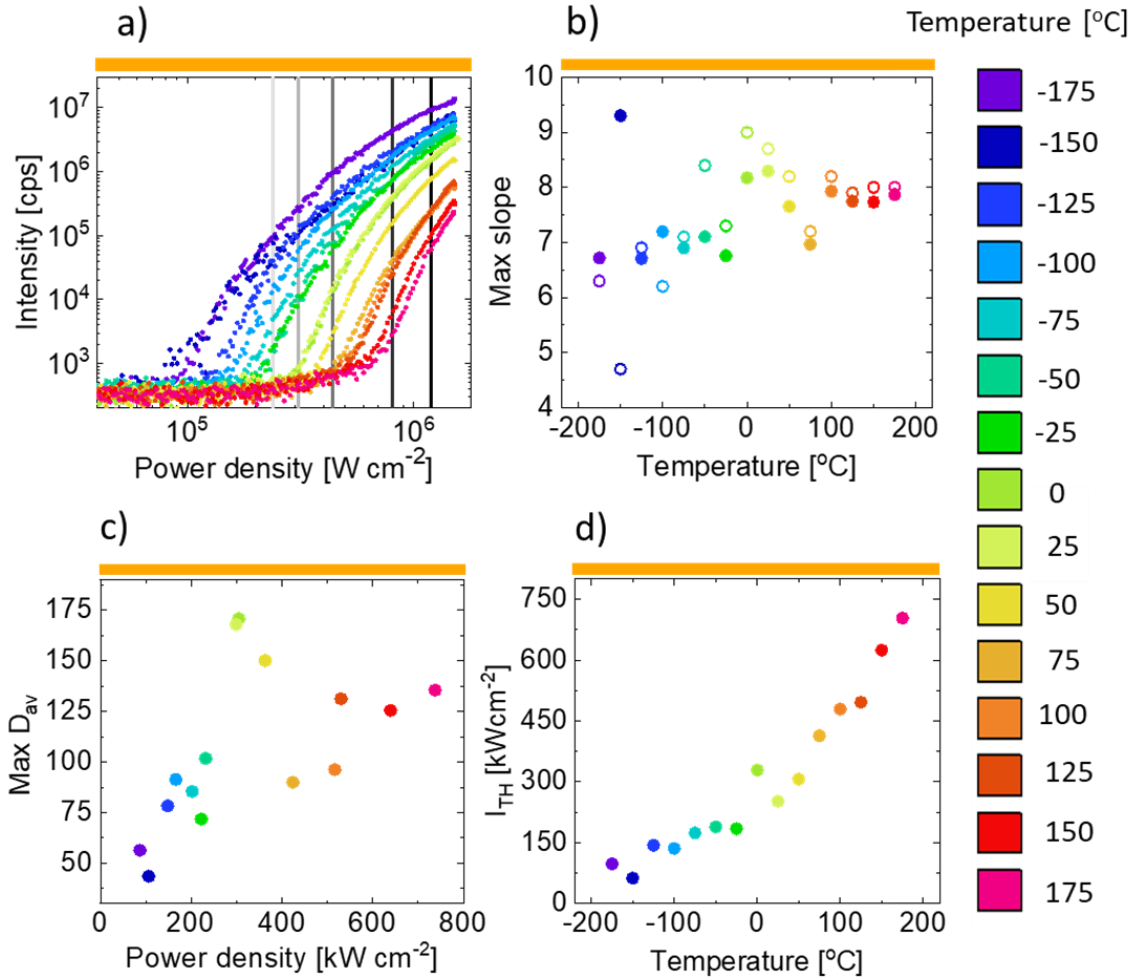


Figure 36. Characteristics of the 607 nm photon avalanche emission in the core-shell NaYF_4 nanocrystals co-doped with 0.5% Pr^{3+} and 15% Yb^{3+} under 852 nm photoexcitation. Panel a) presents photon avalanche emission intensity pump power dependence at various temperatures, b) demonstrates the highest PA non-linearities (S_{max}) derived by the algorithm described in ref.[50] (full circles) and manually (open circles); c) presents maximal PA gain at the excitation intensity corresponding to highest non-linearity (i.e. $D_{AV}(I_{exc}@S_{MAX})$), d) demonstrates PA threshold in a function of temperature. All datasets on b-d) were derived from the measurements of luminescence intensity in a power density function (a) [25].

The SPA emissions were evaluated at wide temperature range, namely from -175°C to 175°C . This is a novel approach for luminescence thermometry, where thermometric parameter is defined as the PA_{TH} . With increase of the temperature, the PA_{TH} gradually shifted from 100 kW/cm^2 to higher 750 kW/cm^2 excitation power densities. A relative temperature sensitivity assured by this approach was above $0.5\%^{\circ}\text{C}^{-1}$. The sensitivity was calculated also based on substantial changes of a single emission band intensity and maximum value of $7.5\%^{\circ}\text{C}^{-1}$ was found. These relationships confirm the suitability of using the PA phenomenon in the luminescence thermometry.

15.3. PA Simulations

In order to explore the SPA mechanism in Pr³⁺, Yb³⁺ co-doped system, I have performed modeling for these ions setup. Considering, that PA emission was not observed in singly Pr³⁺ doped nanocrystals, simulation for single Pr³⁺ ions was also conducted. At the beginning, the expected SPA mechanism was proposed and presented in the energy diagram (**Figure 37**). Compared with earlier proposed [70] in the present work a model exclude ¹D₂ level which enabled to significantly simplify the DRE equation set and speed up data simulations. As expected, 852 nm wavelength is resonant with ESA [¹G₄→³P₁] transition and simultaneously far from resonance with GSA of Pr³⁺ ions, what is the one of key conditions required for PA. The 852 nm is a bit mismatch with absorption from Yb³⁺ ions, however, based on experimental results, Yb³⁺ are unnecessary to obtain PA emission from Pr³⁺ ions in such conditions. Thus, even weak absorption from Yb³⁺ ions certainly exists. ESA and GSA from Pr³⁺ ions as well as absorption from Yb³⁺ ions are described by absorption cross sections occurring from appropriate levels and described as σ_{ESA} , σ_{GSA} and σ_{Yb} , respectively. For efficient ESA, PA requires population of the metastable level, here ¹G₄. To achieve it, three processes are probable. Firstly, cross relaxation (W_{CR1}) between Pr³⁺ ions [³P₁,³H₄]→[¹G₄, ¹G₄], secondly energy transfer from Yb³⁺ to Pr³⁺ ions [Yb³⁺:²F_{5/2}, Pr³⁺:³H₄]→[Yb³⁺:²F_{7/2}, Pr³⁺:¹G₄] assigned as w_{71} and finally w_{65} energy transfer upconversion from Pr³⁺ to Yb³⁺ ions [Yb³⁺:²F_{7/2}, Pr³⁺:³P₁]→[Yb³⁺:²F_{5/2}, Pr³⁺:¹G₄]. A processes going in the opposite direction than w_{71} and w_{65} were also considered and names as w_{64} and w_{74} , respectively. Additionally, the process W_{CR2} as reported during the first PA observation was included in the diagram. Taking into account the emission spectra of Pr³⁺ and Yb³⁺ co-doped nanocrystals (**Figure 31 b, c**), the emissions from ³P₁ level were excluded, in favor of emissions from ³P₀ level, which are much more intense. The emission from ³P₁ level were marked by gray color and excluded from the modeling to simplify the model (**Figure 37**). The rates used to describe emissions are lifetimes - τ . In the present model the emission from ³P₀ level is described with use of this level lifetime (τ_5). Appropriate branching ratios (b_{51} , b_{53} , b_{54}), depending on the ending levels, were used. Emissions from ¹G₄, ³H₆ and ³H₅ levels were considered as a consequence of W_{CR1} and W_{CR2} processes

The DRE were written as was explained in the Experimental section – chapter 13. All gray elements of the energy diagram were excluded from the DRE. Finally, the system of seven following DRE (Eq. 16 – Eq. 22) was resolved using Matlab.

$$\frac{dN_1}{dt} = -F * \sigma_{GSA} * N(1) - w71 * N(7) * N(1) + w64 * N(6) * N(4) - WCR1 * N(1) * N(5) - WCR2 * N(1) * N(3) + \frac{b51 * N(5)}{\tau_5} + \frac{b41 * N(4)}{\tau_4} + \frac{b31 * N(3)}{\tau_3} + \frac{N(2)}{\tau_2} * NR2 * N(2) \quad Eq. 16$$

$$\frac{dN_2}{dt} = 2 * WCR2 * N(1) * N(3) + \frac{b42 * N(4)}{\tau_4} + \frac{b32 * N(3)}{\tau_3} - \frac{N(2)}{\tau_2} + NR32 * N(3) - NR2 * N(2) \quad Eq. 17$$

$$\frac{dN_3}{dt} = -WCR2 * N(1) * N(3) + \frac{b53 * N(5)}{\tau_5} + \frac{b43 * N(4)}{\tau_4} - \frac{N(3)}{\tau_3} - NR32 * N(3) + NR4 * N(4) \quad Eq. 18$$

$$\frac{dN_4}{dt} = F * \sigma_{GSA} * N(1) - F * \sigma_{ESA} * N(4) + w71 * N(7) * N(1) - w64 * N(6) * N(4) + w65 * N(6) * N(5) - w74 * N(7) * N(4) + 2 * WCR1 * N(1) * N(5) - \frac{N(4)}{\tau_4} + \frac{b54 * N(5)}{\tau_5} + NR54 * N(5) - NR4 * N(4) \quad Eq. 19$$

$$\frac{dN_5}{dt} = w74 * N(7) * N(4) - w65 * N(6) * N(5) - WCR1 * N(1) * N(7) - \frac{N(5)}{\tau_5} + F * \sigma_{ESA} * N(4) - NR5 * N(5) \quad Eq. 20$$

$$\frac{dN_6}{dt} = -F * \sigma_{Yb} * N(6) + \frac{N(7)}{\tau_{Yb}} + w71 * N(7) * N(1) - w64 * N(6) * N(4) - w65 * N(6) * N(5) + w74 * N(7) * N(4) \quad Eq. 21$$

$$\frac{dN_7}{dt} = F * \sigma_{Yb} * N(6) - \frac{N(7)}{\tau_{Yb}} - w71 * N(7) * N(1) + w64 * N(6) * N(4) + w65 * N(6) * N(5) - w74 * N(7) * N(4) \quad Eq. 22$$

Initially, the prepared DRE were resolved using the original parameters, which are presented in the **Table 9** together with the units and sources.

Table 9. Parameters adopted for the DRE solution. Based on [189].

Parameter	Description	Basic value	Unit	Reference or justification
τ_2^*	Lifetime of level ³ H ₅ in Pr ³⁺ ions	125.6·10 ⁻³	s	[195]
τ_3^*	Lifetime of level ³ H ₆ in Pr ³⁺ ions	52.4·10 ⁻³	s	[195]
τ_4	Lifetime of level ¹ G ₄ in Pr ³⁺ ions	128·10 ⁻⁶	s	[196]
τ_5	Lifetime of level ³ P ₀ in Pr ³⁺ ions	30·10 ⁻⁶	s	[197]
τ_{Yb}	Lifetime of ² F _{5/2} of Yb ³⁺ ions	7.5·10 ⁻⁴	s	[70]
NR ₅₄ [*]	Rate of nonradiative transition ³ P ₀ → ¹ G ₄ in Pr ³⁺	3.84·10 ⁻⁸	$\frac{1}{s}$	[174]
NR ₄₃ [*]	Rate of nonradiative transition ¹ G ₄ → ³ H ₆ in Pr ³⁺	1.15	$\frac{1}{s}$	[174]

Synthesis, modeling and spectroscopic evaluation of selected Tm³⁺, Pr³⁺, Ho³⁺ doped
and Yb³⁺ co-doped colloidal photon avalanching nanoparticles

NR ₃₂ *	Rate of nonradiative transition ³ H ₆ → ³ H ₅ in Pr ³⁺	89132.2	$\frac{1}{s}$	[174]
NR ₂₁	Rate of nonradiative transition ³ H ₅ → ³ H ₄ in Pr ³⁺	130321.7	$\frac{1}{s}$	[174]
W ₇₁	Rate of ET [Yb ³⁺ : ² F _{5/2} , Pr ³⁺ : ³ H ₄]→[Yb ³⁺ : ² F _{7/2} , Pr ³⁺ : ¹ G ₄]	1.2·10 ⁻¹⁶	$\frac{cm^3}{s}$	[90]
W ₇₄	Rate of ETU [Yb ³⁺ : ² F _{5/2} , Pr ³⁺ : ¹ G ₄]→[Yb ³⁺ : ² F _{7/2} , Pr ³⁺ : ³ P ₁]	1.2·10 ⁻¹⁶	$\frac{cm^3}{s}$	W ₇₄ =W ₇₁
W ₆₄	Rate of ET [Yb ³⁺ : ² F _{7/2} , Pr ³⁺ : ¹ G ₄]→[Yb ³⁺ : ² F _{5/2} , Pr ³⁺ : ³ H ₄]	4·10 ⁻¹⁸	$\frac{cm^3}{s}$	W ₆₄ =W ₇₁ /30
W ₆₅	Rate of ETU [Yb ³⁺ : ² F _{7/2} , Pr ³⁺ : ³ P ₁]→[Yb ³⁺ : ² F _{5/2} , Pr ³⁺ : ¹ G ₄]	1.6·10 ⁻¹⁶	$\frac{cm^3}{s}$	[70]
W _{CR1} *	Rate of [³ P ₁ , ³ H ₄]→[¹ G ₄ , ¹ G ₄] CR process in Pr ³⁺	1.1·10 ⁻¹⁸	$\frac{cm^3}{s}$	[70]
W _{CR2} *	Rate of [³ H ₆ , ³ H ₄]→[³ H ₅ , ³ H ₅] CR process in Pr ³⁺	1.1·10 ⁻¹⁸	$\frac{cm^3}{s}$	W _{CR2} =W _{CR1}
σ _{ESA}	Absorption cross section of Pr ³⁺ ions from excited state	0.7·10 ⁻²⁰	cm ²	[90]
σ _{GSA} *	Absorption cross section of Pr ³⁺ ions from ground state	8·10 ⁻²⁷	cm ²	[70]
σ _{Yb}	Absorption cross section of Yb ³⁺ ions	8·10 ⁻²⁶	cm ²	[70]
b ₅₁	Branching ratio of emission from ³ P ₀	0.294	-	Estimated from emission spectra
b ₅₃	Branching ratio of emission from ³ P ₀	0.686	-	Estimated from emission spectra
b ₅₄	Branching ratio of emission from ³ P ₀	0.020	-	Estimated from emission spectra
b ₄₁	Branching ratio of emission from ¹ G ₄	0.061	-	Estimated based on: [198]
b ₄₂	Branching ratio of emission from ¹ G ₄	0.711	-	Estimated based on: [198]
b ₄₃	Branching ratio of emission from ¹ G ₄	0.228	-	Estimated based on: [198]
b ₃₁	Branching ratio of emission from ³ H ₆	0.566	-	[195]
b ₃₂	Branching ratio of emission from ³ H ₆	0.434	-	[195]

The rates of nonradiative transition were estimated on the basis of the probabilities of nonradiative transitions of Ln³⁺ in a tetragonal LiYF₄ laser crystal in a function of energy gap at T = 0 [174]. The probability of nonradiative transition from starting J level to end J' multiplets, is described as W_{JJ'}. The data were recalculated for RT according to the following equation appropriate for emission processes [93]:

$$W_{JJ'}(T) = W_{JJ'}(T = 0) \cdot (n + 1)^P \quad \text{Equation 23}$$

where

$$n = \left[\exp\left(\frac{\hbar\omega}{k_B \cdot T}\right) - 1 \right]^{-1} \quad \text{Equation 24}$$

k_B is a Boltzmann constant and equals 0.695 cm⁻¹ · K⁻¹. The ħω corresponds the phonon energy in particular matrix (here ħω = 350 cm⁻¹), P indicates the number of phonons required for overcome appropriate energy gap (ΔE_{JJ'}):

$$P = \frac{\Delta E_{JJ'}}{\hbar\omega} \quad \text{Equation 25}$$

As prepared phenomenological model allows to see, how particular parameters influence the PA features. Therefore, beside simulations performed for literature values of the rates, I have also performed calculations by sequentially changing (increasing and decreasing around the nominal literature values) each of individual parameters while the other were constant. The changes of particular variations of the values are presented in the **Table 10**.

Synthesis, modeling and spectroscopic evaluation of selected Tm³⁺, Pr³⁺, Ho³⁺ doped
and Yb³⁺ co-doped colloidal photon avalanching nanoparticles

Table 10. Changes in the values of DRE parameters to check their effect on PA characteristics. *Some parameters had no effect on PA. Based on [189].

Parameter	Lower values		Basic value	Higher values		Unit
τ_2^*	No changes for values of the same order and an order of magnitude smaller		$125.568 \cdot 10^{-3}$	No changes for values of the same order and an order of magnitude bigger		s
τ_3^*	No changes for values of the same order, one and two orders of magnitude smaller		$52.377 \cdot 10^{-3}$	No changes for values of the same order, one and two orders of magnitude higher		s
τ_4	$70 \cdot 10^{-6}$	$100 \cdot 10^{-6}$	$128 \cdot 10^{-6}$	$650 \cdot 10^{-6}$	$3220 \cdot 10^{-6}$	s
τ_5	$1 \cdot 10^{-6}$	$10 \cdot 10^{-6}$	$30 \cdot 10^{-6}$	$90 \cdot 10^{-6}$	$120 \cdot 10^{-6}$	s
τ_{Yb}	$7.5 \cdot 10^{-5}$	$3.5 \cdot 10^{-4}$	$7.5 \cdot 10^{-4}$	$9.5 \cdot 10^{-4}$	$7.5 \cdot 10^{-3}$	s
NR_{54}^*	No changes for values of the same order, one, two and three orders of magnitude smaller		$3.84 \cdot 10^{-8}$	No changes for values of the same order, one, two and three orders of magnitude bigger		$\frac{1}{s}$
NR_{43}^*	No changes for values of the same order, one and two orders of magnitude smaller		1.15	No changes for values of the same order, one and two orders of magnitude higher. For values of four orders of magnitude bigger, changes were observed, however that big increase of NR43 make no sense.		$\frac{1}{s}$
NR_{32}^*	Very minor change for smaller values.		89132.2	Lack of changes for bigger values.		$\frac{1}{s}$
NR_{21}	1303.217	13032.17	130321.7	Lack of changes for bigger values.		$\frac{1}{s}$
W_{71}	$1.2 \cdot 10^{-17}$	$0.2 \cdot 10^{-16}$	$1.2 \cdot 10^{-16}$	$2.3 \cdot 10^{-16}$	$1.0 \cdot 10^{-15}$	$\frac{cm^3}{s}$
W_{74}	$1.2 \cdot 10^{-17}$	$0.2 \cdot 10^{-16}$	$1.2 \cdot 10^{-16}$	$2.3 \cdot 10^{-16}$	$1.0 \cdot 10^{-15}$	$\frac{cm^3}{s}$

W_{64}	$2 \cdot 10^{-19}$	$1 \cdot 10^{-18}$	$4 \cdot 10^{-18}$	$8 \cdot 10^{-18}$	$2 \cdot 10^{-17}$	$\frac{cm^3}{s}$
W_{65}	$1.6 \cdot 10^{-17}$	$0.5 \cdot 10^{-16}$	$1.6 \cdot 10^{-16}$	$5 \cdot 10^{-16}$	$1.6 \cdot 10^{-15}$	$\frac{cm^3}{s}$
W_{CR1}^*	No changes for values of the same order, one and two orders of magnitude smaller		$1.1 \cdot 10^{-18}$	No changes for values of the same order, one and two orders of magnitude higher		$\frac{cm^3}{s}$
W_{CR2}^*	No changes for values of the same order, one and two orders of magnitude smaller		$1.1 \cdot 10^{-18}$	No changes for values of the same order, one and two orders of magnitude higher		$\frac{cm^3}{s}$
σ_{ESA}	$0.2 \cdot 10^{-20}$	$0.4 \cdot 10^{-20}$	$0.7 \cdot 10^{-20}$	$1.3 \cdot 10^{-20}$	$2.5 \cdot 10^{-20}$	cm^2
σ_{GSA}^*	No changes for values up to 3 orders of magnitude smaller		$8 \cdot 10^{-27}$	Very minor change for value two orders of magnitude higher.		cm^2
σ_{Yb}	$8 \cdot 10^{-27}$	$3 \cdot 10^{-26}$	$8 \cdot 10^{-26}$	$20 \cdot 10^{-26}$	$30 \cdot 10^{-26}$	cm^2

The results of described simulations, as a dependence of luminescence intensity in a function of pump power density, are presented in the **Figure 37** panels **b-k**. The panels from **b** to **k** correspond particular parameters, which were changed while all the other were constant. The black curves in all of these panels are the same and represent results obtained for initial parameters. The colored curves show, how the increase (saturated color) or decrease (paler shade) of particular parameters influence the PA performance. There are presented only these parameters, which significantly influence PA and they will be discussed subsequently. As mentioned earlier, the simulations were performed also for singly Pr³⁺ doped system. To do it, all processes responsible for interaction between Pr³⁺ and Yb³⁺ ions, namely W_{74} , W_{65} , W_{71} and W_{64} as well as the absorption of Yb³⁺ ions, σ_{Yb} , were reset. The rate of emissions of Yb³⁺ is described as $\frac{1}{\tau_{Yb}}$, thus, to make the rate close to zero, the τ_{Yb} value was adopted as very high. The results obtained for singly Pr³⁺ ions doped, comparing with co-doped system are presented in the **Figure 37 I**. While luminescence of co-doped system has a characteristic for PA s-shape (blue curve), for singly Pr³⁺ doping (pink line) no PA

features were observed. The results are compatible with experimental observations, thus, the key role of Yb³⁺ ions, which are necessary to observe the PA from Pr³⁺ ions in present experimental conditions was confirmed. Returning to the investigations of individual processes on PA features, it should be reminded, that there are presented only these parameters, which influenced PA features: S and PA_{TH}. What is surprising, the W_{CR1}, which suppose be the key mechanism leading to populate the intermediate ¹G₄ level do not influence PA features, because the other existing processes leading also to populate this level are more intense. Besides, the concentration of Pr³⁺ ions is low, therefore CR and W_{CR2}, processes are not enough efficient to observe PA. The W_{CR2} process was proposed during the first PA observation. However, the excitation conditions were different that in present experiment, i.e. here the level ³H₅ was not directly pumped as in the case of Chivian et al. work [28]. In a present experiment, the key role of populating ¹G₄ level, necessary for efficient ESA, plays the w₆₅ process [90]. The value of the w₆₅ process is higher than W_{CR1}, what confirms the hypothesis, that Yb³⁺ ions are responsible for PA – not only support the process, but are indispensable to observe the PA emission of Pr³⁺ ions in such experimental conditions. Increase of the w₆₅ parameter leads to more efficient ESA process, thus the slopes are steeper (**Figure 37 b** and **38 a**). Besides w₆₅ also the w₇₁ process leads to populate intermediate ¹G₄ level, therefore similarly, higher values of w₇₁ are reflected in a higher slopes (**Figure 37 c** and **38 c**). The w₇₄ process can be compared to ESA, thus higher intense of the process is also the reason of the S increase (**Figure 37 d** and **38 c**). The last w₆₄ process of energy transfer between Pr³⁺ and Yb³⁺ ions leads to depopulate the intermediate ¹G₄ level of Pr³⁺ ions, at the same time not populating higher energy levels of this ions. Therefore, increase of the w₆₄ parameter impedes PA existence, which is illustrated by higher PA_{TH} values simultaneously lowering the S (**Figure 37 e** and **38 d**). On the other hand, the w₆₄ leads to pump the Yb³⁺ ions, which are necessary for PA. However, the Yb³⁺ ions are very susceptible to surface quenching by overtones of water vibrations (3300 cm⁻¹), therefore the surface effects have also significant impact. On this account, the role of Yb³⁺ ions is twofold. On the one hand, the Yb³⁺ ions enables and support PA, but on the other hand facilitates quenching on the surface. A shorter Yb³⁺ ions lifetime, τ_{Yb}, hinders PA by increasing of PA_{TH} (**Figure 37 f** and **38 e**). It can be caused by surface quenching. Decreasing of the τ_{Yb} contributes to more

effective w_{64} and w_{65} processes and in a consequence the PA_{TH} increases (**Figure 37 f** and **38 e**). The other radiative lifetimes are τ_4 and τ_5 , which correspond lifetime of levels 1G_4 and 3P_0 , respectively. Longer τ_4 facilitated PA process (PA_{TH} is lower) because contributes to more effective ESA process, however the S decreases (**Figure 37 g** and **38 f**). The τ_5 changes not significantly influence PA features. Only significant reduction in the τ_5 value is a reason of decrease of S (**Figure 37 h** and **38 g**). The τ_2 and τ_3 lifetimes do not caused changes in s-shape character. These values determine the population of 3H_6 and 3H_5 energy levels, which take a part in W_{CR2} process. The processes will be crucial for scheme adopted by Chivian et al. [28], where the ESA occurred from the 3H_5 level. However, in a present work, with use of 852 nm excitation, are not considerable, what also means, that ET between Yb³⁺ and Pr³⁺ ions is more significant, than processes going between pairs of Pr³⁺ ions. Due to the lifetimes considered here are radiative, non-radiative transitions are also included in the model. In order to simplify the model, certain Pr³⁺ levels were not taken into account and the multi-phonon relaxation transitions between $^3P_0 \rightarrow ^1G_4$ (10 800 cm⁻¹) and $^1G_4 \rightarrow ^3H_6$ (5 600 cm⁻¹) were described using NR₅₄ and NR₄₃, respectively. Due to the large energy gaps of these transitions, the probabilities of the processes are not very high. However, it is worth to mention, that these transitions could be more efficient in experimental conditions than in a presented numerical considerations, because here the intermediate 1D_2 , $^3F_{3,4}$ and 3F_2 levels were excluded. However these energy levels originally exist and the energy gaps are lower, what should facilitate the non-radiative transitions. The calculations with increase and decrease of the NR₅₄ and NR₄₃ values were performed even up to three orders of magnitude smaller or larger than the original values. However, no clear differences in the s-shape were observed. Two remaining non-radiative processes, namely NR₃₂ and NR₂₁ are closely connected with the W_{CR2} process and not greatly influence the PA features. Only NR₂₁ process has an impact on S value, namely lower NR₂₁ values decrease slope (**Figure 38 h**). This indicates the essence of finding Pr³⁺ ions in the ground state, which leads to the initiation of the PA process. One of key conditions to observe PA emission is a large excited state absorption cross section and simultaneously a negligible ground state absorption cross section. The conditions are fulfilled by 852 nm excitation

wavelength, which is resonant with ESA and off-resonant with GSA of Pr^{3+} ions. These assumptions are reflected in simulations. The σ_{GSA} parameter do not influence PA emission features, while σ_{ESA} significantly changes the PA_{TH} value. For higher σ_{ESA} , the PA_{TH} moves for lower values, what facilitates PA, but in the opposite situation, lower σ_{ESA} increases PA_{TH} , what is compatible with predictions (**Figure 37 j**). Moreover, bigger σ_{ESA} is a reason to observe higher S values (**Figure 38 i**). The simulations confirm, that σ_{ESA} plays the key role in PA process and higher values of the parameter are beneficial for PA. Considering the σ_{Yb} parameter, the changes in s-shape character are minor. For lower values of σ_{Yb} the PA_{TH} moves to higher power densities, however the slopes are steeper (**Figure 37 k, 38 j**). Two processes leading to populate the $^1\text{G}_4$ intermediate level need the Yb^{3+} ions. In the case of w_{65} there are necessary Yb^{3+} ions in a ground state, while w_{71} requires Yb^{3+} ions in an excited state. Increase of values of these both processes lead to observe higher slopes, however the w_{65} process is more intense, thus Yb^{3+} ions in the ground state contribute more to increasing S than excited Yb^{3+} ions.

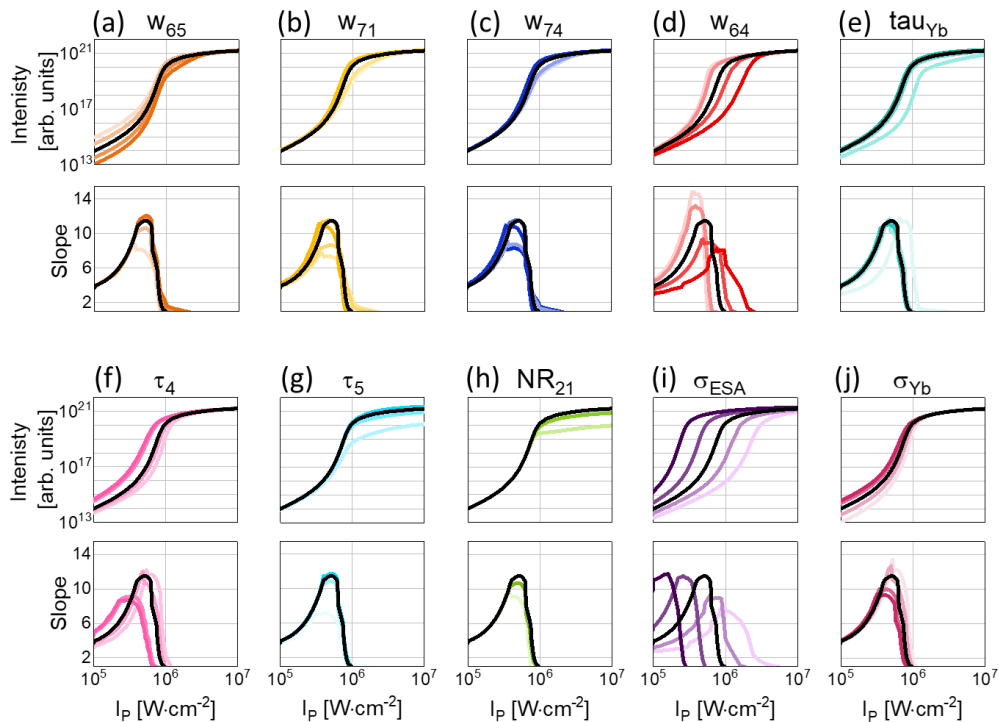


Figure 38. PA simulated results for system co-doped with Pr^{3+} , Yb^{3+} ions: each panel consists of two elements: pump power dependent luminescence intensity of PA emission and corresponding values of slopes of these s-shaped curves. Each of the panels illustrate how changes of particular parameters, namely nonradiative transitions: (a) w_{65} , (b) w_{71} , (c) w_{74} , (d) w_{64} (h) NR_{21} , radiative lifetimes: (e) τ_{Yb} (f) τ_4 , (g) τ_5 , and absorption cross sections: (i) σ_{ESA} , (j) σ_{Yb} affect PA properties. Saturated colors correspond to higher values of the parameters, while the black curves were obtained for pristine (literature) values. Based on [189].

15.4. Conclusions

In summary, all synthesized core and core-shell nanocrystals doped with Pr³⁺ ions (wide range concentration) as well as co-doped with Pr³⁺ (0.1, 0.3, 0.5 or 0.7%) and Yb³⁺ (15%) ions shown crystallographic pure β-NaYF₄ phase. The presence of an inert shell was evidenced indirectly by estimation of core and core-shell nanocrystals dimensions on the basis of TEM images as well as directly by mapping of the composition of representative nanocrystal. In order to check existence of PA emission, all materials were investigated under excitation with 852 nm, which is resonant with ESA and simultaneously far from the resonance with GSA of Pr³⁺ ions. Multicolor emission was successfully observed in Pr³⁺, Yb³⁺ co-doped core and core-shell nanocrystals, while singly Pr³⁺ doped nanoparticles showed no emission under the same excitation wavelength. It indicates the key role of Yb³⁺ ions, which are necessary to observe the PA emission from Pr³⁺ ions under chosen excitations conditions. The PA features were measured for the most intense beams, namely at 482 nm, ³P₀→³H₄, and 607 nm ³P₀→³H₆ transitions. PA emission features were successfully observed at both these emission for all β-NaYF₄ nanocrystals co-doped with Pr³⁺ and Yb³⁺ ions. The luminescence intensity of core-shell crystals was higher than for core only samples. Moreover, higher slopes and lower thresholds were obtained for core-shells compared with cores. Both these facts indicate the protective role of the inert shell, which has a beneficial influence for photoluminescence, in particular PA emission, because diminishes the impact of chemical environment on sensitizing-migrating Yb³⁺ and emitting Pr³⁺ ions. The biggest slopes, namely 8.6 and 9 as well as the smallest PA_{TH}, i.e. 286 kW/cm² and 281 kW/cm² were found for NaYF₄: 0.5% Pr³⁺, 15% Yb³⁺@NaYF₄ for emissions at 482 nm and 607 nm, respectively, thus this sample composition was confirmed as an optimal [70]. In the present work, both Stokes and PA emission measurement led to assign the emission at 607 nm as coming from ³P₀ level, while some sources report the emissions comes from the ¹D₂ energy level [70]. As a consequence, among others the exclusion of ¹D₂ energy level from analysis allowed to simplify the energy diagram used to prepare the phenomenological model of PA in Pr³⁺, Yb³⁺ ions setup. The phenomenological model enabled to predict the influence of particular energy transfer processes of PA behavior as well as was adapted to perform the simulations

for singly Pr^{3+} doped crystals. Results obtained for $\text{Pr}^{3+}, \text{Yb}^{3+}$ co-doped system led to observe characteristic s-shape curve of luminescence intensity in a function of pump power density, while a solution for singly Pr^{3+} doped setup showed no PA features. Therefore, the important role of Yb^{3+} ions in a discussed PA process was confirmed theoretically. The presented experimental and theoretical results allowed to understand the key role of Yb^{3+} ions during the PA process achieved in Pr^{3+} and Yb^{3+} co-doped system under 852 nm excitation.

16. Other PA investigations

The results presented in the Chapters 14 and 15 are composed of completed and published data. In the present chapter will be presented these results, which have not been published so far and require more measurements, however clear strides have been made in this research, so it is included in the present dissertation. The PA is quite capricious and unfortunately not all attempts to obtain PA have been successful. Nevertheless, I have synthesized a number of materials, i.e. doped with Tm^{3+} and co-doped with Tm^{3+} and Yb^{3+} ions, doped with Ho^{3+} and co-doped with Ho^{3+} and Yb^{3+} ions as well as co-doped with Er^{3+} and Yb^{3+} ions, which were structurally and morphologically characterized. Preliminarily examined the dependence of luminescence intensity as a function of excitation power. PA emission was observed for nanocrystals doped with Tm^{3+} and co-doped with Tm^{3+} and Yb^{3+} ions. For Ho^{3+} doped and Ho^{3+} , Yb^{3+} co-doped nanocrystals no signs of avalanche emission were observed - the reason may be the lack of knowledge of the actual ESA spectra, or it is necessary to have either a tunable laser, which we do not have. In addition, it took a long time to create a setup to measure PA properties, which delayed some measurements.

16.1. PA in Tm^{3+} doped as well as Tm^{3+} and Yb^{3+} co-doped NaYF_4 nanocrystals

Following in the footsteps of SPA observed in Pr^{3+} and Yb^{3+} it has become interesting, how the presence of Yb^{3+} ions influence PA emission of Tm^{3+} ions. The series of core and core-shell NaYF_4 nanocrystals doped with Tm^{3+} as well as co-doped with Tm^{3+} and Yb^{3+} ions was synthesized. All nanoparticles exhibited a pure hexagonal β - NaYF_4 crystallographic phase (**Figure 39**).

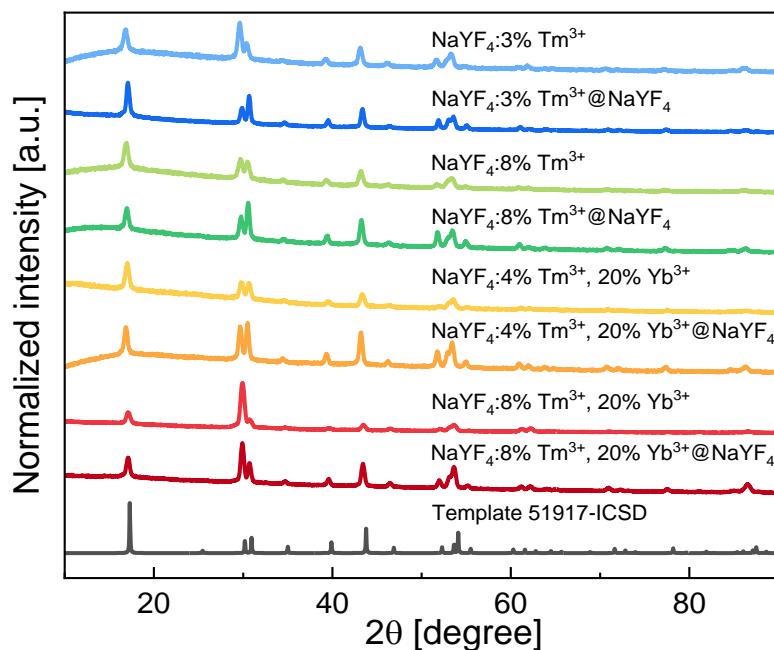


Figure 39. XRD of $\beta\text{-NaYF}_4$ crystallographic structure (Template) and $\beta\text{-NaYF}_4$ nanocrystals doped with Tm^{3+} as well as co-doped with Yb^{3+} and Tm^{3+} ions in both core and core-shell architecture.

The average sizes of the nanoparticles were estimated based on TEM images (Figure 40 a-h) and are presented in the histograms (Figure 40 i-i). The samples display narrow sizes distributions. The core nanoparticles have an average diameters from ~18 nm to ~21 nm. Core-shell width is in the range 18-22 nm and length 21-30 nm.

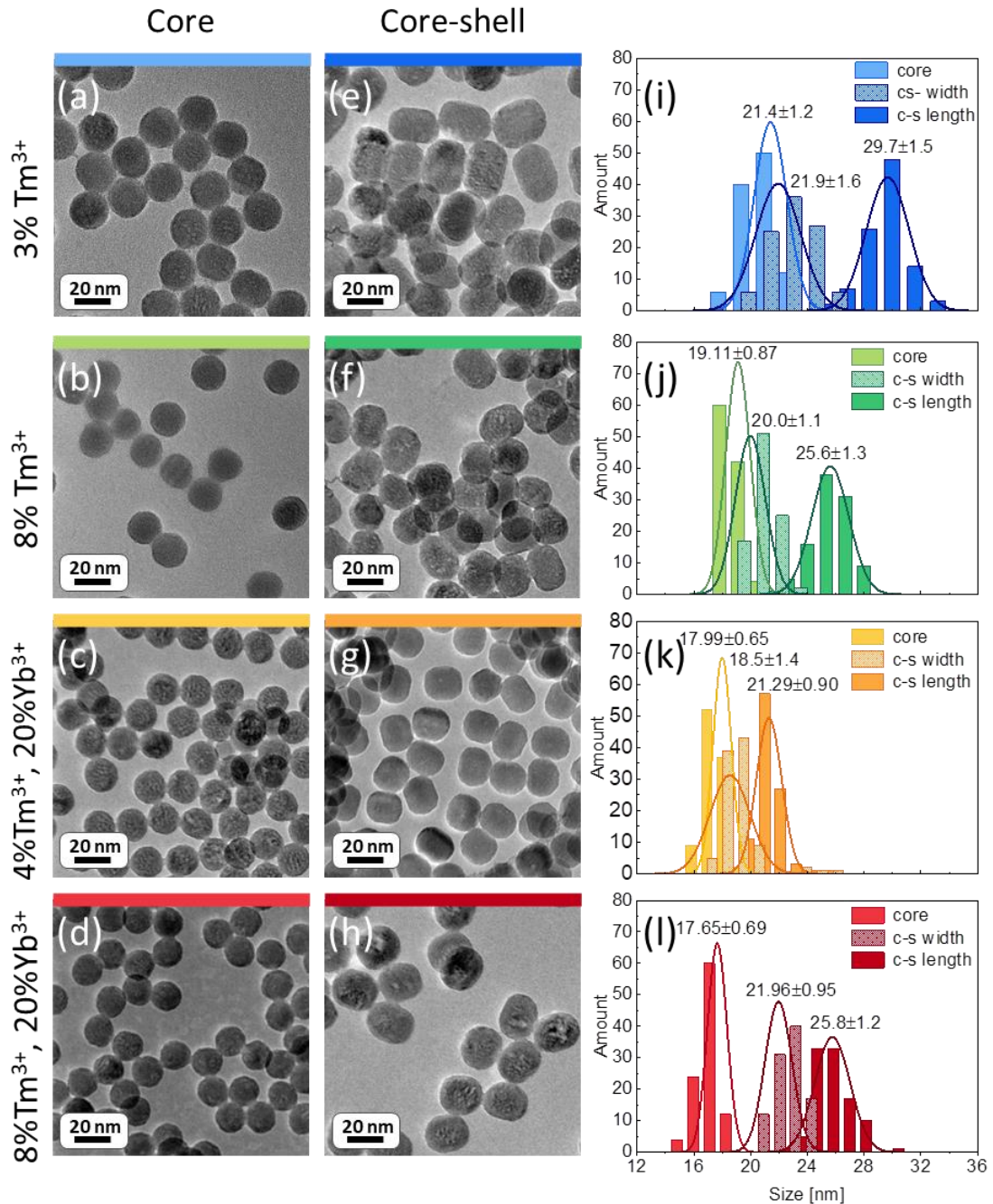


Figure 40. Morphology characteristics of core and core-shell NaYF₄ nanocrystals doped with 3% Tm³⁺, 8% Tm³⁺ and co-doped with 4% Tm³⁺, 20% Yb³⁺ ions as well as 8% Tm³⁺, 20% Yb³⁺: TEM images of core nanocrystals **a, b, c, d**; TEM images of core-shell nanoparticles **e, f, g, h**; histograms **i, j, k, l**, respectively.

During the initial investigations core-shell nanocrystals emission at 810 nm was monitoring under both 1059 nm and 976 nm excitation (**Figure 41**). The pump-power dependent luminescence measurements were conducted by Dr Eng. Marcin Szalkowski.

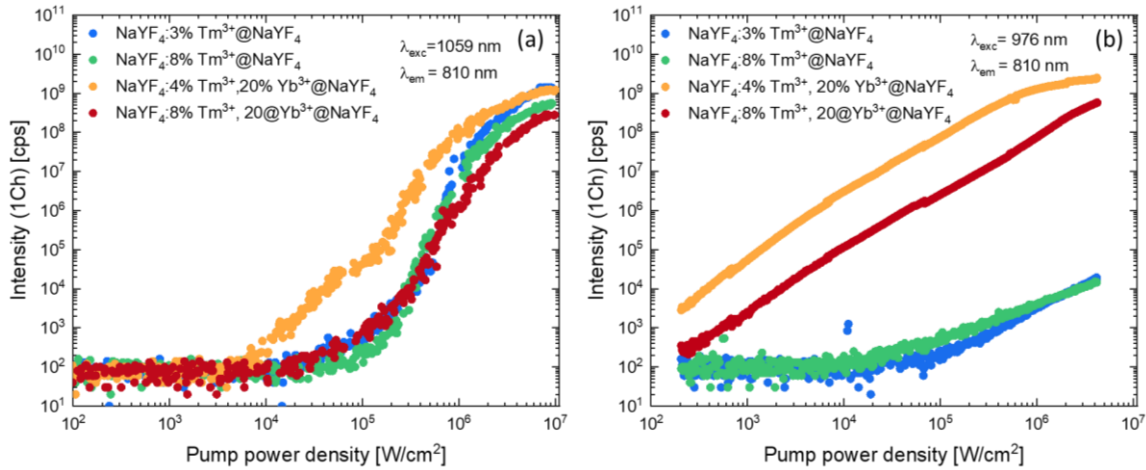


Figure 41. Intensity of photoluminescence at 810 nm of nanocrystal doped with Tm^{3+} as well as co-doped with Tm^{3+} and Yb^{3+} ions in a function of pump power density under: (a) 1059 nm and (b) 976 nm excitation source.

The PA emission features were clearly observed under an excitation with 1059 nm, while under excitation with 976 nm were absent. Considering results obtained under excitation with 1059 nm, the PA_{TH} of core-shell nanocrystals co-doped with 4% Tm^{3+} and 20% Yb^{3+} ions is clearly lower than in the remaining cases. In the case of excitation with 976 nm, the nanocrystals with sensitization of Yb^{3+} ions, which efficiently absorb this excitation wavelength, shown higher luminescence intensity than singly Tm^{3+} doped nanocrystals. It seems clear, due to weak absorption of 976 nm by Tm^{3+} ions. Comparing the co-doped nanocrystals with different, concentration of Tm^{3+} ions (4% and 8%), higher luminescence intensity was observed for lower – 4% Tm^{3+} ions concentration. It is connected with the concentration quenching effect, which is more probable in 8% Tm^{3+} co-doped nanoparticles. Further studies of these presented samples will be considered in the future.

16.2. Ho^{3+} doped as well as Ho^{3+} and Yb^{3+} co-doped NaYF_4 nanocrystals

There are some reports of PA in Ho^{3+} doped materials. Therefore, I have synthesized a series of $\beta\text{-NaYF}_4$ core and core-shell nanocrystals doped with Ho^{3+} (0.5% and 2%) ions as well as co-doped with Yb^{3+} (constant 20% amount) and Ho^{3+} (0.5%, 1%, 2%, 4% or 8%) ions. All these samples were synthesized by me and shown pure $\beta\text{-NaYF}_4$ crystal phase (**Figure 42**).

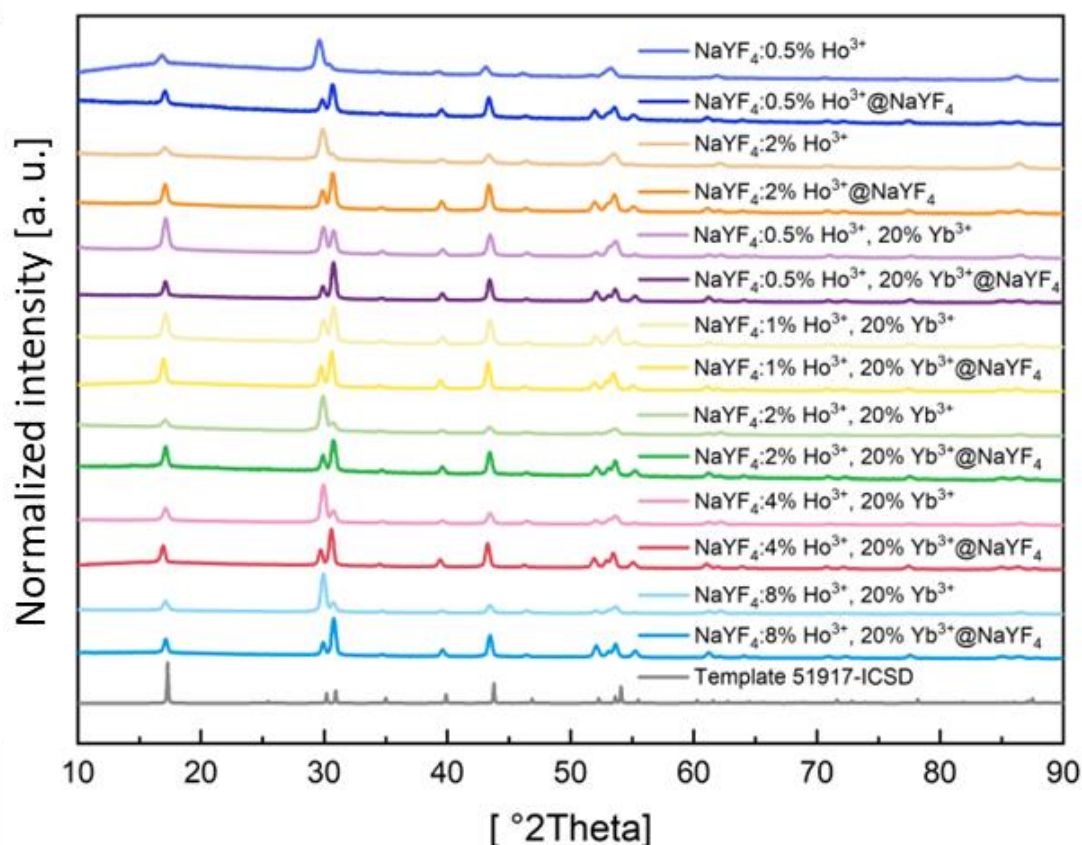


Figure 42. XRD of $\beta\text{-NaYF}_4$ core and core-shell nanocrystals singly doped with Ho^{3+} ions (0.5% and 2%) as well as co-doped with Yb^{3+} ions (constant amount of 20%) and Ho^{3+} ions (0.5%, 1%, 2%, 4% or 8%) together with template for $\beta\text{-NaYF}_4$ crystal phase.

The average sizes of these nanocrystals were estimated based on TEM images of appropriate core (**Figure 43 a, d, g, j, m, p, s**) and core-shell (**Figure 43 b, e, h, k, n, q, t**) samples and are presented in the histograms (**Figure 43 c, f, i, l, o, r, u**). The nanocrystals shown wide range of distributions. The diameters of core nanocrystals are in the range of 16.5-21 nm while core-shells from 21 nm to 29.5 nm.

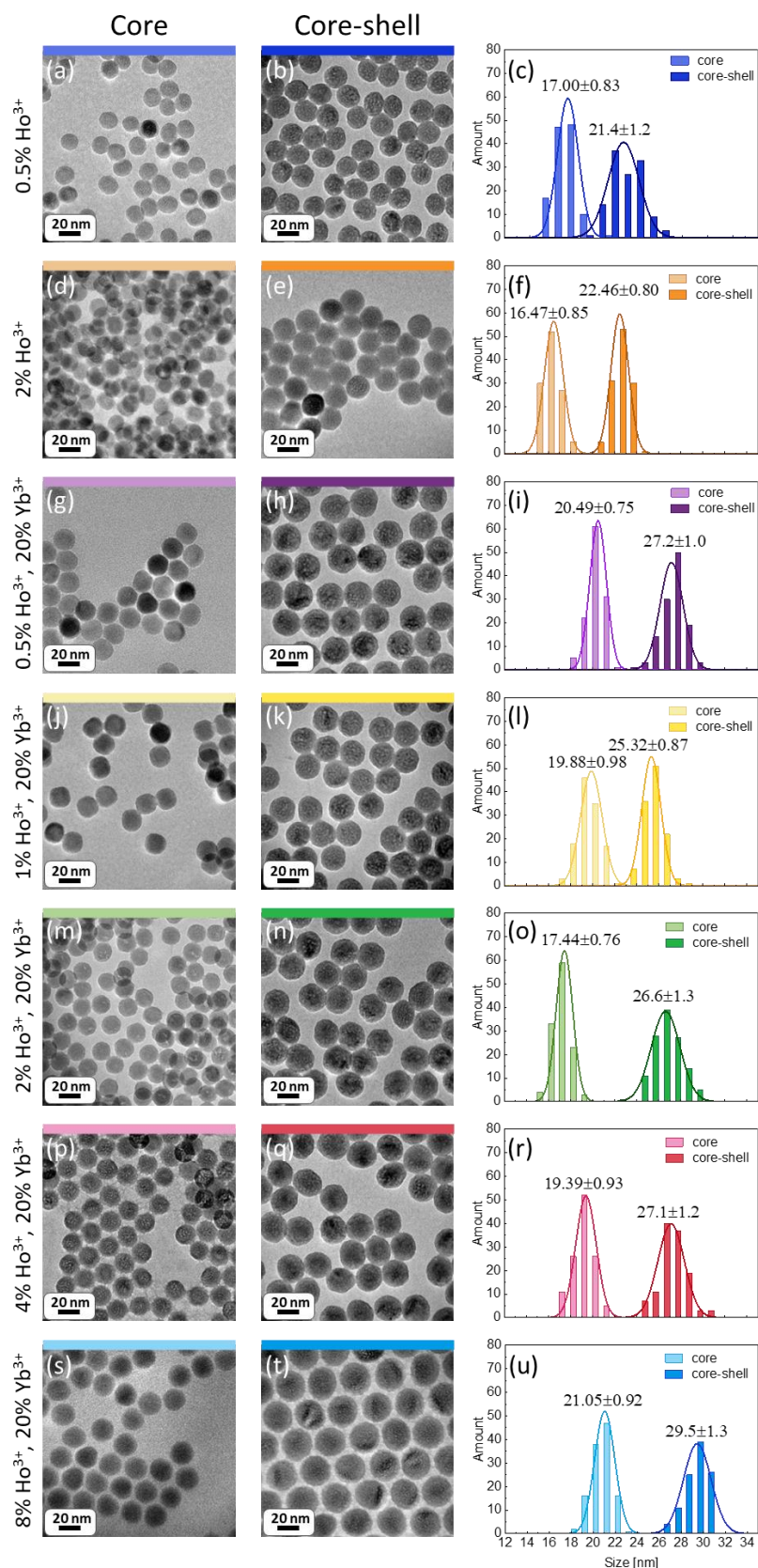


Figure 43. Morphology characteristics of Ho^{3+} doped as well as Ho^{3+} and Yb^{3+} co-doped core and core-shell NaYF_4 nanocrystals. Particular rows of the figure are composed of TEM images as well as histogram for crystals doped with: (a, b, c): 0.5% Ho^{3+} ; (d, e, f): 2% Ho^{3+} ; (g, h, i): 0.5% Ho^{3+} , 20% Yb^{3+} ; (j, k, l): 1% Ho^{3+} , 20% Yb^{3+} ; (m, n, o): 2% Ho^{3+} , 20% Yb^{3+} (p, q, r): 4% Ho^{3+} , 20% Yb^{3+} ; (s, t, u): 8% Ho^{3+} , 20% Yb^{3+} ions.

Absorption spectra for all synthesized nanocrystals were measured and are presented in the **Figure 44**.

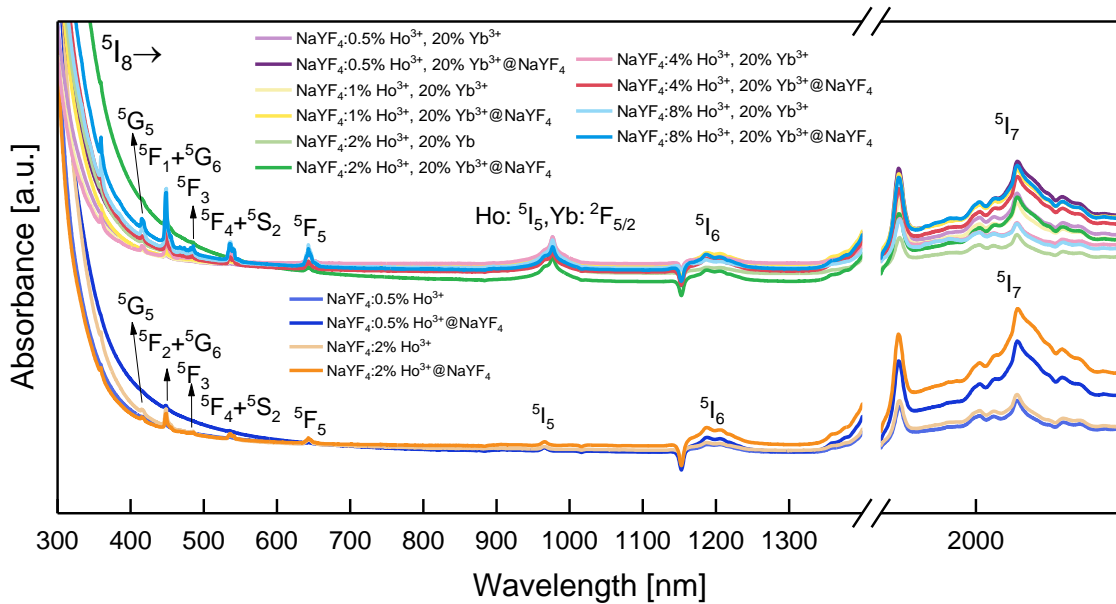


Figure 44. Absorption spectra of core and core-shell nanocrystals singly doped with Ho^{3+} ions (0.5% and 2%) as well as co-doped with Yb^{3+} ions (constant amount of 20%) and Ho^{3+} ions (0.5%, 1%, 2%, 4% or 8%).

In order to check the PA emission existence, the synthesized nanocrystals were investigated under particular excitations at 808 nm, 852 nm, 975 nm and 1059 nm. In the case of 808 nm and 852 nm excitation no emission was observed, while nanocrystals excited with 975 nm and 1059 nm showed emission in the range from 500 nm to 800 nm (**Figure 45**). More intense photoluminescence was observed under excitation at 975 nm, which matches Yb^{3+} excited state. Thus, Yb^{3+} ions also in this case, promote upconversions process.

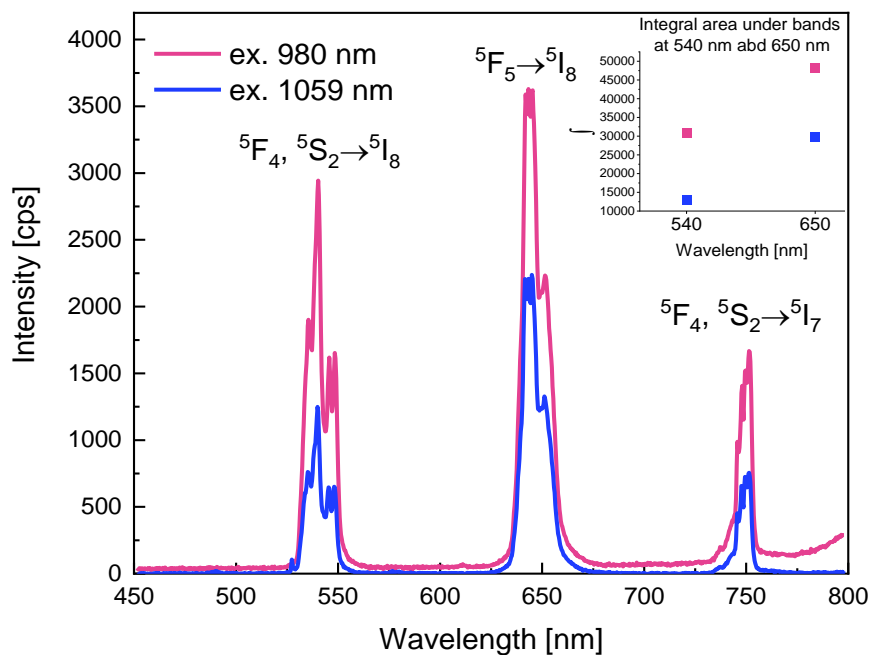


Figure 45. Emission spectra of NaYF_4 : 1% Ho^{3+} , 20% Yb^{3+} @ NaYF_4 nanocrystals under excitations at 975 and 1059 nm. Inset contains integral area under the bands 540 nm and 650 nm for both 975 nm (pink points) and 1059 nm (blue points) excitations.

For two the most intense peaks, namely at 540 nm and 650 nm, the photoluminescence intensity was measured in a function of the pump power density of excitation sources: 975 nm and 1059 nm (**Figure 46**). The measurements under 1059 nm were performed for all core-shell nanocrystals. In the case of 975 nm excitation, there were investigated only samples containing Yb^{3+} ions, because the wave is resonant with absorption of these ions. Unfortunately, no PA emission was observed. The slopes were relatively low, around 3. Thus, as in a more of literature sources, pure features of PA ions were no observed. However, further studies are planned, which will require to get knowledge about more appropriate photoexcitation wavelength matching ESA but simultaneously staying out of resonance with GSA in Ho^{3+} or Yb^{3+} ions.

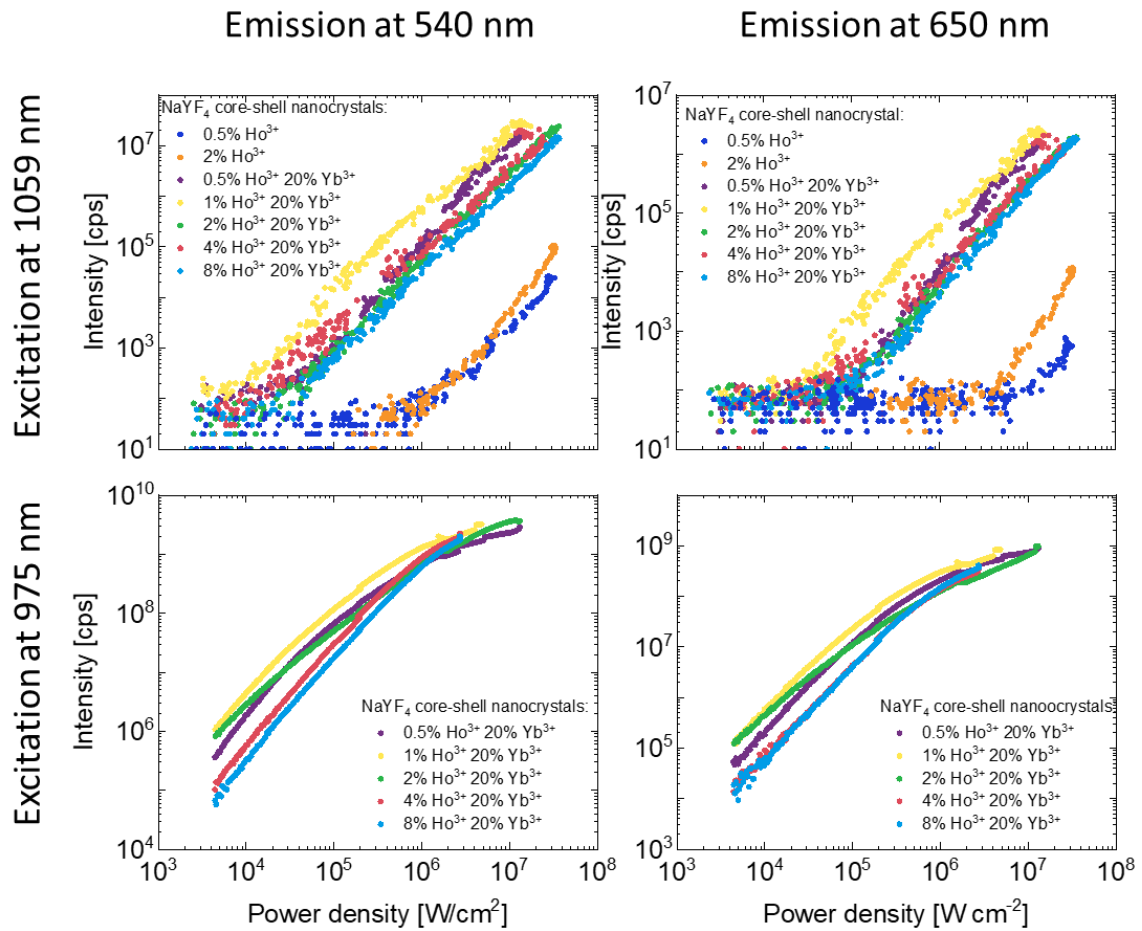


Figure 46. The luminescence intensities of emissions monitored at 540 nm (first column) and 650 nm (second column) in a function of pump power densities of excitation sources, namely 1059 nm (first row) and 975 nm (second row) for core-shell nanocrystals doped with Ho³⁺ as well as co-doped with Ho³⁺ and Yb³⁺ ions.

16.3. Er^{3+} and Yb^{3+} co-doped NaYF_4 nanocrystals

The Yb^{3+} , Er^{3+} ions system is known to be one of the most efficient for upconversion of energy. PA emission has been reported in materials doped with Er^{3+} ions and co-doped with Yb^{3+} and Er^{3+} ions under excitation around 980 nm [199]–[201]. The excitation wavelengths around 560 nm and 690 nm are non-resonant with absorption from the ground state and at the simultaneously resonant with absorption from the excited state of Er^{3+} ions. The wavelength of 579 nm corresponds to the $^4\text{I}_{11/2} \rightarrow ^4\text{G}_{9/2}$ transition, and 690 nm is resonant with $^4\text{I}_{11/2} \rightarrow ^2\text{G}_{9/2}$ [202] ($^2\text{G}_{9/2}$ is sometimes called as $^2\text{G}(1)_{9/2}$ [174]) and furthermore with $^4\text{I}_{13/2} \rightarrow ^4\text{F}_{7/2}$ and $^4\text{I}_{9/2} \rightarrow ^4\text{G}_{11/2}$. Because of this, an experiment was planned to test the presence of avalanche emission in nanocrystals co-doped with Er^{3+} and Yb^{3+} ions and to check the effect of Er^{3+} ion concentration on possible PA emission. The following samples were synthesized:

NaYF_4 : 2% Er^{3+} , 20% Yb^{3+} @ NaYF_4

NaYF_4 : 20% Er^{3+} , 20% Yb^{3+} @ NaYF_4 .

The pure β - NaYF_4 crystallographic structure was evidenced by XRD measurements (Figure 47).

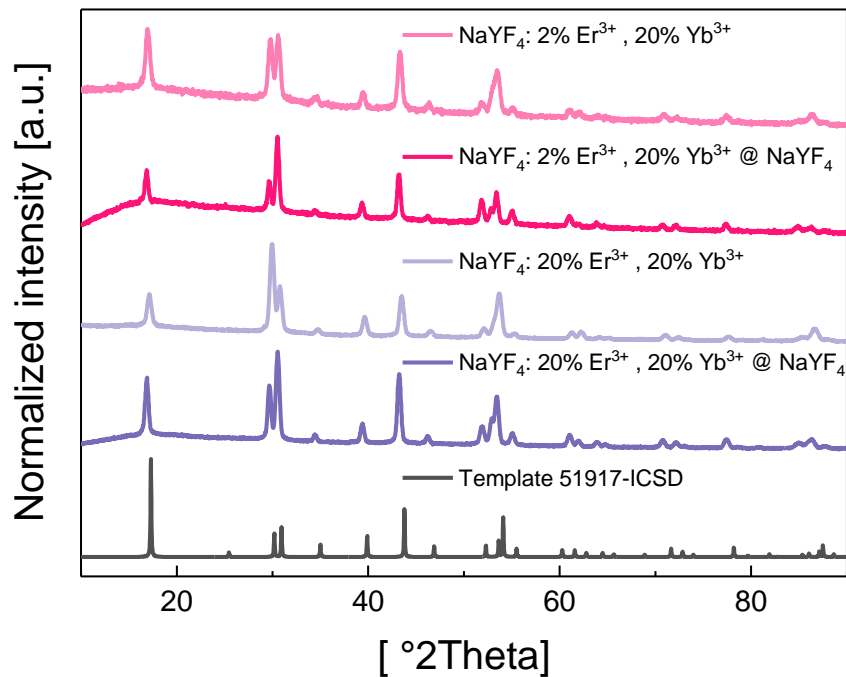


Figure 47. X-ray powder diffractions of nanocrystals co-doped with Er^{3+} and Yb^{3+} ions as well as the template for β - NaYF_4 crystal phase.

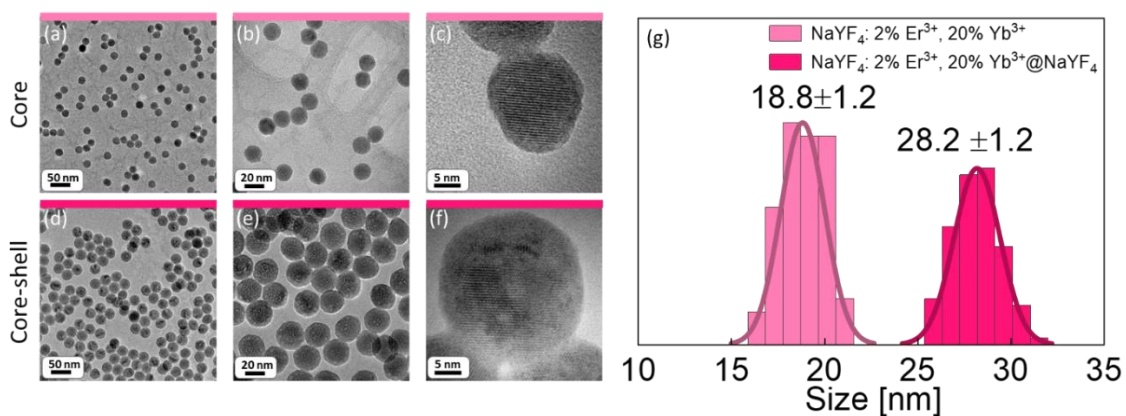


Figure 48. Characteristics of core and core-shell nanocrystals co-doped with 2% Er^{3+} and 20% Yb^{3+} ions. TEM images of: **a, b, c:** core and **d, e, f:** core-shell nanocrystals as well as **g** histogram with average sizes.

The TEM images and histograms with average sizes were prepared for core and core-shell nanocrystals co-doped with 2% Er^{3+} , 20% Yb^{3+} ions and are presented in the **Figure 48**. The average dimension of core is around 19 nm and core-shell near 28 nm, thus the shell thickness is around 5 nm. The spectroscopic studies of these samples are to be planned.

17. Conclusions

In summary, the goals of present dissertations were achieved.

- The setup to synthesize fluoride colloidal NaYF₄ and LiYF₄ nanocrystals was designed and built.
- The thermal decomposition of lanthanide salts synthesis method was optimized to prepare nanocrystals in a core and core-shell architecture.
- All the synthesized nanocrystals were crystallographically pure and showed narrow size distributions, confirming the reproducibility of the syntheses.
- For selected nanocrystals, namely doped with Pr³⁺, Ho³⁺ as well as co-doped with Pr³⁺ or Ho³⁺ and Yb³⁺ ions absorption spectra were measured and analyzed.
- Moreover, for nanocrystals doped with Pr³⁺ ions as well as co-doped with Pr³⁺ and Yb³⁺ ions emission and excitation spectra in a Stokes mode were measured and interpreted.
- The crystals doped with Tm³⁺, Pr³⁺, Ho³⁺ as well as co-doped with Yb³⁺ ions were investigated for the existence of PA.

The achievement of PA at nanoscale offers the possibility of new applications of these PA materials, however for their implementation it is important to understand the mechanism of the process as well as its characteristics depending on various factors, such as the size of the avalanching materials or the dopant concentration.

- PA emission at 800 nm (³H₄→³H₆) was successfully observed in Tm³⁺ NaYF₄ crystals under excitation with single mode laser diode generating wavelength at 1064 nm, which matches the ESA (³F₄→³F₂) of Tm³⁺ ions.
- For the first time, the relationships between PA features and materials sizes were investigated. LiYF₄:8%Tm³⁺ and LiYF₄:3%Tm³⁺ were synthesized as core and core-shell nanocrystals as well as microcrystals, moreover bulk NaYF₄: 3%Tm³⁺ crystal was investigated and compared to nano- and micro-sized materials. PA_{TH} values shifted to higher values with decrease of crystal size. Dependence of the S values on material size was not monotonic however, generally, higher values were observed for smaller materials and were in the range from 6 to around 12.

- The theoretical absorption spectra were calculated for different matrices doped with Tm³⁺ ions aiming to predict ESA spectra.
- Additionally, PASSI sub-diffraction imaging of LiYF₄:3% Tm³⁺@ LiYF₄ nanocrystals doped with 3% of Tm³⁺ ions was performed and spatial resolution of 125 nm was achieved.
- Moreover, theoretical DRE model was prepared to understand the role of energy processes occurring in Tm³⁺ ions during PA process. It was presented, how radiative and non-radiative rates as well as cross-relaxations and ESA affect the PA phenomenon.
- The PA emission was also successfully observed in Pr³⁺ (0.1%, 0.3%, 0.5% or 0.7%) and Yb³⁺ (15%) co-doped core and core-shell NaYF₄ nanocrystals. The materials were investigated under single mode diode excitation of 852 nm, which is resonant with ESA of Pr³⁺ ions (¹G₄→³P₁).
- The same experiment was performed for singly Pr³⁺ doped nanoparticles, however only in the case of double Pr³⁺ and Yb³⁺ doping, the PA emission was successfully observed at 482 nm (³P₀→³H₄) and 607 nm (³P₀→³H₆).
- The PA emission of Pr³⁺ ions at 607 nm, compared to some sources reporting it as coming from ¹D₂ energy level, was correctly associated with ³P₀→³H₆ transition.
- The PA features were investigated in a function of nanocrystals architecture, namely for core and core-shell materials. The nanoparticles with inert shell, responsible for protecting optically active ions from the environment influence, showed higher S values and lower PA_{TH} comparing with cores.
- Moreover, the influence of Pr³⁺ ions concentration on PA features was investigated. The highest S parameters. i.e. 8.6 and 9.0 as well as the lowest PA_{TH}, namely 286 kW/cm² and 281 kW/cm² were observed for core-shell nanocrystals co-doped with 0.5% of Pr³⁺ ions and 15% of Yb³⁺ for emission at 607 nm and 482 nm, respectively.
- Beside the experimental investigations, simulations of PA process in Pr³⁺, Yb³⁺ co-doped system were performed. The phenomenological model enabled to investigate the influence of particular radiative and non-radiative transitions

on PA features. Learning about the mechanism of PA process will enable predicting the properties of PA materials and will facilitate their intentional design before they are synthesized.

- The key role of Yb^{3+} ions which are necessary to observe the PA from Pr^{3+} ions under 852 nm photoexcitation was confirmed with use the theoretical investigations.
- The investigation of PA emission existence were performed also for nanocrystals doped with Ho^{3+} as well as co-doped with Ho^{3+} and Yb^{3+} ions. The nanocrystal were synthesized in a core and core-shell architecture and were investigated upon different excitation beams, namely 808 nm, 852 nm, where no emission was observed as well as under 975 nm and 1059 nm and in these cases the emission was monitored at 540 nm and 650 nm, however no PA features were observed. Further experiments are planned with additional laser lines.
- Moreover, the core and core-shell nanocrystals co-doped with Er^{3+} and Yb^{3+} were synthesized and in terms of morphology characterized, however spectroscopic investigations were not conducted yet because of missing appropriate photoexcitation laser.

18. References

- [1] S. Kumar Sharma Editor Dalip Singh Verma Latif Ullah Khan Shalendra Kumar Sher Bahadar Khan Associate Editors, 'Handbook of Materials Characterization'.
- [2] S. F. Himmelstoß and T. Hirsch, 'A critical comparison of lanthanide based upconversion nanoparticles to fluorescent proteins, semiconductor quantum dots, and carbon dots for use in optical sensing and imaging', *Methods Appl Fluoresc*, vol. 7, no. 2, Mar. 2019, doi: 10.1088/2050-6120/ab0bfa.
- [3] V. Biju, T. Itoh, and M. Ishikawa, 'Delivering quantum dots to cells: Bioconjugated quantum dots for targeted and nonspecific extracellular and intracellular imaging', *Chem Soc Rev*, vol. 39, no. 8, pp. 3031–3056, Jul. 2010, doi: 10.1039/b926512k.
- [4] S. J. Soenen *et al.*, 'The effect of intracellular degradation on cytotoxicity and cell labeling efficacy of inorganic ligand-stabilized colloidal CdSe/CdS quantum dots', *J Biomed Nanotechnol*, vol. 11, no. 4, pp. 631–643, Apr. 2015, doi: 10.1166/JBN.2015.1853.
- [5] D. Lisjak, O. Plohl, M. Ponikvar-Svet, and B. Majaron, 'Dissolution of upconverting fluoride nanoparticles in aqueous suspensions', *RSC Adv*, vol. 5, no. 35, pp. 27393–27397, 2015, doi: 10.1039/c5ra00902b.
- [6] R. Li *et al.*, 'Enhancing the imaging and biosafety of upconversion nanoparticles through phosphonate coating', *ACS Nano*, vol. 9, no. 3, pp. 3293–3306, Mar. 2015, doi: 10.1021/acsnano.5b00439.
- [7] O. Plohl *et al.*, 'Optically detected degradation of NaYF₄:Yb,Tm-based upconversion nanoparticles in phosphate buffered saline solution', *Langmuir*, vol. 33, no. 2, pp. 553–560, Jan. 2017, doi: 10.1021/acs.langmuir.6b03907.
- [8] S. Lahtinen *et al.*, 'Disintegration of hexagonal NaYF₄:Yb³⁺,Er³⁺ upconverting nanoparticles in aqueous media: The role of fluoride in solubility equilibrium', *Journal of Physical Chemistry C*, vol. 121, no. 1, pp. 656–665, Jan. 2017, doi: 10.1021/acs.jpcc.6b09301.
- [9] O. Dukhno, F. Przybilla, V. Muhr, M. Buchner, T. Hirsch, and Y. Mély, 'Time-dependent luminescence loss for individual upconversion nanoparticles upon dilution in aqueous solution', *Nanoscale*, vol. 10, no. 34, pp. 15904–15910, Sep. 2018, doi: 10.1039/c8nr03892a.
- [10] S. Shiri, N. Pajouheshpoor, H. Khoshshafar, S. Amidi, and H. Bagheri, 'An electrochemical sensor for the simultaneous determination of rifampicin and isoniazid using a C-dots@CuFe₂O₄ nanocomposite modified carbon paste electrode', *New Journal of Chemistry*, vol. 41, no. 24, pp. 15564–15573, 2017, doi: 10.1039/c7nj03029k.
- [11] X. Tian, H. Peng, Y. Li, C. Yang, Z. Zhou, and Y. Wang, 'Highly sensitive and selective paper sensor based on carbon quantum dots for visual detection of TNT residues in groundwater', *Sens Actuators B Chem*, vol. 243, pp. 1002–1009, 2017, doi: 10.1016/j.snb.2016.12.079.
- [12] Uniwersytet Śląski, 'Principles of Chemistry, Lanthanides'.
- [13] 'INORGANIC CHEMISTRY Saito'. [Online]. Available: <https://LibreTexts.org>

- [14] S. K. Sharma, *Complex magnetic nanostructures: Synthesis, assembly and applications*. Springer International Publishing, 2017. doi: 10.1007/978-3-319-52087-2.
- [15] X. Qin, X. Liu, W. Huang, M. Bettinelli, and X. Liu, 'Lanthanide-Activated Phosphors Based on 4f-5d Optical Transitions: Theoretical and Experimental Aspects', *Chem Rev*, vol. 117, no. 5, pp. 4488–4527, Mar. 2017, doi: 10.1021/acs.chemrev.6b00691.
- [16] M. Sato, S. W. Kim, Y. Shimomura, T. Hasegawa, K. Toda, and G. Adachi, 'Rare Earth-Doped Phosphors for White Light-Emitting Diodes', in *Handbook on the Physics and Chemistry of Rare Earths*, vol. 49, Elsevier B.V., 2016, pp. 1–128. doi: 10.1016/bs.hpcre.2016.03.001.
- [17] G. Blasse *et al.*, 'Springer-Verlag'.
- [18] A. Nadort, J. Zhao, and E. M. Goldys, 'Lanthanide upconversion luminescence at the nanoscale: Fundamentals and optical properties', *Nanoscale*, vol. 8, no. 27. Royal Society of Chemistry, pp. 13099–13130, Jul. 21, 2016. doi: 10.1039/c5nr08477f.
- [19] J. F. Suyver, J. Grimm, M. K. Van Veen, D. Biner, K. W. Krämer, and H. U. Güdel, 'Upconversion spectroscopy and properties of NaYF₄ doped with Er³⁺, Tm³⁺ and/or Yb³⁺', *J Lumin*, vol. 117, no. 1, pp. 1–12, Mar. 2006, doi: 10.1016/j.jlumin.2005.03.011.
- [20] S. Heer, K. Kömpe, H. U. Güdel, and M. Haase, 'Highly efficient multicolour upconversion emission in transparent colloids of lanthanide-doped NaYF₄ nanocrystals', *Advanced Materials*, vol. 16, no. 23–24, pp. 2102–2105, Dec. 2004, doi: 10.1002/adma.200400772.
- [21] K. W. Krämer, D. Biner, G. Frei, H. U. Güdel, M. P. Hehlen, and S. R. Lüthi, 'Hexagonal Sodium Yttrium Fluoride Based Green and Blue Emitting Upconversion Phosphors', *Chemistry of Materials*, vol. 16, no. 7, pp. 1244–1251, Apr. 2004, doi: 10.1021/cm031124o.
- [22] F. Wang and X. Liu, 'Recent advances in the chemistry of lanthanide-doped upconversion nanocrystals', *Chem Soc Rev*, vol. 38, no. 4, pp. 976–989, Mar. 2009, doi: 10.1039/b809132n.
- [23] A. Yin, Y. Zhang, L. Sun, and C. Yan, 'Colloidal synthesis and blue based multicolor upconversion emissions of size and composition controlled monodisperse hexagonal NaYF₄:Yb,Tm nanocrystals', *Nanoscale*, vol. 2, no. 6, pp. 953–959, 2010, doi: 10.1039/b9nr00397e.
- [24] C. Lee *et al.*, 'Giant nonlinear optical responses from photon-avalanching nanoparticles', *Nature*, vol. 589, no. 7841, pp. 230–235, Jan. 2021, doi: 10.1038/s41586-020-03092-9.
- [25] Z. Korczak *et al.*, 'Sensitized photon avalanche nanothermometry in Pr³⁺ and Yb³⁺ co-doped NaYF₄ colloidal nanoparticles', *Low Temperature Physics*, vol. 49, no. 3, pp. 322–329, Mar. 2023, doi: 10.1063/10.0017243.
- [26] N. Bloembergen, 'Solid state infrared quantum counters', *Phys Rev Lett*, vol. 2, no. 3, pp. 84–85, 1959.
- [27] M. F. Joubert, 'Photon avalanche upconversion in rare earth laser materials', *Opt Mater (Amst)*, vol. 11, no. 2–3, pp. 181–203, Jan. 1999, doi: 10.1016/S0925-3467(98)00043-3.

-
- [28] J. S. Chivian, W. E. Case, and D. D. Eden, 'The photon avalanche: A new phenomenon in Pr³⁺-based infrared quantum counters', *Appl Phys Lett*, vol. 35, no. 2, pp. 124–125, Aug. 1979, doi: 10.1063/1.91044.
- [29] N. J. Krasutsky, '10- μ m samarium based quantum counter', *J Appl Phys*, vol. 54, no. 3, pp. 1261–1267, Mar. 1983, doi: 10.1063/1.332189.
- [30] N. Pelletier-Allard and R. Pelletier, 'An internal quantum counter for lifetime measurements', *Opt Commun*, vol. 81, no. 3–4, pp. 247–250, 1991, doi: 10.1016/0030-4018(91)90647-V.
- [31] W. Lenth and R. M. Macfarlane, 'Excitation mechanisms for upconversion lasers', *J Lumin*, vol. 45, no. 1–6, pp. 346–350, Jan. 1990, doi: 10.1016/0022-2313(90)90190-M.
- [32] M. E. Koch, A. W. Kueny, and W. E. Case, 'Photon avalanche upconversion laser at 644 nm', *Appl Phys Lett*, vol. 56, no. 12, pp. 1083–1085, Mar. 1990, doi: 10.1063/1.103328.
- [33] A. W. Kueny, W. E. Case, and M. E. Koch, 'Nonlinear-optical absorption through photon avalanche', *Journal of the Optical Society of America B*, vol. 6, no. 4, p. 639, Apr. 1989, doi: 10.1364/josab.6.000639.
- [34] T. Hebert, R. Wannemacher, R. M. MacFarlane, and W. Lenth, 'Blue continuously pumped upconversion lasing in Tm:YLiF₄', *Appl Phys Lett*, vol. 60, no. 21, pp. 2592–2594, May 1992, doi: 10.1063/1.106919.
- [35] H. Ni and S. C. Rand, 'Avalanche upconversion in Tm:YALO₃', *Opt Lett*, vol. 16, no. 18, p. 1424, Sep. 1991, doi: 10.1364/ol.16.001424.
- [36] A. W. Kueny, W. E. Case, and M. E. Koch, 'Infrared-to-ultraviolet photon-avalanche-pumped upconversion in Tm:LiYF₄', *Journal of the Optical Society of America B*, vol. 10, no. 10, p. 1834, Oct. 1993, doi: 10.1364/josab.10.001834.
- [37] F. Auzel and Y. Chen, 'LUMINESCENCE Photon avalanche luminescence of Er³⁺ ions in LiYF₄ crystal', 1995.
- [38] W. Zhao and J. A. Rowlands, 'To cite this article: Yihong Chen and F Auzel', 1995.
- [39] T. R. Gosnell, 'Avalanche assisted upconversion in Pr³⁺/Yb³⁺-doped ZBLAN glass', *Electron Lett*, vol. 33, no. 5, p. 411, Feb. 1997, doi: 10.1049/el:19970220.
- [40] F. Wang *et al.*, 'Tuning upconversion through energy migration in core-shell nanoparticles', *Nat Mater*, vol. 10, no. 12, pp. 968–973, 2011, doi: 10.1038/nmat3149.
- [41] X. Chen, D. Peng, Q. Ju, and F. Wang, 'Photon upconversion in core-shell nanoparticles', *Chem. Soc. Rev.*, vol. 44, no. 6, pp. 1318–1330, 2015, doi: 10.1039/C4CS00151F.
- [42] X. Xie, N. Gao, R. Deng, Q. Sun, Q.-H. Xu, and X. Liu, 'Mechanistic Investigation of Photon Upconversion in Nd³⁺-Sensitized Core-Shell Nanoparticles', *J Am Chem Soc*, vol. 135, no. 34, pp. 12608–12611, Aug. 2013, doi: 10.1021/ja4075002.
- [43] G. Yi and G. Chow, 'Core / Shell / Shell Nanoparticles with Significant Enhancement of Upconversion Fluorescence', *Chemistry of Materials*, vol. 19, no. 5599, pp. 341–343, 2007, doi: 10.1021/cm062447y.

- [44] C. Song, Z. Ye, G. Wang, J. Yuan, and Y. Guan, 'Core-shell nanoarchitectures: A strategy to improve the efficiency of luminescence resonance energy transfer', *ACS Nano*, vol. 4, no. 9, pp. 5389–5397, 2010, doi: 10.1021/nn100820u.
- [45] G. Chen, H. Qiu, P. N. Prasad, and X. Chen, 'Upconversion nanoparticles: Design, nanochemistry, and applications in Theranostics', *Chemical Reviews*, vol. 114, no. 10. American Chemical Society, pp. 5161–5214, May 2014. doi: 10.1021/cr400425h.
- [46] H. Dong, L.-D. Sun, and C.-H. Yan, 'Energy transfer in lanthanide upconversion studies for extended optical applications', *Chem. Soc. Rev.*, vol. 44, no. 6, 2015, doi: 10.1039/C4CS00188E.
- [47] H. Dong *et al.*, 'Lanthanide Nanoparticles: From Design toward Bioimaging and Therapy', *Chem Rev*, vol. 115, no. 19, pp. 10725–10815, Oct. 2015, doi: 10.1021/acs.chemrev.5b00091.
- [48] A. Gnach and A. Bednarkiewicz, 'Lanthanide-doped up-converting nanoparticles: Merits and challenges', *Nano Today*, vol. 7, no. 6, pp. 532–563, 2012, doi: 10.1016/j.nantod.2012.10.006.
- [49] H. H. Gorris and O. S. Wolfbeis, 'Photon-Upconverting Nanoparticles for Optical Encoding and Multiplexing of Cells, Biomolecules, and Microspheres', *Angewandte Chemie International Edition*, vol. 52, no. 13, pp. 3584–3600, Mar. 2013, doi: 10.1002/anie.201208196.
- [50] M. Dudek *et al.*, 'Size-Dependent Photon Avalanching in Tm³⁺ Doped LiYF₄ Nano, Micro, and Bulk Crystals', *Adv Opt Mater*, vol. 10, no. 19, Oct. 2022, doi: 10.1002/adom.202201052.
- [51] M. Rathaiah *et al.*, 'Photon avalanche upconversion in Ho³⁺-doped gallium nanogarnets', *Opt Mater (Amst)*, vol. 39, pp. 16–20, 2015, doi: 10.1016/j.optmat.2014.10.050.
- [52] P. Babu *et al.*, 'Photon avalanche upconversion in Ho³⁺-Yb³⁺ co-doped transparent oxyfluoride glass-ceramics', *Chem Phys Lett*, vol. 600, pp. 34–37, Apr. 2014, doi: 10.1016/j.cplett.2014.03.048.
- [53] H. Deng, C. Liu, S. Yang, S. Xiao, Z. K. Zhou, and Q. Q. Wang, 'Additive-mediated splitting of lanthanide orthovanadate nanocrystals in water: Morphological evolution from rods to sheaves and to spherulites', *Cryst Growth Des*, vol. 8, no. 12, pp. 4432–4439, 2008, doi: 10.1021/cg800207z.
- [54] H. Deng, S. Yang, S. Xiao, H. M. Gong, and Q. Q. Wang, 'Controlled synthesis and upconverted avalanche luminescence of cerium(III) and neodymium(III) orthovanadate nanocrystals with high uniformity of size and shape', *J Am Chem Soc*, 2008, doi: 10.1021/ja0778141.
- [55] S. Xiao, L. Zhou, Q. Q. Wang, H. Deng, and S. H. Yang, 'Energy transfer and avalanche upconversion of ndxy_{1-x}vo₄ nanocrystals', *Chinese Physics Letters*, vol. 26, no. 12, pp. 1–5, 2009, doi: 10.1088/0256-307X/26/12/124209.

References

- [56] L. Marciniak, A. Bednarkiewicz, and K. Elzbieciak, 'NIR-NIR photon avalanche based luminescent thermometry with Nd 3+ doped nanoparticles +', *J. Mater. Chem. C*, vol. 7568, p. 7568, 2018, doi: 10.1039/c8tc01553h.
- [57] Z. Zhang *et al.*, 'Tuning Phonon Energies in Lanthanide-doped Potassium Lead Halide Nanocrystals for Enhanced Nonlinearity and Upconversion', *Angewandte Chemie - International Edition*, vol. 62, no. 1, Jan. 2023, doi: 10.1002/anie.202212549.
- [58] A. Strzęp, M. Głowacki, M. Szatko, K. Potrząsaj, R. Lisiecki, and W. Ryba-Romanowski, 'Spectroscopic properties of thulium doped (Lu_{0.25}Gd_{0.75})₂SiO₅ (LGSO) single crystals', *J Lumin*, vol. 220, Apr. 2020, doi: 10.1016/j.jlumin.2019.116962.
- [59] Z. Jia *et al.*, 'Enhancement of 800 nm upconversion emission in a thulium doped tellurite microstructured fiber pumped by a 1560 nm femtosecond fiber laser', *J Appl Phys*, vol. 119, no. 16, Apr. 2016, doi: 10.1063/1.4947278.
- [60] M. Misiak, K. Prorok, B. Cichy, A. Bednarkiewicz, and W. Stręk, 'Thulium concentration quenching in the up-converting α -Tm³⁺/Yb³⁺ NaYF₄ colloidal nanocrystals', *Opt Mater (Amst)*, vol. 35, no. 5, pp. 1124–1128, 2013, doi: <https://doi.org/10.1016/j.optmat.2013.01.002>.
- [61] S. Guy, M. F. Joubert, and B. Jacquier, 'Photon avalanche upconversion in various Tm³⁺-doped materials', *J Alloys Compd*, vol. 275–277, pp. 186–190, 1998, doi: 10.1016/S0925-8388(98)00300-4.
- [62] E. Bielejec, E. Kisel, and A. Silversmith, 'Red to blue up-conversion in Y₂SiO₅:Tm³⁺', *J Lumin*, vol. 72–74, pp. 62–64, Jun. 1997, doi: 10.1016/S0022-2313(96)00163-9.
- [63] M. F. Joubert, S. Guy, C. Linares, B. Jacquier, and J. L. Adam, 'Avalanche upconversion in Tm³⁺-doped BiGaZr glass', *J Non Cryst Solids*, vol. 184, pp. 98–102, May 1995, doi: 10.1016/0022-3093(95)00090-9.
- [64] I. R. Martín *et al.*, 'Room-temperature photon avalanche upconversion in Tm³⁺: Y₂O₃ crystals', *Phys Rev B*, vol. 60, no. 10, pp. 7252–7257, Sep. 1999, doi: 10.1103/PhysRevB.60.7252.
- [65] S. Guy, D. P. Shepherd, M. F. Joubert, B. Jacquier, and H. Poignant, 'Blue avalanche upconversion in Tm:ZBLAN fiber', *Journal of the Optical Society of America B*, vol. 14, no. 4, p. 926, Apr. 1997, doi: 10.1364/josab.14.000926.
- [66] I. R. Martín, V. D. Rodríguez, Y. Guyot, S. Guy, G. Boulon, and M. F. Joubert, 'Room temperature photon avalanche upconversion in Tm³⁺-doped fluoroindate glasses', *Journal of Physics Condensed Matter*, vol. 12, no. 7, pp. 1507–1516, 2000, doi: 10.1088/0953-8984/12/7/331.
- [67] J. M. Dyson, S. M. Jaffe, H. Eilers, M. L. Jones, W. M. Dennis, and W. M. Yen, 'Observation of avalanche-like behavior in Tm³⁺: Y₂O₃', *J Lumin*, vol. 60–61, no. C, pp. 668–671, Apr. 1994, doi: 10.1016/0022-2313(94)90246-1.
- [68] A. Bednarkiewicz, E. M. Chan, A. Kotulska, L. Marciniak, and K. Prorok, 'Photon avalanche in lanthanide doped nanoparticles for biomedical applications: Super-resolution imaging', *Nanoscale Horiz*, vol. 4, no. 4, 2019, doi: 10.1039/c9nh00089e.

- [69] Y. Liu *et al.*, 'Amplified stimulated emission in upconversion nanoparticles for super-resolution nanoscopy', *Nature*, vol. 543, no. 7644, pp. 229–233, 2017, doi: 10.1038/nature21366.
- [70] Y. Liang *et al.*, 'Migrating photon avalanche in different emitters at the nanoscale enables 46th-order optical nonlinearity', *Nature Nanotechnology* 2022, pp. 1–7, Apr. 2022, doi: 10.1038/s41565-022-01101-8.
- [71] B. Xu, P. Camy, J.-L. Doualan, Z. Cai, and R. Moncorgé, 'Visible laser operation of Pr³⁺-doped fluoride crystals pumped by a 469 nm blue laser', *Opt Express*, 2011, doi: 10.1364/oe.19.001191.
- [72] T. Sandrock, H. Scheife, E. Heumann, and G. Huber, 'High-power continuous-wave upconversion fiber laser at room temperature', *Opt Lett*, 1997, doi: 10.1364/ol.22.000808.
- [73] P. Xie and T. R. Gosnell, 'Room-temperature upconversion fiber laser tunable in the red, orange, green, and blue spectral regions', *Opt Lett*, 1995, doi: 10.1364/ol.20.001014.
- [74] R. G. Smart *et al.*, 'CW room temperature operation of praseodymium-doped fluorozirconate glass fibre lasers in the blue-green, green and red spectral regions', 1991.
- [75] J. L. Adam, W. A. Sibley, and D. R. Gabbe, 'Optical absorption and emission of LiYF₄:Pr³⁺', *J Lumin*, vol. 33, no. 4, pp. 391–407, 1985, doi: 10.1016/0022-2313(85)90109-7.
- [76] J. K. Lawson and S. A. Payne, 'Excited-state absorption of Pr³⁺-doped fluoride crystals', *Opt Mater (Amst)*, 1993, doi: 10.1016/0925-3467(93)90018-V.
- [77] M. Eyal, E. Greenberg, R. Reisfeld, and N. Spector, 'Spectroscopy of praseodymium(III) in zirconium fluoride glass', *Chem Phys Lett*, vol. 117, no. 2, pp. 108–114, 1985, doi: 10.1016/0009-2614(85)85216-7.
- [78] G. M. Renfro, J. C. Windscheif, W. A. Sibley, and R. F. Belt, 'Optical transitions of Pr³⁺ and Er³⁺ ions in LiYF₄', *J Lumin*, 1980, doi: 10.1016/0022-2313(80)90045-9.
- [79] A. Remillieux *et al.*, 'Upconversion mechanisms of a praseodymium-doped fluoride fibre amplifier', *J Phys D Appl Phys*, 1996, doi: 10.1088/0022-3727/29/4/004.
- [80] A. Pandey and V. K. Rai, 'Pr³⁺-Yb³⁺ codoped Y₂O₃ phosphor for display devices', *Mater Res Bull*, vol. 57, pp. 156–161, Sep. 2014, doi: 10.1016/j.materresbull.2014.04.071.
- [81] S. Golovynskyi *et al.*, 'Optical windows for head tissues in near-infrared and short-wave infrared regions: Approaching transcranial light applications', *J Biophotonics*, vol. 11, no. 12, p. e201800141, Dec. 2018, doi: 10.1002/jbio.201800141.
- [82] D. V. Milojkov *et al.*, 'Fabrication and characterization of luminescent Pr³⁺ doped fluorapatite nanocrystals as bioimaging contrast agents', *J Lumin*, vol. 217, p. 116757, Jan. 2020, doi: 10.1016/j.jlum.2019.116757.
- [83] P. Xiong, M. Peng, K. Qin, F. Xu, and X. Xu, 'Visible to Near-Infrared Persistent Luminescence and Mechanoluminescence from Pr³⁺-Doped LiGa₅O₈ for Energy Storage and Bioimaging', *Adv Opt Mater*, vol. 7, no. 24, p. 1901107, Dec. 2019, doi: 10.1002/adom.201901107.

-
- [84] S. Espinoza *et al.*, 'Characterization of Micro- and Nanoscale LuPO₄:Pr³⁺,Nd³⁺ with Strong UV-C Emission to Reduce X-Ray Doses in Radiation Therapy', *Particle & Particle Systems Characterization*, vol. 36, no. 10, p. 1900280, Oct. 2019, doi: 10.1002/ppsc.201900280.
- [85] K. Popovich *et al.*, 'LuAG:Pr³⁺-porphyrin based nanohybrid system for singlet oxygen production: Toward the next generation of PDTX drugs', *J Photochem Photobiol B*, vol. 179, pp. 149–155, Feb. 2018, doi: 10.1016/j.jphotobiol.2018.01.015.
- [86] T. J. de Prinse *et al.*, 'Dual Laser Study of Non-Degenerate Two Wavelength Upconversion Demonstrated in Sensitizer-Free NaYF₄:Pr Nanoparticles', *Adv Opt Mater*, vol. 9, no. 7, Apr. 2021, doi: 10.1002/adom.202001903.
- [87] M. Yin, J. C. Krupa, E. Antic-Fidancev, V. N. Makhov, and N. M. Khaidukov, 'Excitation spectroscopy of K₂YF₅:Pr³⁺ crystals', 2003.
- [88] L. Lunga and N. Hons, 'Red emission of Praseodymium ions (Pr³⁺)', 2011.
- [89] A. S. L. Gomes, G. S. Maciel, R. E. de Araújo, L. H. Acioli, and C. B. de Araújo, 'Diode pumped avalanche upconversion in Pr³⁺-doped fibers', *Opt Commun*, vol. 103, no. 5–6, pp. 361–364, 1993, doi: 10.1016/0030-4018(93)90157-Z.
- [90] V. Lupei, 'Sensitized photon avalanche', *Spectrochim Acta A Mol Biomol Spectrosc*, vol. 54, no. 11, pp. 1615–1632, 1998, doi: 10.1016/S1386-1425(98)00089-4.
- [91] S. Kück *et al.*, 'Avalanche up-conversion processes in Pr, Yb-doped materials', *J Alloys Compd*, 2000, doi: 10.1016/S0925-8388(99)00734-3.
- [92] G. Huang *et al.*, 'Upconversion nanoparticles for super-resolution quantification of single small extracellular vesicles', *eLight*, vol. 2, no. 1, Dec. 2022, doi: 10.1186/s43593-022-00031-1.
- [93] M. Szalkowski *et al.*, 'Predicting the impact of temperature dependent multi-phonon relaxation processes on the photon avalanche behavior in Tm³⁺: NaYF₄ nanoparticles', *Optical Materials: X*, vol. 12, Dec. 2021, doi: 10.1016/j.omx.2021.100102.
- [94] S. Kuck and I. Sokólska, 'The up-conversion of near-infrared excitation radiation in Ho³⁺-doped LiYF₄', *Chem Phys Lett*, vol. 325, no. 1–3, pp. 257–263, 2000, doi: 10.1016/S0009-2614(00)00652-7.
- [95] A. Wnuk *et al.*, 'Infrared to visible up-conversion in holmium-doped materials', 2002. [Online]. Available: www.elsevier.com/locate/jallcom
- [96] M. Malinowski, R. Piramidowicz, Z. Frukacz, G. Chadeyron, R. Mahiou, and M. F. Joubert, 'Spectroscopy and upconversion processes in YAlO₃:Ho³⁺ crystals'.
- [97] F. Lahoz, I. R. Martín, and J. M. Calvilla-Quintero, 'Ultraviolet and white photon avalanche upconversion in Ho³⁺-doped nanophase glass ceramics', *Appl Phys Lett*, vol. 86, no. 5, pp. 1–3, Jan. 2005, doi: 10.1063/1.1861975.
- [98] F. Lahoz, I. R. Martín, V. L. Guadalupe, J. Méndez-Ramos, V. D. Rodríguez, and U. R. Rodríguez-Mendoza, 'Room temperature photon avalanche up-conversion in Ho³⁺-doped fluorindate glasses under excitation at 747 nm', in *Optical Materials*, Elsevier, 2004, pp. 209–213. doi: 10.1016/S0925-3467(03)00271-4.

- [99] Y. Kalisky, S. R. Rotman, G. Boulon, C. Pedrini, and A. Brenier, 'Spectroscopy, modelling and laser operation of holmium doped laser crystals', *Opt Mater (Amst)*, vol. 4, no. 1, pp. 25–30, 1994, doi: [https://doi.org/10.1016/0925-3467\(94\)90051-5](https://doi.org/10.1016/0925-3467(94)90051-5).
- [100] L. V Klimov, I. A. Shcherbakov, and V. B. Tsvetkov, 'Room Temperature 2- μ m Laser Action of Ho³⁺-Doped YSGG, GSAG, YSAG, and YAG Crystals', in *Advanced Solid State Lasers*, Optica Publishing Group, 1993, p. ML7. doi: 10.1364/ASSL.1993.ML7.
- [101] B. M. Antipenko *et al.*, 'LASERS Periodic-pulse operation of holmium lasers using YAG and YSGG crystals', 1993.
- [102] S. Kampantais, P. Dimopoulos, A. Tasleem, P. Acher, K. Gordon, and A. Young, 'Assessing the Learning Curve of Holmium Laser Enucleation of Prostate (HoLEP). A Systematic Review', *Urology*, vol. 120. Elsevier Inc., pp. 9–22, Oct. 01, 2018. doi: 10.1016/j.urology.2018.06.012.
- [103] O. K. Alimov, M. E. Doroshenko, V. A. Konyushkin, F. Gan, J. Wang, and Y. Chen, 'Nonlinear luminescence of and ions in ZBLAN fluoride glasses Selective laser spectroscopy of SrF₂ crystal doped with Pr³⁺ ions Nonlinear luminescence of Ho³⁺ and Yb³⁺ ions in ZBLAN fluoride glasses', 1996.
- [104] O. K. Liu, Y. H. Chen, and J. V. Beitz, 'Photon avalanche up-conversion in Ho³⁺ doped fluoride glasses', *J Lumin*, vol. 81, no. 1, pp. 7–12, Jan. 1999, doi: 10.1016/S0022-2313(98)00059-3.
- [105] M. Malinowski *et al.*, 'Room temperature photon avalanche in Ho³⁺ doped YAG, YAP, YLF and ZBLAN', in *Journal of Alloys and Compounds*, Elsevier, Jul. 2001, pp. 731–735. doi: 10.1016/S0925-8388(01)01064-7.
- [106] F. Lahoz, I. R. Martín, and A. Briones, 'Infrared-laser induced photon avalanche upconversion in Ho³⁺-Yb³⁺ codoped fluoroindate glasses', *J Appl Phys*, vol. 95, no. 6, pp. 2957–2962, Mar. 2004, doi: 10.1063/1.1649809.
- [107] E. Osiac, I. Sok ! Olska, and S. K. Uck, 'Avalanche-like mechanisms and up-conversion processes under infrared pumping in Ho³⁺, Yb³⁺:YAIO₃', 2001.
- [108] Y. Dwivedi, A. Bahadur, and S. B. Rai, 'Optical avalanche in Ho : Yb : Gd₂O₃ nanocrystals', vol. 043103, no. 2011, 2016, doi: 10.1063/1.3622624.
- [109] L. Esterowitz, A. Schnitzler, J. Noonan, and J. Bahler, 'Rare Earth Infrared Quantum Counter'.
- [110] N. J. Krasutsky, W. E. Case, and J. S. Chivian, 'Performance characteristics of a Pr-based infrared quantum-counter imaging system', *J Appl Phys*, vol. 50, no. 5, pp. 3142–3145, 1979, doi: 10.1063/1.326395.
- [111] P. Goldner and F. Pellé, 'Photon avalanche fluorescence and lasers', *Opt Mater (Amst)*, vol. 5, no. 4, pp. 239–249, May 1996, doi: 10.1016/0925-3467(96)00003-1.
- [112] E. Osiac *et al.*, 'Avalanche mechanism generating laser oscillation in Pr³⁺, Yb³⁺:BaY₂F₈', in *Conference on Lasers and Electro-Optics Europe - Technical Digest*, 2003. doi: 10.1109/CLEOE.2003.1312090.

References

- [113] W. Chen *et al.*, 'Continuous-wave frequency upconversion with a molecular optomechanical nanocavity'. [Online]. Available: <https://www.science.org>
- [114] L. F. Johnson and H. J. Guggenheim, 'Infrared-pumped visible laser', *Appl Phys Lett*, vol. 19, no. 2, pp. 44–47, 1971, doi: 10.1063/1.1653816.
- [115] R. Scheps, 'Upconversion laser processes', *Progress in Quantum Electronics*, vol. 20, no. 4. Elsevier Ltd, pp. 271–358, Jan. 1996. doi: 10.1016/0079-6727(95)00007-0.
- [116] T. Sandrock, E. Heumann, G. Huber, and B. H. T. Chai, 'Continuous-Wave Pr, Yb:LiYF₄ Upconversion Laser in the Red Spectral Range at Room Temperature', in *Advanced Solid State Lasers*, Optica Publishing Group, 1996, p. PM1. doi: 10.1364/ASSL.1996.PM1.
- [117] E. Osiac *et al.*, 'Spectroscopic characterisation of the upconversion avalanche mechanism in Pr³⁺, Yb³⁺:BaY₂F₈', *Opt Mater (Amst)*, 2003, doi: 10.1016/S0925-3467(03)00089-2.
- [118] E. Osiac *et al.*, 'Orange and red upconversion laser pumped by an avalanche mechanism in Pr³⁺, Yb³⁺:BaY₂F₈', *Appl Phys Lett*, 2003, doi: 10.1063/1.1579561.
- [119] E. S. Levy *et al.*, 'Energy-Looping Nanoparticles: Harnessing Excited-State Absorption for Deep-Tissue Imaging.', *ACS Nano*, vol. 10, no. 9, pp. 8423–33, Sep. 2016, doi: 10.1021/acsnano.6b03288.
- [120] A. Fernandez-Bravo *et al.*, 'Continuous-wave upconverting nanoparticle microlasers', doi: 10.1038/s41565-018-0161-8.
- [121] Y. Liu *et al.*, 'Controlled Assembly of Upconverting Nanoparticles for Low-Threshold Microlasers and Their Imaging in Scattering Media', *ACS Nano*, vol. 14, no. 2, pp. 1508–1519, Feb. 2020, doi: 10.1021/acsnano.9b06102.
- [122] A. Fernandez-Bravo *et al.*, 'Ultralow-threshold, continuous-wave upconverting lasing from subwavelength plasmons', doi: 10.1038/s41563-019-0482-5.
- [123] D. Jaque and F. Vetrone, 'Luminescence nanothermometry', *Nanoscale*, vol. 4, no. 15. Royal Society of Chemistry, pp. 4301–4326, Aug. 07, 2012. doi: 10.1039/c2nr30764b.
- [124] C. D. S. Brites, A. Millán, and L. D. Carlos, 'Lanthanides in Luminescent Thermometry', in *Handbook on the Physics and Chemistry of Rare Earths*, vol. 49, Elsevier B.V., 2016, pp. 339–427. doi: 10.1016/bs.hpcre.2016.03.005.
- [125] Miroslav Dramićanin, *Luminescence Thermometry*. 2018. doi: 10.1016/c2016-0-01905-8.
- [126] A. Rabhiou, J. Feist, A. Kempf, S. Skinner, and A. Heyes, 'Phosphorescent thermal history sensors', *Sens Actuators A Phys*, vol. 169, no. 1, pp. 18–26, Sep. 2011, doi: 10.1016/j.sna.2011.04.022.
- [127] B. del Rosal, E. Ximendes, U. Rocha, and D. Jaque, 'In Vivo Luminescence Nanothermometry: from Materials to Applications', *Advanced Optical Materials*, vol. 5, no. 1. Wiley-VCH Verlag, Jan. 2017. doi: 10.1002/adom.201600508.
- [128] C. D. S. Brites *et al.*, 'Thermometry at the nanoscale', *Nanoscale*, vol. 4, no. 16. The Royal Society of Chemistry, pp. 4799–4829, Aug. 2012. doi: 10.1039/c2nr30663h.

- [129] X. D. Wang, O. S. Wolfbeis, and R. J. Meier, 'Luminescent probes and sensors for temperature', *Chem Soc Rev*, vol. 42, no. 19, pp. 7834–7869, Sep. 2013, doi: 10.1039/c3cs60102a.
- [130] C. Abram, B. Fond, and F. Beyrau, 'Temperature measurement techniques for gas and liquid flows using thermographic phosphor tracer particles', *Prog Energy Combust Sci*, vol. 64, pp. 93–156, 2018, doi: 10.1016/j.pecs.2017.09.001.
- [131] J. Drabik, R. Kowalski, and L. Marciniak, 'Enhancement of the sensitivity of single band ratiometric luminescent nanothermometers based on Tb³⁺ ions through activation of the cross relaxation process', *Sci Rep*, vol. 10, no. 1, pp. 1–11, 2020, doi: 10.1038/s41598-020-68145-5.
- [132] J. Drabik and L. Marciniak, 'Excited State Absorption for Ratiometric Thermal Imaging', 2020, doi: 10.1021/acsami.0c18570.
- [133] K. Trejgis, R. Lisiecki, A. Bednarkiewicz, and L. Marciniak, 'Nd³⁺ doped TZPN glasses for NIR operating single band ratiometric approach of contactless temperature readout', *J Lumin*, vol. 224, p. 117295, Aug. 2020, doi: 10.1016/j.jlumin.2020.117295.
- [134] K. Trejgis, K. Maciejewska, A. Bednarkiewicz, and L. Marciniak, 'Near-Infrared-to-Near-Infrared Excited-State Absorption in LaPO₄:Nd³⁺ Nanoparticles for Luminescent Nanothermometry', *ACS Appl Nano Mater*, vol. 3, no. 5, pp. 4818–4825, May 2020, doi: 10.1021/acsnm.0c00853.
- [135] K. Trejgis, A. Bednarkiewicz, and L. Marciniak, 'Engineering excited state absorption based nanothermometry for temperature sensing and imaging', *Nanoscale*, vol. 12, no. 7, pp. 4667–4675, Feb. 2020, doi: 10.1039/c9nr09740f.
- [136] J. Drabik and L. Marciniak, 'KLaP₄O₁₂:Tb³⁺ Nanocrystals for Luminescent Thermometry in a Single-Band-Ratiometric Approach', *ACS Appl Nano Mater*, vol. 3, no. 4, pp. 3798–3806, Apr. 2020, doi: 10.1021/acsnm.0c00485.
- [137] J. Drabik, K. Ledwa, and Ł. Marciniak, 'Implementing Defects for Ratiometric Luminescence Thermometry', *Nanomaterials*, vol. 10, no. 7, p. 1333, Jul. 2020, doi: 10.3390/nano10071333.
- [138] Y. Xu *et al.*, 'Recent advances in luminescent materials for super-resolution imaging: Via stimulated emission depletion nanoscopy', *Chemical Society Reviews*, vol. 50, no. 1. Royal Society of Chemistry, pp. 667–690, Jan. 07, 2021. doi: 10.1039/d0cs00676a.
- [139] A. Fine, W. B. Amos, R. M. Durbin, and P. A. McNaughton, 'Confocal microscopy: applications in neurobiology', *Trends Neurosci*, vol. 11, no. 8, pp. 346–351, 1988, doi: [https://doi.org/10.1016/0166-2236\(88\)90056-2](https://doi.org/10.1016/0166-2236(88)90056-2).
- [140] K. W. Dunn, M. M. Kamocka, and J. H. McDonald, 'A practical guide to evaluating colocalization in biological microscopy', *American Journal of Physiology - Cell Physiology*, vol. 300, no. 4. Apr. 2011. doi: 10.1152/ajpcell.00462.2010.
- [141] 'paddock-2018-confocal-laser-scanning-microscopy'.
- [142] K. Konig, 'Multiphoton microscopy in life sciences', *Journal of Microscopy*, vol. 200, no. 2. Blackwell Publishing Ltd., pp. 83–104, 2000. doi: 10.1046/j.1365-2818.2000.00738.x.

-
- [143] A. Bio, K. Frączkowska, P. Wrocławska, W. Podstawowych, and P. Techniki, 'Listy do Redakcji / Letters to Editor NAGRODA NOBLA Z CHEMII W 2014 ROKU ZA ROZWÓJ WYSOKOROZDZIELCZEJ MIKROSKOPII FLUORESCENCYJNEJ THE NOBEL PRIZE IN CHEMISTRY 2014 FOR THE DEVELOPMENT OF SUPER-RESOLVED FLUORESCENCE MICROSCOPY', 2014.
- [144] S. W. Hell and J. Wichmann, 'Breaking the diffraction resolution limit by stimulated emission: stimulated-emission-depletion fluorescence microscopy', *Opt. Lett.*, vol. 19, no. 11, pp. 780–782, Jun. 1994, doi: 10.1364/OL.19.000780.
- [145] T. A. Klar, S. Jakobs, M. Dyba, A. Egner, and S. W. Hell, 'Fluorescence microscopy with diffraction resolution barrier broken by stimulated emission'. [Online]. Available: www.pnas.org
- [146] W. E. Moerner and L. Kador, 'Optical Detection and Spectroscopy of Single Molecules in a Solid', 1989.
- [147] E. Betzig and R. J. Chichester, 'Single Molecules Observed by Near-Field Scanning Optical Microscopy', *Science (1979)*, vol. 262, no. 5138, pp. 1422–1425, 1993, doi: 10.1126/science.262.5138.1422.
- [148] E. Betzig, 'Proposed method for molecular optical imaging', *Opt. Lett.*, vol. 20, no. 3, pp. 237–239, Feb. 1995, doi: 10.1364/OL.20.000237.
- [149] E. Betzig *et al.*, 'Imaging intracellular fluorescent proteins at nanometer resolution', *Science (1979)*, 2006, doi: 10.1126/science.1127344.
- [150] R. Kolesov, R. Reuter, K. Xia, R. Stöhr, A. Zappe, and J. Wrachtrup, 'Super-resolution upconversion microscopy of praseodymium-doped yttrium aluminum garnet nanoparticles', *Phys. Rev. B*, vol. 84, 2011.
- [151] C. Chen *et al.*, 'Multi-photon near-infrared emission saturation nanoscopy using upconversion nanoparticles', *Nat Commun*, vol. 9, no. 1, pp. 4–9, 2018, doi: 10.1038/s41467-018-05842-w.
- [152] M. J. Rust, M. Bates, and X. Zhuang, 'Sub-diffraction-limit imaging by stochastic optical reconstruction microscopy (STORM)', *Nat Methods*, 2006, doi: 10.1038/nmeth929.
- [153] N. Mauser and A. Hartschuh, 'Tip-enhanced near-field optical microscopy', *Chemical Society Reviews*. 2014. doi: 10.1039/c3cs60258c.
- [154] M. G. L. Gustafsson, 'Surpassing the lateral resolution limit by a factor of two using structured illumination microscopy', *J Microsc*, 2000, doi: 10.1046/j.1365-2818.2000.00710.x.
- [155] A. A. Zuber, E. Klantsataya, and A. Bachhuka, '3.06 - Biosensing', in *Comprehensive Nanoscience and Nanotechnology (Second Edition)*, Second Edition., D. L. Andrews, R. H. Lipson, and T. Nann, Eds., Oxford: Academic Press, 2019, pp. 105–126. doi: <https://doi.org/10.1016/B978-0-12-803581-8.10410-2>.
- [156] T.-M. Liu, J. Conde, T. Lipiński, A. Bednarkiewicz, and C.-C. Huang, 'Smart NIR linear and nonlinear optical nanomaterials for cancer theranostics: Prospects in photomedicine',

- Prog Mater Sci*, vol. 88, pp. 89–135, 2017, doi: <https://doi.org/10.1016/j.pmatsci.2017.03.004>.
- [157] T. M. Liu, J. Conde, T. Lipiński, A. Bednarkiewicz, and C. C. Huang, 'Revisiting the classification of NIR-absorbing/emitting nanomaterials for in vivo bioapplications', *NPG Asia Materials*, vol. 8, no. 8. Nature Publishing Group, Aug. 05, 2016. doi: 10.1038/am.2016.106.
- [158] F. Auzel, 'Upconversion and Anti-Stokes Processes with f and d Ions in Solids', *Chem Rev*, vol. 104, no. 1, pp. 139–173, 2004, doi: 10.1021/cr020357g.
- [159] Y. Zhong *et al.*, 'Elimination of photon quenching by a transition layer to fabricate a quenching-shield sandwich structure for 800 nm excited upconversion luminescence of Nd³⁺-sensitized nanoparticles', *Advanced Materials*, vol. 26, no. 18, pp. 2831–2837, May 2014, doi: 10.1002/adma.201304903.
- [160] A. Bednarkiewicz, E. M. Chan, and K. Prorok, 'Enhancing FRET biosensing beyond 10 nm with photon avalanche nanoparticles', *Nanoscale Adv*, vol. 2, no. 10, pp. 4863–4872, Oct. 2020, doi: 10.1039/d0na00404a.
- [161] S. Wen, J. Zhou, K. Zheng, A. Bednarkiewicz, X. Liu, and D. Jin, 'Advances in highly doped upconversion nanoparticles', *Nat Commun*, vol. 9, no. 1, Dec. 2018, doi: 10.1038/s41467-018-04813-5.
- [162] I. Medintz and N. Hildebrandt, *FRET – Förster Resonance Energy Transfer*. Wiley-VCH Verlag GmbH & Co. KGaA, 2014.
- [163] E. M. Chan *et al.*, 'Combinatorial discovery of lanthanide-doped nanocrystals with spectrally pure upconverted emission', *Nano Lett*, vol. 12, no. 7, pp. 3839–3845, Jul. 2012, doi: 10.1021/nl3017994.
- [164] G. Tian *et al.*, 'Mn²⁺ dopant-controlled synthesis of NaYF₄:Yb/Er upconversion nanoparticles for in vivo imaging and drug delivery', *Advanced Materials*, vol. 24, no. 9, pp. 1226–1231, Mar. 2012, doi: 10.1002/adma.201104741.
- [165] A. Jha, C. Huang, and P. R. Prucnal, 'Reconfigurable all-optical nonlinear activation functions for neuromorphic photonics', *Opt Lett*, vol. 45, no. 17, p. 4819, Sep. 2020, doi: 10.1364/ol.398234.
- [166] C. Lee *et al.*, 'Indefinite and bidirectional near-infrared nanocrystal photoswitching', *Nature*, vol. 618, no. 7967, pp. 951–958, Jun. 2023, doi: 10.1038/s41586-023-06076-7.
- [167] A. Bednarkiewicz, M. Szalkowski, M. Majak, Z. Korczak, M. Misiak, and S. Maćkowski, 'All-Optical Data Processing with Photon-Avalanching Nanocrystalline Photonic Synapse', *Advanced Materials*, Oct. 2023, doi: 10.1002/adma.202304390.
- [168] X. Deng, M. Yu, X. Zhou, Z. Xia, X. Chen, and S. Huang, 'Highly bright and sensitive thermometric LiYF₄:Yb, Er upconversion nanocrystals through Mg²⁺ tridoping', *Journal of Materials Science: Materials in Electronics*, vol. 31, no. 4, pp. 3415–3425, 2020, doi: 10.1007/s10854-020-02890-1.
- [169] C. Yan, H. Zhao, D. F. Perepichka, and F. Rosei, 'Lanthanide Ion Doped Upconverting Nanoparticles: Synthesis, Structure and Properties', *Small*, pp. 3888–3907, 2016, doi: 10.1002/smll.201601565.

- [170] The Materials Project, 'Materials Data on NaYF₄ by Materials Project'.
- [171] The Materials Project, 'Materials Data on LiYF₄ by Materials Project'.
- [172] K. A. Abel, J. C. Boyer, and F. C. J. M. Van Veggel, 'Hard proof of the NaYF₄/NaGdF₄ nanocrystal core/shell structure', *J Am Chem Soc*, vol. 131, no. 41, pp. 14644–14645, Oct. 2009, doi: 10.1021/ja906971y.
- [173] Z. Qiu, S. Wang, W. Wang, and S. Wu, 'Polymer Composites Entrapped Ce-Doped LiYF₄ Microcrystals for High-Sensitivity X-ray Scintillation and Imaging', *ACS Appl Mater Interfaces*, vol. 12, no. 26, pp. 29835–29843, Jul. 2020, doi: 10.1021/acami.0c07765.
- [174] A. A. Kaminskii, *Crystalline Lasers: Physical Processes and Operating Schemes*.
- [175] J. Xiong, H. Peng, P. Hu, Y. Hang, and L. Zhang, 'Optical characterization of Tm³⁺ in LiYF₄ and LiLuF₄ crystals', *J Phys D Appl Phys*, vol. 43, no. 18, 2010, doi: 10.1088/0022-3727/43/18/185402.
- [176] P. Loiko *et al.*, 'Emission properties of Tm³⁺-doped CaF₂, KY₃F₁₀, LiYF₄, LiLuF₄ and BaY₂F₈ crystals at 1.5 μm and 2.3 μm', *J Lumin*, vol. 225, Sep. 2020, doi: 10.1016/j.jlumin.2020.117279.
- [177] R. Lisiecki *et al.*, 'Comparative optical study of thulium-doped YVO₄, GdVO₄, and LuVO₄ single crystals', *Phys Rev B Condens Matter Mater Phys*, vol. 74, no. 3, 2006, doi: 10.1103/PhysRevB.74.035103.
- [178] Y. Yang, B. Yao, B. Chen, C. Wang, G. Ren, and X. Wang, 'Judd-Ofelt analysis of spectroscopic properties of Tm³⁺, Ho³⁺ doped GdVO₄ crystals', *Opt Mater (Amst)*, vol. 29, no. 9, pp. 1159–1165, 2007, doi: 10.1016/j.optmat.2006.06.003.
- [179] O. Silvestre, M. C. Pujol, M. Rico, F. Güell, M. Aguiló, and F. Díaz, 'Thulium doped monoclinic KLu(WO₄)₂ single crystals: Growth and spectroscopy', *Appl Phys B*, vol. 87, no. 4, pp. 707–716, Jun. 2007, doi: 10.1007/s00340-007-2664-0.
- [180] M. N. Polyanskiy, 'Refractive index database'. Accessed: Dec. 06, 2023. [Online]. Available: <https://refractiveindex.info>
- [181] C. Zhao *et al.*, 'Optical spectroscopy of Nd³⁺ in LiLuF₄ single crystals', *J Phys D Appl Phys*, vol. 43, no. 49, Dec. 2010, doi: 10.1088/0022-3727/43/49/495403.
- [182] L. Guillemot *et al.*, 'Close look on cubic Tm:KY₃F₁₀ crystal for highly efficient lasing on the 3 H₄ → 3 H₅ transition', *Opt Express*, vol. 28, no. 3, p. 3451, Feb. 2020, doi: 10.1364/oe.382650.
- [183] 'Teledyne FLIR Scientific Materials'. Accessed: Dec. 06, 2023. [Online]. Available: <https://www.flir.eu/>
- [184] H. C. Liang, J. C. Tung, C. H. Tsou, K. W. Su, and Y. F. Chen, 'Exploring optical properties of Nd-doped vanadates with intracavity self-mode locking', in *Solid State Lasers XXII: Technology and Devices*, SPIE, Mar. 2013, p. 859920. doi: 10.1117/12.2003846.
- [185] V. V. Filippov, N. V. Kuleshov, and I. T. Bodnar, 'Negative thermo-optical coefficients and athermal directions in monoclinic KGd(WO₄)₂ and KY(WO₄)₂ laser host crystals in the

- visible region', *Appl Phys B*, vol. 87, no. 4, pp. 611–614, Jun. 2007, doi: 10.1007/s00340-007-2666-y.
- [186] M. C. Pujol *et al.*, 'Growth, optical characterization, and laser operation of a stoichiometric crystal KYb(WO₄)₂', *Phys Rev B Condens Matter Mater Phys*, vol. 65, no. 16, pp. 1651211–1651211, Apr. 2002, doi: 10.1103/PhysRevB.65.165121.
- [187] 'Journal of Applied Crystallography'. Accessed: Dec. 06, 2023. [Online]. Available: <https://journals.iucr.org/j/>
- [188] V. François, F. Pellé, P. Goldner, and D. Simkin, 'Pump-probe measurement of the avalanche up-conversion gain in Tm³⁺: YLF', *J Lumin*, vol. 65, no. 2, pp. 57–63, Jul. 1995, doi: 10.1016/0022-2313(95)00059-Y.
- [189] M. Dudek *et al.*, 'Understanding Yb³⁺-sensitized photon avalanche in Pr³⁺ co-doped nanocrystals: modelling and optimization', *Nanoscale*, 2023, doi: 10.1039/d3nr04409b.
- [190] P. Boutinauda, R. Mahiou, N. Martin, and M. Malinowski, 'Luminescence from Pr³⁺ 3P₁ and 3P₂ states in P-NaYF₄: Pr³⁺', 1997.
- [191] S. Hao *et al.*, 'Tuning the size and upconversion emission of NaYF₄:Yb³⁺/Pr³⁺ nanoparticles through Yb³⁺ doping', *RSC Adv*, vol. 4, no. 99, pp. 56302–56306, 2014, doi: 10.1039/c4ra11357h.
- [192] M. Y. Tsang *et al.*, 'Pr³⁺ doped NaYF₄ and LiYF₄ nanocrystals combining visible-to-UVC upconversion and NIR-to-NIR-II downconversion luminescence emissions for biomedical applications', *Nanoscale*, vol. 14, no. 39, pp. 14770–14778, Sep. 2022, doi: 10.1039/d2nr01680j.
- [193] K. Yoshimoto, A. Masuno, M. Ueda, H. Inoue, H. Yamamoto, and T. Kawashima, 'Low phonon energies and wideband optical windows of La₂O₃-Ga₂O₃ glasses prepared using an aerodynamic levitation technique', *Sci Rep*, vol. 7, Mar. 2017, doi: 10.1038/srep45600.
- [194] A. J. Stevenson, H. Serier-Brault, P. Gredin, and M. Mortier, 'Fluoride materials for optical applications: Single crystals, ceramics, glasses, and glass-ceramics', *J Fluor Chem*, vol. 132, no. 12, pp. 1165–1173, 2011, doi: <https://doi.org/10.1016/j.jfluchem.2011.07.017>.
- [195] P. Babu and C. K. Jayasankar, 'Spectroscopy of Pr³⁺ ions in lithium borate and lithium fluoroborate glasses', *Physica B Condens Matter*, 2001, doi: 10.1016/S0921-4526(01)00239-3.
- [196] B. E. Bowlby and B. Di Bartolo, 'Applications of the Judd-Ofelt theory to the praseodymium ion in laser solids', *J Lumin*, vol. 100, no. 1–4, pp. 131–139, 2002, doi: 10.1016/S0022-2313(02)00451-9.
- [197] P. Wu *et al.*, 'Spectral analysis of new-wavelength transitions originated from 1D₂ level of Pr:YLF crystal', *J Lumin*, vol. 235, no. December 2020, p. 118028, 2021, doi: 10.1016/j.jlumin.2021.118028.
- [198] Z. Wang *et al.*, 'Spectral analysis of 1G₄ level in the Pr³⁺:YLF crystal', *J Lumin*, vol. 247, Jul. 2022, doi: 10.1016/j.jlumin.2022.118870.

References

- [199] Y. Li *et al.*, 'BiOCl:Er³⁺ Nanosheets with Tunable Thickness for Photon Avalanche Phosphors', *ACS Appl Nano Mater*, vol. 2, no. 12, pp. 7652–7660, Dec. 2019, doi: 10.1021/acsanm.9b01735.
- [200] A. Kumar and A. Bahadur, 'Intense green upconversion emission by photon avalanche process from Er³⁺/Yb³⁺ co-doped NaBi(WO₄)₂ phosphor', *J Alloys Compd*, vol. 857, p. 158196, 2021, doi: <https://doi.org/10.1016/j.jallcom.2020.158196>.
- [201] T. Xiao *et al.*, 'Modification photon avalanche emission of BiOCl: Er³⁺ nanosheets through facile solvent-thermal synthesis', *Inorg Chem Commun*, vol. 117, Jul. 2020, doi: 10.1016/j.inoche.2020.107934.
- [202] Z. Luo and Y. Huang, 'Springer Series in Materials Science 289 Physics of Solid-State Laser Materials'. [Online]. Available: <http://www.springer.com/series/856>

V. Annexes

Table 11. List of samples synthesized by author of the dissertation

Lp.	Described in the dissertation	Lp.	Described in the dissertation
1.	NaYF ₄ : 0.1% Pr ³⁺	31.	NaYF ₄ : 4% Tm ³⁺ , 20% Yb ³⁺ @ NaYF ₄
2.	NaYF ₄ : 0.5% Pr ³⁺	32.	NaYF ₄ : 8% Tm ³⁺ , 20% Yb ³⁺
3.	NaYF ₄ : 1% Pr ³⁺	33.	NaYF ₄ : 8% Tm ³⁺ , 20% Yb ³⁺ @ NaYF ₄
4.	NaYF ₄ : 3% Pr ³⁺	34.	NaYF ₄ : 0.5% Ho ³⁺
5.	NaYF ₄ : 5% Pr ³⁺	35.	NaYF ₄ : 0.5% Ho ³⁺ @ NaYF ₄
6.	NaYF ₄ : 8% Pr ³⁺	36.	NaYF ₄ : 2% Ho ³⁺
7.	NaYF ₄ : 0.1% Pr ³⁺ @ NaYF ₄	37.	NaYF ₄ : 2% Ho ³⁺ @ NaYF ₄
8.	NaYF ₄ : 0.5% Pr ³⁺ @ NaYF ₄	38.	NaYF ₄ : 0.5% Ho ³⁺ , 20%Yb ³⁺
9.	NaYF ₄ : 1% Pr ³⁺ @ NaYF ₄	39.	NaYF ₄ : 0.5% Ho ³⁺ , 20%Yb ³⁺ @ NaYF ₄
10.	NaYF ₄ : 3% Pr ³⁺ @ NaYF ₄	40.	NaYF ₄ : 1% Ho ³⁺ , 20%Yb ³⁺
11.	NaYF ₄ : 5% Pr ³⁺ @ NaYF ₄	41.	NaYF ₄ : 1% Ho ³⁺ , 20%Yb ³⁺ @ NaYF ₄
12.	NaYF ₄ : 8% Pr ³⁺ @ NaYF ₄	42.	NaYF ₄ : 2% Ho ³⁺ , 20%Yb ³⁺
13.	NaYF ₄ : 0.1% Pr ³⁺ , 15% Yb ³⁺	43.	NaYF ₄ : 2% Ho ³⁺ , 20%Yb ³⁺ @ NaYF ₄
14.	NaYF ₄ : 0.3% Pr ³⁺ , 15% Yb ³⁺	44.	NaYF ₄ : 4% Ho ³⁺ , 20%Yb ³⁺
15.	NaYF ₄ : 0.5% Pr ³⁺ , 15% Yb ³⁺	45.	NaYF ₄ : 4% Ho ³⁺ , 20%Yb ³⁺ @ NaYF ₄
16.	NaYF ₄ : 0.7% Pr ³⁺ , 15% Yb ³⁺	46.	NaYF ₄ : 8% Ho ³⁺ , 20%Yb ³⁺
17.	NaYF ₄ : 0.1% Pr ³⁺ , 15% Yb ³⁺ @ NaYF ₄	47.	NaYF ₄ : 8% Ho ³⁺ , 20%Yb ³⁺ @ NaYF ₄
18.	NaYF ₄ : 0.3% Pr ³⁺ , 15% Yb ³⁺ @ NaYF ₄	48.	NaYF ₄ : 2% Er ³⁺ , 20%Yb ³⁺
19.	NaYF ₄ : 0.5% Pr ³⁺ , 15% Yb ³⁺ @ NaYF ₄	49.	NaYF ₄ : 2% Er ³⁺ , 20%Yb ³⁺ @ NaYF ₄
20.	NaYF ₄ : 0.7% Pr ³⁺ , 15% Yb ³⁺ @ NaYF ₄	50.	NaYF ₄ : 20% Er ³⁺ , 2%Yb ³⁺
21.	NaYF ₄ : 40% Yb ³⁺	51.	NaYF ₄ : 20% Er ³⁺ , 2%Yb ³⁺ @ NaYF ₄
22.	NaYF ₄ : 40% Yb ³⁺ @ NaYF ₄ :0.5%Pr ³⁺	Other synthesized colloidal nanocrystals	
23.	NaYF ₄ : 40% Yb ³⁺ @ NaYF ₄ :0.5%Pr ³⁺ @ NaYF ₄		
24.	NaYbF ₄	52.	NaYF ₄ : 0.5% Tm ³⁺ , 20% Yb ³⁺
25.	LiYF ₄ : 3% Tm ³⁺ @ LiYF ₄	53.	NaYF ₄ : 0.5% Tm ³⁺ , 20% Yb ³⁺ @ NaYF ₄
26.	NaYF ₄ : 3% Tm ³⁺	54.	NaYF ₄ : 0.2% Tm ³⁺ , 20% Yb ³⁺
27.	NaYF ₄ : 3% Tm ³⁺ @ NaYF ₄	55.	NaYF ₄ : 5% Nd ³⁺ , 15% Yb ³⁺
28.	NaYF ₄ : 8% Tm ³⁺	56.	NaYF ₄ : 5% Nd ³⁺ , 15% Yb ³⁺ @ NaYF ₄
29.	NaYF ₄ : 8% Tm ³⁺ @ NaYF ₄	57.	NaYF ₄ : 8% Pr ³⁺ , 20% Yb ³⁺
30.	NaYF ₄ : 4% Tm ³⁺ , 20% Yb ³⁺	58.	NaYF ₄ : 8% Pr ³⁺ , 20% Yb ³⁺ @ NaYF ₄

Index of Figures

Figure 1. Illustrations of (a, b) Stokes and (c, d) anti-Stokes luminescence features: (a, c) Schematic illustration of changes of energy going between ion's levels (b, d) Charts presenting of absorption and emission bands.	37
Figure 2. Simplified illustration of the effect of Coulombic field, spin-orbital coupling, and crystal field interaction on the splitting of the $[Xe]4f^n$ configuration [15].....	41
Figure 3. Energy level structure of lanthanides based on computed crystal-field energies in the range of $0-50\,000\text{ cm}^{-1}$ with labels of ^{2S+1}L and/or J, where the dominant character of the levels can be clearly assigned [1].	45
Figure 4. Schematic presentation of upconversion emission mechanisms occurring in lanthanide ions: (a) excited state absorption (ESA), (b) energy transfer upconversion (ETU), (c) photon avalanche (PA), (d) cooperative energy transfer (CET) and cooperative luminescence (CL), (e) Energy migrated-mediated upconversion (EMU) in nanocrystals of core-shell architecture.	49
Figure 5. Characteristic features and mechanism of PA emission: (a) example of PA s-shape curve of luminescence intensity in a function of pump power density measured for $\text{NaYF}_4: 0.5\%\text{Pr}^{3+}, 15\%\text{Yb}^{3+}$ @ NaYF_4 nanocrystals with indication of PA parameters: S and PA_{TH} , (b) schematic energy diagram for two neighboring ions illustrating PA key conditions.	52
Figure 6. Transitions and energy transfers responsible for PA in Tm^{3+} doped materials. Presented excitation wavelengths were proposed in the literature as leading to observe PA. GSA indicates how particular wavelength matches ground state absorption. The example CR processes are presents with the energy mismatch. In the diagram are included typically emissions reported as PA emissions.	58
Figure 7. Transitions and energy transfers responsible for PA in Pr^{3+} singly doped as well as Yb^{3+} and Pr^{3+} co-doped materials. Presented excitation wavelengths were proposed in the literature as leading to observe PA. GSA indicates how particular wavelength matches ground state absorption. The example CR processes are presents with the energy mismatch. In the diagram are included typically emissions reported as PA emissions.	60
Figure 8. Transitions and energy transfers responsible for PA-like mechanism in Ho^{3+} singly doped as well as Yb^{3+} and Ho^{3+} co-doped materials. Presented excitation wavelengths were proposed in the literature as leading to observe PA. GSA indicates how particular wavelength matches ground state absorption. The example CR processes are presents with the energy mismatch. In the diagram are included typically emissions reported as PA emissions.	62
Figure 9. Crystallographic cell of a) $\beta\text{-NaYF}_4$ and b) LiYF_4 crystal.	71
Figure 10. Scheme of the precursors preparation: (a) steps required to obtain lanthanide acetates, (b) steps leading to obtain lanthanide trifluoroacetates, (c) drying of precursor prepared according (a) or (b).	73
Figure 11. Colloidal fluoride nanocrystals synthesis scheme: adding of high-boiling solvents to precursor *and sodium trifluoroacetate in the case of spherical shell deposition; removing of residual water and oxides; adding solution of NH_4F and NaOH in methanol (MeOH) in the case of core synthesis or core nanoparticles while spherical shell deposition *or both during ellipsoidal shell deposition; solvents evaporation; appropriate synthesis.	74
Figure 12. Home-built microscopic setup used for measurements of luminescence intensity in a function of excitation source pump power density as well as luminescence rise- / decay- times.	79

Figure 13. Exemplary energy diagram illustrating energy transfers between two ions under wavelength excitation matched ESA and off-resonant with GSA. This diagram was used to write DRE (Equations 10-13) aiming to explain description of particular processes. 84

Figure 14. XRD pattern of LiYF_4 crystals with XRD patterns of synthesized materials doped with (a) 3% and (b) 8% of Tm^{3+} ions. Based on [50]. 86

Figure 15. Size comparison of investigated LiYF_4 crystals: TEM pictures of cANP (a),(e) and csANP (b),(f) doped with 3% and 8% of Tm^{3+} ions, respectively; SEM of 3% (c) and 8% (g) Tm^{3+} doped μAP ; bAC (d). Based on [50]. 87

Figure 16. Theoretical excited state absorption spectra calculated for Tm^{3+} ions in LiYF_4 matrix for (a) ${}^3\text{F}_4 \rightarrow {}^3\text{F}_2$ and (b) ${}^3\text{F}_4 \rightarrow {}^3\text{F}_3$ transition. 89

Figure 17. Theoretical excited state absorption spectra calculated for Tm^{3+} ions in different matrices for (a) ${}^3\text{F}_4 \rightarrow {}^3\text{F}_2$ and (b) ${}^3\text{F}_4 \rightarrow {}^3\text{F}_3$ transition. 90

Figure 18. Thulium photon avalanche pump power dependent at 800 nm luminescence characteristics for nano, micro and bulk PA crystals doped with a) 8% and b) 3% Tm^{3+} ions. Pump power dependent comparison of: row 1 – PA emission intensity, row 2 – PA slopes, row 3 – PA gains and row 4 – 50% risetimes. Based on [50]. 92

Figure 19. Characteristics of PA emission at 475 nm (1064 nm excitation) of: bulk crystals (green), microcrystals (blue), core nanocrystals (gray), and core-shell nanocrystals (red) for the LiYF_4 materials doped with 3% (right column) and 8% (left column) of Tm^{3+} ions. The slopes (S), gains (D_{AV}) as well as risetimes ($t_{50\%}$) were calculated automatically with use of a home developed software. Based on [50]. 93

Figure 20. a) Energy diagram of Tm^{3+} ions with transitions leading to obtain PA emission, absorption spectra of Tm^{3+} in LiYF_4 : left – measured ground state absorption spectra, right – calculated excited state absorption spectra. Bottom: Power dependent simulated behavior of PA emission – [middle row: (b), (d), (f), (h), (j), (l)] PA emission intensity and [bottom row: (c), (e), (g), (i), (k), (m)] PA slopes in response to changes of phenomenological parameters: $A_2 = 250, 200, 150, 100, 50, 20 \text{ s}^{-1}$, $A_3 = 1000, 500, 250, 100, 50, 25 \text{ s}^{-1}$, $f_{\text{ESA}} = 5, 2, 1, 0.5, 0.2, 0.1, 0.05, 0.02, 0.01$; $k_2 = 1000, 500, 250, 100, 50, 25 \text{ s}^{-1}$, $k_3 = 2000, 1000, 500, 250, 50, 25 \text{ s}^{-1}$ and $f_{\text{CR}} = 0.5, 0.2, 0.1, 0.05, 0.02, 0.01$. Individual parameters were varied one at a time, while the other were fixed. More saturated color indicates higher values. Black dotted lines correspond experimental data obtained for 8% Tm^{3+} -doped $\text{NaYF}_4@ \text{NaYF}_4$ colloidal nanocrystals at RT. Based on [50]. 95

Figure 21. PASSI imaging demonstrations on single LiYF_4 : 3% Tm^{3+} @ NaYF_4 nanocrystal at various pumping powers. a–c) presents PASSI maps for different pumping intensities, d) PA emission cross sections for particular power densities, e) values of FWHM (left axis) and S (right axis) corresponding to the cross-sections and f) demonstration of the imaged spot FWHM changes with varying S (left axis) and the resolution enhancement (right axis). Based on [50]. 96

Figure 22. XRD for singly doped with 0.1%, 0.5%, 1%, 3%, 5% and 8% of Pr^{3+} ions core and core-shell $\beta\text{-NaYF}_4$ nanocrystals as well as the template of the $\beta\text{-NaYF}_4$ structure. 98

Figure 23. Morphology characteristics of $\beta\text{-NaYF}_4$ nanocrystals singly doped with Pr^{3+} ions: TEM images as well as histograms presenting average sizes of the core and core-shell nanocrystals doped singly with (a) 0.1%, (b) 0.5%, (c) 1% and (d) 3%, (e) 5% and (f) 8% of Pr^{3+} ions. 99

Figure 24. XRD for core and core-shell $\beta\text{-NaYF}_4$ nanocrystals co-doped with x% Pr^{3+} and 15% Yb^{3+} ions as well as the template of the $\beta\text{-NaYF}_4$ structure. 101

Figure 25. Characteristic of β-NaYF₄ nanocrystals co-doped with Pr³⁺ and Yb³⁺ ions: TEM pictures of core nanoparticles (a, d, g, j); TEM of core-shell nanocrystals (b, e, h, k); Histograms presenting average sizes of core and core-shell nanocrystals (c, f, i, l).....	101
Figure 26. (a) EDS map and (b) EDS profile of Yb ³⁺ and Y ³⁺ ions in NaYF ₄ : 0.5% Pr ³⁺ , 15%Yb ³⁺ @ NaYF ₄ nanocrystal.	102
Figure 27. Characteristics of NaYbF₄ crystals: (a) XRD of NaYbF ₄ crystal phase (template) and for synthesized sample; (b),(c) TEM images; (d) Histogram with average particles sizes.	103
Figure 28. XRD of β -NaYF ₄ structure (template) and of NaYF ₄ :40%Yb ³⁺ , NaYF ₄ :40%Yb ³⁺ @ NaYF ₄ :0.5%Pr ³⁺ and NaYF ₄ :40%Yb ³⁺ @ NaYF ₄ :0.5%Pr ³⁺ @NaYF ₄ crystals.	103
Figure 29. TEM images of: (a,b) NaYF ₄ :40%Yb ³⁺ , (c,d) NaYF ₄ :40%Yb ³⁺ @ NaYF ₄ :0.5%Pr ³⁺ and (e,f) NaYF ₄ :40%Yb ³⁺ @ NaYF ₄ :0.5%Pr ³⁺ @NaYF ₄ crystals as well as (g) corresponding histograms with average particles sizes.....	104
Figure 30. Spectroscopic measurements for β-NaYF₄ nanocrystals: Absorption and scattering spectra of β -NaYF ₄ nanocrystals: (a) cores and core-shells co-doped with Pr ³⁺ and Yb ³⁺ ions (b) core-shells doped with Pr ³⁺ ions; Excitation spectra for (c) cores and core-shells co-doped with Pr ³⁺ and Yb ³⁺ ions monitoring emission at 980 nm (d) core-shells doped with Pr ³⁺ ions monitoring emission at 607 nm; Emission spectra under excitation with 444 nm for (e) cores and core-shells co-doped with Pr ³⁺ and Yb ³⁺ ions (f) core-shells doped with Pr ³⁺ ions. Inserted plots: in absorption and scattering spectra (a) and (b) present integral area under the peak at 444 nm; in excitation spectra show changes of the integral area under the peak at 444 nm with concentration of Pr ³⁺ ions for (c) core and core-shell samples co-doped with Pr ³⁺ , Yb ³⁺ ions (d) core-shell singly Pr ³⁺ doped nanocrystals; in emission spectra show changes of the integral area under the peak at 482 nm with concentration of Pr ³⁺ ions for (e) core and core-shell samples co-doped with Pr ³⁺ , Yb ³⁺ ions (f) core-shell singly Pr ³⁺ doped nanocrystals.....	106
Figure 31. Anti-Stokes emission spectra of β-NaYF₄ nanocrystals (a) core-shells singly doped with Pr ³⁺ ions, (b) cores co-doped with x% Pr ³⁺ , 15% Yb ³⁺ , (c) x% Pr ³⁺ , 15% Yb ³⁺ co-doped cores with passive shell, with assigned transitions. Presented emission spectra were measured under 852 nm excitation (1.5 MW/cm ²) at RT. Based on [189].....	107
Figure 32. Fluorescence lifetime decay curves of NaYF ₄ :0.5 % Pr ³⁺ , 15% Yb ³⁺ @ NaYF ₄ nanocrystals measured at 482 nm (blue curve) and 607 nm (orange curve) under 444 nm excitation wavelength at RT. Based on [189].....	109
Figure 33. Parameters of short and long components of fluorescence lifetime decay curves of NaYF ₄ :0.5 % Pr ³⁺ , 15% Yb ³⁺ @ NaYF ₄ nanocrystals measured at wide range of temperatures at (a-b) 482 nm and (c-d) 607 nm. Based on [189].....	109
Figure 34. Spectroscopic PA characteristics of core and core-shell β-NaYF₄ nanocrystals co-doped with 15% Yb³⁺ and x% Pr³⁺ ions (x=0.1, 0.3, 0.5 or 0.7). PA features recorded for core (●) and core-shell (○) nanoparticles top row: at 482 nm and bottom row: at 607 nm: (a),(b) pump-power dependence of PA luminescence; (c),(d) Maximum values of S, which are a measure of nonlinearity of the PA process (Equation 2); (e),(f) PA _{TH} pump powers in a function of concentration of Pr ³⁺ ions. (g),(h) Mean values of D _{AV} parameters indicating efficiency of PA process. Average values and standard deviations for (c, d, e, f) were calculated based on a few (2-4) measurements of curve of intensity in a function of pump power density. Based on [189].	111
Figure 35. Core NaYF₄:0.5%Pr³⁺, 15%Yb³⁺ and core-shell NaYF₄:0.5%Pr³⁺, 15%Yb³⁺@NaYF₄ nanocrystals characteristics. a) XRD patterns, b) histograms presenting materials sizes, c) core and e) core-shell nanocrystals TEM image; d) core and f) core-shell nanocrystals high-resolution transmission electron microscopy (HRTEM) images; g) EDS map and h) EDS profiles of Yb ³⁺ and Y ³⁺ ions in the representative core-shell nanocrystal [25].	113

Figure 36. Characteristics of the 607 nm photon avalanche emission in the core-shell $NaYF_4$ nanocrystals co-doped with 0.5% Pr^{3+} and 15% Yb^{3+} under 852 nm photoexcitation. Panel a) presents photon avalanche emission intensity pump power dependence at various temperatures, b) demonstrates the highest PA non-linearities (S_{max}) derived by the algorithm described in ref.[50] (full circles) and manually (open circles); c) presents maximal PA gain at the excitation intensity corresponding to highest non-linearity (i.e. $D_{AV}(I_{exc}@S_{MAX})$), d) demonstrates PA threshold in a function of temperature. All datasets on b-d) were derived from the measurements of luminescence intensity in a power density function (a) [25]. 114

Figure 37. a) Energy levels of Pr^{3+} and Yb^{3+} ions with transitions leading to obtain SPA emission. The DRE have been written based on the presented energy diagram, excluding a gray elements. Simulated PA emission behavior is presented in the panels from (b) to (k). Each panels show, how variation of particular parameters, i.e. nonradiative transitions (w_{65} , w_{71} , w_{74} , w_{64} , NR_{21}), radiative lifetimes (τ_{Yb} , τ_4 , τ_5) as well as absorption cross sections (σ_{ESA} , σ_{Yb}) used in the developed model influenced the s-shape profiles. Saturated colors correspond to higher values of the parameters, while the black curve was obtained for pristine (literature) values. (l) Pump power dependent profiles of PA luminescence intensity obtained from theoretical modeling for Yb^{3+} , Pr^{3+} (navy blue) and for pure Pr^{3+} (pink) doped systems. Based on [189]. 116

Figure 38. PA simulated results for system co-doped with Pr^{3+} , Yb^{3+} ions: each panel consists of two elements: pump power dependent luminescence intensity of PA emission and corresponding values of slopes of these s-shaped curves. Each of the panels illustrate how changes of particular parameters, namely nonradiative transitions: **(a)** w_{65} , **(b)** w_{71} , **(c)** w_{74} , **(d)** w_{64} **(h)** NR_{21} , radiative lifetimes: **(e)** τ_{Yb} **(f)** τ_4 , **(g)** τ_5 , and absorption cross sections: **(i)** σ_{ESA} , **(j)** σ_{Yb} affect PA properties. Saturated colors correspond to higher values of the parameters, while the black curves were obtained for pristine (literature) values. Based on [189]. 124

Figure 39. XRD of β - $NaYF_4$ crystallographic structure (Template) and β - $NaYF_4$ nanocrystals doped with Tm^{3+} as well as co-doped with Yb^{3+} and Tm^{3+} ions in both core and core-shell architecture. 128

Figure 40. Morphology characteristics of core and core-shell $NaYF_4$ nanocrystals doped with 3% Tm^{3+} , 8% Tm^{3+} and co-doped with 4% Tm^{3+} , 20% Yb^{3+} ions as well as 8% Tm^{3+} , 20% Yb^{3+} : TEM images of core nanocrystals **a, b, c, d**; TEM images of core-shell nanoparticles **e, f, g, h**; histograms **i, j, k, l**, respectively 129

Figure 41. Intensity of photoluminescence at 810 nm of nanocrystal doped with Tm^{3+} as well as co-doped with Tm^{3+} and Yb^{3+} ions in a function of pump power density under: (a) 1059 nm and (b) 976 nm excitation source. 130

Figure 42. XRD of β - $NaYF_4$ core and core-shell nanocrystals singly doped with Ho^{3+} ions (0.5% and 2%) as well as co-doped with Yb^{3+} ions (constant amount of 20%) and Ho^{3+} ions (0.5%, 1%, 2%, 4% or 8%) together with template for β - $NaYF_4$ crystal phase. 131

Figure 43. Morphology characteristics of Ho^{3+} doped as well as Ho^{3+} and Yb^{3+} co-doped core and core-shell $NaYF_4$ nanocrystals. Particular rows of the figure are composed of TEM images as well as histogram for crystals doped with: **(a, b, c)**: 0.5% Ho^{3+} ; **d, e, f**: 2% Ho^{3+} ; **(g, h, i)**: 0.5% Ho^{3+} , 20% Yb^{3+} ; **(j, k, l)**: 1% Ho^{3+} , 20% Yb^{3+} ; **(m, n, o)**: 2% Ho^{3+} , 20% Yb^{3+} **(p, q, r)**: 4% Ho^{3+} , 20% Yb^{3+} ; **(s, t, u)**: 8% Ho^{3+} , 20% Yb^{3+} ions. 132

Figure 44. Absorption spectra of core and core-shell nanocrystals singly doped with Ho^{3+} ions (0.5% and 2%) as well as co-doped with Yb^{3+} ions (constant amount of 20%) and Ho^{3+} ions (0.5%, 1%, 2%, 4% or 8%). 133

-
- Figure 45.** Emission spectra of NaYF₄: 1% Ho³⁺, 20% Yb³⁺ @ NaYF₄ nanocrystals under excitations at 975 and 1059 nm. Inset contains integral area under the bands 540 nm and 650 nm for both 975 nm (pink points) and 1059 (blue points) excitations. 134
- Figure 46.** The luminescence intensities of emissions monitored at 540 nm (first column) and 650 nm (second column) in a function of pump power densities of excitation sources, namely 1059 nm (first row) and 975 nm (second row) for core-shell nanocrystals doped with Ho³⁺ as well as co-doped with Ho³⁺ and Yb³⁺ ions. 135
- Figure 47.** X-ray powder diffractions of nanocrystals co-doped with Er³⁺ and Yb³⁺ ions as well as the template for β-NaYF₄ crystal phase. 136
- Figure 48. Characteristics of core and core-shell nanocrystals co-doped with 2% Er³⁺ and 20% Yb³⁺ ions.** TEM images of: **a, b, c:** core and **d, e, f:** core-shell nanocrystals as well as **g** histogram with average sizes. 137

Index of Tables

Table 1. Lanthanides with atomic number and electron configuration	40
Table 2. The values of Ω parameter for particular matrices.....	80
Table 3. Squared Reduced-Matrix Elements $ \langle 4f^{11}\alpha[SL] J \ U^{(t)} \ 4f^{11}\alpha[S'L'] J' \rangle ^2$ parameters for Tm^{3+} ion for transition from level start J to level end J'	81
Table 4. <i>Refractive indexes used in calculations of theoretical absorption spectra.</i>	82
Table 5. Average dimensions for Tm^{3+} doped cANP, csANP, μ AP and bAC.	88
Table 6. Average dimensions and shell thicknesses of β -NaYF ₄ nanocrystals singly doped with Pr^{3+} ions.	100
Table 7. Average dimensions and shell thicknesses of β -NaYF ₄ nanocrystals co-doped with Pr^{3+} and Yb^{3+} ions. Based on [189].	102
Table 8. Values of average maximum slopes and average thresholds with standard deviations of PA emission at 482 nm and 607 nm of core-shell nanocrystals co-doped with 15% Yb^{3+} and 0.1%, 0.3%, 0.5% or 0.7% of Pr^{3+} ions. Based on [189].....	112
Table 9. Parameters adopted for the DRE solution. Based on [189].	117
Table 10. Changes in the values of DRE parameters to check their effect on PA characteristics. *Some parameters had no effect on PA. Based on [189].	120
Table 11. List of samples synthesized by author of the dissertation	159